Magneto-optical spectroscopy of multilayer graphene and graphene-hexagonal boron nitride hetero-structures

Younes Henni

▶ **To cite this version:**

Younes Henni. Magneto-optical spectroscopy of multilayer graphene and graphene-hexagonal boron nitride hetero-structures. Physics [physics]. Université Grenoble Alpes, 2016. English. NNT : 2016GREAY060 . tel-01588425

HAL Id: tel-01588425
https://theses.hal.science/tel-01588425

Submitted on 15 Sep 2017

HAL is a multi-disciplinary open access archive for the deposit and dissemination of scientific research documents, whether they are published or not. The documents may come from teaching and research institutions in France or abroad, or from public or private research centers.

L'archive ouverte pluridisciplinaire **HAL**, est destinée au dépôt et à la diffusion de documents scientifiques de niveau recherche, publiés ou non, émanant des établissements d'enseignement et de recherche français ou étrangers, des laboratoires publics ou privés.

Communauté
UNIVERSITÉ Grenoble Alpes

THÈSE

Pour obtenir le grade de

DOCTEUR DE LA COMMUNAUTÉ UNIVERSITÉ GRENOBLE ALPES

Spécialité : **Physique de la matière condensée et du rayonnement**

Arrêté ministériel : 25 mai 2016

Présentée par

Younes HENNI

Thèse dirigée par **Clément Faugeras** et
codirigée par **Marek Potemski**

préparée au sein du **Laboratoire national des champs magnétiques intenses, CNRS, Grenoble, France**
dans **l'École Doctorale de physique de Grenoble**

Etudes magnéto-Raman de systèmes – graphène multicouches et hétérostructures de graphène-nitrure de bore

Thèse soutenue publiquement le **24 Octobre 2016**
devant le jury composé de :

Dr. Matteo Calandra
Directeur de recherche, IMPMC, Université Paris-Diderot, Président
Dr. Guillaume Cassabois
Professeur, Laboratoire Charles Coulomb-CNRS, Université de Montpellier, Rapporteur
Dr. Adam Babinski
Professeur, Institut de physique expérimentale, Université de Varsovie, Rapporteur
Dr. Johann Coraux
Chargé de recherche, Institut Néel-CNRS, Grenoble, Examinateur
Dr. Clément Faugeras
Chargé de recherche, LNCMI-CNRS, Grenoble, Directeur de thèse
Dr. Marek Potemski
Directeur de recherche, LNCMI-CNRS, Grenoble, Co-Directeur de thèse

Part of my work has been achieved with the tremendous help from my collaborators in Bariloche, Argentina: Hector Pablo Ojeda Collado, and his supervisors Dr. Gonzalo Usaj, and Dr. Carlos Balseiro. They contributed significantly to build the theoretical model that was relevant for the analysis and the interpretation of my experimental data. Many thanks to you.

During these years, I had the chance to build strong connections with some people from our lab. They always stand by my side and together, we surely spent memorable times outside the work place. My thanks go in particular to: Maciej Koperski, Remi Blinder, Laurant Lozano, Artur Slobodeniuk, Julien Jousset, Julien Marpaud, Tara Benkel, Isabelle Bisotto, Robert Pankov, and Stefan Kramer.

Every time I needed help or any kind of assistance, I found it from the people working in our lab. I am very thankful to the I.T. people: Thomas Dolmazon and Sebastien Buisson, and the Administration staff: Amelie Pic, Natacha Hubert, and Alexandra Gasparini. Special thanks go to Sandrine Ferrari at the Ecole Doctorale de Physique, for her huge efforts regarding the administrative tasks related to obtaining this PhD diploma.

I kindly acknowledge the funding support from the European Research Council, under the project: magneto-optics of layered materials: exploring many-body physics in electronic systems with unconventional bands (ERC MOMB).

It is my pleasure to thank Dr. Guillaume Cassabois and dr.hab. Adam Babinski for accepting to be the referees of this thesis manuscript. My thanks also go to Dr. Matteo Calandra and Dr. Johann Coraux for accepting to be part of the jury of my defense.

Finally, I would like to thank my family and friends: my beloved parents for their endless support and encouragement, my dear aunt in Strasbourg, who helped me a lot in the beginning when I first arrived to France, and my brothers and sister for strongly believing in me. For this work, I had big moral support from my childhood friends; Hamza Abdat, Rami Kota, Fouzi Metina, and Adel Betina.

Résumé

Introduction (English)

As the fourth most abundant element in the universe, Carbon plays an important role in the emerging of life in earth as we know it today. The industrial era has seen this element at the heart of technological applications due to the different ways in which carbon forms chemical bonds, giving rise to a series of allotropes each with extraordinary physical properties. For instance, the most thermodynamically stable allotrope of carbon, graphite crystal, is known to be a very good electrical conductor, while diamond very appreciated for its hardness and thermal conductivity is nevertheless considered as an electrical insulator due to different crystallographic structure compared to graphite. The advances in scientific research have shown that crystallographic considerations are not the only determining factor for such a variety in the physical properties of carbon based structures. Recent years have seen the emergence of new allotropes of carbon structures that are stable at ambient conditions but with reduced dimensionality, resulting in largely different properties compared to the three dimensional structures. These new classes of carbon allotropes are namely: carbon nanotubes (one dimensional), fullerene (zero dimensional), and the last discovered allotrope of carbon, also known as the first two-dimensional material: graphene.

The successful isolation of monolayers of graphene challenged a long established belief in the scientific community: the fact that purely 2D materials cannot exist at ambient conditions. The Landau-Peierls instability theorem states that purely 2D materials are very unstable due to increasing thermal fluctuations when the material in question extends in both dimensions. To minimize its energy, the material will break into coagulated islands, an effect known as island growth. Graphene happens to overcome such barrier by forming continuous ripples on the surface of its substrate and thus is stable even at room temperature and atmospheric pressure.

A great intention from the scientific community has been given to graphene, after the first published results on the electronic properties of this material. Both fundamental and mechanical properties of graphene are fascinating. Thanks to its carbon atoms that are packed in a sp^2 hybridized fashion, thus forming a hexagonal lattice structure, graphene has the largest young modulus and stretching power, yet it is hundreds of times stronger than steel. It conducts heat and electricity very efficiently, achieving an electron mobility as high as 10^7 $cm^{-2}V^{-1}$ s^{-1} when suspended over the substrate.

The most fascinating aspect about graphene is the nature of its low energy charge carriers. Indeed, graphene has a linear energy dispersion at the charge neutrality, giving the charge carriers in graphene a relativistic nature. Many phenomena observed in this

material are consequences of this relativistic nature of its carriers. Ballistic transport, universal optical conductivity, absence of back-scattering, and a new class of room temperature quantum Hall effect are good examples of newly discovered phenomena in this material.
Graphene has become an active research area in condensed matter physics since 2004. It is however still early to state that all the physical properties of this material are well understood. In this thesis we conducted magneto-Raman spectroscopy experiments to address some of the open questions in the physics of graphene, such as the effect of electron-electron coupling on the energy spectrum of monolayer graphene, and the change in the physical properties of multilayer graphene as a function of the crystallographic stacking order. In all our experiments, the graphene-based systems have been subject to strong continuous magnetic fields, applied normal to the graphene layers. We study the evolution of its energy excitation spectra in the presence of the magnetic field, and also the coupling between these excitations and specific vibrational modes that are already in the system. This experimental approach allows us to deduce the band structure of the studied system in the absence of magnetic fields, as well as many other low energy properties.

This work is organized as the following:

Chapter 1:
In the first chapter of the doctoral thesis, a general introduction to the physics of graphene is established. We introduce its crystal structure, which is the constituent base for other allotropes of carbon, including graphite and carbon nanotubes. Then its electronic band structure at low energy is derived based on the tight binding model. The case of multilayer graphene, with stacks of several layers one upon the other, is discussed from a stacking geometry point of view: Bernal or rhombohedral. The band structure which corresponds to each type of multilayer is then derived using a model similar to the tight binding approach of monolayer graphene.
The application of a uniform magnetic field perpendicular to the surface of graphene induces a quantization of its energy levels. This effect is also discussed for the case of multi-layer graphene in both types of stacks Bernal or rhombohedral, and for bulk graphite.

Chapter 2:
In chapter 2 the experimental technique, called Raman spectroscopy and used along the thesis, is discussed. Firstly, we introduce the Raman scattering effect which is the basis of this spectroscopic technique. We will discuss the selection rules for Raman scattering and the most prominent vibrational modes in the Raman spectra of graphene and multilayer graphene.

We will trace the work that has been done so far on graphene and multilayer graphene using Raman spectroscopy. How this experimental technique allows to extract a large number of information on the studied system: such as the number of layers, the crystallographic order, and the presence of charge doping or mechanical strain.
The effect of magnetic field on the excitation spectra is then discussed. Two major effects will be highlighted: (i) The inter-band electron-hole excitations between Landau levels, which are observed in the Raman spectra of graphene in a magnetic field. (Ii) The coupling between the Raman modes in graphene and the inter-Landau level transitions.

Chapter 3:
In chapter 3, we introduce the experimental tools that were necessary to achieve this thesis. Firstly, we discuss the micro-Raman spectroscopy tool at room temperature, necessary for the characterization of samples. Then, we introduce the apparatus for magneto-Raman spectroscopy at low temperatures. It comprises a micro-Raman probe that is operational at liquid helium temperature, placed into the cryostat. The cryostat is coupled to an electromagnet which delivers a continuous magnetic field up to 30 Tesla. For Raman spectroscopy at low frequencies, the free beam Raman probe is presented along the triple stages spectrometer which allows a maximum filtering of the scattered light.

Chapter 4:
In chapter 4, we discuss results in our magneto-Raman study of graphene and graphene bilayer structures on top of hexagonal boron nitride layers. In magnetic fields up to 30 Tesla, we trace the evolution of inter-Landau levels electronic excitations. We also study the coupling of Raman modes at the *Gamma* point with the electronic excitations in these systems.
This study highlights the effects of Coulomb interactions for charge carriers in graphene. The Coulomb interactions are manifested by a band velocity changing logarithmically as a function of the magnetic field, and as a function of the Landau level index. This band velocity re-normalization is in clear contrast to the single particle picture, usually used to describe the electronic properties of graphene. However, our results confirm recent studies on the effect of the Coulomb interactions on the dispersion of the energy bands at the charge neutrality point.
The experimental results are reproduced by a theoretical model based on first order perturbation theory and the random phase approximation.

Chapter 5:
Chapter 5 is devoted to the results obtained in the magneto-Raman study of multilayer graphene with rhombohedral stacking of its atomic layers. This work was motivated by the lack of consistent study of the band structure of rhombohedral multilayer graphene

with a number of layers greater than four. Especially that some theoretical work suggested that this stacking hosts strongly correlated electrons, in which new effects can be observed, such as ferromagnetism and superconductivity.
Using magneto-Raman spectroscopy, we trace the changes in magnetic field of the electronic excitations in a graphene flake partially suspended over the substrate. The analysis of this dispersion by a theoretical model, based on the tight binding approach, allowed to deduce a pure rhombohedral stacking of graphene layers up to 15.
Another region in the flake shows signatures of the two types of stacking: Bernal and rhombohedral. The magneto-Raman study of this mixed stacking has a very rich electronic excitation spectrum, but that can be reproduced theoretically by a simple model with only two free parameters.

Annex:
In the appendix we discuss the methods of manufacturing that were followed to produce the structures studied in this thesis and presented in chapters 4 and 5: (i) graphene encapsulated within boron nitride. (ii) multilayer rhombohedral graphene.
The calculations of the Raman contrast in chapter 5 are also explained in details.

Introduction (Français)

Comme le quatrième élément le plus abondant dans l'univers, le carbone joue un rôle important dans l'émergence de la vie sur la terre comme nous la connaissons aujourd'hui. L'ère industrielle a vu cet élément au cœur des applications technologiques en raison des différentes façons dont les atomes forment les liaisons chimiques, ce qui donne lieu à une série d'allotropies chacun ayant des propriétés physiques extraordinaires. Par exemple, l'allotrope le plus thermodynamiquement stable du carbone, le cristal de graphite, est connu pour être un très bon conducteur électrique, tandis que le diamant, très apprécié pour sa dureté et sa conductivité thermique, est néanmoins considéré comme un isolant électrique en raison de sa structure cristallographique différente par rapport au graphite. Les progrès de la recherche scientifique ont montré que les considérations cristallographiques ne sont pas le seul facteur déterminant pour une telle variété dans les propriétés physiques des structures à base de carbone. Ces dernières années ont vu l'émergence de nouvelles formes allotropiques de structures de carbone qui sont stables dans les conditions ambiantes, mais avec dimensionnalité réduite, ce qui entraîne des propriétés largement différentes par rapport aux structures en trois dimensions. Ces nouvelles classes d'allotropes de carbone sont notamment : les nanotubes de carbone (à une dimension), fullerène (zéro dimension), et le dernier allotrope découvert du carbone, également connu comme étant le premier matériau à deux dimensions : le graphène.
L'isolation réussi de monocouches de graphène a contesté une croyance établie depuis longtemps dans la communauté scientifique : le fait que les matériaux purement 2D ne peuvent pas exister dans les conditions ambiantes. Le théorème d'instabilité de Landau-Peierls atteste que les matériaux purement 2D sont très instables en raison de l'augmentation des fluctuations thermiques lorsque le matériau en question se prolonge dans les deux dimensions. Afin de minimiser son énergie, le matériau se brisera en îlots coagulées, un effet connu comme la croissance des îlots. Le graphène arrive cependant à surmonter cette barrière en formant des ondulations continues sur la surface du substrat et est stable même à température ambiante et pression atmosphérique.
Une grande intention de la part de la communauté scientifique a été donnée au graphène, après les premiers résultats publiés sur les propriétés électroniques de ce matériau. Les propriétés fondamentales et mécaniques du graphène sont fascinants. Grace aux atomes de carbone qui sont emballés dans un mode sp ^{2} hybridé, formant ainsi une structure de réseau hexagonal, le graphène possède le plus grand module de Young et la plus grande capacité d'étirement, en même temps des centaines de fois plus dur que l'acier. Il conduit la chaleur et l'électricité de manière très efficace, réalisant ainsi une mobilité électrique aussi élevé que 10^{7} cm $^{-2}$ V $^{-1}$ s $^{-1}$ lorsque suspendu au-dessus du substrat. L'aspect le plus fascinant à propos du graphène est surement la nature de ses porteurs de charge à basse énergie. En effet, le graphène présente une dispersion d'énergie linéaire

au point de neutralité de charge, donnant aux porteurs de charge dans le graphène une nature relativiste. De nombreux phénomènes observés dans ce matériau sont des conséquences de cette nature relativiste de ses porteurs. Le transport balistique, la conductivité optique universelle, absence de rétrodiffusion, et une nouvelle classe d'effet Hall quantique à température ambiante sont de bons exemples de phénomènes nouvellement découverts dans ce matériau.
Le graphène est devenu un domaine de recherche actif en physique de la matière condensée depuis 2004. Il est cependant encore trop tôt pour affirmer que toutes les propriétés physiques de ce matériau sont bien comprises. Dans cette thèse, nous avons mené des expériences de spectroscopie magnéto-Raman pour répondre à certaines des questions ouvertes dans la physique du graphène, notamment l'effet de couplage électron-électron sur le spectre d'énergie du graphène monocouche, et le changement dans les propriétés physiques du graphène multicouche en fonction de l'ordre d'empilement cristallographique. Dans toutes nos expériences, les systèmes à base de graphène ont été soumis à de forts champs magnétiques continus, appliqués perpendiculairement aux couches de graphène. On étudie l'évolution de son spectre d'excitation d'énergie en présence du champ magnétique, ainsi que le couplage entre ces excitations et des modes vibratoires spécifiques. Cette approche expérimentale permet de déduire la structure de bande du système étudié, en l'absence de champs magnétiques, ainsi que de nombreuses autres propriétés à faible énergie.

Ce travail de thèse est organisé comme suit :

Chapitre1 :
Dans le premier chapitre de ce manuscrit de thèse, une introduction générale à la physique du graphene est établie. On introduira sa structure cristalline qui est la base constituante de plusieurs autres allotropes du carbone, notamment le graphite et les nanotubes de carbone. Ensuite sa structure de bande électronique a basse énergie est dérivée en se basant sur le model des liaisons fortes. Le cas du graphene multicouche, avec des empilements de plusieurs couches l'une sur l'autre, est discuté dans une perspective de géométrie d'empilement : Bernal ou rhomboédrique. La structure de bande qui correspond à chaque type d'empilement est ensuite dérivée à l'aide d'un model similaire à celui de la monocouche.
L'application d'un champ magnétique uniforme perpendiculaire à la surface du graphene induit une quantification des niveaux d'énergies électroniques. Cet effet est aussi discuté pour les cas du graphene multicouches dans les deux types d'empilements Bernal et rhomboédrique, et le graphite.

Chapitre2 :
Dans le chapitre 2 la technique expérimentale, appelé spectroscopie Raman et utilise le

long de cette thèse, est discutée. On introduit tout d'abord l'effet de diffusion Raman qui est à la base de cette technique de spectroscopie. On discutera les règles de sélections de la diffusion Raman et les modes vibrationnels les plus observes dans les spectres Raman du graphene et graphene multicouche.
On retracera les travaux de spectroscopie Raman qui ont été fait jusqu'à présent sur le graphene et le graphene multicouches. Comment cette méthode expérimentale permet d'avoir un nombre important d'informations sur le system étudie, tel que le nombre de couches, le type d'empilent, mais aussi la présence de dopage ou de tension mécanique. L'effet du champ magnétique sur les spectres d'excitations est ensuite discuté. Deux effets majeurs seront mis en évidence : (i) Les excitations inter-bande de type électron-trou entre niveaux de Landau, qui sont observé dans les spectres Raman du graphene sous champ magnétique. (ii) Le couplage entre les modes Raman dans le graphene est les excitations électroniques inter-bande dans sa structure de niveaux de Landau sous champ magnétique.

Chapitre3 :
Dans le chapitre 3 on introduit les outils expérimentaux nécessaires à la réalisation de ce travail de thèse. Tout d'abord en discute l'outil de spectroscopie micro-Raman à température ambiante, nécessaire à la caractérisation des échantillons. Ensuite on introduit l'appareillage pour la spectroscopie magnéto-Raman a basse température. Il comprend la sonde micro-Raman qui est opérationnelle a température de l'Hélium liquide, et qui peut être introduite dans le cryostat. Ce cryostat est couplé à un électro-aimant qui délivre un champ magnétique continue jusqu'à 30 Tesla.
Pour la spectroscopie Raman a basse fréquence, on discute la sonde Raman à espace libre, et le spectromètre à trois étages qui permet un filtrage maximal de la lumière diffusée.

Chapitre4 :
Dans le chapitre 4 nous discuteront les résultats obtenus dans notre étude magnéto-Raman sur des structures de graphene et graphene bicouche sur des couches de nitrure de bore hexagonal. Dans des champs magnétiques allant jusqu'à 30 Tesla, on trace l'évolution des excitations électroniques inter-niveaux de Landau. En étudie aussi le couplage des modes Raman au point Γ avec les excitations électroniques dans ces systèmes.
Cette étude permet de mettre en évidence les effets de l'interaction Coulombienne pour les porteurs de charges dans le graphene. Ces interactions Coulombienne se manifestent par une vitesse de bande qui évolue de manière logarithmique en fonction du champ magnétique, ainsi qu'en fonction de l'indice du niveau de Landau. Cette re-normalisation de la vitesse de bande va à l'encontre du modèle de la particule libre, longuement utilisé pour décrire les propriétés électroniques du graphene. Cependant, nos résultats viennent

confirmer de récentes études sur l'effet de l'interaction Coulombienne sur la dispersion des bandes d'énergie au niveau de Fermi.
Les résultats expérimentaux sont reproduits par un modèle théorique se basant sur la théorie des perturbations ainsi que l'approximation de phase aléatoire.

Chapitre5 :
Le chapitre 5 est consacré aux résultats obtenues dans l'étude magnéto-Raman du graphene multicouche avec empilement rhomboédrique de ces couches atomiques. Ce travail a été motivé par l'absence d'étude consistante de la structure de bande du graphene multicouche rhomboédrique avec un nombre de couche supérieur à quatre. Surtout que certains travaux théoriques proposent cet empilement comme un système électronique fortement corrélés, dans lequel de nouveaux effets peuvent être observés, tel que le ferromagnétisme et la supraconductivité.
En utilisant la spectroscopie magnéto-Raman, on a tracé l'évolution en champ magnétique des excitations électroniques dans un flocon de graphene partiellement suspendu sur le substrat. L'analyse de cette dispersion par un modèle théorique, basé sur la méthode des liaisons fortes, a permis de déduire un empilement rhomboédrique d'un nombre de couches allant jusqu'à 15.
Une autre région dans le flocon présente les deux types d'empilement : Bernal et rhomboédrique. L'étude magnéto-Raman de cet empilement mixte présente un spectre d'excitation électroniques très riche, mais qui peut être reproduit théoriquement par un simple model a deux paramètres libres.

Annexe :
Dans l'annexe en discute les méthodes de fabrications qui ont été suivies pour produire les structures étudié dans ce travail de thèse et présenté dans les chapitres 4 et 5 : (i) graphene encapsule dans du nitrure de bore. (ii) graphene multicouche rhomboédrique. Les calculs du contraste Raman dans le chapitre 5 y sont aussi detaillés.

Contents

Chapter 1

Introduction to graphene multilayers

1.1 Graphene monolayer

1.1.1 Crystal structure

Carbon atom, which is the basic constituent of graphene, graphene multilayers, and graphite crystals, is a chemical element from the periodic table (symbol: C) with an atomic number Z = 6. Although carbon atoms usually contain 6 protons and 6 electrons with a varying number of neutrons, the two most stable isotopes on earth are C^{12} (6 protons, 6 neutrons) and C^{13} (6 protons, 7 neutrons) [1]. In order to understand the crystallographic structure of graphene and graphene-based structures in general, it is useful to review the basic chemical bonding properties of carbon atoms. Since C^{12} is by far the most stable configuration of the carbon atom [1], all our studies will be focused on this isotope.

In the ground state, the electronic configuration of the carbon atom is $1s^2\ 2s^2\ 2p^2$ [2]. Thus, the inner shell 1s, which is close to the nucleus and is irrelevant for chemical reactions, is filled with two electrons. Another four electrons occupy the outer shell of the 2s and the 2p orbitals. Because the 2p orbitals ($2p_x$, $2p_y$, and $2p_z$) are roughly 4 eV higher in energy than the 2s orbital, it is energetically favorable to put two electrons in the 2s orbital and only two of them in the 2p orbitals (see Figure 1.1). It turns out, however, that in the process of chemical bonding with other atoms, such as hydrogen or oxygen, it is favorable for the carbon atom to excite one electron from the 2s to the $2p_z$ orbital, in order to form covalent bonds with the other atoms. In the excited state, we therefore have four equivalent quantum-mechanical states $|2s\rangle$, $|2p_x\rangle$, $|2p_y\rangle$,

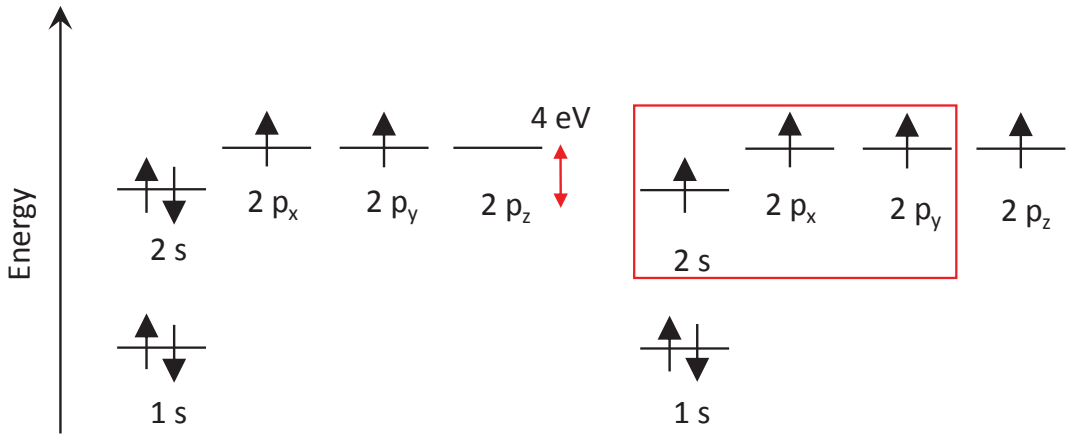

FIGURE 1.1: Electronic configurations for carbon in the ground state (left panel) and in the excited state (right panel). The 2s and the (p_x, p_y) will hybridize to form the sp^2 orbital (region boxed in red), leaving one electron in the p_z orbital.

and $|2p_z\rangle$. A quantum-mechanical superposition of the state $|2s\rangle$ with n $|2p_i\rangle$ states is called sp^n hybridization. The sp^1 hybridization, for example, plays an important role in the context of organic chemistry (such as the formation of acetylene) and the sp^3 hybridization gives rise to the formation of diamond. However, our focus will be on the sp^2 hybridization, which is the basic ingredient for the covalent bonds in graphene, graphene multilayers, and bulk graphite. Figure 1.2a shows the crystal structure of monolayer graphene, where the carbon atoms are arranged in a so-called honeycomb or hexagonal lattice [2]. The crystallography of graphene is a consequence of the sp^2 hybridization, the three sp^2-hybridized orbitals are oriented in the atomic plane and have mutual 120° angles, while the remaining non hybridized $2p_z$ orbital is perpendicular to the atomic plane [3]. As a consequence, the in plane sp^2 orbitals for the carbon atoms overlap, giving rise to the so-called σ bonding. The associated wave function with the σ bonding is highly localized in the space between the atoms, which makes it responsible of the amazing mechanical properties of graphene. On the other hand, the remaining non hybridized $2p_z$ orbital will weakly overlap with the $2p_z$ of the adjacent atoms, thus forming the so-called π bonding. In graphene, it is the π bonding that will contribute to the electronic properties of this material.

As we discussed above, the carbon atoms in graphene are arranged in a honeycomb lattice due to their sp^2 hybridization. The honeycomb lattice of graphene does not satisfy the symmetry conditions to be a Bravais lattice, and this is easily understood by the following observation: any translation by a vector that is connecting two nearest neighboring atoms cannot conserve the symmetry of the lattice. Taken alone, the triangular atomic sublattices A or B (indicated by black and blue colored dots in Figure 1.2a respectively) are Bravais lattices. Graphene hexagonal lattice can thus be considered as a hexagonal Bravais lattice with a basis of two atoms, labeled A and B [4].

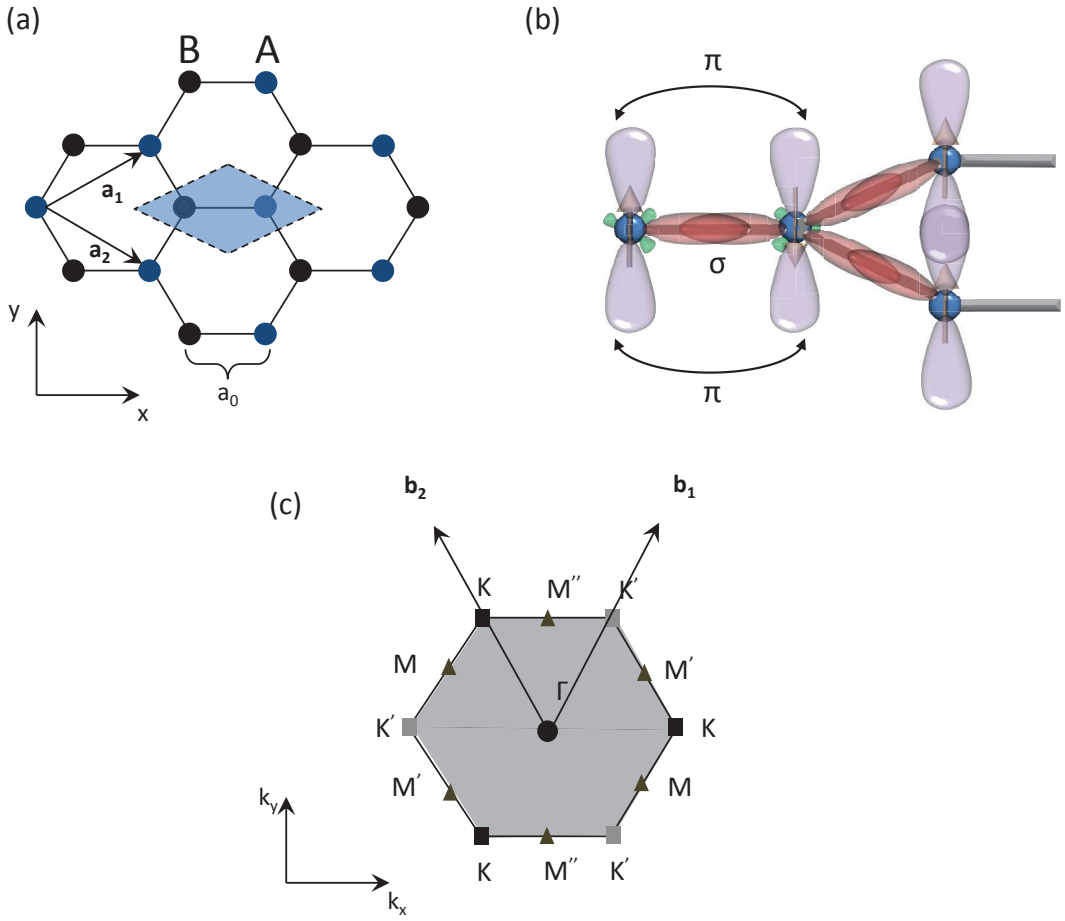

FIGURE 1.2: (a) Graphene honeycomb lattice. The vectors $\mathbf{a}_1$ and $\mathbf{a}_2$ are basis vectors of the triangular Bravais lattice. The unit cell is indicated by the blue shaded region. (b) Atomic orbitals of the hexagonal lattice. The hybridized sp^2 orbitals are located in the atomic plane between adjacent carbon atoms, forming σ bonds. The remaining p_z orbital for each atom is out of plane, forming π bonding with adjacent atoms. (c) Reciprocal lattice of the triangular lattice. Its primitive lattice vectors are $\mathbf{b}_1$ and $\mathbf{b}_2$. The shaded grey region represents the first Brillouin zone (BZ).

In the following, we will use a Cartesian coordinate system with x and y axes in the atomic plane, and a z axis perpendicular to the graphene plane. The in-plane vectors will thus be expressed in terms of x and y coordinates, so that the primitive vectors for the A or B sublattices can be expressed as following:

$$\mathbf{a}_1 = \left(\frac{\sqrt{3}a}{2}, \frac{a}{2}\right), \mathbf{a}_2 = \left(-\frac{\sqrt{3}a}{2}, \frac{a}{2}\right), \tag{1.1}$$

where $a = |\mathbf{a}_1| = |\mathbf{a}_2| = 2.46$ A° is the lattice parameter (i.e., the distance between unit cells). The lattice parameter is related to the carbon-carbon bond length by: $a_{CC} = a/\sqrt{3} = 1.42$ A° [2].

From the triangular Bravais lattice, we define the associated reciprocal lattice. The vectors of the reciprocal lattice $\mathbf{b}_1$ and $\mathbf{b}_2$ are defined as to satisfy the relation $a_i.b_j = 2\pi\delta_{ij}$

($\delta_{ij} = 1$ if $i = j$ and $\delta_{ij} = 0$ otherwise), thus taking the form:

$$\mathbf{b}_1 = \left(\frac{2\pi}{\sqrt{3}a}, \frac{2\pi}{a}\right), \mathbf{b}_2 = \left(-\frac{2\pi}{\sqrt{3}a}, \frac{2\pi}{a}\right). \tag{1.2}$$

The resulting reciprocal lattice of graphene (as shown in Figure 1.2c) is a hexagonal Bravais lattice. We can now define the unit cell of the reciprocal lattice, or the first Brillouin zone (BZ) as the set of nonequivalent points that cover all the reciprocal space by translational symmetry [5].

For the reciprocal lattice of graphene, the first Brillouin zone is hexagonal (shaded grey region in Figure 1.2c). A set of high symmetry points are defined in the BZ of graphene, as seen in Figure 1.2c. The Γ point lies at the center of the BZ, while K and K$'$ points are located at its corners, intersected by the points M and M$'$. As we will show in the next section about the energy dispersion in monolayer graphene, it is at the corners of the BZ (i.e., K and K$'$) that the valence and the conduction bands are touching each other. Their coordinates in the reciprocal space are [4]:

$$\mathbf{K} = \left(\frac{2\pi}{\sqrt{3}a}, \frac{2\pi}{3a}\right), \mathbf{K}' = \left(\frac{2\pi}{\sqrt{3}a}, -\frac{2\pi}{3a}\right). \tag{1.3}$$

Therefore, most of the low energy electronic properties of graphene and multilayer graphene are described by the band dispersion around the K and K$'$ points.

1.1.2 Band structure

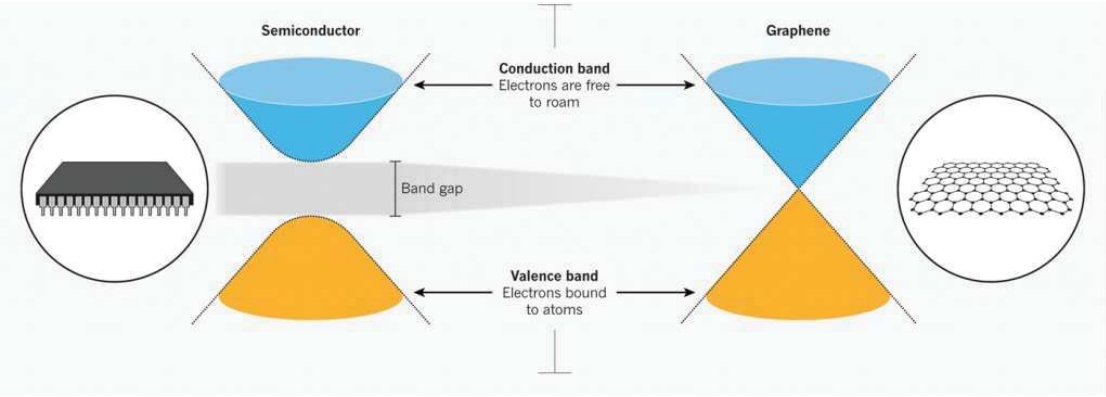

FIGURE 1.3: Energy dispersion in conventional semi-conductors (left panel) compared to the energy dispersion in graphene (right panel). Graphene is seen as a zero gap semi conductor.

So far, conventional two dimensional electron gas in condensed matter systems always exhibit a parabolic-like dispersion (see Figure 1.3), characteristic of their massive particles. The non-relativistic Schrödinger equation dominates the behavior of particles in these systems. However, the energy dispersion, observed in monolayer graphene, is

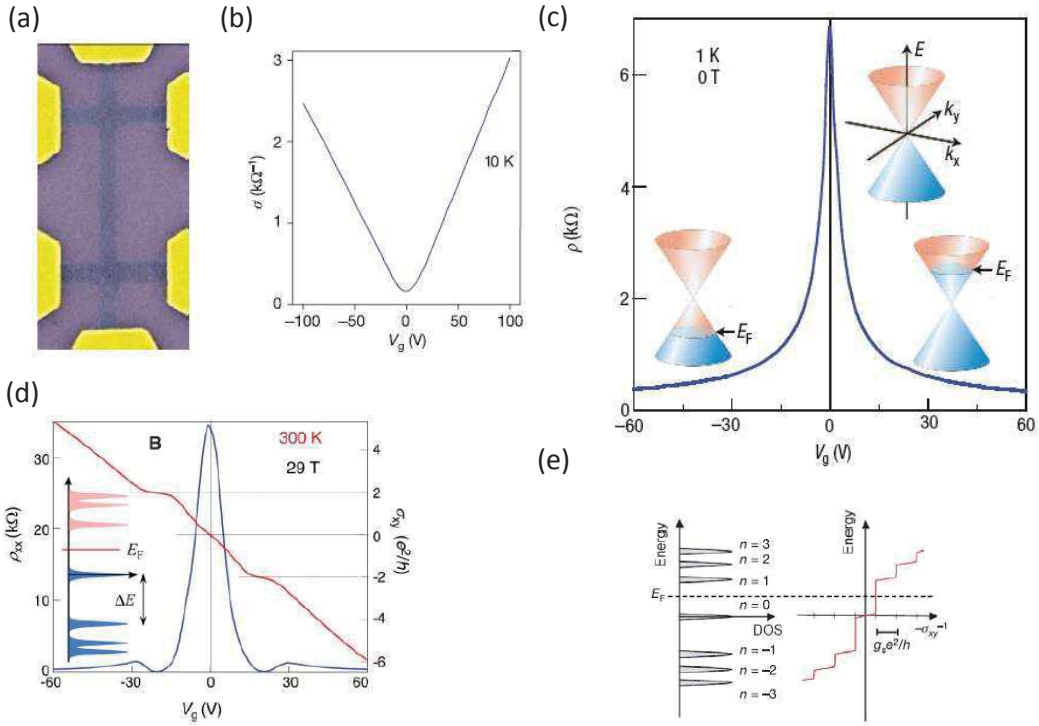

FIGURE 1.4: (a) A four terminal bar is used to perform transport studies in graphene [6]. (b) Graphene's conductivity as a function of the gate voltage. (c) Ambipolar electric field effect in monolayer graphene. The insets show the low energy Dirac cone dispersion, indicating changes in the position of the Fermi energy E_F with changing gate voltage V_g. Positive (negative) V_g induce electrons (holes) doping [7]. (d) Hall conductivity (red) and longitudinal resistivity (blue) for monolayer graphene at T = 300 K and B = 29 T [8]. (e) Schematic diagram of the Landau level density of states (DOS) and the corresponding quantum Hall conductance (σ_{xy}) as a function of the energy [9].

linear at low energy [6] and thus, resembles the conical dispersion of light in the theory of relativity. This has considerable consequences in the study of low energy carriers in graphene. Since the Schrödinger equation fails to describe the electronic properties of such particles, charge carriers in monolayer graphene are governed by the Dirac equation [7]. Consequently, graphene is seen as a system that offers the possibility to study quantum electrodynamics phenomena using simple experimental set ups.

In the following we will give a few examples on how the peculiar band structure of monolayer graphene allowed important discoveries on this material, that are of major interest both for fundamental science and technological applications. We will also give a derivation of its low energy band dispersion.

In the course of 2005, two papers appeared simultaneously in the journal *Nature* reporting the first experimental studies on monolayer graphene by means of transport measurements [6, 9]. In these studies, Novoselov *et al.* [6] observed a linear dependence of the resistivity as a function of the gate voltage in an exfoliated graphene flake (Figure 1.4a,b), which is a behavior characteristic of particles with zero rest mass. Both studies

reported the observation of an unusual quantum Hall effect (QHE), different from the integer QHE observed in standard two dimensional electron gas systems, with quantized plateaus that are shifted by half an integer [6, 9]. These magneto-transport measurements show that graphene is characterized by a zeroth Landau level for both electrons and holes, located at the Fermi level (see the Landau levels density of states in Figure 1.4e). The QHE in graphene can be observed even at room temperature (Figure 1.4d), as was reported shortly after the discovery of graphene [8].

Two of the most remarkable findings in graphene are the absence of back-scattering [10, 11] and the universal optical conductivity [12, 13]. The absence of back-scattering, also known as Klein tunneling [14], is characteristic of particles that obey the Dirac equation. It pushes the charge carriers to tunnel through long potential barriers with no probability of being back-scattered. This makes the charge carriers in graphene travel ballistically thousands of inter-atomic distances without scattering [6, 7, 9, 15, 16]. The absorbance of light by graphene is found to be independent of the frequency of incident light and has a magnitude given by $\pi\alpha \sim 2.9\%$, where α is the fine structure constant of quantum electrodynamics. Hence, in monolayer graphene, the absorbance of light is universal, and is given by α which describes the strength of interaction between light and matter.

These findings triggered a rapid interest in graphene, which is seen as a suitable system to study the rich physics of relativistic quantum effects in a simple bench-top experiment.

Low energy dispersion of the honeycomb lattice:

The band structure calculations for graphene go back to the first work by Wallace in 1947 [17]. Since then, many theoretical works that describe the band dispersion of electrons in graphene and graphene based-systems have been published [17–19]. The amount of scientific research on the physical properties of this material increased significantly after its first experimental isolation, the observation of an ambipolar electric field effect as well as a half integer QHE [6, 9, 15, 20].

To calculate the low energy band structure of graphene, the tight binding (TB) method is the easiest approach. Within this method, only the energy bands of the π orbitals are taken into account, since the σ orbitals have energies far from the Fermi level, they do not play any significant role in describing the electronic properties of this material.

Our unit cell has two atoms, thus we may introduce a total wave function for the system as the following [2]

$$\psi_{\mathbf{k}}(\mathbf{r}) = a_{\mathbf{k}}\psi^{A}_{\mathbf{k}}(\mathbf{r}) + b_{\mathbf{k}}\psi^{B}_{\mathbf{k}}(\mathbf{r}), \tag{1.4}$$

where ($a_{\mathbf{k}}$,$b_{\mathbf{k}}$) are complex coefficients, and ($\psi^A_{\mathbf{k}}$,$\psi^B_{\mathbf{k}}$) are the so-called Bloch's wave functions for the sublattices A and B respectively, defined as:

$$\psi^{(j)}_{\mathbf{k}}(\mathbf{r}) = \sum_{\mathbf{R}_l} e^{i(\mathbf{k}.\mathbf{R}_l)} \varphi^{(j)}(\mathbf{r} + \boldsymbol{\delta}_j - \mathbf{R}_l), \tag{1.5}$$

where $j = \alpha$ or β labels the atoms of the two sublattices A and B. The vectors δ_j connects sites of the Bravais lattice with the site of the j atom inside the unit cell. The $\varphi^{(j)}(\mathbf{r}+\boldsymbol{\delta}_j-\mathbf{R}_l)$ are atomic orbitals for electrons in the vicinity of the j atom at position $\mathbf{R}_l - \delta_j$ at the lattice site $\mathbf{R}_l$.

Now let us seek solutions to the Schrodinger equation $H\psi_{\mathbf{k}} = \epsilon_{\mathbf{k}}\psi_{\mathbf{k}}$. We rewrite the equation in a matrix form:

$$\psi^*_{\mathbf{k}} H \psi_{\mathbf{k}} = \epsilon_{\mathbf{k}} \psi^*_{\mathbf{k}} \psi_{\mathbf{k}} \Rightarrow (a^*_{\mathbf{k}}, b^*_{\mathbf{k}})\, \mathcal{H}_{\mathbf{k}} \begin{pmatrix} a_{\mathbf{k}} \\ b_{\mathbf{k}} \end{pmatrix} = \epsilon_{\mathbf{k}}\, (a^*_{\mathbf{k}}, b^*_{\mathbf{k}})\, \mathcal{S}_{\mathbf{k}} \begin{pmatrix} a_{\mathbf{k}} \\ b_{\mathbf{k}} \end{pmatrix} \tag{1.6}$$

Where:

$$\mathcal{H}_{\mathbf{k}} = \begin{pmatrix} \psi^{(A)*}_{\mathbf{k}} H \psi^{(A)}_{\mathbf{k}} & \psi^{(A)*}_{\mathbf{k}} H \psi^{(B)}_{\mathbf{k}} \\ \psi^{(B)*}_{\mathbf{k}} H \psi^{(A)}_{\mathbf{k}} & \psi^{(B)*}_{\mathbf{k}} H \psi^{(B)}_{\mathbf{k}} \end{pmatrix} = \mathcal{H}^{\dagger}_{\mathbf{k}}, \tag{1.7}$$

is the Hamiltonian matrix, and:

$$\mathcal{S}_{\mathbf{k}} = \begin{pmatrix} \psi^{(A)*}_{\mathbf{k}} \psi^{(A)}_{\mathbf{k}} & \psi^{(A)*}_{\mathbf{k}} \psi^{(B)}_{\mathbf{k}} \\ \psi^{(B)*}_{\mathbf{k}} \psi^{(A)}_{\mathbf{k}} & \psi^{(B)*}_{\mathbf{k}} \psi^{(B)}_{\mathbf{k}} \end{pmatrix} = \mathcal{S}^{\dagger}_{\mathbf{k}}, \tag{1.8}$$

is the overlap matrix that accounts for the non orthogonality of the wave functions. The energy band dispersion is obtained from the eigenvalues of $\epsilon_{\mathbf{k}}$ of the secular equation [2]:

$$det[\mathcal{H}_{\mathbf{k}} - \epsilon^{\lambda}_{\mathbf{k}} \mathcal{S}_{\mathbf{k}}] = 0, \tag{1.9}$$

where λ accounts for the number of energy bands.

As shown in Figure 1.5a by red arrows, we introduce the vectors that connect the sites on sublattice A with a next neighbor (nn) on the sublattice B as:

$$\boldsymbol{\delta}_1 = \frac{a}{2}\left(-\sqrt{3}\mathbf{e}_x + \mathbf{e}_y\right), \boldsymbol{\delta}_2 = \frac{a}{2}\left(\sqrt{3}\mathbf{e}_x - \mathbf{e}_y\right), \boldsymbol{\delta}_3 = a\mathbf{e}_y, \tag{1.10}$$

where ($\mathbf{e}_x$, $\mathbf{e}_y$) are unitary vectors along the $\{x, y\}$ axes. In the following, we choose the Bravais lattice to be the A sublattice, i.e., $\boldsymbol{\delta}_A = 0$ and $\boldsymbol{\delta}_B = \boldsymbol{\delta}_{AB} = \boldsymbol{\delta}_3$ (see Figure 1.5).

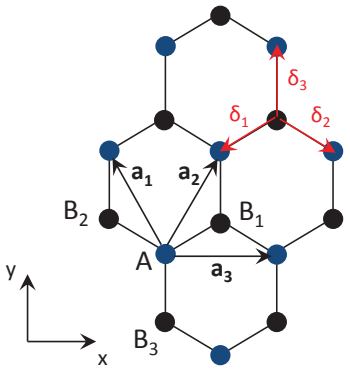

FIGURE 1.5: Tight binding model for graphene honeycomb lattice.

To go further in the resolution of the secular equation, we rewrite the Hamiltonian as: $H = H^a + \Delta V$, with: $H^a = -(\hbar^2/2m)\Delta + V(\mathbf{r} + \delta_j - \mathbf{R}_l)$ being the Hamiltonian of

an atomic orbital, and ΔV is a perturbation part that accounts for other interactions that are not included in H^a. By injecting (1.5) in the secular equation, the following quantities appear:

$$t_{nnn} = \int d^2r\varphi^{A*}(\mathbf{r})\Delta V\varphi^B(\mathbf{r}+\boldsymbol{a}_1), \tag{1.11}$$

$$t = \int d^2r\varphi^{A*}(\mathbf{r})\Delta V\varphi^B(\mathbf{r}+\boldsymbol{\delta}_3), \tag{1.12}$$

$$s = \int d^2r\varphi^{A*}(\mathbf{r})\varphi^B(\mathbf{r}+\boldsymbol{\delta}_3), \tag{1.13}$$

these quantities are called: next nearest-neighbors (nnn) hopping amplitude, nearest-neighbors (nn) hopping amplitude, and the overlap correction, respectively. By introducing the sum of the nn phase factors [2] $\gamma_{\mathbf{k}} \equiv 1 + e^{i\mathbf{k}.\mathbf{a}_2} + e^{i\mathbf{k}.\mathbf{a}_3}$, one can define the following matrix elements:

$$t^{AA}_{\mathbf{k}} = t^{BB}_{\mathbf{k}} = 2t_{nnn}\sum_{i=1}^{3}\cos(\mathbf{k}.\mathbf{a}_i) = t_{nnn}(|\gamma^*_{\mathbf{k}}|^2 - 3), \tag{1.14}$$

$$t^{AB}_{\mathbf{k}} = t\gamma^*_{\mathbf{k}} = (t^{BA}_{\mathbf{k}})^*, \tag{1.15}$$

$$s^{AB}_{\mathbf{k}} = s\gamma^*_{\mathbf{k}} = (s^{BA}_{\mathbf{k}})^*, \tag{1.16}$$

the secular equation (1.9) will transform as the following:

$$\det\begin{bmatrix} t^{AA}_{\mathbf{k}} - \epsilon_{\mathbf{k}} & (t - s\epsilon_{\mathbf{k}})\gamma^*_{\mathbf{k}} \\ (t - s\epsilon_{\mathbf{k}})\gamma_{\mathbf{k}} & t^{AA}_{\mathbf{k}} - \epsilon_{\mathbf{k}} \end{bmatrix} = 0, \tag{1.17}$$

which yield for $\lambda = \pm 1$ the following energy dispersion [2]:

$$\epsilon^{\lambda}_{\mathbf{k}} = \frac{t^{AA}_{\mathbf{k}} + \lambda t|\gamma_{\mathbf{k}}|}{1 + \lambda s|\gamma_{\mathbf{k}}|}. \tag{1.18}$$

Based on the fact that $(s, t_{nnn}) << 1$, our dispersion relation will take the form:

$$\epsilon^{\lambda}_{\mathbf{k}} = 2t'_{nnn}\sum_{i=1}^{3}\cos(\mathbf{k}.\mathbf{a}_i) + \lambda t\sqrt{3 + 2\sum_{i=1}^{3}\cos(\mathbf{k}.\mathbf{a}_i)}, \tag{1.19}$$

where we have introduced the effective next nn hopping amplitude $t'_{nnn} = t_{nnn} - st$. Since each carbon atom contributes one π electron with either a spin up or a spin down state, the lower band with $\lambda = -1$, also called the valence band, will be completely filled and the one with $\lambda = 1$ will be completely empty. The Fermi level is, therefore, located at the points where the valence and conduction bands touch each other. Knowing that the Dirac points are located where the energy dispersion is zero, the coordinates of the

Dirac points are easily obtained by solving: $\epsilon^{\lambda}_{\mathbf{k},D} = 0$. This yields:

$$\mathbf{k}^D = \pm\left(\frac{2\pi}{\sqrt{3}a}, \frac{2\pi}{3a}\right). \tag{1.20}$$

The Dirac points are thus exactly located at the corners of the BZ: $\mathbf{k}_D = \pm\mathbf{K}$.

The Dirac Hamiltonian:

We will now focus on the energy dispersion around the ±K, where most of the electronic properties are located. We introduce the following Hamiltonian [2, 4]:

$$\mathcal{H}_{\mathbf{k}} = t_{nnn}|\gamma_{\mathbf{k}}|^2\mathbb{I} + t\begin{pmatrix} 0 & \gamma^*_{\mathbf{k}} \\ \gamma_{\mathbf{k}} & 0 \end{pmatrix}. \tag{1.21}$$

Here, $\mathbb{I}$ is the (2×2) identity matrix $\mathbb{I} = \begin{pmatrix} 1 & 0 \\ 0 & 1 \end{pmatrix}$. The eigenstates of such a Hamiltonian are spinors:

$$\Psi^{\lambda}_{\mathbf{k}} = \frac{1}{\sqrt{2}}\begin{pmatrix} 1 \\ \lambda e^{i\varphi_{\mathbf{k}}} \end{pmatrix}, \tag{1.22}$$

where $\varphi_{\mathbf{k}} = \arctan(\mathrm{Im}\gamma_{\mathbf{k}}/\mathrm{Re}\gamma_{\mathbf{k}})$.

Around the ±K points, the wave vector is given by: $\mathbf{q} = \pm\mathrm{K} + \mathbf{k}$, where $|\mathbf{k}| << |\mathbf{K}| \sim 1/a \Rightarrow |\mathbf{k}|a << 1$.

By multiplying the sum of the phase factors by $e^{i\mathbf{k}.\boldsymbol{\delta}_3}$ and expanding to the first order in ka, we will have:

$$\gamma^{\pm}_{\mathbf{k}} = \mp\frac{3a}{2}(k_x \pm ik_y), \tag{1.23}$$

this yields the so-called Dirac Hamiltonian:

$$\mathcal{H}_{\mathbf{k}} = \pm\hbar v_F(k_x\sigma^x \pm k_y\sigma^y), \tag{1.24}$$

where we have defined the Fermi velocity for graphene:

$$v_F \equiv \frac{3|t|a_{CC}}{2\hbar}, \tag{1.25}$$

and (σ^x, σ^y) are Pauli matrices defined by:

$$\sigma^x = \begin{pmatrix} 0 & 1 \\ 1 & 0 \end{pmatrix}, \sigma^y = \begin{pmatrix} 0 & -i \\ i & 0 \end{pmatrix}. \tag{1.26}$$

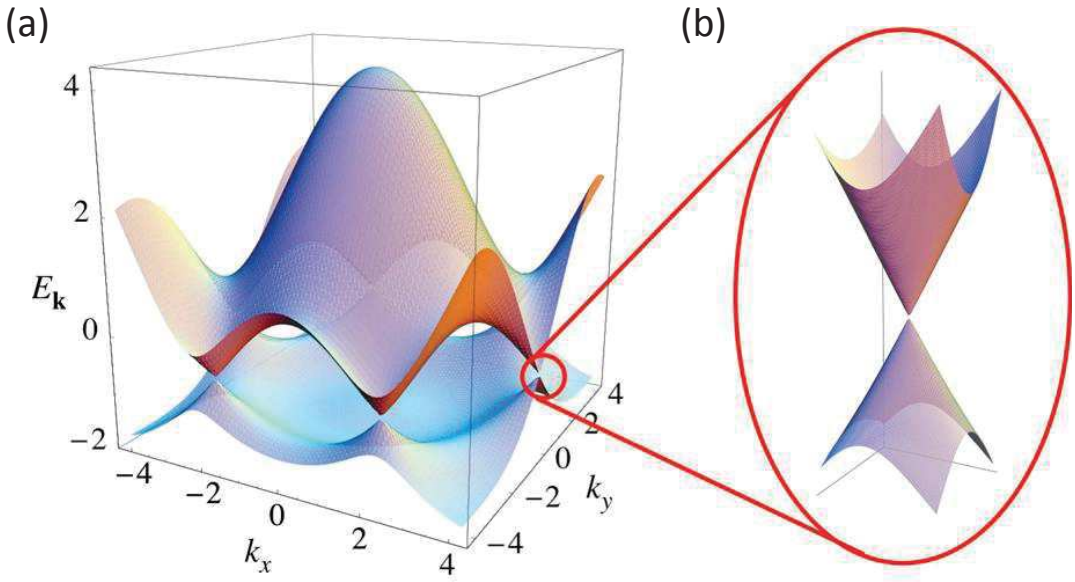

FIGURE 1.6: (a) Energy dispersion in monolayer graphene as a function of the wavevector components k_x and k_y, obtained from the tight-binding calculations. We set $t_{nnn} = 0.1t$. The Fermi level is situated at the points where the valence band touches the conduction band. (b) Zoom on the low linear energy dispersion at the corners of the BZ, where the Dirac cone is located [21].

By setting $\sigma \equiv (\sigma^x, \sigma^y)$, $p = \hbar|\mathbf{k}|$, and introducing the unit vector $\mathbf{n}_1$, the Dirac Hamiltonian will have the final form [2, 4]:

$$\mathcal{H}_{\mathbf{k}} = \upsilon_F p \boldsymbol{\sigma}.\mathbf{n}_1, \tag{1.27}$$

the energy dispersion will therfore reads [2, 4, 6]:

$$\epsilon_{\mathbf{q},\lambda} = \lambda \hbar \upsilon_F |\mathbf{k}|. \tag{1.28}$$

The low energy dispersion in monolayer graphene (at the corners of the BZ) is then linear with the wave-vector $\mathbf{k}$, as seen in Figure 1.6b. This linear dispersion became a fingerprint of monolayer graphene. The particles described by (1.28) are called *massless Dirac Fermions* [6], and their low energy dispersion in monolayer graphene (in the single particle approximation) at the corners of the BZ are since known as the *Dirac cone*.

1.2 Multilayer graphene and graphite

The discovery of massless Dirac fermions in graphene, and the rich physics that is offered in this system, re-surfaced an increasing interest on its parent crystal, bulk graphite. Experiments have shown that the band structure of graphene is strongly altered when

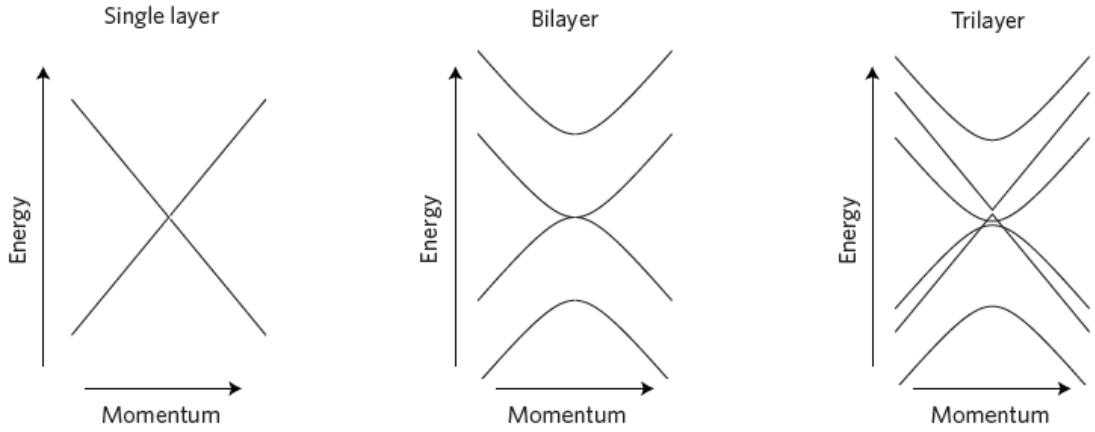

FIGURE 1.7: Band structure of multilayer graphene changes when changing the number of graphene layers on the system [22].

adding single layers of graphene on top of each other [22]. The band structure of graphene can be engineered by tuning the number of layers and their stacking configuration (see Figure 1.7), which offers a high degree of freedom to tune its electronic properties. In the following section we will introduce many layer graphene systems, and present their properties that are intimately related to the symmetry of the crystal and the number of graphene sheets coupled to each other.

1.2.1 Bernal vs rhombohedral stacking

Graphite, the parent crystal from which graphene is produced by mechanical cleavage or exfoliation, has a layered, planar structure (Figure 1.8a). Each layer is a sheet of graphene, weakly bonded to other layers via the Van der Waals (VdW) interactions [23].

Two different forms of crystallographic stacking configurations are known in graphite crystals; the most thermodynamically stable configuration is the Bernal or ABA stacking [23], while the other is known as the rhombohedral or ABC stacked multilayer graphene [24].

Soon after the discovery of graphene, it has been shown that the low energy linear dispersion changes drastically when stacking graphene layers on top of each other to make multilayer graphene (N-LG, N is the number of monolayers) [25, 26]. Since

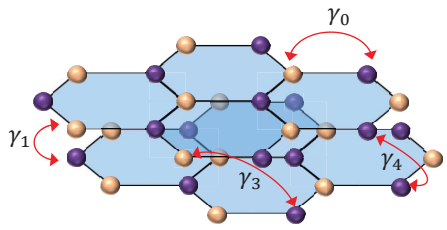

FIGURE 1.8: Crystal structure of bilayer graphene with the corresponding hopping parameters.

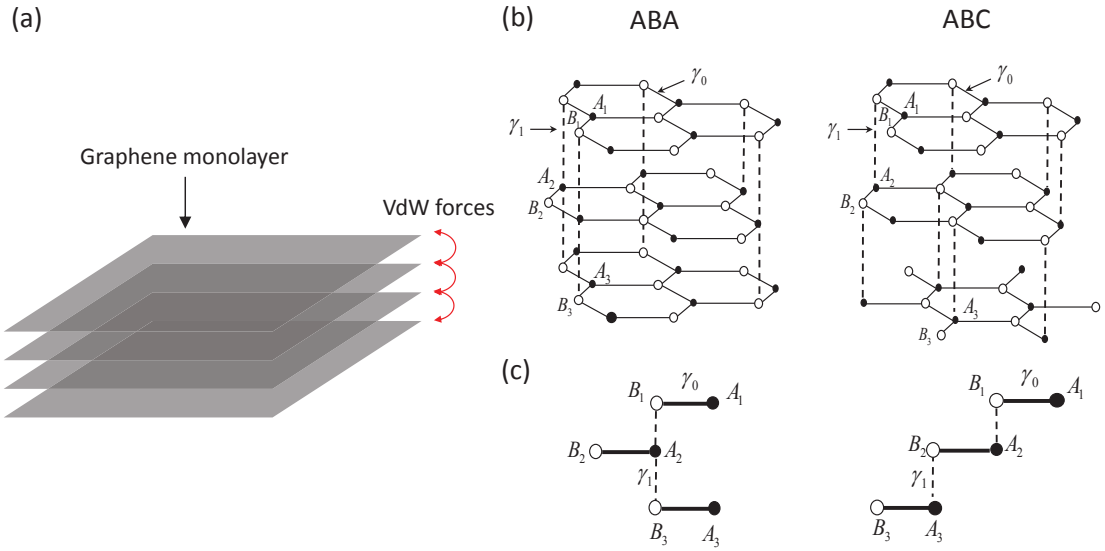

FIGURE 1.9: (a) Schematics of the layered structure found in graphite crystals, where each atomic plane represents a monolayer graphene sheet. (b) Schematics of the crystal structure of ABA and ABC N-LG. Open circles and black dots are carbon atoms of the A and B sublattices, respectively. (c) Side views of the unit cells of ABA and of ABC N-LG.

Bernal-stacked graphite occurs much more in graphite crystals than the rhombohedral stacking [27], the physical properties of Bernal stacked N-LG have been much more investigated since the past decade than the rhombohedral stacked N-LG.

Bilayer graphene, which represents the basic unit cell of N-LG, has been shown to hold a very interesting physics after the discovery of an anomalous quantum Hall effect (QHE) by Novoselov *et al.* in this system [28]. Consequently, despite the parabolic energy dispersion in bilayer graphene, charge carriers in this material do not behave exactly like typical massive particles, which led to naming these carriers as *chiral massive Dirac fermions*.

The observation of an electrically tunable band gap in bilayer graphene [29], relevant for transistor based electronics, made this system a serious candidate for technological applications, since such an effect cannot exist in monolayer graphene. Moreover, bilayer graphene electronic structure has been very useful in the study of N-LG (N≥3) physical properties, where the theoretical and experimental investigation of the band structure evolution of ABA N-LG is shown to be accounted for by a so-called *effective bilayer model* [30, 31]. In this model, the band structure of Bernal stacked N-LG is seen as a series of graphene bilayers coupled to one another. A 4×4 Hamiltonian, as for bilayer graphene, is used to obtain the low energy dispersion, but with an effective inter-layer coupling that changes its value as a function of the number of ABA stacked layers in the system.

The ABC stacking is less common in natural graphite crystals; the exfoliated thin graphite flakes usually display an ABA stacking configuration, while the ABC sequence,

if it exists, is very thin. About 3 to 5 ABC-stacked layers have been reported in literature so far [27, 32–38]. Due to this, most of the optical and transport studies on N-LG ($N \gg 3$) were centered around the ABA stacking. Nevertheless, theoretical studies of the band structure of ABC stacked N-LG, from 3-LG to the bulk limit have shown a promising rich physics in this material. Due to the existence of nearly flat bands at the charge neutrality point, that extend over a larger region in k-space when the ABC sequence gets longer, high correlation effects are expected in this system as a consequence of the highly degenerate density of states, such as magnetic order or superconductivity [39–41].

Recent experimental investigations of ABC 3-LG and 4-LG have shown the existence of a large electrically tunable band gap [37, 38], and an anomalous QHE [34] with massive chiral particles. These studies point to the important role of high correlations in this system, even for the thinnest 3 to 4 ABC-stacked layers.

Throughout the following sections, we will adopt a similar approach as for monolayer graphene, by using a tight binding model with several hopping parameters. Either by considering an ABA or an ABC stacking, the starting point for the band structure calculation for N-LG is the bilayer graphene, where one graphene monolayer is on top of another graphene layer. From a historical point of view, this approach was used by Slonczewski, Weiss and McClure [18, 19], in which they used the bilayer graphene as the unit cell to model the band structure of bulk graphite. Their model became known in the literature as the SWM model.

In the SWM model, the band structure calculations are based on a tight binding approach for the π electrons, similar to monolayer graphene. Several hopping integrals are introduced to describe interactions with different neighboring atoms, both in the same layer and the adjacent layers. Figure 1.8 is a schematic presentation of these hopping parameters, where we have used the same symbolic as in the original papers. The total number of these parameters is seven [18, 19], and computing the eigenvalues of the Hamiltonian with all these parameters happens to be a tedious approach. On the other hand, for the sake of low energy physics in graphene multilayers, it is sufficient in some cases to keep only the two parameters describing interactions with the nearest neighboring atoms in the same layer γ_0, and across adjacent layers γ_1. These two hopping parameters are enough for describing the low energy properties of graphene and N-LG systems.

1.2.2 Band dispersion in Bernal stacked multilayer graphene

Using the full SWM model, B. Partoens and F.M. Peeters [42] studied the evolution of the band structure from monolayer graphene to bulk graphite. In order to calculate the

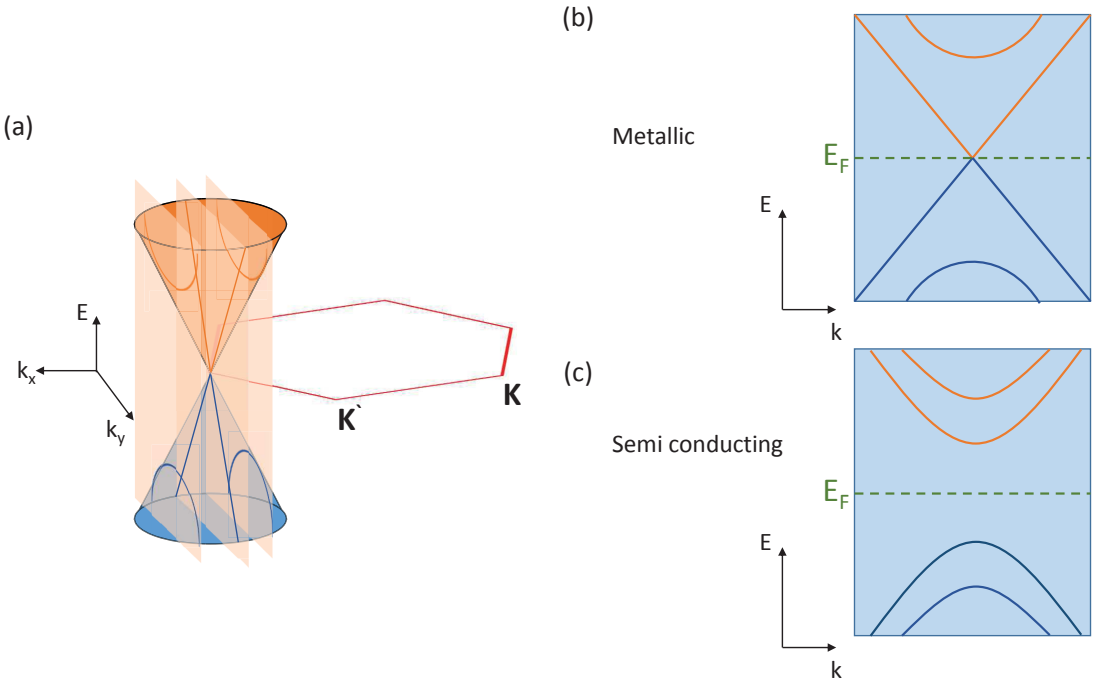

FIGURE 1.10: (a) Schematic presentation of the 2D electronic structure of 1-LG and the corresponding zone-folding scheme that generates states satisfying the periodic boundary conditions for nanotubes. The resulting states are either metallic (b) or semiconducting nanotubes (c).

low energy band dispersion for the ABA-stacked N-LG, we use a much simpler approach than the SWM model, called the effective bilayer model. This model is based on a technique used many years ago in the band structure calculations of several condensed matter systems, called the zone folding method (ZF). A similar approach was recently used by Koshino and Ando to calculate the band structure of ABA N-LG [43]. Soon after their theoretical work, the effective bilayer model [43] was intensively used to fit experimental data obtained from the optical and magneto-optical studies of N-LG with a Bernal stacking [25, 31, 44]. In the following, we should give a quick derivation of the effective bilayer model and illustrate its application to calculate the band structure of ABA-stacked N-LG.

Basically, the band structure for carbon nanotubes is obtained starting from the tight binding electronic dispersion relation of the π-orbitals in graphene. The graphene electronic band structure is then sectioned along the directions given by the nanotube 1D Brillouin zones or cutting lines [26, 45], with spacing and lengths that satisfy the periodic boundary conditions for nanotubes, so that one finally gets the nanotube electronic band structure. When a cutting line crosses the graphene BZ special points K and K$'$, the nanotube is metallic, otherwise the nanotube is semiconducting with a nonzero energy gap at the Fermi level as seen in Figure 1.10. Based on a similar approach, we will show in more details how to use the ZF method to produce the low energy band dispersion of

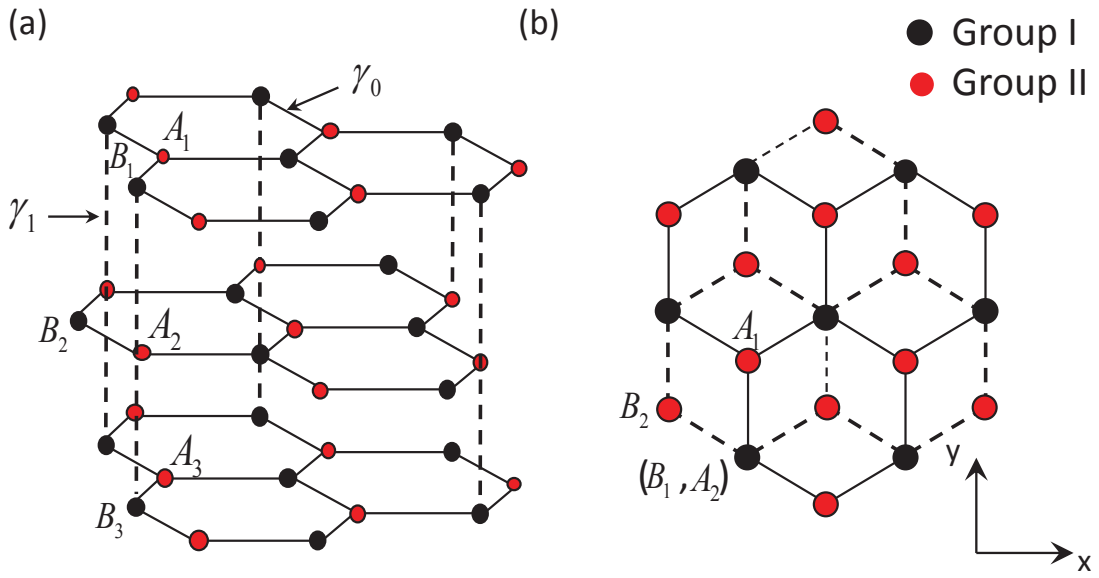

FIGURE 1.11: (a) Atomic structure of Bernal stacked N-LG.(b) Top view of the Bernal stracked N-LG. Atoms from group I are indicated by black circles while those in group II are in red circles.

N-LG, from monolayer to bulk graphite.

In order to proceed with the calculations, we divide the atoms in the ABA N-LG system into two separate groups, as shown in Figure 1.11. Group I is composed of the atoms that are arranged along vertical columns normal to the layer plane (i.e., $B_1, A_2, B_3, \dots$), while group II are the atoms that are at the center of hexagons in the neighboring layers (i.e., $A_1, B_2, A_3, \dots$). The Hamiltonian of N-LG around the K point is written in the basis $\{|A_1\rangle, |B_1\rangle; |A_2\rangle, |B_2\rangle; \dots |A_N\rangle, |B_N\rangle\}$ as [45]

$$\mathcal{H}_{ABA} = \begin{pmatrix} H_0 & V & & & \\ V^\dagger & H_0 & V^\dagger & & \\ & V & H_0 & V & \\ & & \ddots & \ddots & \ddots \end{pmatrix}_{2N\times 2N} \tag{1.29}$$

with

$$V = \begin{pmatrix} 0 & \gamma' k_+ \\ \gamma_1 & 0 \end{pmatrix} \text{ and } H_0 = \begin{pmatrix} 0 & \gamma k_- \\ \gamma k_+ & 0 \end{pmatrix}, \tag{1.30}$$

we have set: $\gamma = \frac{\sqrt{3}}{2} a\gamma_0, \gamma' = \frac{\sqrt{3}}{2}\gamma_3, k_\pm = k_x \pm ik_y$. Notice that the Hamiltonian for K′ is obtained by exchanging k_+ and k_- and replacing γ_1 by $-\gamma_1$.

We now rearrange the basis in the order of group I and group II so we can block diagonalize the Hamiltonian. As we will see in the following, this procedure allow us to get rid of the dependence on the wave vector $\mathbf{k}$. The new basis is given by:

$\{|B_1\rangle, |A_2\rangle, |B_3\rangle, ...; |A_1\rangle, |B_2\rangle, |A_3\rangle, ...\}$. Equation 1.29 becomes:

$$\mathcal{H}_{ABA} = \begin{pmatrix} \mathcal{H}_{11} & \mathcal{H}_{12} \\ \mathcal{H}_{12}^{\dagger} & \mathcal{H}_{22} \end{pmatrix}, \tag{1.31}$$

with $\mathcal{H}_{ij}$ being $N \times N$ matrices defined as:

$$\mathcal{H}_{11} = \gamma_1 \begin{pmatrix} 0 & 1 & & & \\ 1 & 0 & 1 & & \\ & \ddots & \ddots & \ddots & \\ & & 1 & 0 & 1 \\ & & & 1 & 0 \end{pmatrix}_{N\times N}, \tag{1.32}$$

$$\mathcal{H}_{22} = \gamma' \begin{pmatrix} 0 & k_+ & & & & \\ k_- & 0 & k_- & & & \\ & k_+ & 0 & k_+ & & \\ & & \ddots & \ddots & \ddots & \\ & & & k_{\mp} & 0 & k_{\mp} \\ & & & & k_{\pm} & 0 \end{pmatrix}_{N\times N}, \mathcal{H}_{12} = \gamma \begin{pmatrix} k_+ & & & & \\ & k_- & & & \\ & & k_+ & & \\ & & & \ddots & \\ & & & & k_{\pm} \end{pmatrix}_{N\times N}. \tag{1.33}$$

At the K point ($\mathbf{k} = 0$) only $\mathcal{H}_{11}$ remains, which is equivalent to the Hamiltonian of a 1D tight-binding chain with the nearest neighbor coupling γ_1. The eigenvalues for H_{11} are thus given as:

$$\varepsilon_m = \gamma_1 \lambda_{N,m}, \quad \text{and} \quad \lambda_{N,m} = 2\sin\left(\frac{m\pi}{2(N+1)}\right), \tag{1.34}$$

with: $m = -(N-1), -(N-3), ..., N-1$. Since m and N have opposite parities (i.e., m odd/N even, m even/N odd), m is equal to zero only for odd N. The wave function of $\mathcal{H}_{11}$, at the j^{th} atomic site, is given by:

$$\psi_m(j) = \sqrt{\frac{2}{N+1}} \sin\left[\frac{(-m+N+1)\pi}{2(N+1)} j\right], \tag{1.35}$$

this allows the construction of a new basis from the atoms of group I and group II:

$$\begin{cases} |\phi_m^{(\mathrm{I})}\rangle = \psi_m(1)|B_1\rangle + \psi_m(2)|A_2\rangle + \psi_m(3)|B_3\rangle + ..., \\ |\phi_m^{(\mathrm{II})}\rangle = \psi_m(1)|A_1\rangle + \psi_m(2)|B_2\rangle + \psi_m(3)|A_3\rangle + ... \end{cases} \tag{1.36}$$

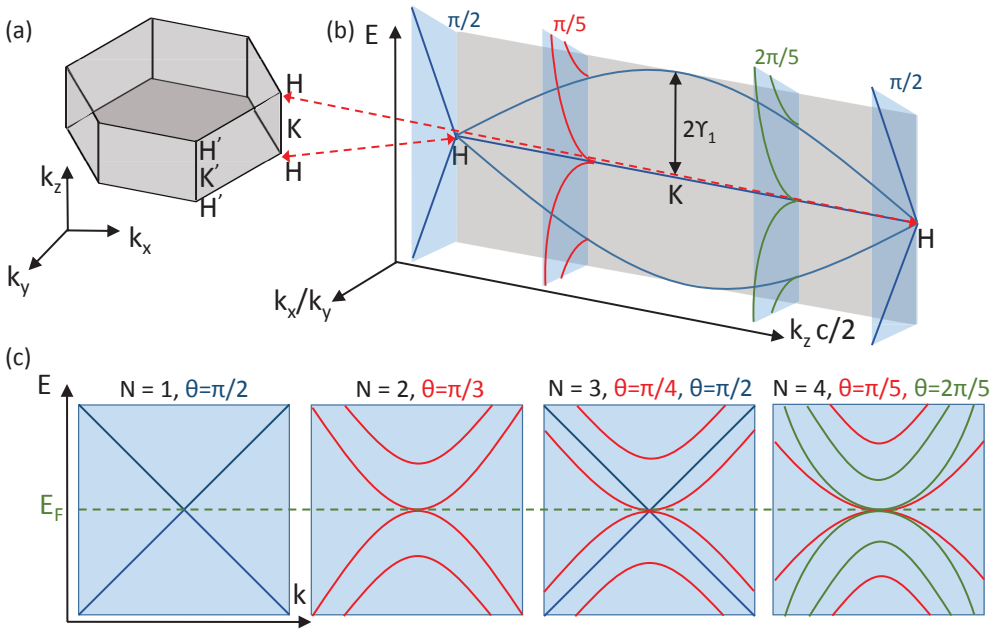

FIGURE 1.12: (a) 3D Brillouin zone of bulk graphite [46]. (b) Band structure of 4-LG along the H-K line and the zone-folding scheme that generates planes cutting at specific values of k_z. (c) Generation of massless and massive Dirac fermions in the band structure of N-LG from the zone folding method for N = 1, 2, 3 and 4 LG.

It is shown in reference [45] that the total Hamiltonian is closed in the subspace $\left\{|\phi_m^{(\mathrm{I})}\rangle, |\phi_{-m}^{(\mathrm{I})}\rangle, |\phi_m^{(\mathrm{II})}\rangle, |\phi_{-m}^{(\mathrm{II})}\rangle\right\}$ for any value of m. We finally obtain:

$$\mathcal{H}_{m=0} = \begin{pmatrix} 0 & \gamma k_- \\ \gamma k_+ & 0 \end{pmatrix}, \mathcal{H}_{m>0} = \begin{pmatrix} 0 & \gamma k_- & 0 & \lambda\gamma' k_+ \\ \gamma k_+ & 0 & \lambda\gamma_1 & 0 \\ 0 & \lambda\gamma_1 & 0 & \gamma k_- \\ \lambda\gamma' k_- & 0 & \gamma k_+ & 0 \end{pmatrix}, \tag{1.37}$$

were we have set $\lambda = \lambda_{N,m}$.

The 2×2 matrix ($m = 0$) is equivalent to the Hamiltonian of monolayer graphene, while the 4×4 matrix ($m > 0$) is equivalent to the Hamiltonian of bilayer graphene [46] except that the hopping parameters γ_1 and γ' are replaced by the effective hopping parameters: $\tilde{\gamma_1} = \lambda\gamma_1$ and $\tilde{\gamma'} = \lambda\gamma'$.

Thus, when the number of layers N is odd, the Hamiltonian of ABA N-LG is composed of one monolayer type and (N-1)/2 bilayer type subbands, while for even N, it is composed of even number of bilayer like subbands and no monolayer.

Figure 1.12 shows how the energy dispersion of ABA

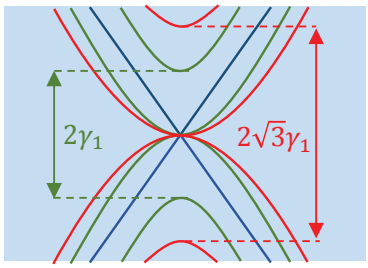

FIGURE 1.13: Low energy band structure of ABA-stacked 5-LG using the effective bilayer model described in the text.

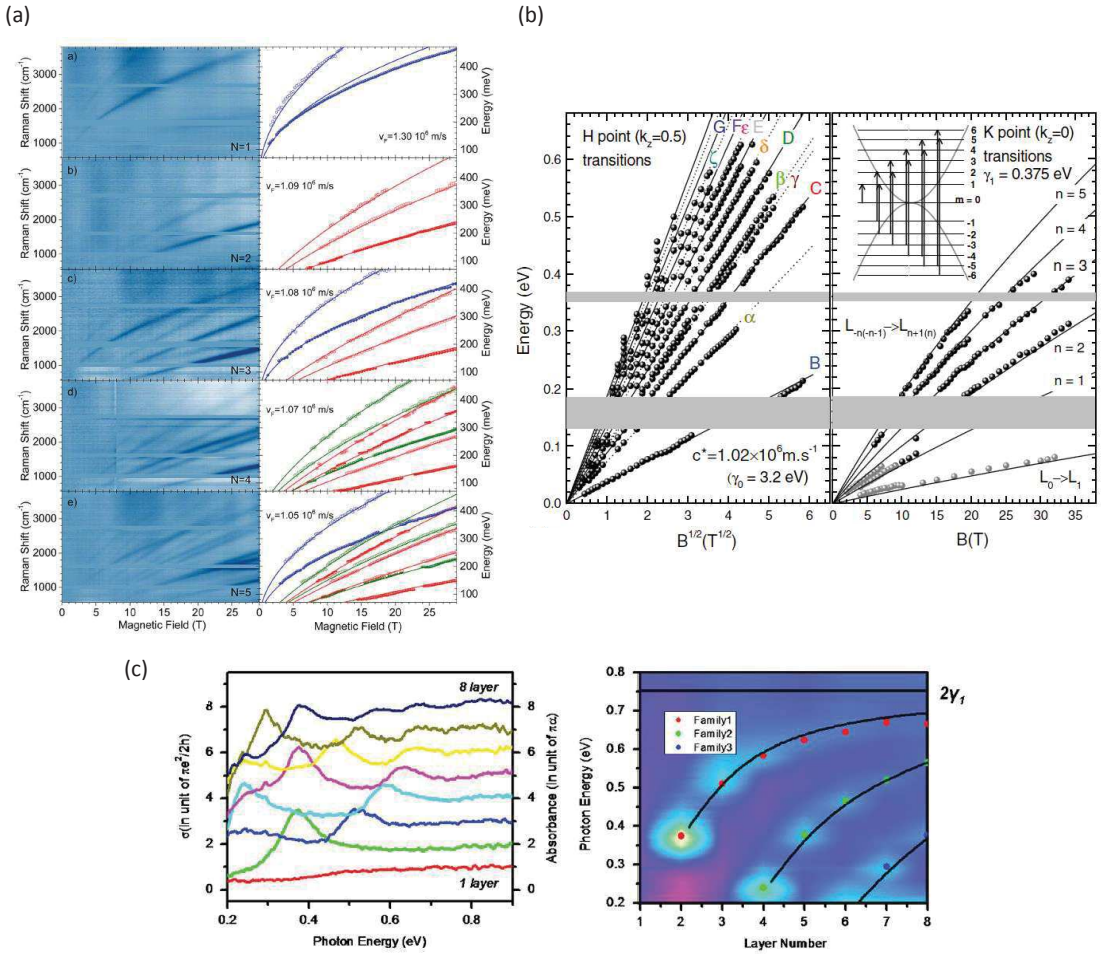

FIGURE 1.14: (a) Magneto-Raman spectra on Bernal 3, 4, and 5-LG (left panel) and the fitting of the experimental data using the effective bilayer model (right panel) [31]. (b) Infrared transmission spectra of FLG samples (left panel), and a contour plot of the infrared conductivity as a function of photon energy and N (right panel). The dots identify experimental data, while the solid curves are the theoretical predictions based on the effective bilayer model [25]. (c) Magneto-infrared spectroscopy of bulk graphite. Landau level transitions from the H point (left panel)and the K point (right panel) in the 3D Brillouin zone of graphite [44]. The dots are calculated dispersions using the effective bilayer model.

N-LG is obtained using the effective bilayer model. The planes normal to the H-K line are cutting at values $k_z c/2$. As an example, we apply the effective bilayer model to compute the band structure of 5-LG. To do so, we need to calculate the effective hopping parameter $\tilde{\gamma_1}$:

$$\tilde{\gamma_1} = \lambda\gamma_1 = 2\sin\left(\frac{m\pi}{2(N+1)}\right)\gamma_1 = 2\cos\left(\frac{\pi}{2} - \frac{m\pi}{2(N+1)}\right)\gamma_1 = 2\cos\left(\frac{p\pi}{N+1}\right)\gamma_1 = 2\cos(\theta)\gamma_1, \tag{1.38}$$

where $\theta = k_z c/2 = p\pi/(N+1)$. Since $m : -(N-1), ..., N-1$, p will vary as: $\pm 1, \pm 2, ..., \pm\lceil N + 1/2\rceil$ [31], where $\lceil\rceil$ denotes the integer part.

For ABA 5-LG, we have: $p = \{\pm 1, \pm 2, \pm 3\} \Rightarrow \theta = \{\frac{\pi}{6}, \frac{\pi}{3}, \frac{\pi}{2}\}$.

The band structure of ABA 5-LG is then made of a monolayer graphene bands, and two effective bilayers with the coupling parameters: $\tilde{\gamma_1} = 2\gamma_1$ and $\tilde{\gamma_1} = 2\sqrt{3}\gamma_1$ respectively (Figure 1.13).

Numerous experimental studies of the band structure evolution in ABA-stacked multilayer graphene came as a solid proof to the robustness of the effective bilayer model. Various experimental techniques are used to probe the band structure of graphene, such as angular resolved photo-emission and scanning tunneling spectroscopy. However, optical spectroscopy techniques, such as infra-red absorption and Raman spectroscopy, are our method of predilection due to the possibility to combine these techniques with strong magnetic fields. The evolution of the band structure for a given material is revealed in optical spectroscopy through the study of its excitation spectrum. This latter is a direct probe of the material's joint density of states (JDOS), which provides a measure of the number of allowed optical transitions between the occupied valence band and the unoccupied conduction band electronic states separated by the photon energy $\hbar\omega$.

Figure 1.14 shows a series of optical spectroscopy experiments on multilayer graphene, with a varying thickness. In Figure 1.14a, a multilayer graphene flake is placed under strong magnetic fields [31]. The magnetic field, as we will show in the next section, induces a Landau quantization. The change in the band structure of the material is revealed through its inter-Landau level excitations spectrum. The data obtained are fitted by the two parameters effective bilayer model, for a number of layers from 1 to 5 monolayers. The same approach has been used to fit experimental data on multilayer graphene, studied by far infrared conductivity [25] (Figure 1.14b).

The effective bilayer model also accounts for the band structure of ABA-stacked bulk graphite, with an infinite number of graphene layers. This is seen in Figure 1.14c from an infra-red spectroscopy study of its excitation spectrum that reveals the existence of massless Dirac fermions at the H point, and massive Dirac fermions at the K point in its 3D BZ, but with an effective mass of carriers that is twice enhanced with respect to that of bilayer graphene [44]. All these studies confirm the robustness of the effective bilayer model in studying the electronic properties of ABA-stacked N-LG.

1.2.3 Band dispersion in rhombohedral multilayer graphene

Most of the theoretical and experimental studies on graphite and N-LG have been focused on the Bernal stacking of the atomic layers. However, the Bernal stacking is not the only stable crystallographic order found within graphite crystals. Both electron [47] and X-ray diffraction experiments [48] have shown the presence of extra lines that cannot be attributed to the Bernal stacking structure [23]. Lipson and Stokes [49] suggested a

new crystallographic structure (refer to Figure 1.9c) to explain the anomalous lines observed in diffraction experiments. Their structure consists of each three graphene layers, shifted with respect to each other, that repeat successively to form bulk graphite.
Their study suggested that graphite crystals, either natural or kish (i.e., graphite obtained from the casting of carbon-rich steel), exhibit a Bernal stacking of 80% , 6% disorder, while the rhombohedral stacking presents 14%. Following these experimental observations, R. R. Haering used a tight binding approach, similar to the SWM model, to calculate the band structure of bulk rhombohedral graphite [24]. We should give here a derivation of such band structure.
As in the case of graphene monolayer and ABA stacked N-LG, we consider only the wave function of the π orbital electrons in N-LG around the corners of the BZ, i.e., the K and K$^{'}$ points.
The total Hamiltonian for N-LG is given by [50]

$$\mathcal{H} = \sum_{\mathbf{p}} \psi^{\dagger}_{\mathbf{p}} H(\mathbf{p}) \psi_{\mathbf{p}}, \tag{1.39}$$

where

$$\psi_{\mathbf{p}} = [C_{1,\alpha,\mathbf{p}}, C_{1,\beta,\mathbf{p}}, .., C_{N,\alpha,\mathbf{p}} C_{N,\beta,\mathbf{p}}]^{T}, \tag{1.40}$$

is the total wavefunction of the system and $C_{l,\mu,\mathbf{p}}$ is the wave function of an electron in layer $l = 1 \rightarrow N$, sublattice $\mu = \alpha, \beta$ and a momentum $\mathbf{p} = (p_x, p_y)$ measured from K or K$^{'}$ point.
In the ABC stacking configuration, the atoms of the A sublattice in each layer (labeled α as shown in Figure 1.15a) are exactly under the atoms of the B sublattice (labeled β) in the upper layer (see Figure 1.15b). Consequently, the interlayer coupling will link the wave function of the α atom from one layer to the wave function of the β atom in the upper layer as seen in Figure 1.15c.
We use the Dirac notation for the quantum states of the atoms in the A or B sublattices: $C_{l,\mu,\mathbf{p}} = \langle \mathbf{p} | \mu \rangle, \mu = \alpha, \beta$. Thus, for a given number of layers N, we will have $2N$ quantum states that correspond to A or B sublattices.
In order to build the matrix elements of the ABC Hamiltonian, we consider for simplicity the case for ABC tri-layer ($N = 3$) graphene. The total quantum state is given by:

$$|\psi\rangle = \{|\alpha_1\rangle, |\beta_1\rangle, |\alpha_2\rangle, |\beta_2\rangle, |\alpha_3\rangle, |\beta_3\rangle\}, \tag{1.41}$$

for each graphene layer, indexed by the symbol i, we defined the states for the α atoms and the β atoms, respectively. Knowing that γ_0 connects states in the same layer, while γ_1 connects an $|\alpha_i\rangle$ state with a $|\beta_{i+1}\rangle$ state from the next layer, the Hamiltonian for

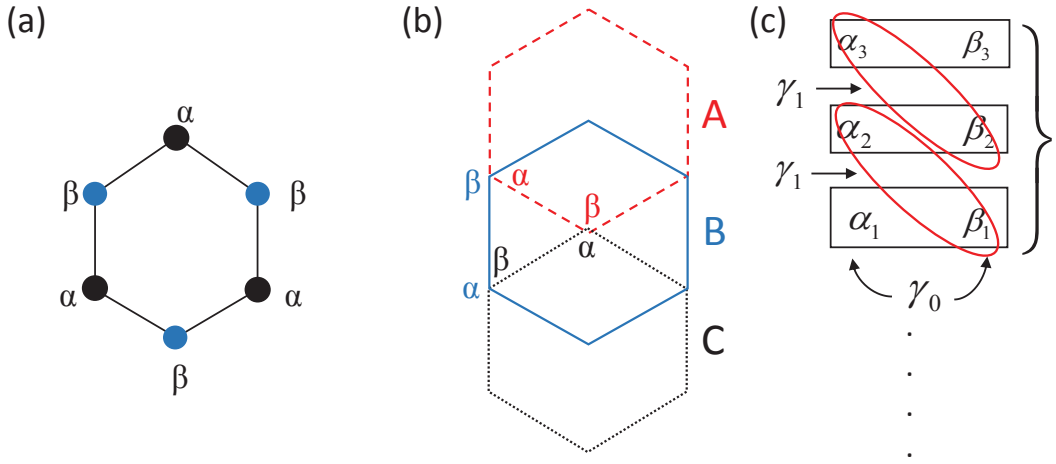

FIGURE 1.15: (a) The atoms in the two triangular sublattices are labeled α and β. (b) Schematics of the ABC stacking configuration. (c) Side view of the ABC stacking, showing how the interlayer coupling γ_1 connects the atoms α and β in adjacent layers.

ABC trilayer graphene is represented by the following 6×6 matrix [50–52]:

$$\mathcal{H}_{ABC} = \begin{pmatrix} 0 & \varepsilon_{\mathbf{p}}^{*} & 0 & 0 & 0 & 0 \\ \varepsilon_{\mathbf{p}} & 0 & \gamma_1 & 0 & 0 & 0 \\ 0 & \gamma_1 & 0 & \varepsilon_{\mathbf{p}}^{*} & 0 & 0 \\ 0 & 0 & \varepsilon_{\mathbf{p}} & 0 & \gamma_1 & 0 \\ 0 & 0 & 0 & \gamma_1 & 0 & \varepsilon_{\mathbf{p}}^{*} \\ 0 & 0 & 0 & 0 & \varepsilon_{\mathbf{p}} & 0 \end{pmatrix}, \tag{1.42}$$

where the matrix elements (following the logic discussed above) are given by

$$\langle \beta_i | H | \alpha_i \rangle = \varepsilon_{\mathbf{p}}, \langle \beta_i | H | \alpha_i \rangle = \varepsilon_{\mathbf{p}}^{*}, \langle \beta_i | H | \alpha_{i+1} \rangle = \langle \beta_{i+1} | H | \alpha_i \rangle = \gamma_1, \tag{1.43}$$

and the onset energies are expressed as a function of the intralayer coupling as

$$\varepsilon_{\mathbf{p}} = \upsilon_F p_+ = \upsilon_F (p_x + i p_y), \varepsilon_{\mathbf{p}}^{*} = \upsilon_F p_- = \upsilon_F (p_x - i p_y). \tag{1.44}$$

The low energy Hamiltonian for the K$^{'}$ point is obtained by exchanging p_+ and p_-. This approach can be easily generalized to an arbitrary number of ABC stacked layers. The eigenstates are then given by the basis:

$$|\psi_N\rangle = \{|\alpha_1\rangle, |\beta_1\rangle, |\alpha_2\rangle, |\beta_2\rangle, |\alpha_3\rangle, |\beta_3\rangle, ..., |\alpha_N\rangle, |\beta_N\rangle\}, \tag{1.45}$$

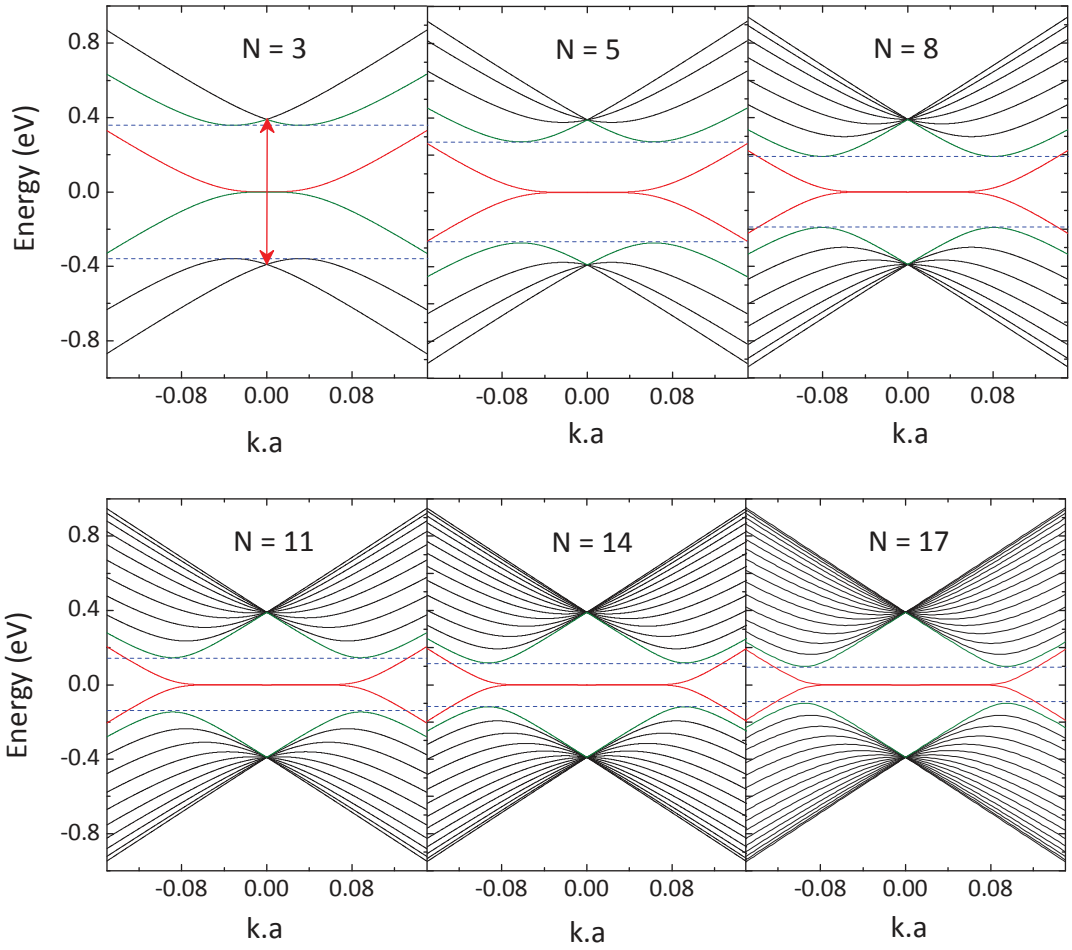

FIGURE 1.16: Tight binding model of the low energy band structure of rhombohedral multilayer graphene (number of layers N= 3, 5, 8, 11, 14, 17).

the Hamiltonian for ABC stacked N-LG is then given by:

$$\mathcal{H}_{ABC} = \begin{pmatrix} 0 & v_F p_- & & & & \\ v_F p_+ & 0 & \gamma_1 & & & \\ & \gamma_1 & 0 & v_F p_- & & \\ & & v_F p_+ & 0 & \gamma_1 & \\ & & & \gamma_1 & \ddots & \ddots \\ & & & & \ddots & \ddots \end{pmatrix}_{2N\times 2N} \tag{1.46}$$

Figure 1.16 shows the band structure obtained from the numerical diagonalization of Hamiltonian 1.46 (for: N=3, 5, 8, 11, 14, 17).

The band structure of ABC-stacked N-LG is composed of 2N branches. In the case of an ABC trilayer, it is composed of 3 valence bands and 3 electronic bands. Two of these bands are touching at the charge neutrality. The four remaining bands have a crossing point which is located at an energy equal to γ_1, the interlayer coupling. This crossing

point is related only to the interlayer coupling, and is independent of the number of layers.

When the number of ABC-stacked layers increases, two main changes are observed in the band structure. The bands touching at the charge neutrality (red colored bands in Figure 1.16) are flattened over a larger k-space region, resulting in a singular electronic density of states. At the same time, the energy separation between the gaped bands, plotted in green colors in Figure 1.16, is decreasing with increasing number of layers, and ultimately closes for ABC graphite. Figure 1.17 plots the density of states (DOS) for the gapped bands in ABC-stacked N-LG as a function of N. At the bulk limit the DOS resembles the one in monolayer graphene. Thus, the low energy carriers in ABC graphite are predicted to behave as three dimensional massless Dirac fermions [52].

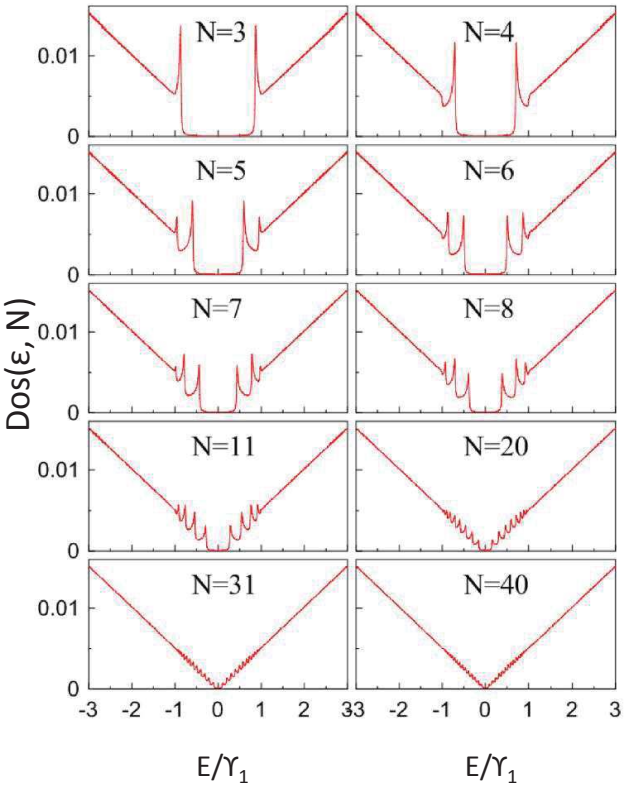

FIGURE 1.17: Density of states for the gapped bands as a function of the number of layers [52].

These changes in the band structure of ABC N-LG as function of N can be probed experimentally, as we will show in Chapter 5. The band structure of ABC N-LG is currently the subject of intensive research, motivated by the existence of the flat bands at the Fermi level. The induced high electronic density of states associated with these flat bands promises the observation of strongly correlated states in multilayer graphene. On the other hand, isolating thick rhombohedral multilayer graphene flakes (i.e., with a large ABC sequence) is a challenging task, since graphene layers relax into a Bernal stacking (more thermodynamically stable configuration) to form bulk graphite crystals. It has been shown that by epitaxial growth of graphene on the cubic phase of silicon carbide (3C-SiC), we can easily obtain a rhombohedral coverage up to 70%. These domains are about 40-50 nm large, with sequences of 4 to 5 monolayers [53]. By performing scanning tunneling spectroscopy (STS), and angular resolved photoemission spectroscopy

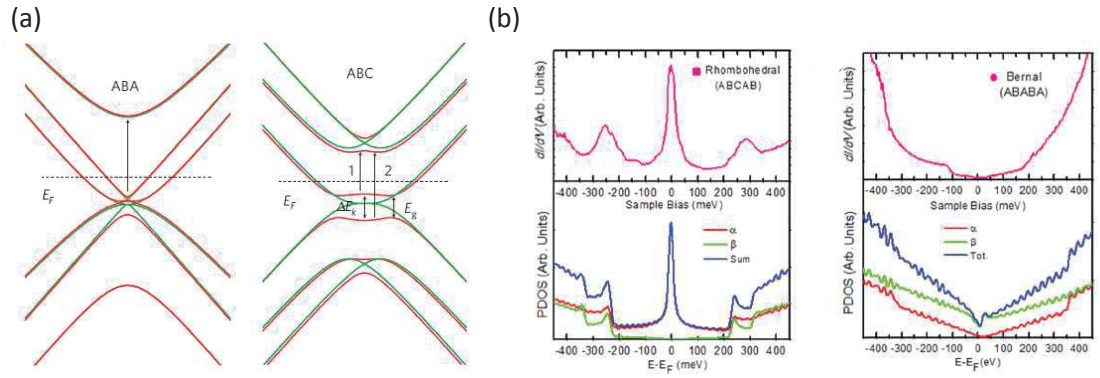

FIGURE 1.18: (a) Effect of an electric field on the band structure of trilayer graphene. A band gap opens in the ABC-stacked flake, while no significant changes are observed in Bernal trilayer [32]. (b) Comparison of the density of states by STS between ABC-stacked and ABA-stacked multilayer graphene. The upper panels are experimental results, while the lower panels are theoretical simulations [53].

(ARPES), the existence of the flat bands at the charge neutrality has been confirmed in these systems (see Figure 1.18b). The experimental observation are in line with the theoretical predictions based on density functional theory (DFT), as shown in the lower panels of Figure 1.18b.

Transport experiments on ABC tri-layers showed that electron-electron interactions are responsible for a band gap opening, when applying an electrical field normal to the atomic planes [32, 38]. On the other hand, no band gap opening has been observed on its ABA counterpart (see Figure 1.18a). Evidence of an intrinsic bang gap has been reported for suspended ABC trilayer graphene, thus not suffering from interaction with substrate. The observation of this band gap, of the order of 42 meV, has been reported even without the application of an electric field [54].

Owing to its singular density of states at the Fermi level, magnetic order might be expected for rhombohedral N-LG. Olsen *et al.* [41] used at tight binding model in the presence of long-range Coulomb interactions, to show that the total energy for ABC-trilayer graphene is minimized for a ferromagnetic state. This ferromagnetism is one order of magnitude more robust compared to un-screened bilayer graphene. This results are in contrast to the well-known diamagnetic behavior usually observed in Bernal-stacked natural graphite.

The ABC stacking belongs to the family of topological nodal semi-metals [55, 56]. In this sense, the electronic states present a non-trivial topology, as evidenced from band structure calculations based on a tight binding approach [57], and *ab initio* methods [58]. This topological order of the electronic states is protected by means of symmetry transformations, such as time reversal and inversion symmetries. As a consequence of this classification, the flat bands at the Fermi level are predicted as electronic surface states, localized in the outermost layers, while the gapped bands are bulk states, which

means they are confined inside the bulk [52, 56–58].
In addition to these promising phenomena in rhombohedral N-LG, the topologically protected flat bands are predicted to induce high temperature surface superconductivity [40, 59]. This superconducting state prevails even when the topological protection of the surface flat band is lifted. These theoretical works were motivated by the observation of high temperature superconductivity, that has been reported by several groups, on the surface of highly oriented pyrolytic graphite crystals (HOPG) [60, 61], and graphite powders [62, 63], with no solid explanation concerning its origin.
These experimental observations, along with the theoretical predictions, renders the study of rhombohedral N-LG properties very appealing.

1.3 Multilayer graphene under magnetic fields

The role of magnetic fields in studying the band structure of crystals is of major importance. The Lorentz force acting on the electronic charge bends the trajectories of the electrons, which affects the transport properties of metals and semi-conductors. The electronic kinetic energy in the direction transverse to the magnetic field becomes quantized into discrete levels. Thus, the presence of a magnetic field transforms the energy dispersion of solids in the momentum space, which is made of continuous bands, into discrete quantized energy levels. These energy levels can be accessed in experiments through their excitation spectra. To illustrate the major role played by magnetic field in condensed matter physics, we give in the following few examples of its effect on well-known quantum systems.
For example, the energy level structure in quantum dots (QDs are zero dimensional systems of highly confined electrons), as it is well known, is composed of discrete levels. However, the presence of a magnetic field, introduces another electronic confinement which superposes with the geometrical one, leading to interesting physical phenomena. This allows to access individual electronic states that are not observed in the absence of magnetic fields [64]. The application of magnetic fields to quantum dots offers interesting possibilities to study few-electron systems. Since the cyclotron energy $\hbar\omega_c$ can be made much larger than the binding energy of the confining electric potential, one can examine the transition from electrically bound states to Landau levels in this system [65]. The effect of magnetic field causes rearrangement of energy levels leading to formation of surface states and bulk-like Landau states [66]. A recent study has shown the role of magnetic field in demonstrating coherent manipulation of coupled electron spins in QDs devices, relevant to the advance in the field of quantum computation [67].
The application of magnetic field to quantum systems is not limited to probing already existing states. Magnetic fields can also be used to create new states of matter, that do

not exist in the absence of magnetic fields. The fractional quantum Hall effects (FQHE), in which the quasi-particles are composite fermions, as well as the suppression of superconductivity in metallic systems by a critical magnetic field (H_c), are good examples of magnetic field-induced quantum states [68, 69]. Superconductivity and the FQHE are quantum states created through a process called symmetry breaking. Superconductivity is generated through gauge and time reversal symmetry breaking [70], and the application of a magnetic field stronger than H_c will destroy the superconducting state, leading to a magnetic induced phase transition.

As we will show in Chapter 2, the application of a magnetic field along the c-axis of a crystal allows the observation of discrete excitations in the optical spectra of a given material such as graphene. By extracting the energies of the magnetic induced features and their line-widths, one can obtain considerable information about the behavior of particles in the studied system.

All these magnetic field-induced phenomena render the application of magnetic fields to graphene based systems, and 2D materials in general, a very important factor in the study of the fundamental properties of these systems.

1.3.1 Electronic states in monolayer graphene

2DES under a uniform magnetic field:

Before we derive the energy dispersion of monolayer graphene in the presence of magnetic field, let us first discuss the general case of a 2 dimensional electron system (2DES) under the influence of a constant uniform magnetic field $\mathbf{B}$. For simplicity, the intrinsic magnetic field moment, the electron spin, will be ignored. These terms can be included later on after the derivation of the eigen-states and eigenvalues of a 2DES system under magnetic field. The Hamiltonian of a charged particle in a magnetic field is [71]

$$H_{\mathbf{B}} = \frac{1}{2m}[\mathbf{p} - e\mathbf{A}]^2, \tag{1.47}$$

where $\mathbf{p} = \hbar/i\nabla$ is the quantum momentum operator at zero magnetic field. When the magnetic field is switched on, the momentum operator change as: $\mathbf{\Pi} = \mathbf{p} - e\mathbf{A}$. Π is called the substitute momentum operator for a particle in a magnetic field. This substitution is known as the Peierls substitution [72], with $\mathbf{A}$ being the vector potential of the magnetic field. The time independent Schrödinger equation reads:

$$H_{\mathbf{B}}\psi = \psi E, \tag{1.48}$$

The vector potential is related to the field by: $\mathbf{B} = \nabla \times \mathbf{A}$. Thus, the choice of the vector potential is not unique, since any gauge transformation as: $\mathbf{A} \rightarrow \mathbf{A} + \nabla\phi$ will

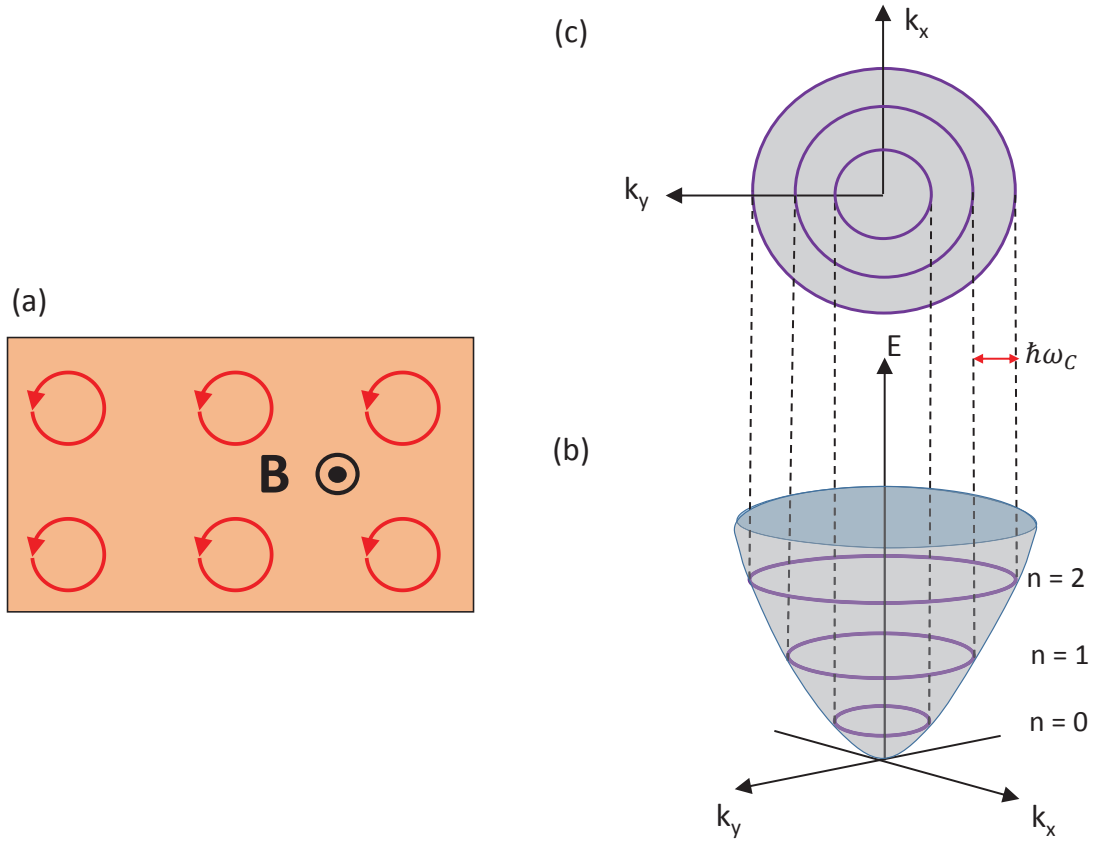

FIGURE 1.19: (a) Cyclotron motion of electrons in a plane normal to the uniform magnetic field. (b-c) Parabolic dispersion of 2DES electrons and the corresponding Landau levels in the presence of a magnetic field. The Landau levels energy gap corresponds to the cyclotron energy $\hbar\omega_c$.

not induce any change in the solutions of the Schrödinger equation [73]. In order to fix the vector potential, we follow the approach of Landau [71] for a particle in a constant uniform **B**, applied along the z-direction:

$$\mathbf{B} = \nabla \times \mathbf{A} = (0, 0, B), A_x = -By, A_y = A_z = 0. \tag{1.49}$$

This condition is called the Landau gauge, and even though other gauges might be used to uniquely fix **A**, the Landau gauge is usually applied to condensed matter systems and to study the properties of crystals under magnetic fields.
In the Landau gauge, the Hamiltonian becomes:

$$\frac{1}{2m}\left[(p_x + \frac{eB}{\hbar}y)^2 + p_y^2 + p_z^2\right]\psi = E\psi. \tag{1.50}$$

If the eigenstates of such an equation are assumed to take the form [71]: $\psi = \tilde{\psi}(x)e^{-ik_y y}$, we obtain the following equation for $\tilde{\psi}(x)$:

$$\frac{\partial^2\tilde{\psi}}{\partial x^2} + \frac{2m}{\hbar^2}\left[\left(E - \frac{p_z^2}{2m}\right) - \frac{1}{2}m\omega_c^2\left(x - x_0\right)^2\right]\tilde{\psi} = 0, \tag{1.51}$$

where: $x_0 = p_y eB = \hbar k_y eB$ and $\omega_c = eB/m$ is called the cyclotron frequency. The above equation is identical to the Schrödinger equation for a quantum harmonic oscillator (QHO) with a frequency ω_c. The eigenvalues of such a system are:

$$E_n = \hbar\omega_c\left(n + \frac{1}{2}\right), \tag{1.52}$$

These eigenvalues give the discrete energy levels corresponding to the circular motion of charged particles in a plane perpendicular to the magnetic field direction (Figure 1.19a); they are called *Landau levels*, with $n = 0, 1, 2\ldots$ being the Landau level index.
Thus, the energy of electrons in a 2DES with parabolic dispersion (i.e., $E = \hbar^2k^2/2m$) will split, under the effect of the magnetic field, into discrete Landau levels (LLs) with energies: $E_n = \hbar\omega_c(n+1/2)$ as shown in Figure 1.19b,c. The LLs, in the case of a 2DES, are equally separated by gaps of value: $\Delta = \hbar\omega_c$.
Finally, we would like to stress on the fact that the energy evolution of the LLs is expected to be linear with the field, since $E \sim B$ as seen in 1.52. Experiments in which we probe the energy of the LLs a function of the magnetic field represent a powerful probe of the band structure in crystals. Consequently, LLs with a linear dispersion as a function of the magnetic field are regarded as a signature of systems with parabolic dispersion of their energy in momentum space.

Monolayer graphene under a uniform magnetic field:
Let us now come back to the case of monolayer graphene, and see how the magnetic field affects the energy dispersion of the carriers on this material.
We showed above that the band structure of graphene is considered to be composed of Dirac cones located around the K and K′ points at Brillouin zone corners. In the vicinity of these points the electron energy depends linearly on its momentum: $E(\mathbf{p}) = \upsilon_F|\mathbf{p}|$, described by the Dirac equation for zero rest mass particles, with an effective velocity υ_F, which replaces the speed of light. Due to this linear dispersion, the LLs structure in graphene is expected to be completely different from the case of conventional 2DES. This has been confirmed by numerous experimental studies that probe the Landau level energy diagram of graphene under magnetic fields.
To obtain the energy dispersion of LLs, we apply the Peierls substitution to the Hamiltonian of monolayer graphene:

$$\mathcal{H}(\mathbf{p}) \rightarrow \mathcal{H}(\mathbf{\Pi}) = \mathcal{H}\left(\mathbf{p} - e\mathbf{A}\right) = H_B(\mathbf{p}, \mathbf{r}). \tag{1.53}$$

The momentum operator satisfies the following commutations relations:

$$[\Pi_x, \Pi_y] = -ie\hbar\left(\frac{\partial A_y}{\partial x} - \frac{\partial A_x}{\partial y}\right) = -i\frac{\hbar^2}{l_B^2}, \tag{1.54}$$

where we introduced a fundamental length known as *the magnetic length*:

$$l_B = \sqrt{\frac{\hbar}{eB}} \approx 26nm/\sqrt{B(T)}. \tag{1.55}$$

Since electrons are moving in circles when under a perpendicular magnetic field, l_B is seen as the smallest size of a circular orbit in a magnetic field that is allowed for a charged particle by the uncertainty principle.
In the derivation of the energy spectrum of crystals under the effect of a magnetic field, a conventional approach is to introduce the ladder operators similarly to the case of the quantum harmonic oscillator [2, 51]

$$a = \frac{l_B}{\sqrt{2}\hbar}(\Pi_x - i\Pi_y) = \frac{l_B}{\sqrt{2}\hbar}\Pi_- \quad \text{and} \quad a^\dagger = \frac{l_B}{\sqrt{2}\hbar}(\Pi_x + i\Pi_y) = \frac{l_B}{\sqrt{2}\hbar}\Pi_+, \tag{1.56}$$

the Hamiltonian of monolayer graphene becomes:

$$H_B = \sqrt{2}\frac{\hbar\upsilon_F}{l_B}\begin{pmatrix} 0 & a \\ a^\dagger & 0 \end{pmatrix}. \tag{1.57}$$

By solving the eigen equation: $H_B\psi_n = E_n\psi_n$, we obtain the energy spectrum for monolayer graphene under magnetic field [2]

$$E_{\lambda,n} = \lambda\frac{\hbar\upsilon_F}{l_B}\sqrt{2n}. \tag{1.58}$$

$\lambda = \pm 1$ labels the states of positive and negative energy, respectively. This quantum number plays the same role as the band index in the zero-B field case discussed earlier. Thus, $\lambda = +1$ for the conduction band and $\lambda = -1$ for the valence band.
In stark contrast to conventional 2DES, equation (1.55) describes relativistic LLs that disperse as $\sqrt{B}$ in a varying magnetic field. The $\sqrt{B}$ dependence has since become a fingerprint of graphene monolayer under magnetic fields, and of related materials with a Dirac cone dispersion in their low energy band structure.

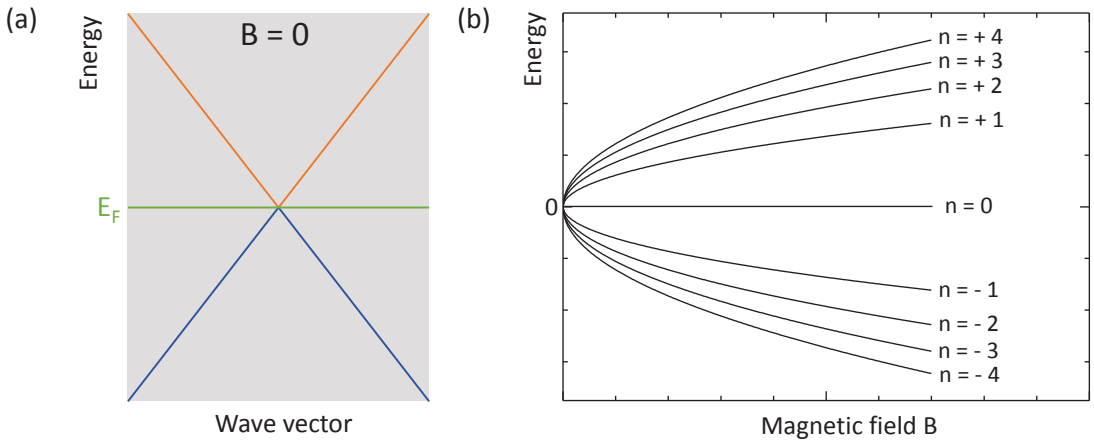

FIGURE 1.20: Relativistic Landau levels as a function of the magnetic field in monolayer graphene (b). Their dispersion is a direct consequence of the linear energy dispersion at zero field(a) [ref:goerbig].

1.3.2 Case of Bernal-stacked multilayer graphene

Using the *effective bilayer model*, the band structure of ABA stacked N-LG along the H-K-H line is given by [45, 46]:

$$\mathcal{H}_{ABA} = \begin{pmatrix} 0 & \gamma k_- & 0 & 0 \\ \gamma k_+ & 0 & \tilde{\gamma_1} & 0 \\ 0 & \tilde{\gamma_1} & 0 & \gamma k_- \\ 0 & 0 & \gamma k_+ & 0 \end{pmatrix}, \tag{1.59}$$

where $\tilde{\gamma_1} = \lambda\gamma_1 = 2\gamma_1 \cos(\pi k_z)$. This Hamiltonian is similar to the Hamiltonian of a bilayer graphene [74], but with an effective coupling parameter tuned by the momentum k_z [45, 46].

Under the effect of a magnetic field normal to the atomic planes, the Hamiltonian will transform as [4]

$$\mathcal{H}_{ABA}(B) = \begin{pmatrix} 0 & \epsilon_0 a & 0 & 0 \\ \epsilon_0 a^\dagger & 0 & \tilde{\gamma_1} & 0 \\ 0 & \tilde{\gamma_1} & 0 & \epsilon_0 a \\ 0 & 0 & \epsilon_0 a^\dagger & 0 \end{pmatrix}, \tag{1.60}$$

where we kept the same definitions for the ladder operators as in monolayer graphene. In the frame of the effective bilayer model, the energy L_n^θ ($L_{-n}^\theta = -L_n^\theta$) of the n^{th} electron (hole) Landau level arising from the lowest energy bands is given by [45]:

$$L_{|n|}^\theta = \sqrt{\frac{\tilde{\gamma_1}^2}{2} + \left(|n| + \frac{1}{2}\right) E_1^2 - \sqrt{\frac{\tilde{\gamma_1}^4}{4} + \left(|n| + \frac{1}{2}\right) E_1^2 \tilde{\gamma_1}^2 + \frac{E_1^4}{4}}}. \tag{1.61}$$

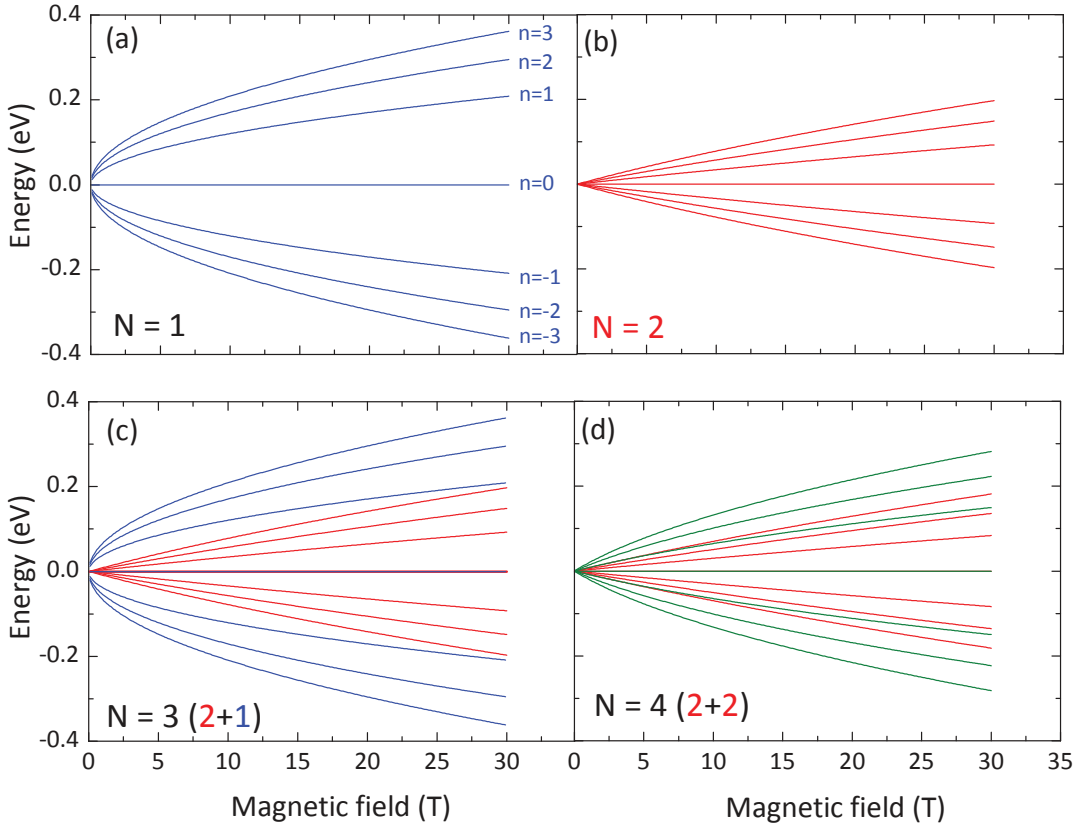

FIGURE 1.21: (a-d) Low energy Landau levels of Bernal stacked N-LG for N=1, 2, 3, 4, respectively. The effective bilayer model is used for the calculated dispersion.

Where we introduced: $E_1 = v_F\sqrt{2e\hbar B}$. For an effective interlayer coupling $\tilde{\gamma}_1$ at $\theta = k_z c/2 = \pi/2$ (see effective bilayer coupling), we recover the $\sqrt{B}$-dependence of LLs in monolayer graphene, while $\theta = \pi/3$ gives us the nearly linear in B LLs dispersion for bilayer graphene [74]. Based on the effective bilayer model, the LLs dispersion for N=1, 2, 3, 4 are presented in Figure 1.21, respectively.

1.3.3 Case of rhombohedral-stacked multilayer graphene

Let us now discuss the effect of a transverse uniform magnetic field on the band structure of ABC stacked N-LG. As in the case of monolayer graphene, and ABA N-LG, the Peierls

substitution: $\mathbf{\Pi} = \boldsymbol{p} - e\boldsymbol{A}$ is applied to the ABC Hamiltonian which will take the form:

$$\mathcal{H}_{ABC} = \begin{pmatrix} 0 & \epsilon_0 a & & & & \\ \epsilon_0 a^\dagger & 0 & \gamma_1 & & & \\ & \gamma_1 & 0 & \epsilon_0 a & & \\ & & \epsilon_0 a^\dagger & 0 & \gamma_1 & \\ & & & \gamma_1 & \ddots & \ddots \\ & & & & \ddots & \ddots \end{pmatrix}_{2N\times 2N} \tag{1.62}$$

where $\epsilon_0 = \sqrt{2}\hbar v_F / l_B \simeq 36\sqrt{B\,[T]}$ meV is the cyclotron energy in monolayer graphene. The 2N-components eigenstates corresponding to Hamiltonian (1.62) have the following structure [50, 51]

$$|\psi_n^\alpha\rangle = \left[c_{A_1}^\alpha\, \varphi_{n-1}, c_{B_1}^\alpha\, \varphi_n, c_{A_2}^\alpha\, \varphi_n, c_{B_2}^\alpha\, \varphi_{n+1}, c_{A_3}^\alpha\, \varphi_{n+1}, c_{B_3}^\alpha\, \varphi_{n+2}, \ldots\right]^T \tag{1.63}$$

where $\varphi_n \equiv \varphi_{n,k}\,(x,y,z) \sim e^{iky} e^{-z^2/2} H_n\,(z)$ is the wave function of a harmonic oscillator with $z = \left(x - kl_B^2\right)/l_B$ and $H_n\,(z)$ is the Hermite polynomial. As in the usual one-dimensional harmonic oscillator, the ladder operators will act on the wave functions in the following way:

$$a\varphi_n = \sqrt{n}\varphi_{n-1} \tag{1.64}$$

$$a^\dagger \varphi_n = \sqrt{n+1}\varphi_{n+1}. \tag{1.65}$$

Then, for each value of n, one needs to diagonalize the following matrix

$$\begin{pmatrix} 0 & \epsilon_0\sqrt{n} & & & & \\ \epsilon_0\sqrt{n} & 0 & \gamma_1 & & & \\ & \gamma_1 & 0 & \epsilon_0\sqrt{n+1} & & \\ & & \epsilon_0\sqrt{n+1} & 0 & \gamma_1 & \\ & & & \gamma_1 & \ddots & \ddots \\ & & & & \ddots & \ddots \end{pmatrix}_{2N\times 2N} . \tag{1.66}$$

in order to obtain the set of $2N$ Landau levels (LLs) and the corresponding coefficients $\{c_{A_i}^\alpha, c_{B_i}^\alpha\}$ that determine the eigenstates $|\psi_n^\alpha\rangle$ with $\alpha = 1, \ldots, 2N$. In Eq. (1.66), the index n is required to be positive. However, we note that Eq. (1.62) supports eigenstates

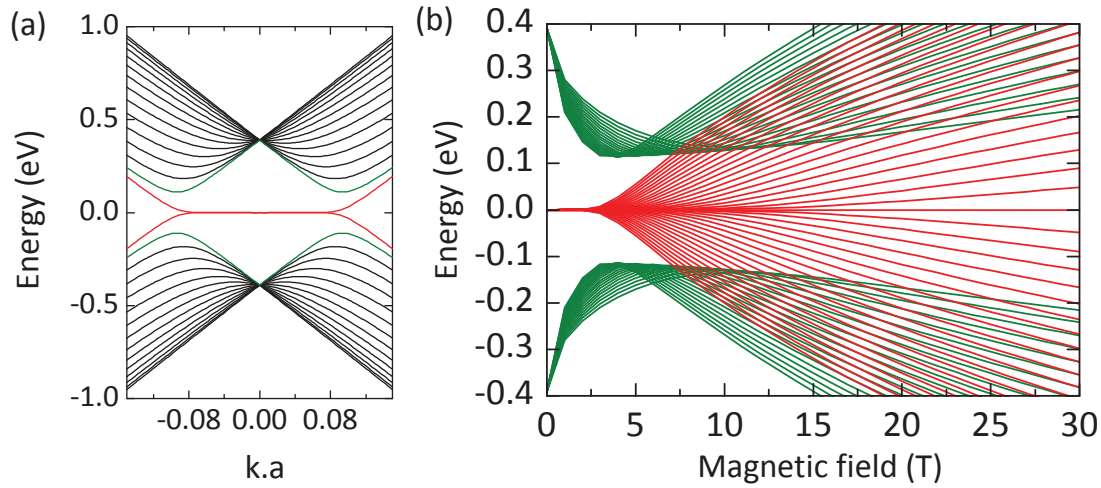

FIGURE 1.22: (a) Low energy band dispersion of ABC stacked 15-LG. (b) The corresponding Landau levels dispersion for the flat bands (red colors) and the lowest in energy gapped bands (green colors). The Landau levels are plotted for a varying Landau level index from $n = 0$ to 20.

with the following structure:

$$|\psi_0\rangle = \begin{pmatrix} 0 \\ c_{B_1}\varphi_0 \\ c_{A_2}\varphi_0 \\ c_{B_2}\varphi_1 \\ c_{A_3}\varphi_1 \\ c_{B_3}\varphi_2 \\ c_{A_4}\varphi_2 \\ c_{B_4}\varphi_3 \\ \vdots \end{pmatrix}, |\psi_{-1}\rangle = \begin{pmatrix} 0 \\ 0 \\ 0 \\ c_{B_2}\varphi_0 \\ c_{A_3}\varphi_0 \\ c_{B_3}\varphi_1 \\ c_{A_4}\varphi_1 \\ c_{B_4}\varphi_2 \\ \vdots \end{pmatrix}, |\psi_{-2}\rangle = \begin{pmatrix} 0 \\ 0 \\ 0 \\ 0 \\ 0 \\ c_{B_3}\varphi_0 \\ c_{A_4}\varphi_0 \\ c_{B_4}\varphi_1 \\ \vdots \end{pmatrix}, \ldots |\psi_{-N+1}\rangle = \begin{pmatrix} 0 \\ 0 \\ 0 \\ 0 \\ \vdots \\ \vdots \\ \vdots \\ \varphi_0 \end{pmatrix}. \tag{1.67}$$

These eigenstates can be obtained from (1.63) by extending the range of possible values of n to $n \geq -N + 1$ and using the rule that harmonic oscillator wavefunction with negative subindices must be replaced by zero. The corresponding eigenvalues can be obtained by applying $\mathcal{H}_{ABC}$ to these states and solving for the nontrivial part of the eigenvalue equation. For each one of the different form of the eigenstates in Eq. (1.67) there is always one eigenstate with zero energy while the remaining possible states appear around $\sim \pm\gamma_1$ for small magnetic field. Hence, there are N nontrivial eigenstates with zero energy for ABC-stacked N-LG [50].

Figure 1.22b shows the magnetic evolution of the first $n = 20$ LLs for the four lowest in energy bands (indicated by red and green colors in Figure 1.22a). Since the red bands are flatten over a large k-space region, their Landau quantization gives a Landau level

dispersion with a finite magnetic onset, which seems to be dependent on the number of layers N [52, 75].

Chapter 2

Experimental technique: Raman spectroscopy

2.1 Principle of the Raman scattering effect

In condensed matter physics, experimental techniques based on the interaction of light with solids (i.e., semi-conductors, metals...etc.) are powerful tools to probe the fundamental properties of materials. The dominant light-matter interaction processes in materials are: absorption, reflection, and photo-luminescence. However, due to inhomogeneities in the medium, light can also undergo a scattering process. Depending if the inhomogeneities are static (as crystal defects) or dynamic, such as atomic vibrations in the crystal lattice, the incident light can be scattered either elastically (i.e., no change in frequency) or inelastically (the frequencies of incident and scattered light are no longer the same).

The inelastic scattering of light was theoretically predicted and experimentally discovered by several independent groups of physicists: L. Brillouin and A. Smekal have predicted the inelastic scattering theoretically in 1923, while C.V. Raman and K. Krishnan have made the first measurements to probe this effect in liquids in 1928 [76]. Shortly after, L. Mandelstam and G. Landsberg proved the effect in solids [77]. For discovering the inelastic light scattering, C. V. Raman was awarded the Physics Nobel prize in 1930. The inelastic scattering of light is mostly referred to nowadays in literature as the *Raman scattering* effect.

Today, Raman spectroscopy is a powerful tool in optical spectroscopy. It is widely used to study crystals and chemical compounds, classify and identify different constituents in complex materials, and has been demonstrated in recent years to be a technique of choice in the study of two dimensional materials such as graphene and multilayer graphene.

In the Raman scattering process, the incident photon, with an energy E_i and a momentum k_i, is in-elastically scattered so its final energy E_s and momentum k_s are given by [78]:

$$E_s = E_i \pm E_q, \quad k_s = k_i \pm q. \tag{2.1}$$

The couple (E_q, q) can be associated with many forms of excitations in the target medium. However, the Raman scattering process is generally associated with the vibrational modes of molecules in matter (solid or fluid), also called *phonons* [78]. The couple (E_q, q) is then associated with the energy and momentum of a phonon. Since each material possess a unique set of vibrational modes, Raman spectroscopy can be used as a very accurate characterization tool.

2.1.1 Classical description of the Raman effect

The photon, from a classical point of view, is seen as an electromagnetic radiation with a periodic oscillation that propagates in space. When an electric dipole (see the schematic presentation in Figure 2.1a), expressed as $\mathbf{P} = Q\mathbf{L}$, is subject to an electric field $\mathbf{E}$, a torque $\mathbf{M} = \mathbf{P} \times \mathbf{E}$ acts on the dipole to align it with the electric field as seen in Figure 2.1b. Raman scattering is then pictured as the ability of an electric field to polarize the charged system. Figure 2.1c shows a schematic of the CO_2 molecule, with the oxygen atoms stretching far or near the carbon atom. The bigger the charge separation of the molecule (i.e., oxygen atoms far away from the carbon atom), the easier for the electric field to polarize the electron cloud.

When light is shined on a sample, the electromagnetic radiation will redistribute the charges of the molecules in the sample. The negatively charged electrons will go toward the positive pole, while the positively charged ions go to the negative pole as depicted in Figure 2.1b. This charge separation will induce an electric dipole moment expressed as:

$$\mathbf{P}(\mathbf{r}, t) = \chi(\mathbf{k}_i, \omega_i)\mathbf{E}_i(\mathbf{k}_i, \omega_i), \tag{2.2}$$

where χ is the electrical susceptibility or the so-called *polarizability*. In solids, χ is usually a second rank tensor [78], hence the following matrix form for the dipole moment:

$$\begin{pmatrix} P_x \\ P_y \\ P_z \end{pmatrix} = \begin{pmatrix} \chi_{xx} & \chi_{xy} & \chi_{xz} \\ \chi_{yx} & \chi_{yy} & \chi_{yz} \\ \chi_{zx} & \chi_{zy} & \chi_{zz} \end{pmatrix} \begin{pmatrix} E_x \\ E_y \\ E_z \end{pmatrix}, \tag{2.3}$$

For optical spectroscopy on crystals, the electric field of an incident light and the lattice vibrational mode have an oscillatory behavior. The incident electrical field $\mathbf{E}(\mathbf{r}, t)$, as

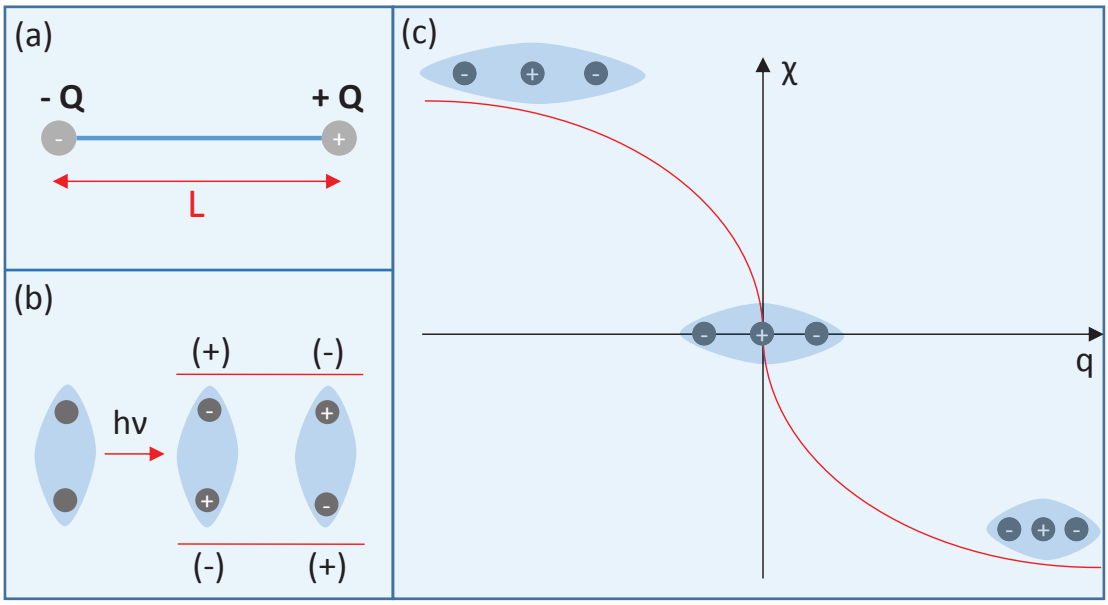

FIGURE 2.1: (a) Electric dipole moment induced by the spatiale separation of two charged particles. (b) Effect of light in charged particles. Charged molecules align their poles with the electric field of light. (c) Change in the polarizability χ (red curve) for the CO_2 molecule as a function of the distance between the oxygen atoms and the carbon atom.

well as the atomic displacement associated with a phonon $\mathbf{Q}(\mathbf{r},t)$, are given by:

$$\mathbf{E}(\mathbf{r},t) = \mathbf{E}_i(\mathbf{k},\omega)\cos(\mathbf{k}_i.\mathbf{r} - \omega_i t), \quad \mathbf{Q}(\mathbf{r},t) = \mathbf{Q}(\mathbf{q},\omega_q)\cos(\mathbf{q}.\mathbf{r} - \omega_0 t), \tag{2.4}$$

where $\mathbf{q}$ and ω_q are the phonon wave vector and frequency, respectively. The lattice vibration will modulate the susceptibility and hence the polarizability χ of the atoms, so χ will change as a function of the displacement. For small amplitudes of the atomic displacement $Q = |\mathbf{Q}|$, the polarizability χ is linear with Q, we can then expand it as a Taylor series of $\mathbf{Q}(\mathbf{r},t)$:

$$\chi(\mathbf{k}_i,\omega_i,\mathbf{Q}) = \chi_0(\mathbf{k}_i,\omega_i) + \left(\frac{\partial\chi}{\partial \boldsymbol{Q}}\right)_{Q=Q_0} \boldsymbol{Q}(\mathbf{r},t) + \cdots . \tag{2.5}$$

Usually the expansion is limited to the first order, it is then referred to as the dipole approximation. The first term at the right hand of equation 2.5 represents the polarizability of the medium at equilibrium (i.e., in the absence of fluctuations), while the second term is an induced polarization by the lattice vibrations in the medium [79]. The polarization of the medium, in the presence of atomic vibrations, can be written as:

$$\mathbf{P}(\mathbf{r},t,\mathbf{Q}) = \mathbf{P}_0(\mathbf{r},t) + \mathbf{P}_{ind}(\mathbf{r},t,\mathbf{Q}) = \left(\chi_0 + \left(\frac{\partial\chi}{\partial \boldsymbol{Q}}\right) Q\right)(\mathbf{E}_0\cos\omega_i t) = \mathbf{E}_0\chi_0\cos(\mathbf{k}_i.\mathbf{r} - \omega_i t) +$$
$$\frac{1}{2}\left(\frac{\partial\chi}{\partial \boldsymbol{Q}}\right) Q_0\mathbf{E}_0\left(\cos\left[(\mathbf{k}_i+\mathbf{q}).\mathbf{r} - (\omega_i+\omega_q)\,t\right] + \cos\left[(\mathbf{k}_i+\mathbf{q}).\mathbf{r} - (\omega_i-\omega_q)\,t\right]\right) \tag{2.6}$$

From equation 2.6, we see that $\mathbf{P}_0(\mathbf{r},t)$ will induce an elastic scattering of light, this means there will be no change in the frequency ω_i of the scattered light with respect to the incident light. On the other hand, $\mathbf{P}_{ind}(\mathbf{r},t,\mathbf{Q})$ induces an inelastic scattering, with the frequency ω_i being downshifted by an amount $(\omega_i - \omega_q)$ or upshifted by $(\omega_i + \omega_q)$, resulting in a Raman scattering process.
In the literature, the elastic scattering of light is referred to as the *Rayleigh* scattering, while the downshift and the upshift are called *Stokes* and anti-*Stokes* scattering, respectively. Even though it is well known that only a tiny amount of the incident light is Raman scattered, there are no qualitative ways to estimate the amount of the Raman scattered light with respect to the elastically scattered one using the classical approach above. Thus, Raman scattering is fully described by considering the quantum nature of light-matter interaction, as we will show in the following.

2.1.2 Quantum description of the Raman effect

From a quantum mechanical point of view, the Raman scattering is a process in which excitation is either created or destroyed. The excitation we are referring to is a phonon. During a Raman scattering process, phonons are either created or destroyed, making a change in the frequency of the photons interacting with the system. The relative frequency shift of the outgoing photon with respect to the frequency of the incident photon, equals to the phonon frequency, is called the Raman shift and is usually expressed in Raman spectroscopy in the units of wave numbers (cm^{-1}).
As we discussed earlier, it is hard from a classical point of view to estimate the amount of light which will be Raman scattered with respect to the amount of light which is Rayleigh scattered. However, this can be done using a quantum description of the Raman process. A standard approach to estimate the intensity of the Raman process will be to calculate the transition probability per unit time, also called the transition rate, for such a process to occur. This is usually done using the so-called Fermi golden rule [78, 80]:

$$W_f = \left(\frac{2\pi}{\hbar}\right) |\langle f|\,\mathcal{H}\,|i\rangle|^2 \rho(E_f), \tag{2.7}$$

where W_{if} is the transition rate from the initial state $|i\rangle$ to the final state $|f\rangle$. $\mathcal{H}$ is the Hamiltonian of the system, and $\rho(E_f)$ is the density of the final states.
To obtain the intensity of a first order Raman process $I(\omega_q, E_L)$ (i.e., only one phonon is either created or destroyed), one needs to evaluate the transition rate using the Fermi golden rule:

$$I(\omega_q, E_L) = \sum_f |\sum_{n,n'} \frac{M^{op}(\mathbf{k}-\mathbf{q}, in')M^{ep}(\mathbf{q}, n', n)M^{op}(\mathbf{k}, ni)}{(E_L - \Delta E_{ni})(E_L - \hbar\omega_q - \Delta E_{n'i})}|^2, \tag{2.8}$$

where $E_{Laser} = E_L = \hbar\omega_i$ is the energy of an incident photon, while $\mathbf{q}$ and $\hbar\omega_q$ are the momentum and energy of a scattered phonon. As we will show in the following, M^{ij} are physical quantities that depict matrix elements for the different quantum states. The initial state $|i\rangle$ has an energy E_i, the intermediate states $|n\rangle$ and $|n'\rangle$, describing the scattered electron by the photon and the phonon, have energies E_{ni} and $E_{n'i}$, respectively. Figure 2.2 summarizes the first order Raman process using a *Feynman diagram*, which is executed in three steps:

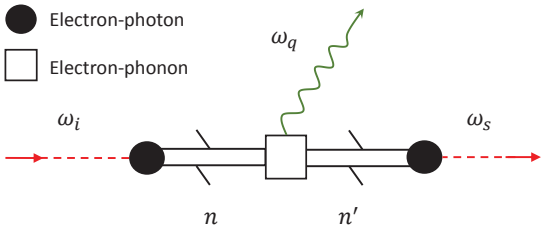

FIGURE 2.2: Feynman diagram depicting a first order Raman scattering process [80]. The black dots indicate an electron-photon interaction, while the square inidicates an electron-phonon interaction.

$$\underset{\text{electron-photon interaction}}{(\hbar\omega_i - e)} \longrightarrow \underset{\text{electron-phonon interaction}}{(e - \hbar\omega_q)} \longrightarrow \underset{\text{electron-photon interaction}}{(e - \hbar\omega_s)} \tag{2.9}$$

The Fermi golden rule for a first order Raman process is thus obtained by using third order time-dependent perturbation theory [78, 80]. The quantities to be evaluated have the from:

$$\frac{\langle n|\,\mathcal{H}_{eR}\,|i\rangle}{[E_L - (E_n - E_i)]}. \tag{2.10}$$

The total transition rate for the first order Raman process is given by [78, 80]:

$$I(\omega_s, E_L) = \left(\frac{2\pi}{\hbar}\right) \Big|\sum_{n,n'} \frac{\langle i|\,\mathcal{H}_{eR}(\omega_s)\,|n'\rangle\,\langle n'|\,\mathcal{H}_{e-ion}\,|n\rangle\,\langle n|\,\mathcal{H}_{eR}(\omega_i)\,|i\rangle}{[E_L - (E_n - E_i)][E_L - \hbar\omega_q - (E_{n'} - E_i)]}\Big|^2 \times \delta\left(E_L - \hbar\omega_q - \hbar\omega_s\right). \tag{2.11}$$

Equation 2.11 implies a Raman efficiency around $10^{-6} - 10^{-7}$ in semiconductor physics [80]. This means that the amount of light scattered due to the Raman effect is only a tiny part of the light going through the sample. One needs to use coherent light sources such as lasers in order to make the observation of the Raman effect more practical.

2.1.3 General discussion

Stokes and anti-Stokes:

As we discussed in the first two parts, the Raman scattering results from the interaction of light with the electric dipole of the molecule (classical picture), or it can also be seen as the result of the interaction between the photons of the electromagnetic radiation with the phonons in the target crystal. Figure 2.3(a,b) shows the first order Raman process

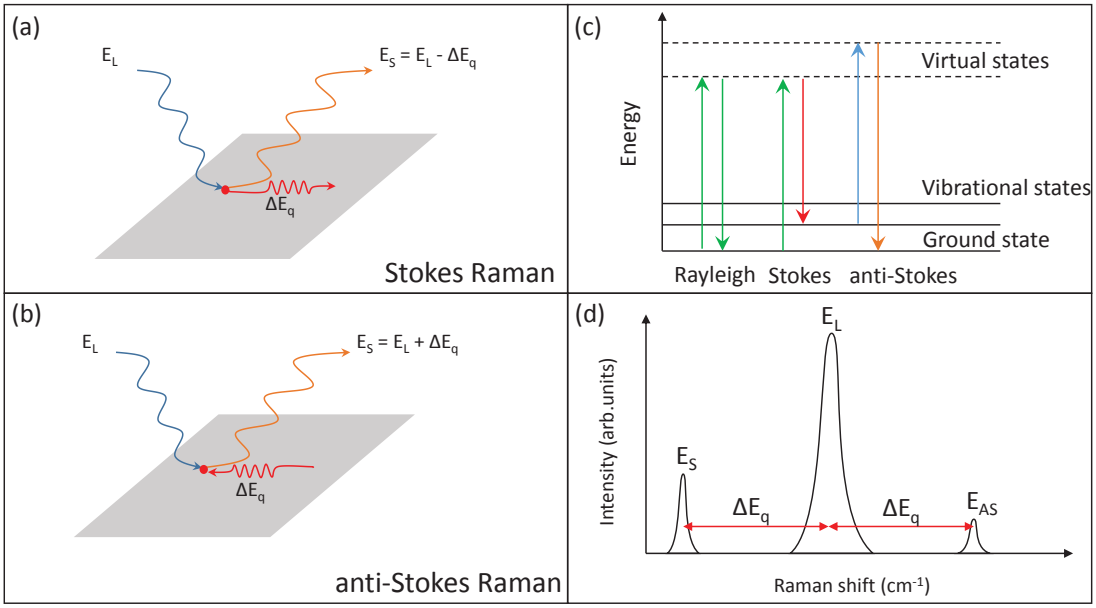

FIGURE 2.3: Schematics of the Stokes and anti-Stokes Raman processes (a,b). (c) Energy diagram comparing the Rayleigh process (elastic scattering) and the Raman process (inelastic scattering). (d) Intensity vs energy specrum showing the Stokes and anti-Stokes peaks. Their relative intensities with respect to the Rayleigh peak are exagerated to show them in the same energy scale.

discussed earlier. The Stokes scattering represents the emission (creation) of a phonon, while the anti-Stokes results from the absorption (destruction) of a phonon. Such process depends on the phonon statistics, which is expressed, at a given temperature T, by the Bose-Einstein statistics:

$$n = \frac{1}{e^{E_q/k_B T} - 1}, \tag{2.12}$$

where k_B is the Boltzmann constant, and E_q the phonon energy. One can estimate the ratio of the Stokes/anti-Stokes scattering from the Bose-Einstein statistics, where the Stokes process will cause the phonon statistics to change as $n \rightarrow n+1$, and the anti-stokes process will change as $n+1 \rightarrow n$:

$$\frac{n+1}{n} = e^{E_q/k_B T}, \tag{2.13}$$

Thus, from an experimental point of view, the Stokes/anti-Stoke ratio can give us key information about the local temperature of the sample, or how much heat is induced by shining a laser on the sample.

The concept of virtual states, and n-order Raman scattering:

The excited state caused by the electron-photon and electron-phonon interactions in light scattering (Rayleigh, Raman) processes are called virtual states. This means they

are not eigen-states for the system [78, 80]. In another word, there is no real absorption of the photon by the electron, unlike other light-matter processes such as photoluminescence or absorption. An exception occurs for resonant Raman scattering, in which the incident photon's energy exactly matches the energy of an electronic transition between real states.

Figure 2.3 sketches the scattering of light from a real ground state or an excited vibrational state (shown by solid lines) to the virtual states, shown by dashed lines. While Rayleigh scattering brings back the photon to a final state which is the same as the initial state, the final state in the Stokes and anti-Stokes scattering is different from the initial state by an amount that equals the phonon energy (Figure 2.3d).

During a Raman process, the total momentum must be conserved:

$$\sum_i \mathbf{q}_i \approx 0. \tag{2.14}$$

For the one phonon Raman process, the momentum is conserved only if the phonon wave vector is zero ($\mathbf{q} \approx 0$). On the other hand, it is possible to have higher order Raman processes that occur for inelastic scattering by more than one phonon. For instance, a second order Raman process will require two phonons with opposite momenta (+**q**, -**q**) to satisfy momentum conservation. As we will see in the following, this condition will restrict the phonon branches that participate in a Raman scattering process from the Brillouin zone of a given crystal, such as graphene and graphite.

For a n-order Raman process, the transition probability is given by:

$$\begin{aligned} &P_{Raman}(\omega_s) \\ &= \left(\frac{2\pi}{\hbar}\right) \Big| \sum_{n_0,\ldots,n_f} \frac{\langle i|\,\mathcal{H}_{eR}(\omega_s)\,|n_0\rangle\,\langle n_0|\,\mathcal{H}_{e-ion}\,|n_1\rangle \ldots \langle n_{f-1}|\,\mathcal{H}_{eR}(\omega_i)\,|n_f\rangle\,\langle n_f|\,\mathcal{H}_{eR}(\omega_i)\,|i\rangle}{[E_L - (E_{n_0} - E_i)][E_L - (E_{n_1} - E_{n_0})]\ldots[E_L - \hbar\omega_q - (E_{n_f} - E_i)]} \Big|^2 \\ &\qquad \times \delta\left(E_L - \hbar\omega_q - \hbar\omega_s\right), \end{aligned} \tag{2.15}$$

where the sum goes over all the intermediate states $\{|n_0\rangle, |n_1\rangle, ..., |n_f\rangle\}$ between the initial and final states $\{|i\rangle, |f\rangle\}$, respectively.

2.1.4 Raman selection rules

General discussion

We have seen that the interaction of an incident radiation with atoms in the crystal induces a polarizability χ. The vibrational modes in a crystal can induce a change of the polarizability inducing a Raman shift in the scattered radiation, as seen in Eq. 2.6. However, not all vibrational modes can induce a change in the polarizability, thus causing a Raman scattering. The determination of the vibrational modes that can change the

polarizability in the system, usually referred to as *Raman-active* modes, is a relevant task in studying the Raman response of a condensed matter system.

From a classical point, a vibrational mode is Raman-active if the following quantity is non zero:

$$R = \left(\frac{\partial \chi}{\partial \boldsymbol{Q}}\right)_{Q=Q_0} \frac{\boldsymbol{Q}}{|\boldsymbol{Q}|} \neq 0. \tag{2.16}$$

The above quantity is a second rank tensor called the *Raman tensor* [79, 81]. In Raman scattering, this tensor is symmetric: $\partial\chi_{xy}/\partial\boldsymbol{Q} = \partial\chi_{yx}/\partial\boldsymbol{Q}$, $\partial\chi_{xz}/\partial\boldsymbol{Q} = \partial\chi_{zx}/\partial\boldsymbol{Q}$, and $\partial\chi_{yz}/\partial\boldsymbol{Q} = \partial\chi_{zy}/\partial\boldsymbol{Q}$.

The Raman tensor expresses a change in the polarizability tensor χ induced by a given vibrational mode. Condition 2.16 is satisfied when at least one of the six Raman tensor components, expressed as $(\partial\chi_{ij}/\partial\boldsymbol{Q})$, is different from zero.

However, to determine if the Raman tensor of a physical system is not equal to zero, especially for complex molecules and crystals, is not an easy task. It happens though that this condition is intimately related to its symmetry. Thus, knowing the symmetry of the Raman tensor, and corresponding it with the symmetry of the vibrational modes of the system enable us to identify which vibrational modes are Raman-active. The identification of the Raman-active modes for molecules and crystals is possible using group theory.

Case of the hexagonal lattice of graphene

A crystal with a given structure, hexagonal for graphene, has a series of transformations that preserve its symmetry. For the honeycomb lattice of graphene, the following transformations have no change on its structure: Rotation about the normal axis by $2\pi/n$ (denoted C_n), inversion with respect to the center of the hexagon (denoted by i), reflection in a plane normal to the atomic layer (denoted by σ), and a combination of rotations by $2\pi/n$ and a reflection in a plane perpendicular to the atomic layer. By adding the identity transformation (denoted by E), these transformations form, from the point of view of mathematics, a *symmetry group*. In graphene, both electrons and phonons at the Γ are represented by the same symmetry group. This symmetry group is denoted, following the notation rules by Schoenflies, as: D_{6h} [82]. Each type of transformation (i.e., C_n, S_j, σ, i, and E) is called *a class* of the symmetry group. Each class contains all possible realizations of a given transformation type that can preserve the symmetry of the group. Thus, all the elements of a symmetry group are distributed among its classes.

The symmetric transformations for a given group are represented in the form of matrices. A set of matrices that represent all the transformations that preserve the symmetry of a group is called *a group representation*. Group representations can be decomposed into smaller sub-matrices that hold the symmetry of the group. When a representation can

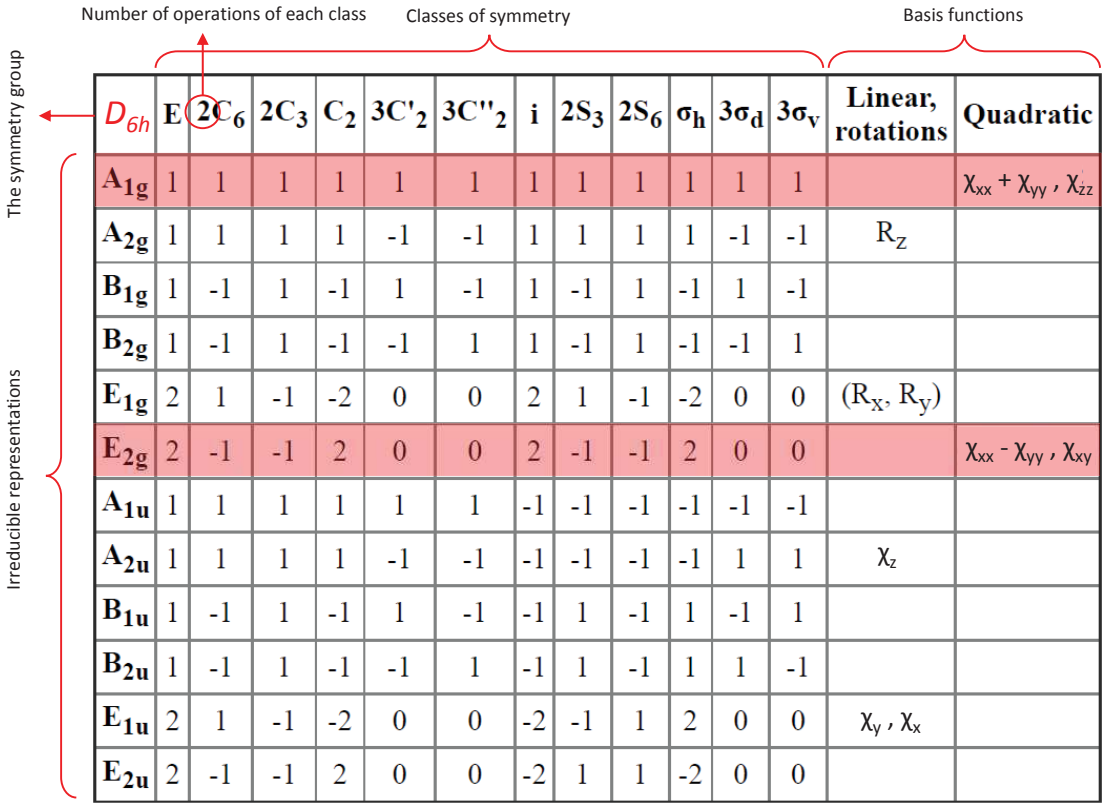

D_{6h}	E	$2C_6$	$2C_3$	C_2	$3C'_2$	$3C''_2$	i	$2S_3$	$2S_6$	σ_h	$3\sigma_d$	$3\sigma_v$	Linear, rotations	Quadratic
A_{1g}	1	1	1	1	1	1	1	1	1	1	1	1		$\chi_{xx} + \chi_{yy}$, χ_{zz}
A_{2g}	1	1	1	1	-1	-1	1	1	1	1	-1	-1	R_z	
B_{1g}	1	-1	1	-1	1	-1	1	-1	1	-1	1	-1		
B_{2g}	1	-1	1	-1	-1	1	1	-1	1	-1	-1	1		
E_{1g}	2	1	-1	-2	0	0	2	1	-1	-2	0	0	(R_x, R_y)	
E_{2g}	2	-1	-1	2	0	0	2	-1	-1	2	0	0		$\chi_{xx} - \chi_{yy}$, χ_{xy}
A_{1u}	1	1	1	1	1	1	-1	-1	-1	-1	-1	-1		
A_{2u}	1	1	1	1	-1	-1	-1	-1	-1	-1	1	1	χ_z	
B_{1u}	1	-1	1	-1	1	-1	-1	1	-1	1	-1	1		
B_{2u}	1	-1	1	-1	-1	1	-1	1	-1	1	1	-1		
E_{1u}	2	1	-1	-2	0	0	-2	-1	1	2	0	0	χ_y , χ_x	
E_{2u}	2	-1	-1	2	0	0	-2	1	1	-2	0	0		

FIGURE 2.4: Character table of the D_{6h} symmetry group of the hexagonal lattice for graphene. The red marked lines represent the Raman-active vibrational modes. Data copied from [webqc.org. D6h - point group symmetry character tables].

no longer be further decomposed, it is then called an irreducible representation (IR). In group theory, IRs can have different types of matrix representation, but with the same symmetry properties. To label IRs we use the *trace*, also called *character*, of their corresponding matrices (i.e., the number of diagonal elements in a matrix). We note that the number of IRs for a symmetry group corresponds to the number of its classes. The IRs for the vibrational modes, and their classes, are grouped in a so-called *character table*. Knowing, the symmetry group of a crystal, it is then possible to find, using group theory, the IRs and their classes, thus deducing the crystal's character table [78]. Each vibrational mode happens to be invariant under the classes of a given IRs. Consequently, there is a correspondence between the normal vibrational modes of a crystal or a molecule, and the set of IRs of its character table.

Table 2.4 represents the character table for the D_{6h} symmetry group of graphene. The numbers indicate the trace of a IR under a given class. The symbols $A_{1,2}$, $B_{1,2}$ indicate IRs that are symmetric or anti-symmetric with respect to rotational symmetries, and $E_{1,2}$ represent twofold degenerate vibrational modes that are symmetric or anti-symmetric with respect to the rotational symmetries (see Table 2.4). The subscript symbols g and u in the IRs are German symbolic for *gerade* (even) and *ungerade* (odd)

for vibrational modes that transform symmetrically or anti-symmetrically with respect to the inversion center of the hexagon.

Following the above introductions from group theory, the condition for a vibrational mode to be Raman-active is satisfied " if the components of the polarizability tensor belong to the same IRs as for the vibrational mode " [81]. For D_{6h} symmetry group, this condition is fulfilled for the combinations $(\chi_{xx} + \chi_{yy})$ and χ_{zz} belonging to the IR A_{1g}. And the combination $(\chi_{xx} - \chi_{yy}, \chi_{xy})$ that belongs to the IR E_{2g}, respectively. This immediately designate A_{1g} and E_{2g} as Raman-active modes in graphene.

In table 2.4, the red marked regions indicate the Raman active-modes in graphene. The A_{1g} mode is a second order process, which needs defects for its activation (as will be discussed in the next section). The E_{2g} mode is a doubly degenerate, Γ point optical phonon, and is always active in the Raman spectrum of sp^2 carbon allotropes, such as carbon nanotubes, multilayer graphene, and bulk graphite.

Finally, it is important to note that even if a set of vibrational modes are Raman-active, their observation in Raman scattering spectroscopy can depend on the polarization of the incident and scattered light [78].

2.2 Raman spectroscopy of graphene, multilayer graphene, and graphite

2.2.1 Prominent Raman peaks

Raman spectroscopy is a powerful tool in the study of graphene, graphene multilayers, and bulk graphite. The most prominent features in the Raman spectra of these systems are the so-called G, D, and 2D bands. While the G and 2D bands are always present in the Raman spectra of graphene, N-LG, and bulk graphite, the D band needs defects to be activated [83, 84]. These defects, such as vacancies or charge impurities, allow for an elastic scattering of the electrons, with no change in the energy. The elastic scattering contributes to the Raman scattering process to produce the D band (see Figure 2.7b).

Two typical Raman spectra for monolayer graphene, in the absence of defects and with defects are shown in Figure 2.5. While in the absence of disorder, the most prominent features are the G and 2D bands, the D peak along similar defect activated modes appear in the Raman scattering spectrum of disordered graphene [84].

Figure 2.6a shows the phonon dispersion in monolayer graphene along the high symmetry axis Γ M K in the BZ of graphene [83, 85–87]. This dispersion displays six phonon branches, all of them originates from the Γ point, which is the highest symmetry point in the BZ and is taken as the origin of the phonon momentum ($q = 0$).

The three branches that have zero energies at the Γ point (see Figure 2.6 a) are called

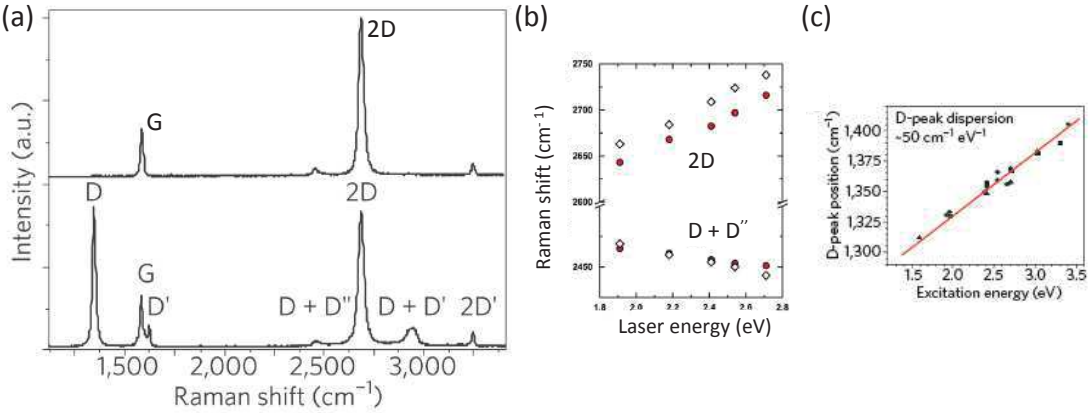

FIGURE 2.5: (a) Two Raman spectra of monolayer graphene. The upper spectrum is taken from a graphene flake with no defects, while the lower spectrum is of highly disordered graphene [84].(b,c) Phonon dipsersions as function of the laser excitation energy for the D,2D and D peaks. The red symbols in (b) are for graphene monolayer, while the lozanges are data from graphite [83, 84].

acoustic phonons. They correspond to symmetric displacement of the carbon atoms in the honeycomb lattice. On the other hand, the three branches that have finite energies at the Γ point correspond to anti-symmetric displacement of the carbon atoms, they are known as optical phonons.

Both optical and acoustic phonons, denoted by capital letters O or A, have either longitudinal (LO, LA) or transverse (TO, TA) character. These vibrational modes correspond to in-plane (i) or out of plane (o) displacement of carbon atoms. In the Raman scattering process, only phonons at the Γ point ($q = 0$) will participate to the first order scattering.

The Raman selection rules, discussed in the previous section, imply that the E_{2g} is Raman active in sp^2 carbon systems. In graphene this mode is doubly degenerate at the Γ point, because it corresponds to in-plane longitudinal and transverse optical phonon modes (iLO, iTO), with an energy at ~ 1580 cm^{-1} [78, 83](see Figure 2.6b). It gives rise to the G band in the Raman spectra of graphene, N-LG, and bulk graphite.

Second order Raman modes are also observed in graphene. The A_{1g} mode (Figure 2.6c) at the K point, located at an energy ~ 1300 cm^{-1}, is activated due to the presence of defects in the sample, it is known in the Raman spectra of defected graphene as the D band.

One of the intriguing results about Raman spectroscopy of graphene and graphite is that the defect peaks, such as the D band, but also the overtone of the D band (i.e., the 2D band) are found to disperse with the excitation energy (Figure 2.5(b,c)). The origin of these two peaks has not been clear, and it was the subject of intense debate within the scientific community [83, 88–91]. However, it is now accepted that the D and 2D bands originate from a *double resonant* Raman scattering process [91–94].

Figure 2.7 (a-c) summarizes the scattering mechanisms responsible for the observation

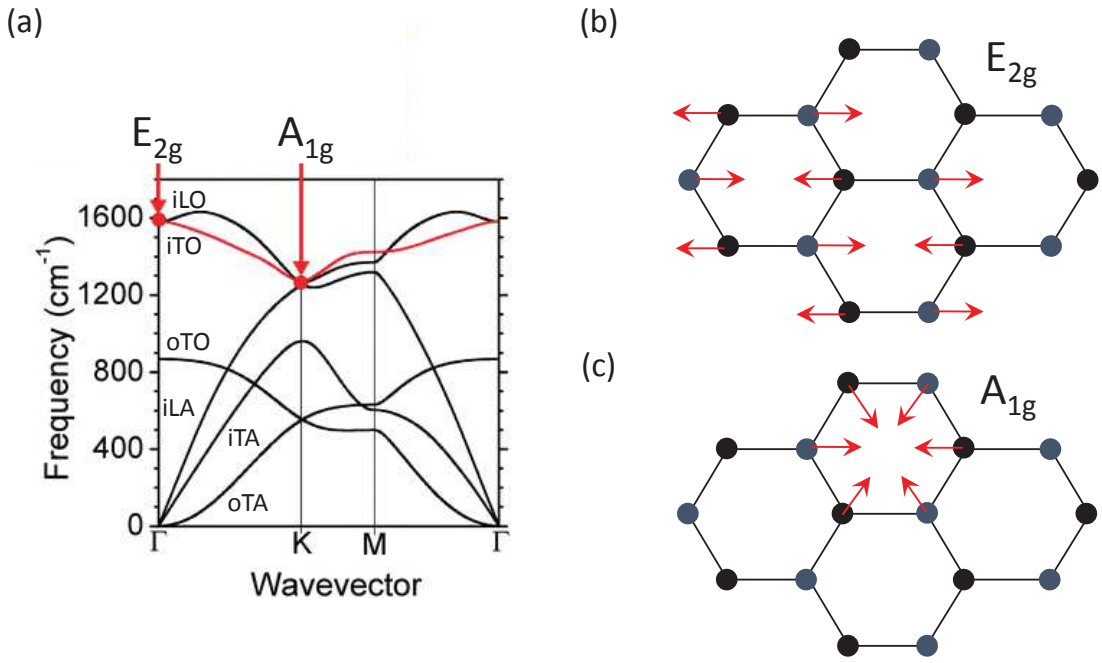

FIGURE 2.6: (a) Phonon dispersion in graphene along a high symmetry axis in its BZ [87]. The E_{2g} phonons at the Γ point contribute to the G band, while the A_{1g} phonons at the K point are related to the disorder induced D band. (b,c) Raman active vibrational modes that are responsible of the observation of the G and D bands in the Raman spectrum of graphene.

of the G, D, and 2D bands in graphene, respectively. The G band is a first order Raman process. For momentum conservation, the phonons involved in its activation have zero momenta, and are located at the center of the BZ at the Γ point. The D and 2D bands require a so-called double resonance (DR) mechanism [92]. This DR condition is shown to occur in two different ways for the D and 2D bands. In the case of the D band (Figure 2.7b), the incoming photon will scatter the electron (with a quasi-zero momentum) from the valence to the conduction band resonantly (indicated by the blue arrow). This means that the energy of the incident photon matches exactly the energy difference between the valence and conduction bands at a given k point. Then a phonon with wave vector $\mathbf{q} = \mathbf{K} + k, (k << \mathrm{K})$ will scatter the electron to the second valley K′, from which the electron will be scattered back elastically to the K valley by a defect. Finally, the electron-hole pair recombines and the total momentum is conserved [92]. The defects that activate the D band might be lattice vacancies, crystal edges, or impurities [83].

The activation mechanism of the 2D band is different. Instead of defects that scatter elastically the electron from one valley to the other, this second order process is due to a DR scattering mechanism that includes two phonons with opposite momenta $+\mathbf{q}$ and $-\mathbf{q}$ ($\mathbf{q} = \mathbf{K} + k, (k << \mathrm{K})$). This inter-valley process is shown in Figure 2.7c, where no defects are necessary to the observation of the 2D band [84, 91–93].

The 2D feature arises from both inner DR process, which selects wave vectors that

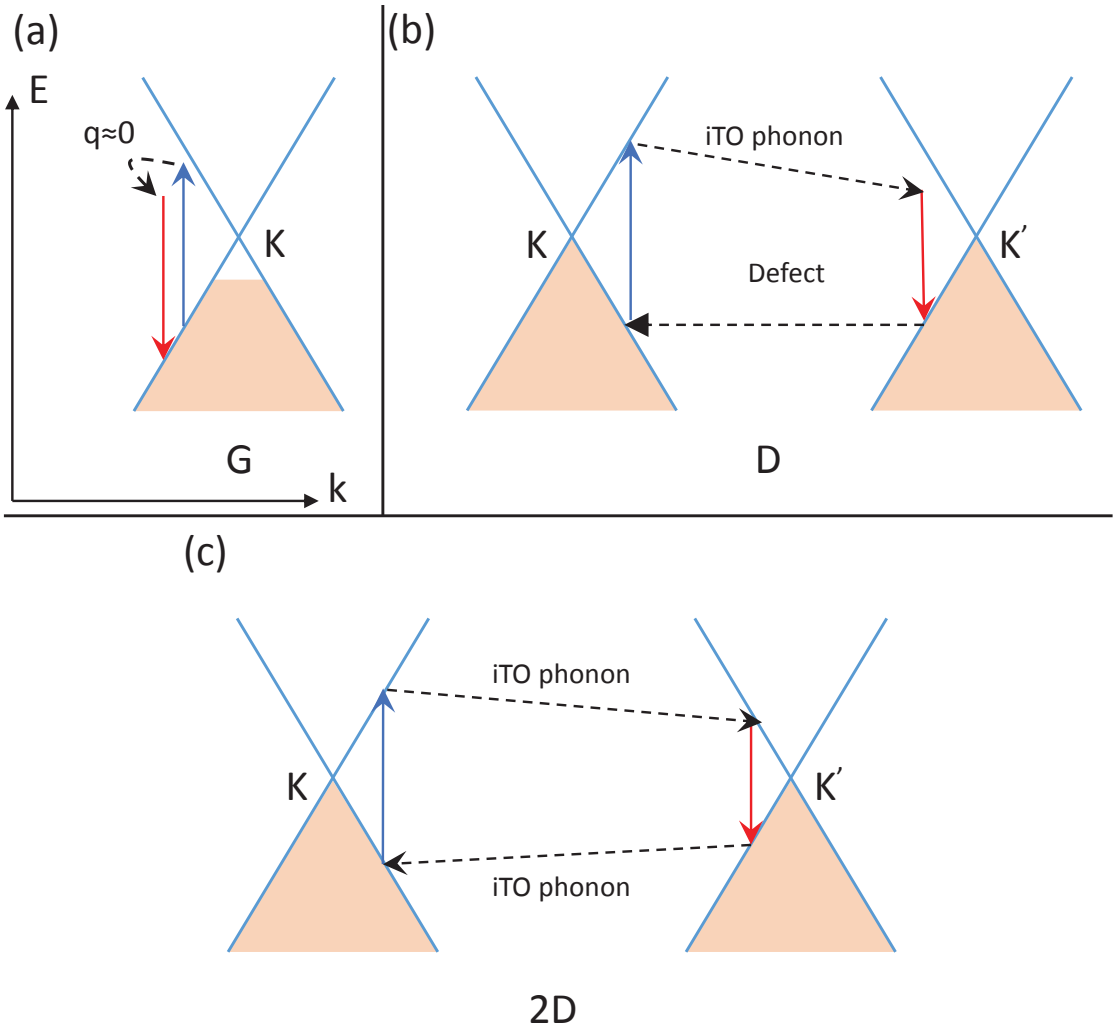

FIGURE 2.7: Schematic diagrams for the phonon processes in the graphene electronic dispersion [84]. (a) Intravalley first order Raman process responsible of the G band. (b,c) Intervalley second order Raman processes for the D and 2D modes, respectively.

connects the inner inter-valley region between the K and K′ points, or from an outer inter-valley process, that connects the outer inter-valley from the K to the K′ points. The fact that most of the graphene flakes are deposited on substrates, such as silicon, the doping induces a broadening of the 2D band feature which is bigger than the energy separation between the inner and outer DR processes, hence a more symmetric line shape of the 2D band in monolayer graphene [95, 96].

One should note that for strongly defected graphene, the D band is not the only additional feature in the Raman spectroscopy of graphene. This is seen in Figure 2.5, where many overtones and bands arise. Nevertheless, the DR model accounts for all the observed features [84]. For instance, the D′ band originates from a double resonant intravalley process (i.e., in the same valley, around the same Dirac cone), involving a scattering by a defect. The D″ is linked with the D band phonons and is originating from the longitudinal acoustic (LA) phonon branch [84].

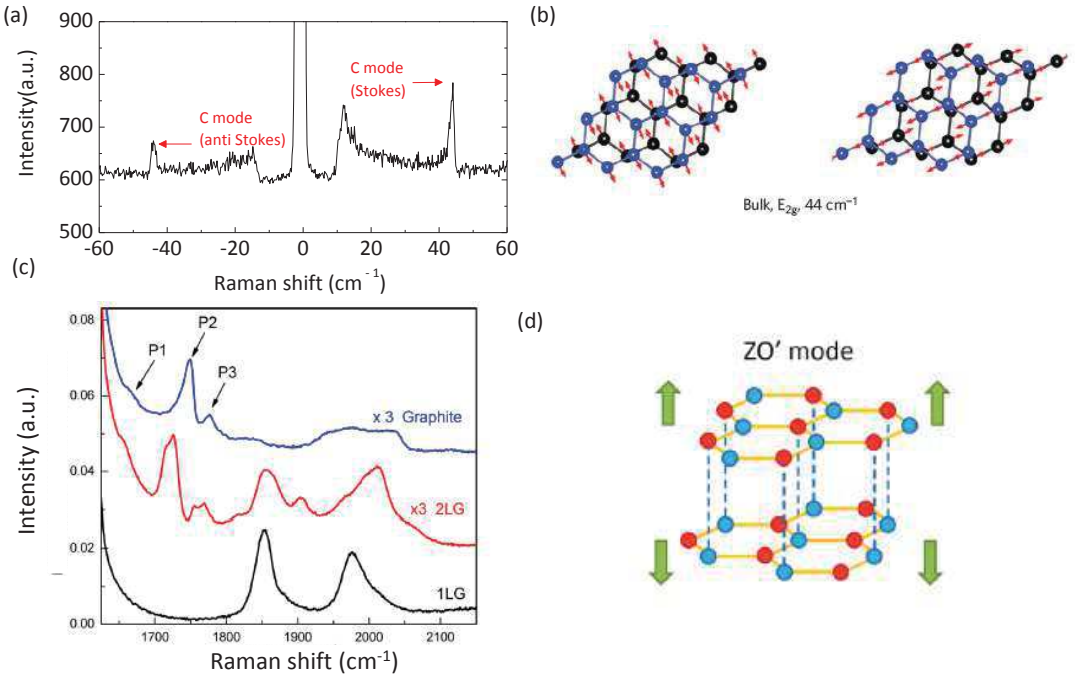

FIGURE 2.8: (a) Raman spectrum showing the Stokes and anti-Stokes of the C mode in bulk graphite, around 44 cm^{-1}. (b) Two degenerate vibrational modes that are responsible of the observation of the Raman active C mode [97]. (c) Raman spectra of LBMs in bilayer graphene and bulk graphite [35], denoted as P1, P2 and P3. (d) Schematics of a LBM for bilayer graphene when the two atomic planes are moving out of phase. The red and blue atoms indicate the two different sublattices.

Two other Raman-active vibrational modes are of major interest in the study of multi-layer graphene and graphite. These modes correspond to adjacent layers moving out of phase in the direction parallel to the atomic planes or perpendicular to the atomic planes, as schematically depicted in Figure 2.8b,d, respectively. The first type are referred to in literature as *shear mode* (or the C mode), seen in the spectrum of Figure2.8a. The second type of these modes are called *layer breathing mode* (LBM), denoted by P1, P2 and P3 in Figure 2.8c. These two modes are related to the inter-layer coupling between atomic planes and can be used as a probe of the number of layers [35, 97, 98]. The shear mode, for instance, can be viewed as a bulk E_{2g} vibrational mode.

The LBMs, indicated in Figure 2.8c have Raman shifts in the range 1615 to 1850 cm^{-1} [35], but also at lower energies starting from 80 up to 300 cm^{-1} [98]. The shear modes are even at lower energies, their Raman shift increases with the number of layers until reaching ~ 44 cm^{-1} in bulk graphite [97]. Thus, their observation in Raman scattering experiments requires maximum rejection of elastically scattered light.

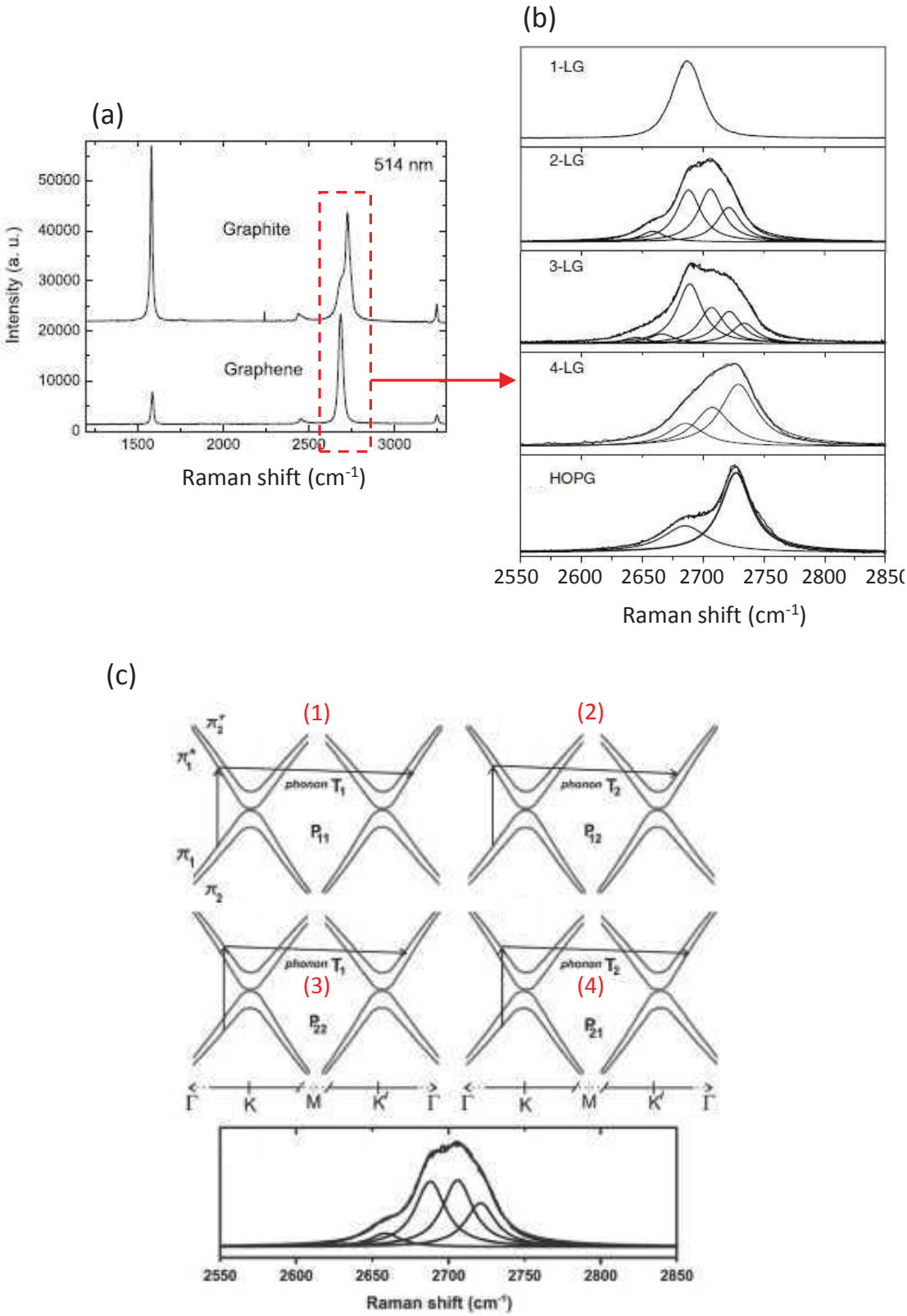

FIGURE 2.9: (a) Two Raman spectra of monolayer graphene and Bernal stacked bulk graphite, taken with 514 nm excitation wavelength [91]. (b) Zoom on the 2D band lineshape from monolayer to few layer graphene up to bulk graphite [83]. (c) The DR model accounts for the lineshape dependence of the 2D band on the number of layers. As it is evidenced for bilayer graphene. [83].

2.2.2 Dependence on the number of graphene layers

When graphene layers are stacked on top of each other in a Bernal fashion (AB stacking), the 2D band lineshape changes as a function of the number of layers. This effect was first evidenced by Ferrari *et al.* [91], who investigated the Raman scattering response of graphene, from monolayer to few layers, up to the bulk limit (i.e., Bernal stacked graphite). Figure 2.9a shows two Raman spectra, one is from monolayer graphene and the other is from bulk graphite, with the 2D band boxed in red. For different N (number of layers) the 2D band has different features. This is shown in Figure 2.9b. For monolayer graphene, the 2D band is a single symmetric peak, but its line-shape changes drastically starting from AB stacked bilayer graphene, and it continues to evolve for few layer graphene until reaching a characteristic two components feature for Bernal bulk graphite [83, 91].

To explain this line-shape dependence on the number of layers, one should consider the phonon and electronic dispersions for graphene as a function of N. When increasing the number of layers, both the electronic and phonon bands split into several components. The phonon branches split due to the vibrations of the carbon atoms in the upper and lower layers. In bilayer graphene, for instance, the atoms in one sublattice move in phase with respect to each other in the two layers, and out of phase in the other sublattice in the two layers [83]. At the same time, the electronic bands split due to interlayer coupling between the atomic planes. The splitting in the phonon branches in the case of bilayer graphene, however, has been shown to be less than 1.5 cm^{-1} [91]. This tiny split cannot account for the 2D band splitting in the Raman scattering of Bernal stacked N-LG.

For bilayer graphene, the interlayer coupling will split the (π, π^*) electronic bands into four branches. Using the DR model introduced in the previous subsection, we find that there are four different electron-phonon scattering processes, labeled (1, 2, 3, 4) in Figure 2.9c, that involve four different phonons with different momenta $\{P_{11}, P_{12}, P_{22}, P_{21}\}$ across the K-K′ line. These four different processes are at the origin of the four components line-shape of the 2D band in AB stacked bilayer graphene [83, 91]. The number of sub-peaks in the 2D band feature increases with the number of layers in Bernal-stacked graphene. At the bulk limit, the 2D band line-shape has a double peak structure [83]. Bulk graphite has a hexagonal 3D BZ that extends in a third k_z direction along the K-H line. The DR process giving rise to the 2D band in graphite not only involves inelastic scattering of electrons by phonons connecting the K and K′ points, but also involves inelastic scattering of electrons by phonons of wave-vector k connecting all possible points belonging to the electronic bands along the K-H line to points with wave vectors k' along the $K' - H'$ line [99, 100].

Another important point is the C mode energy and its line-shape. It has been shown

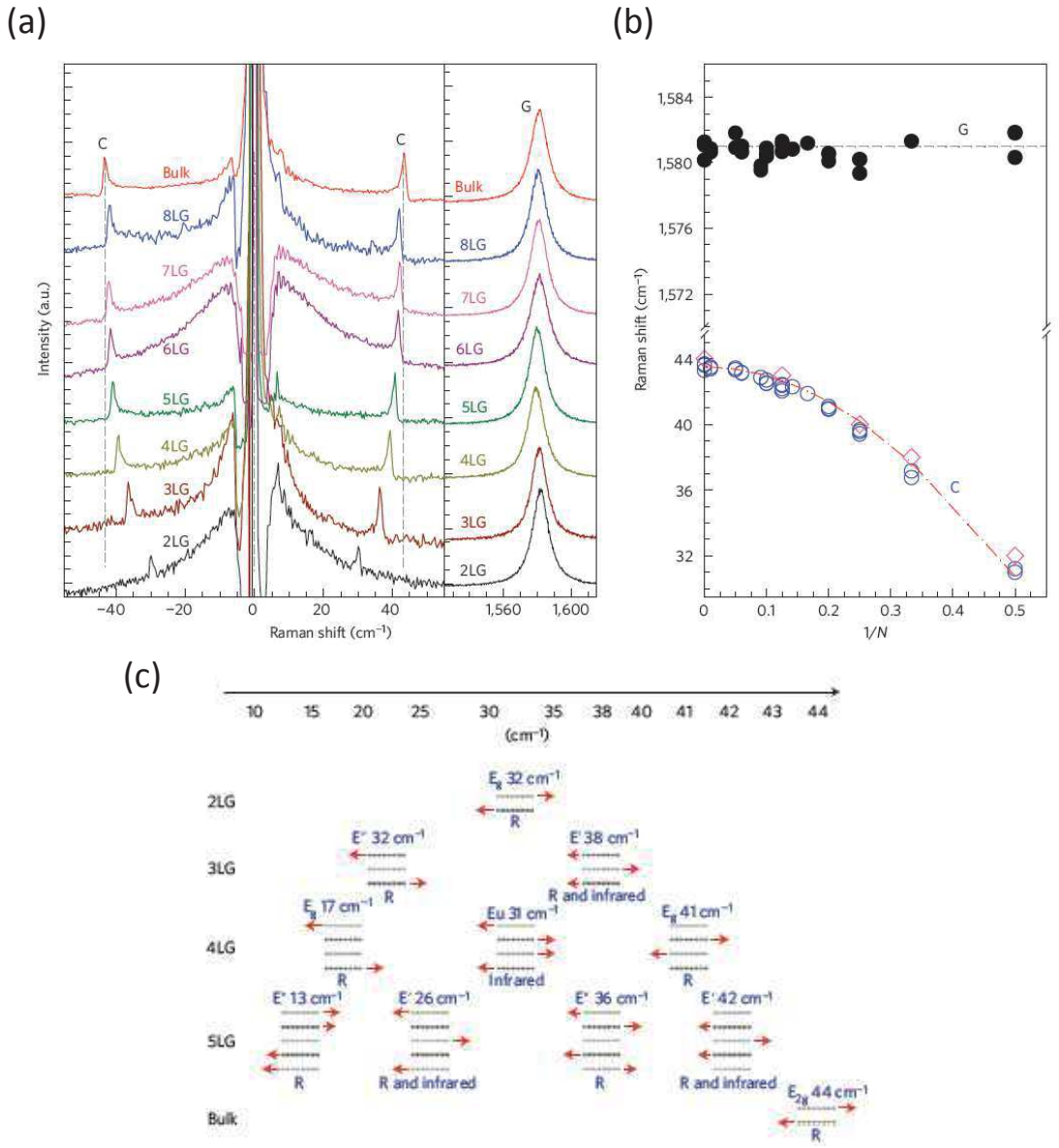

FIGURE 2.10: (a) The left panel shows the C mode energy as a function of the number of layers. The right panel of (a) shows the corresponding G band. (b) Plot of the G band and the C band Raman shifts as a function of the inverse of the number of layers. The fitting is done using 2.17. (c) Schematics of the different shear modes in multilayer graphene and their Raman shift for different number of layers. The figures are taken from [97].

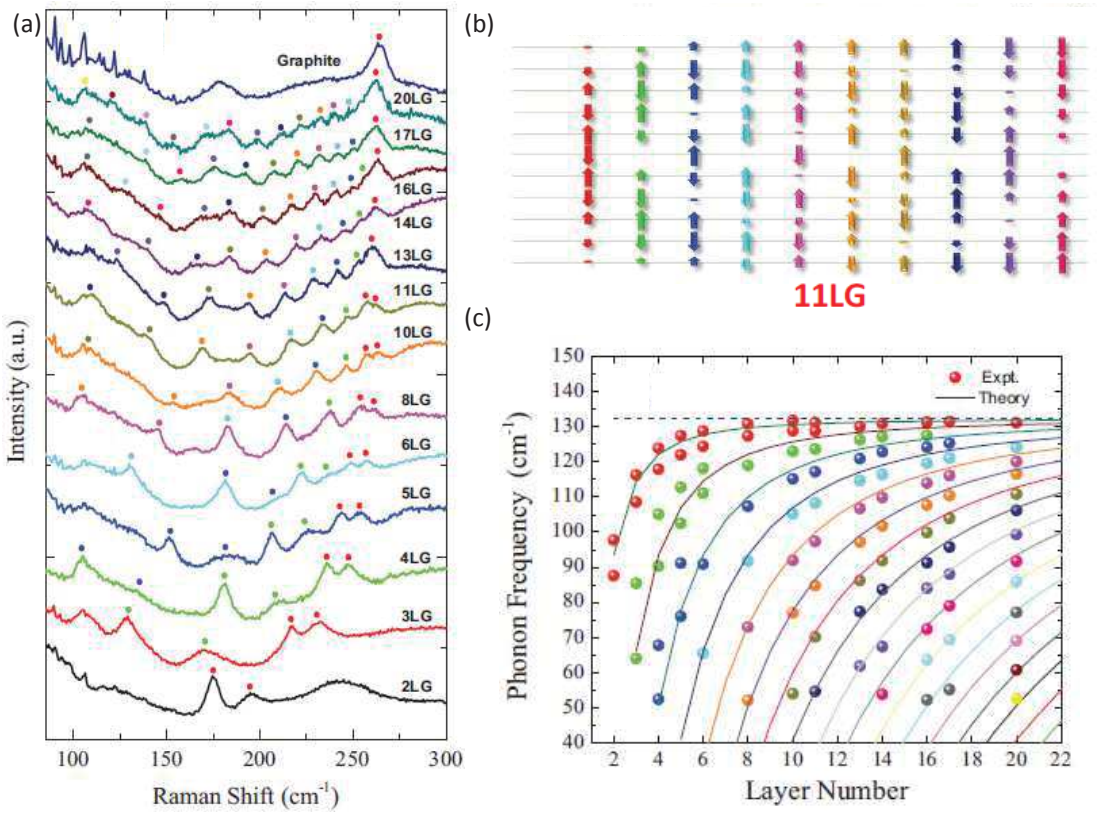

FIGURE 2.11: (a) Raman scattering spectra of the LBMs in N-LG from 2 to 20 stacked monolayers. (b) Different atomic layer displacements for the LBMs in 11-LG. (c) The frequencies of the LBMs as a function of the number of layers. The dots are experimental results while the lines derive from the theoretical model used for the fits. Figures are taken from [98].

that its energy, from bilayer to bulk graphite, is related to the number of ABA stacked layers [97]. Figure 2.10a shows a Raman spectroscopic study of the shear modes performed on a N-LG flake with a thickness ranging from bilayer to bulk graphite. The frequency of the G and C peaks are plotted as as function of N in Figure 2.10b. While the overall G band position (right panel) seems to be layer independent, the C mode energy reflects the number of layers in AB stacked N-LG. The thicker the flake the bigger is the relative Raman shift, which increases from 31 cm^{-1} in bilayer graphene to 44 cm^{-1} for bulk graphite [97]. The position of the C mode, for a given N, follows the formula:

$$\mathrm{Pos(C)}_N = \frac{1}{\sqrt{2}\pi c}\sqrt{\frac{\alpha}{\mu}}\sqrt{1+\cos\left(\frac{\pi}{\mathrm{N}}\right)}, \tag{2.17}$$

where: α is the interlayer force constant per unit area, N the number of layers, μ the monolayer graphene mass per unit area, and c the speed of light in vacuum. The only free parameter in this formula is α. For a fixed value of $12.8 \times 10^{18} N/m^3$, we can fit all the experimental data (red curve in Figure 2.10b). This implies that, in AB stacked N-LG, the hardening of the C mode is not due to a variation of interlayer coupling, but

rather to an increase of the overall restoring force (surface layers are less bound than in the bulk) going from bilayer to bulk graphite [97]. When the number of layers increases, the line-shape of the C mode become more and more asymmetric. Tan *et al.* [97] showed that the C mode feature can be well fitted using a Breit-Wagner-Fano (BWF) function. The BWF line-shape is more pronounced at the bulk limit and arises from coupling of Raman allowed phonon with a continuum of Raman-active electronic transitions.
Lui *et al.* studied the LBMs in N-LG using Raman scattering techniques [35, 98]. Their results show that the LBMs can also be used as an accurate probe for layer thickness in N-LG flakes. The Raman bands associated with these modes are unique for graphene samples of each layer thickness (see Figure 2.11a) as their energies change with increasing number of layers. When increasing the layer thickness, the number of Raman peaks associated with LBMs grows systematically, highlighting the remarkable sensitivity of the LBMs to interlayer interactions. For a given number of layer N, there are N-1 atomic displacement modes (see Figure 2.11b for the case of 11-LG). Similar to the shear modes, the frequency dependence of the LBMs on the number of layers follows a model equivalent to the normal vibration modes of a linear chain of N masses connected by springs [98]. The solution to this problem yields:

$$\omega_{\mathrm{N}}(n) = \omega_0 \sin\left[\frac{(\mathrm{N}-n)\pi}{2\mathrm{N}}\right], \tag{2.18}$$

where $\omega_0 = 132.2\ \mathrm{cm}^{-1}$ denotes the frequency of the shear mode in bulk graphite. The results of Eq 2.18 provides an excellent overall fit to the experimental data for all layer thicknesses, as seen in Figure 2.11c.

2.2.3 Dependence on the polarization of light

Even though the G, 2D, and 2D′ bands are Raman-active modes, their observation can be dependent on the polarization of the incident and scattered light [84, 101–103]. Based on the symmetry of the IRs of the Raman tensor in the character table of graphene, the E_{2g} mode responsible of the G band is not sensitive to the polarization of light. This non sensitivity of the G band to light polarization can be understood by considering its matrix element $\mathcal{M}_G$, described by the lattice displacement $\mathbf{u}$. For incident $\mathbf{e}^{in}$ and scattered $\mathbf{e}^{out}$ light, the intensity of the G band is given by [84]

$$I(G) \propto |\mathcal{M}_G|^2, \tag{2.19}$$

where [84]

$$\mathcal{M}_G \propto (e_x^{in} e_y^{out} + e_y^{in} e_x^{out})u_x + (e_x^{in} e_x^{out} + e_y^{in} e_y^{out})u_y. \tag{2.20}$$

The z direction is chosen to be normal to the graphene layers. In Eq 2.19, the intensity does not depend on $\mathbf{e}^{in}$ and $\mathbf{e}^{out}$. For the 2D and 2D′ modes, however, the intensity is given as:

$$I(2D, 2D') \propto |\boldsymbol{e}^{in}|^2 |\boldsymbol{e}^{out}|^2 + 2(\boldsymbol{e}^{in}.\boldsymbol{e}^{out})^2, \tag{2.21}$$

which gives an intensity that depends on the relative orientation of the electric field components. Eq 2.21 gives a maximum intensity when ($\mathbf{e}^{in}$, $\mathbf{e}^{out}$) are parallel, while it is minimum when ($\mathbf{e}^{in}$, $\mathbf{e}^{out}$) are perpendicular [84, 102, 103].

2.2.4 Dependence on the crystallographic stacking order

2.2.4.1 Rhombohedral stacking

The DR model happens to be a powerful tool to account for the 2D band line-shape dependence on the number of layers in N-LG. It allows for an easy and accurate estimation of the number of layers in few layer graphene flakes. However, much of the studies have been focused on the Bernal-stacked N-LG and little has been done to correlate the 2D band line-shape with the number of layers for ABC-stacked N-LG. A natural question to ask is how the Raman response of ABC stacked N-LG, and its phonon peaks including the 2D band, will be different from the Bernal-stacked N-LG and how does it correlate to the number of layers.

Systematic comparison studies of the Raman response in ABA and ABC trilayer graphene [32, 104] have been reported. For different excitation photon energies, the 2D band line shape in ABC trilayer displays more asymmetric and broader lines than ABA trilayer. In Figure 2.12(a-d), we observed a sharp peak and an enhanced shoulder in the ABC spectra for all excitation photon energies.

Since the G band involves in-plane phonon modes, similar G band line-shape has been observed in ABA and ABC tri-layers (Figure 2.13a,b), in contrast to the 2D band. Following these observations, one can construct false color maps of the Raman scattered intensity that display the change in the width of the 2D band with respect to the stacking order [32]. Figure 2.13(c,d) shows the result of such a procedure, where both the stacking orders coexist in the same flake. Even if the optical microscope image shows no apparent difference, the corresponding Raman color map of the same flake shows a clear contrast between the two domains.

2.2.4.2 Twisted multilayer graphene and graphene superlattice

Another stacking configuration for multilayer graphene is when the atomic layers have a rotational angle with respect to each other. These stacking faults are often found on

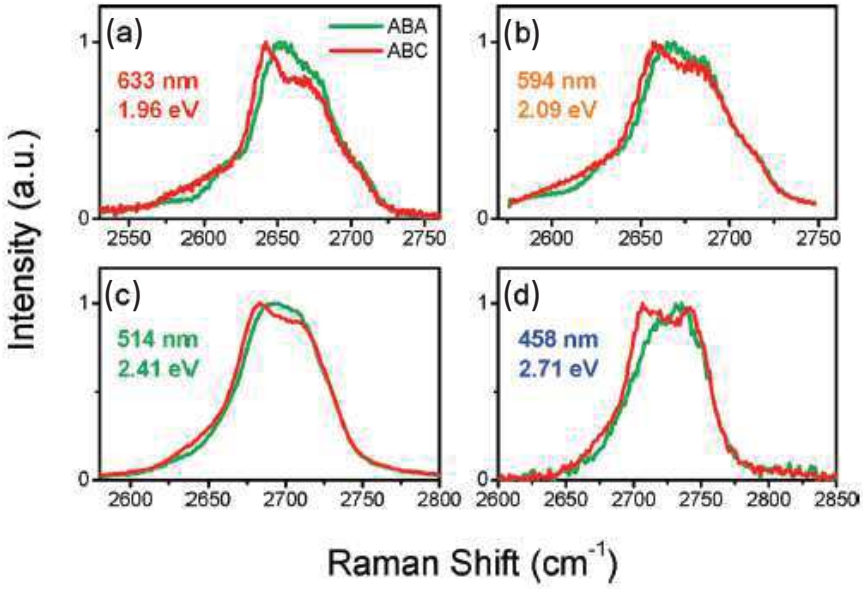

FIGURE 2.12: (a-d) Raman spectra of the 2D band for ABA (green line) and ABC (red line) trilayer graphene. The spectra are recorded at four different laser excitation wavelengths [32].

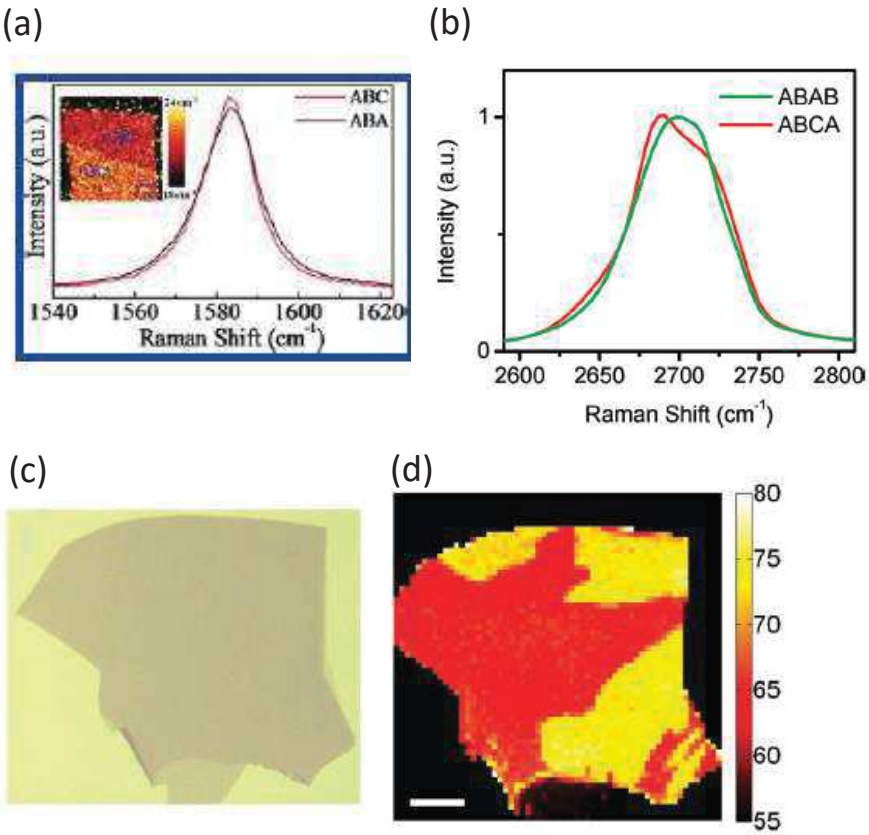

FIGURE 2.13: (a) G band from ABA and ABC trilayer graphene [104]. (b) 2D band from ABA and ABC stacked tetralayer graphene. (c) Optical microscope image of a multilayer graphene flake. (d) Raman imaging of the ABA and ABC stacking domains based on the 2D band lineshape [32].

the surface of bulk graphite, as evidence from scanning tunneling spectroscopy (STS) [105]. The mechanical exfoliation of multilayer graphene [15], as well as the ability to grow multilayer epitaxial graphene on different substrates [106, 107], allowed the investigation of these stacking faults electronic properties. This enabled the discovery of novel phenomena in 2D materials.

Multilayer graphene with a twist

Multilayer graphene with twisted angles can be obtained by thermal decomposition of SiC [20]. The number of graphene layers obtained from this technique depends on the experimental conditions.

It was predicted that a single layer graphene-like band structure should be observed in this configuration [109, 110]. However, the Fermi velocity is significantly reduced as compared to monolayer graphene, especially for small rotational angles [111].

Several magneto-optical studies have been performed on multilayer epitaxial graphene, grown on silicon carbide substrate (SiC) [112–116]. The $\sqrt{B}$-dependence of Landau levels, fingerprint of massless Dirac fermions, has been observed for epitaxial multilayer graphene, thus resembling the behavior of carriers in monolayer graphene.

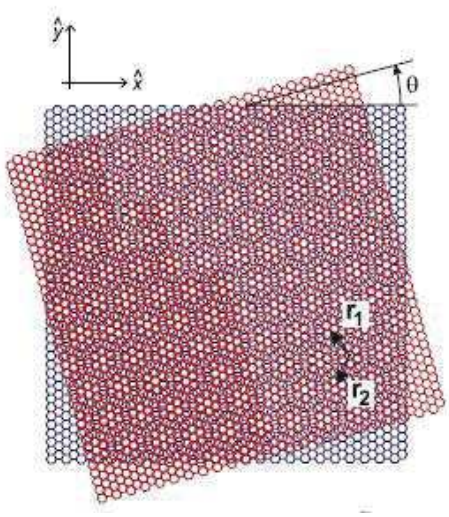

FIGURE 2.14: Bilayer graphene with a twisting angle between atomic layers [108].

Luican *et al.* [117] showed that for twist angles exceeding 3°, the low energy band structure exhibits similarities with massless Dirac fermions, and when exceeding 20°, the layers effectively decouple and the electronic properties are indistinguishable from those in single layer graphene.

Raman characterization studies of twisted bilayer graphene (Figure 2.14) have been reported [108, 118, 119]. In bilayer graphene grown by chemical vapor deposition technique (CVD), two new low frequency Raman peaks (below 100 cm^{-1}) that originate from a layer breathing mode are observed for small range of twist angle [119]. Moreover, strong dependence of the energy, the intensity and of the line-width of the G and 2D bands are observed as a function of the twist angle in exfoliated tBLG samples [108, 118], as seen in Figure 2.15a,b. The modeling of data for tBLG shows the emergence of rotational-angle dependent Van Hove singularities (i.e., divergence in the joint electronic density

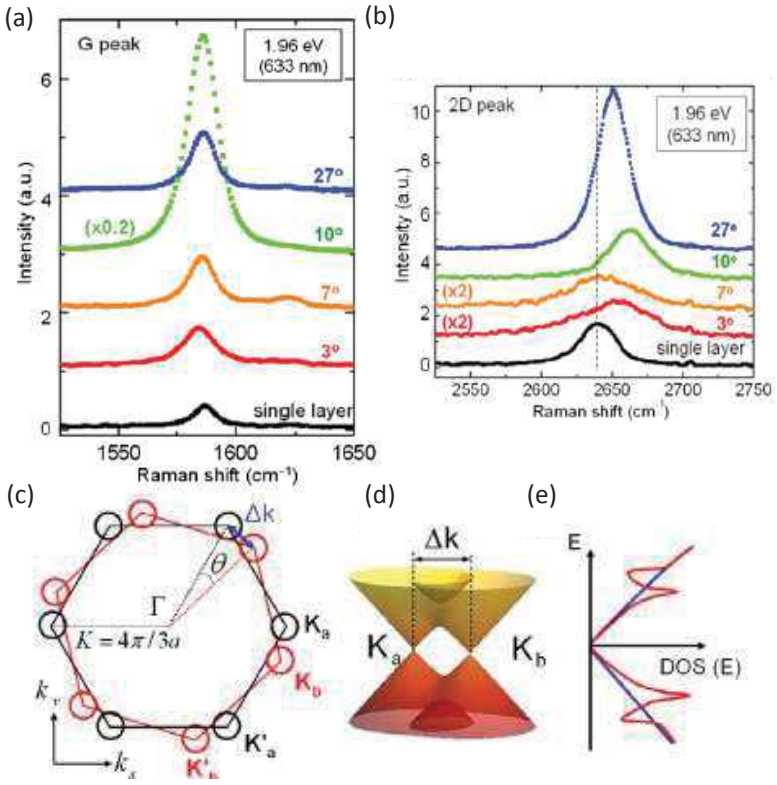

FIGURE 2.15: (a,b) Raman active G and 2D bands recorded for different angles between the graphene planes, respectively. (c) Brillouin zone of twisted bilayer graphene. (d) Electronic band structure around the K points of each layer. (e) The joint density of states for monolayer graphene (blue) and twisted bilayer graphene (red).

of states), that are responsible for the observed spectral features. The energy of these Van Hove singularities can be tuned by changing the twist angle, and for a critical value of the twist angle θ_c, where the energy difference between the valence and conduction Van Hove singularities matches the excitation laser energy used to excite the sample, we observe the enhancement in the intensity of the G and 2D modes [108, 118, 119]. When the twist angle is larger than θ_c, the Raman spectra will resemble those of a single layer graphene since all the optical excitations occur in an isolated simple Dirac cone structure [118].

Graphene superlattice

Another important aspect that emerges from the study of twisted layers in N-LG systems is the concept of superlattice. Superlattices in general are hetero-structures that have, besides the periodicity of their intrinsic structure, an additional periodicity [121].
In two dimensional materials, such as graphene or boron nitride, superlattices are formed when two monolayers are superimposed on top of each other. The superlattice is seen as a so-called Moiré pattern, which is a periodic structure that appears whenever two regular

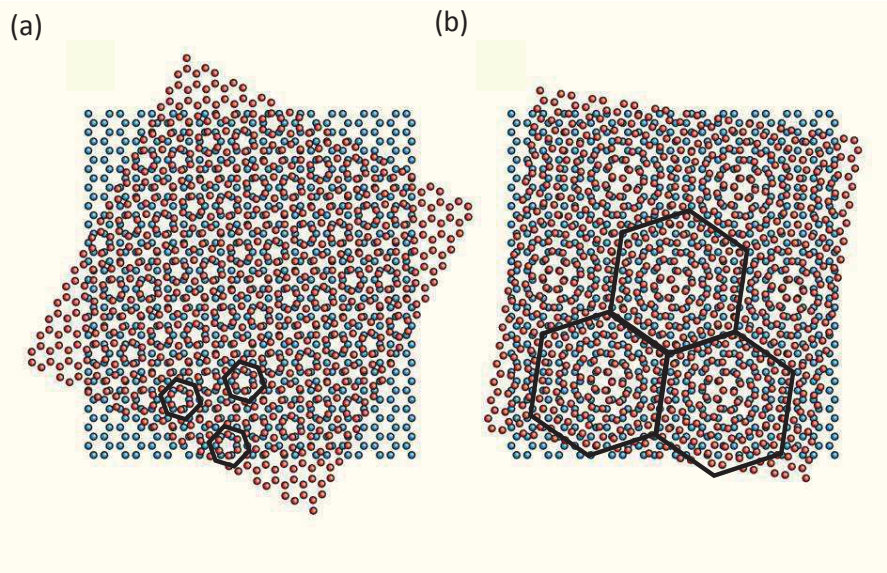

FIGURE 2.16: (a) The two lattices are overlaid at an angle of about 27.8°. The resulting atomic arrangement is precisely periodic. (b) Lattices rotated by 9°. Although the atomic arrangement never precisely repeats, there is a periodic pattern of points in space at which atoms from the two layers are nearly on top of each other, making the structure appear more open in this top view [120].

templates are overlaid with an angle[120]. In 2D systems, superlattices also emerge from a lattice mismatch between two monolayers with different lattice constants brought into contact, such as graphene and hexagonal boron nitride (hBN). The periodicity of the superlattice is related to the twist angle between the atomic layers, as seen in Figure 2.16 [120, 122].

Rich physical phenomena have been predicted and experimentally observed for graphene superlattices. Park *et al.* [123, 124] predicted the generation of new Dirac points in the electronic band structure due to the presence of a periodic potential induced by the Moiré. The first experimental studies on graphene superlattices have been on systems that consist of graphene placed on top of hBN. Both transport and infra-red studies on these hetero-structures have been performed, leading to the observation of the Dirac cone replica and a bang gap opening [125, 126].

The application of magnetic fields to a graphene superlattices has led to the observation of the Hofstadter's butterfly [127–130], which consists of self-similar spectrum of Landau levels replica in the energy spectrum of graphene. Even though the concepts of self-similarity and fractal geometry have been used in the study of the critical properties of phase transitions and are active research areas in mathematics [131], this study has introduced these concepts for the first time in condensed matter physics (see Figure 2.17c,d). Many body effects also play an important role in these systems, in which transport and infrared nano-imaging spectroscopy measurements led to the observation of a quantum Hall ferromagnetism [132], collective electron oscillations or plasmons

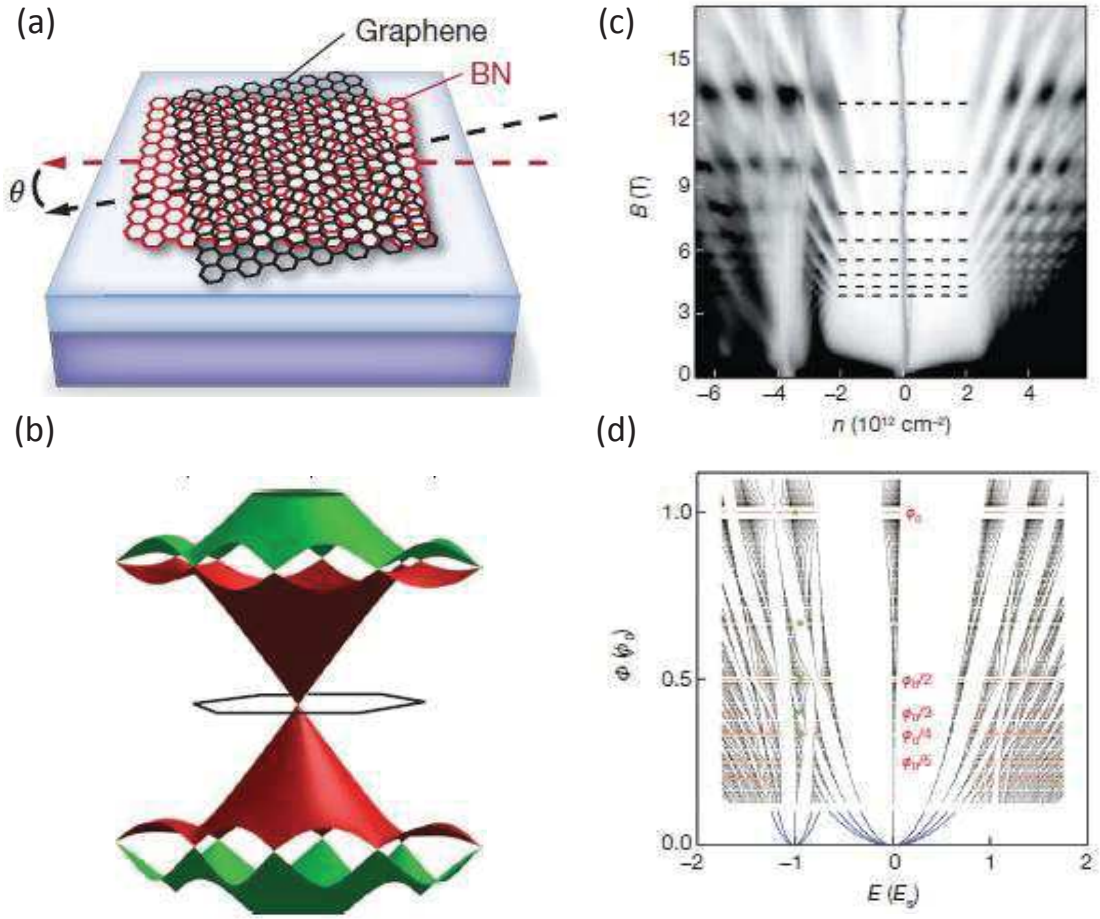

FIGURE 2.17: (a) Schematic of the graphene/hBN superlattice structure used to unravel the emergence of the Hofstadter's butterfly spectrum [127]. (b) Reconstruction of the graphene spectrum induced by the Moiré potential [128]. (c) Longitudinal conductivity as a function of n and B. (d) Graphical explanation of (c) using the Hofstadter butterfly spectrum.

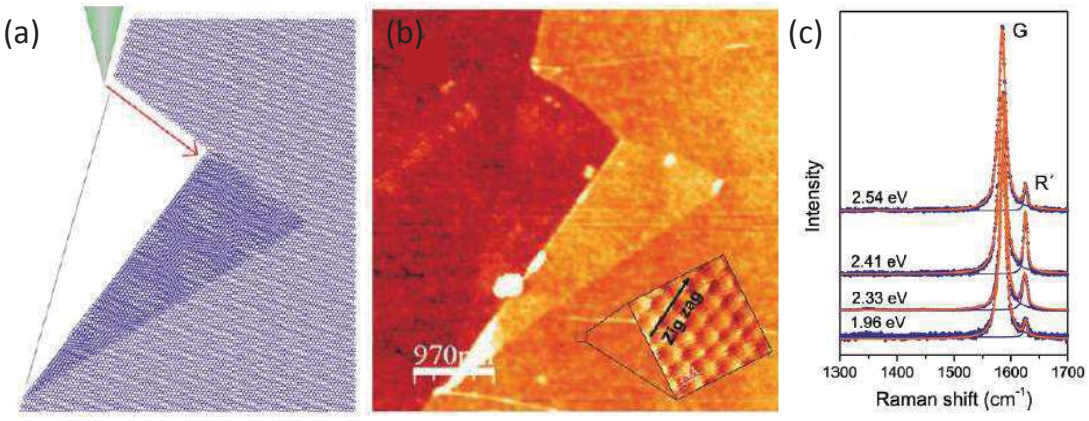

FIGURE 2.18: (a) AFM tip is used to flip a graphene layer to produce a superlattice. (b) AFM image of the folded graphene. The inset shows a high-resolution AFM image which determines the crystallographic orientation of the bottom layer.(c) For four different excitation lasers, the R′ band is present in the spectra of the graphene superlattice. The figures are taken from [122].

[133], and a magnetic field dependent Fermi velocity for the carriers [130].
Raman spectroscopy has been applied to the study of graphene superlattices [122, 134]. By using an AFM tip to flip an exfoliated graphene monolayer on top of another graphene layer, one can produce a tBLG with an angle that allows the observation of a short range Moiré pattern (see Figure 2.18(a,b)).
The electronic structure depends on the rotational angle, and this can be probed by Raman scattering experiments, as was first proposed by Gupta *et al.* [135].
In the Raman spectra of graphene superlattices, the G and 2D band features depend on the rotational angle. Moreover, new phonon modes are observed, called the R and R′ bands [122]. These pics have properties that depend on the twist angle and can be used as an optical signature for graphene superlattices [119, 122, 136].

2.2.5 Effects of strain, doping

Graphene is seen as a promising material for future applications, so it is natural to ask how external factors such as strain and doping can influence the properties of graphene based systems. Numerous studies in the past few years has focused on these matters. Here, we will try to go through the most important results concerning the effect of strain and doping with charge carriers in the properties of graphene and graphene multilayers, seen through Raman spectroscopy.

2.2.5.1 Strain

One of the important question was to investigate a band gap opening, since gaped graphene is strongly sought for electronic applications. Pereira *et al.* [137] found that only huge mechanical strain, that exceeds 20 % and applied along preferred directions, can open a small band gap, which is not practical for applications. On the other hand, sine-like in-homogeneous strain, applied along any direction but the armchair, can in theory open a gap as large as 1 eV [138].
Strain has been found to induce interesting phenomena in graphene, such as the creation of a pseudo magnetic field [139–145]. The pseudo magnetic field generated by strain can reach 300 Tesla [142], which offers a playground to study condensed matter systems under extreme magnetic fields that cannot be reached in nowadays laboratories.
Strains induce significant changes in the Raman spectrum of graphene. Splitting and energy shifts of the Raman G and 2D bands has been reported [146–150]. Figure 2.19 shows a study by Mohiuddin *et al.* in which they probed the Raman spectroscopy of graphene under uniaxial strain [146]. They found that the double degeneracy of the E_{2g} mode at the Γ point is lifted as the G band splits in two components, labeled G^-

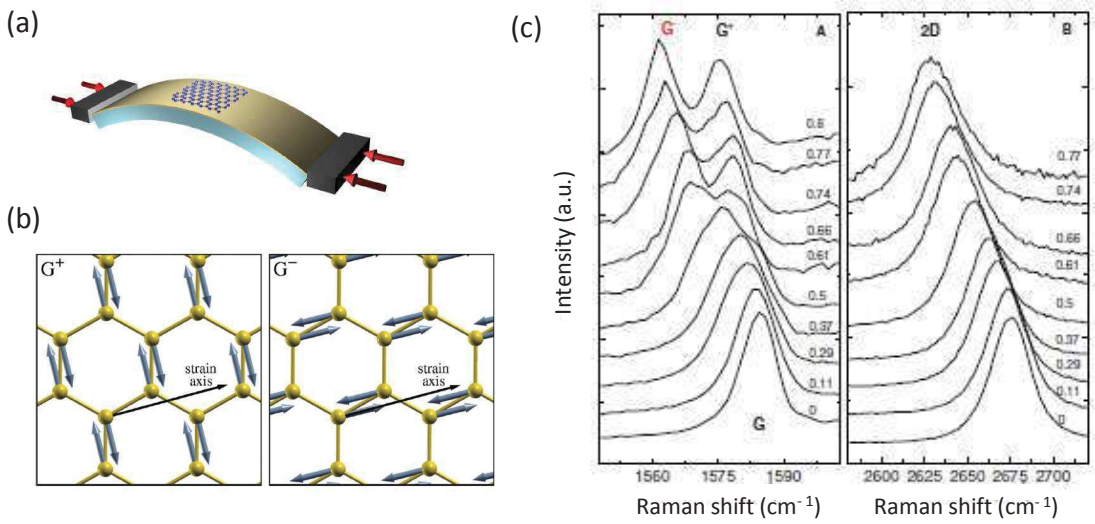

FIGURE 2.19: (a) Graphene flake placed on polymer substrate under uniaxial strain [146]. (b) Schematics of the doubly degenerate E_{2g} vibrational mode responsible of the G band. The strain induces a splitting of the G band in two components, one parallel to the direction of strain and the other one perpendicular to the direction of strain. This splitting is seen in the Raman spectrum of graphene (c).

and G^+. Strain induces a change in the lattice parameter of graphene. This splitting of the G band is due to a bigger change in the lattice parameter of graphene along the direction of the strain compared to the direction perpendicular to the strain (see Figure 2.19b), in analogy to the effect of curvature in nanotubes [151]. The two sub bands G^- and G^+ redshift with increasing strain, while their splitting increases, and their relative intensities vary with the polarization, allowing to probe the sample crystallographic orientation with respect to the strain.

Strain applied along specific directions can also induce a splitting of the 2D band [147, 148, 150]. For stress along zigzag and armchair directions, the 2D mode splits into two distinct sub modes ($2D^+, 2D^-$). The splitting of the 2D band directly reflects a strain-induced modifications of phonon and electronic dispersion. Indeed, first-principles calculations shows that anisotropic modifications of the phonon dispersion together with changes in the electronic structure, such as Dirac cones shifting, are at the origin of the observed modifications [148]. The intensities of the sub modes show strong dependence on both incident and scattered light polarization and the sample orientation, which suggests that the sub modes originate from different scattering paths [147]. Moreover, a strong dependence of the strained 2D mode line shape on the excitation energy is shown [150], which makes Raman measurements using various excitation wavelengths, under well-defined strain conditions, a very important approach for a complete picture of the 2D mode scattering process in strained graphene.

2.2.5.2 Doping

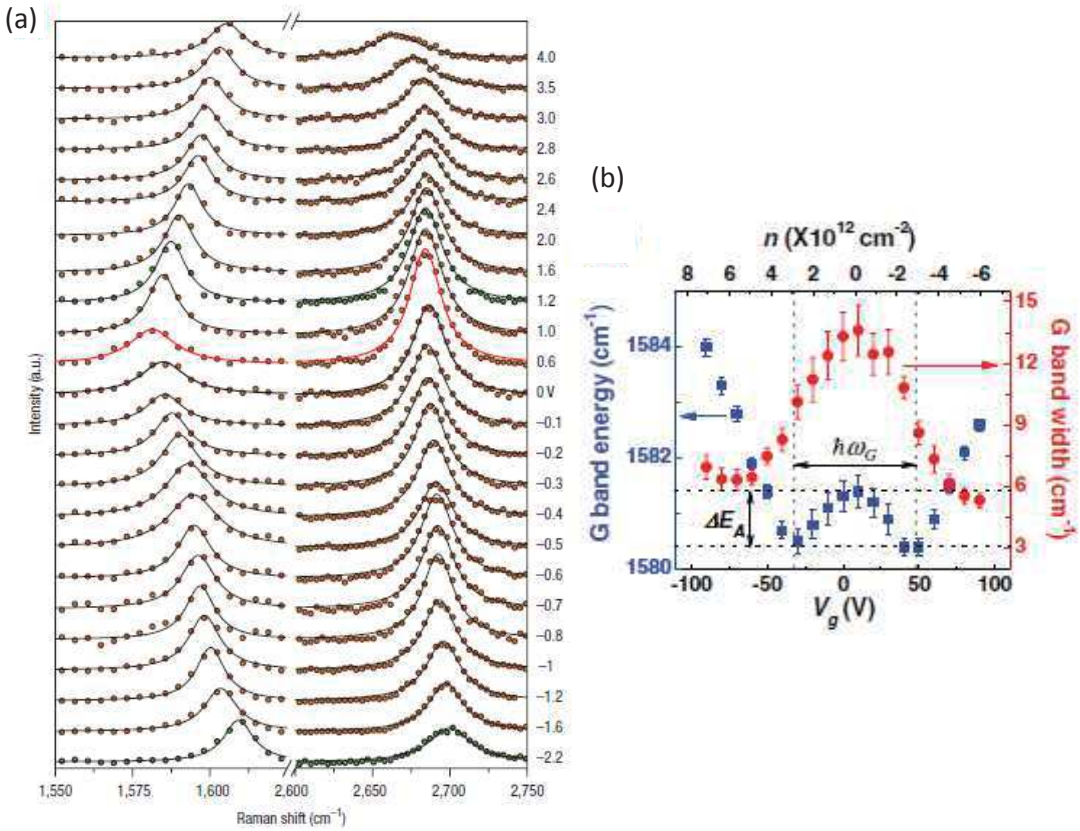

FIGURE 2.20: (a) Raman spectra of graphene as a function of gate voltage [152]. The G peak is on the left and the 2D peak is on the right. The red line corresponds to the Dirac point. (b) Data obtained for gated bilayer graphene [153]. The Blue squares are the G band Raman shift, while the red circles represent G band line-width.

A standard approach to study the electronic properties of graphene is to transfer it on top of a Si substrate covered with a thin layer of SiO_2 (with the oxide thickness ranging from 90 to 300 nm) to render the identification of graphene flakes possible under an optical microscope. However, unlike the surface of graphene, SiO_2 is known to have a rough surface which is usually electrically charged (doped) due to the presence of impurity atoms and dangling bonds. Such a factor cannot be neglected in the study of the intrinsic properties of graphene. It is then legitimate to understand how electrical doping change the electronic properties of graphene.

Doping graphene has been done either unintentionally [154], or by studying graphene that is doped intentionally through the application of a gate voltage [152, 153, 155–157]. Raman scattering spectroscopy is a method of choice to investigate the properties of doped graphene. Indeed, in their seminal works, Yoon *et al.* and Das *et al.* studied graphene flakes-gated structures. They showed that phonons in graphene are sensitive to the applied electrical field. Both the Raman-active G and 2D bands undergo an energy shift and broadening of their line-widths as a function of the applied gate voltage.

Figure 2.20a shows the Raman spectra dependence of gated-graphene on the doping level [152]. While the shift of the 2D is very small, the G band shifts as far as 25 cm^{-1} toward high energy from its equilibrium position (red curve), which reflects a stiffening of the phonon E_{2g} mode. These results show clearly that it is possible to monitor the coupling between the vibrational modes in graphene and Dirac fermions.
The effect of doping on the Raman active modes in gated bilayer graphene has been also reported[153]. Figure 2.20b shows the evolution of the energy and line-width of the G band as a function of the carriers concentration and gate voltage. However, the effect of doping is less pronounced compared to monolayer, where the density of states is zero at the Fermi level, allowing a much pronounced broadening of the Fermi level by charge in-homogeneities [153].

2.3 Electronic Raman scattering

2.3.1 Principle of electronic Raman scattering

In graphene, the band structure is a direct consequence of its honeycomb lattice, described by the hexagonal symmetry $C_{6\nu}$. The Raman-active modes are thus naturally related to the irreducible representations of the point group $C_{6\nu}$ [78]. Inelastic light scattering in graphene is dominated by the generation of zero-momentum inter-band electron-hole modes [158, 159]. When applying magnetic fields, the energy bands are quantized into Landau levels. The electron-hole pair excitations can be observed as inter-Landau level transitions. These inter-Landau level transitions can be observed using magneto-Raman or magneto-infrared spectroscopy, each technique probes transitions with different selection rules [44, 160].

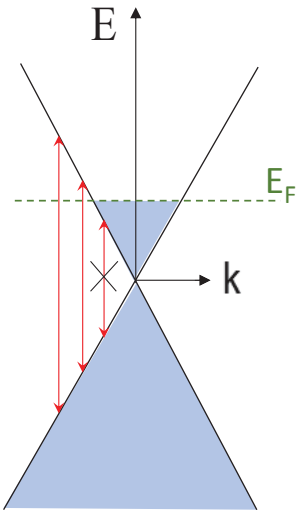

FIGURE 2.21: Zero field electron-hole pair excitations in the Dirac cone structure of monolayer graphene. Excitations with energy lower than $2E_F$ are are Pauli blocked.

At zero magnetic fields, electronic Raman scattering has been observed in carbon nanotubes [161], bulk graphite [162], and recently in gated graphene monolayer structures [163]. Moreover, the observation of inter-Landau level transitions in the presence of a transverse magnetic field has been reported in suspended graphene and N-LG [31], bulk natural graphite [160], graphene domains on the surface of bulk graphite [164, 165], and high quality graphene encapsulated on hBN [166].

Still, the observation of electronic excitations in graphene-based systems is a challenging task. This is mainly due to the interaction with the substrate (in this case SiO_2) that induces a shift of Fermi level from the charge neutrality, and the emergence of microscopic perturbations such as topographic corrugations and electron-density including charge puddles [167, 168]. Thus, high mobility graphene samples are needed for the observation of low energy inter-Landau level transitions. This is either achieved by partially suspending the graphene flakes, or by the appropriate choice of substrate, such as the surface of graphite or hexagonal boron nitride.
In the following we will present an overview of the electronic Raman scattering as presented in the pioneering work by O. Kashuba and V. Fal′ko [158, 159], were they classified all possible Raman active excitations according to their symmetries and the polarization configurations needed to their observation. We present the electronic Raman scattering in the absence of magnetic fields, and then show how magnetic fields allow for the experimental observation of such excitations in monolayer graphene, multilayer graphene, and bulk graphite.

2.3.2 Electronic Raman scattering at zero magnetic field

The model introduced by O. Kashuba and V. Fal′ko is based on the tight binding parameters that we introduced in Chapter 1. However, it is not limited to only γ_0 and γ_1. Including γ_3 (also known as the trigonal warping term) is relevant to account for all the observed excitations using this model. Following this approach, the Dirac-type Hamiltonian of π electrons in graphene interacting with an electro-magnetic wave is then given by:

$$\mathcal{H}_m = \mathcal{H}_0 + \mathcal{H}' = \xi \upsilon \boldsymbol{\sigma}.\mathbf{p} - \frac{\upsilon^2}{6\gamma_0}\left(\sigma^x\left(p_x^2 - p_y^2\right) - 2\sigma^y p_x p_y\right), \tag{2.22}$$

where we introduced the Pauli matrices $\boldsymbol{\sigma} = (\sigma^x, \sigma^y)$ for the two components wave function. The first term in 2.22 gives the linear spectrum $\alpha\upsilon p$ of monolayer graphene, while the second term accounts for the trigonal warping that breaks the rotational symmetry around the K and K′ points of the graphene BZ. The vector potential of light is included in the momentum (measured from the K point) as $\mathbf{p} \to \mathbf{p} - e\mathbf{A}$, where

$$\mathbf{A} = \sum_{\mathbf{I},\mathbf{q},q_z} \frac{\hbar c}{\sqrt{2\Omega}}\left(\mathbf{I} e^{i(\mathbf{q}\mathbf{r} - \Omega t)/\hbar} b_{\mathbf{q},q_z,\mathbf{I}} + \text{h.c.}\right), \tag{2.23}$$

describes an incoming photon with polarization $\mathbf{I}$, in-plane momentum $\mathbf{q}$, energy Ω, and out-of plane momentum $q_z = \sqrt{\Omega^2/c^2 - \mathbf{q}^2}$. The electron-photon interaction part is

given as:

$$\mathcal{H}_{int} = -\frac{ev}{c}\mathbf{J}.\mathbf{A} + \frac{e^2}{2c^2}\sum_{i,j}\left(\partial^2_{p_i p_j} H\right) A_i A_j. \tag{2.24}$$

The two terms in 2.24 give the total Raman scattering amplitude for a photon inelasti-

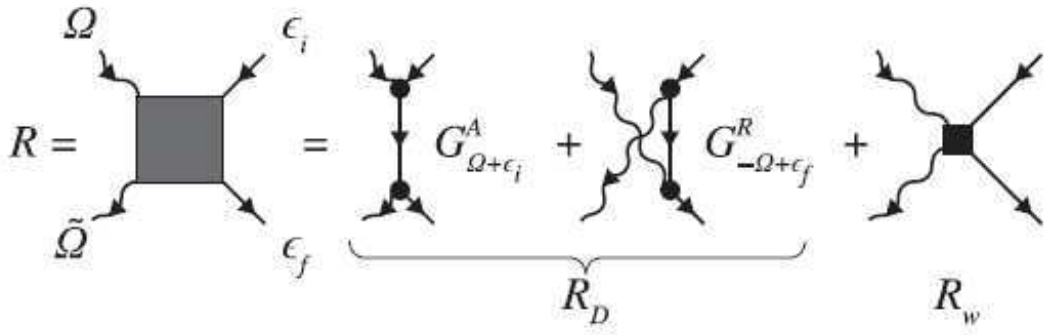

FIGURE 2.22: Feynman diagram of the total Raman scattering amplitude of the photon by the creation of an electron-hole pair [159].

cally scattered by electrons, thus changing its energy, momentum, and polarization from Ω, $\mathbf{q}$, and $\mathbf{I}$ to $\tilde{\Omega} = \Omega - \omega$ (ω being the Raman shift), $\tilde{\mathbf{q}}$, and $\tilde{\mathbf{I}}$. These two terms lead to the Raman scattering amplitude, given by: $R = R_D + R_\omega$, where R_ω is called the contact interaction, while R_D is called the diamagnetic term (see Figure 2.22c).

R_ω describes a one-step scattering process which is mediated by a contact interaction between an electron and two photons, as seen in the last term of the Feynman diagram depicted in Figure 2.22c. The contact interaction appears for Dirac Fermions due to rotational symmetry breaking in Hamiltonian 2.22 through the trigonal warping term. This mechanism leads to the generation of electronic excitations with E_2 symmetry of the $C_{6\nu}$ point group [158].

The diamagnetic interaction (R_D), with the representation A_2 of $C_{6\nu}$, is a two steps process. It consists of an absorption (emission) of a photon with energy $\Omega(\tilde{\Omega})$ transferring an electron from an occupied state in the valence band into a virtual intermediate state, followed by another emission (absorption) of the second photon with energy $\tilde{\Omega}(\Omega)$, which moves the electron to the final state. These two quantities have the following forms for monolayer graphene:

$$R_D = \frac{(e\hbar v)^2}{\Omega^2}\left(-i\sigma^z(\mathbf{I}\times\tilde{\mathbf{I}}^*)_z + \frac{\mathbf{M}.\mathbf{d}}{\Omega}\right) \tag{2.25}$$

$$R_\omega = \frac{e^2 v^2 \hbar^2}{6\Omega\gamma_0}(\mathbf{e}_z \times \boldsymbol{\sigma}).\mathbf{d}, \tag{2.26}$$

where: $\mathbf{M} = \xi v(\sigma_x p_y + \sigma_y p_x, \sigma_x p_x - \sigma_y p_y)$, and $\mathbf{d} = (I_x\tilde{I}^*_y + I_y\tilde{I}^*_x, I_x\tilde{I}^*_x - I_y\tilde{I}^*_y)$.

Generally, the components of the scattering amplitude realize a representation of the lattice symmetry group $C_{6\nu}$. $\mathbf{I}$ and $\tilde{\mathbf{I}}^*$ are polarization operators for the incoming and

scattered photons that belong to E_1 representation. However, E_1 can be expanded into irreducible representations as:

$$E_1 \otimes E_1 = A_1 \oplus A_2 \oplus E_2, \tag{2.27}$$

which leads to a series of combinations for the polarization vectors as functions of the irreducible presentation A_1, A_2, and E_2:

$$\Xi_{A_1} = |\mathbf{I} \times \tilde{\mathbf{I}}^*|^2, \quad \Xi_{A_2} = |\mathbf{I} \cdot \tilde{\mathbf{I}}^*|^2, \quad \Xi_{E_2} = |\mathbf{d}|^2 = 1 + (\mathbf{I} \times \mathbf{I}^*)(\tilde{\mathbf{I}} \times \tilde{\mathbf{I}}^*). \tag{2.28}$$

The scattering probability for a photon from a state $(\mathbf{q}, q_z)$ with energy Ω to a state $(\tilde{\mathbf{q}}, \tilde{q}_z)$ with energy $\tilde{\Omega}$, by exciting and electron-hole pair is then given by [159]:

$$w = w_{A_1}\Xi_{A_1} + w_{A_2}\Xi_{A_2} + w_{E_2}\Xi_{E_2}. \tag{2.29}$$

Ξ_i are seen as weight functions for the scattering probability that is presented as a sum of partial scattering probabilities w_i in a process where polarization vectors transform accordingly to a given representation.
The total contribution from the electronic Raman scattering will be:

$$I = \int g(\omega)\mathrm{d}\omega, \tag{2.30}$$

where $g(\omega)$ is the total spectral density for the scattering process.

2.3.3 Electronic excitations due to inter-Landau level transitions

2.3.3.1 Monolayer graphene

When applying magnetic field perpendicular to the graphene atomic plane, Landau quantization will take place. The electronic dispersion will split into quantized Landau levels. As a result of this quantization, inelastic scattering of photons is caused by inter-Landau level excitations (see Figure 2.21). These electronic excitations manifest in the magneto-Raman and magneto-infrared spectra of graphene, N-LG, and bulk graphite as a series of pronounced structures moving with the magnetic field. These inter-Landau level transitions, denoted $L_{n,m}$ (n, m, are Landau level indexes), can be classified as Raman active or infra-red active according to their point group symmetry [78]. Some of these modes are referred to as silent modes, since they are neither Raman nor infra-red active.

The electronic dispersion around the K point is isotropic with respect to continuous rotations of electronic momentum around the energy axis, as seen in the top view dispersion of graphene in Figure 2.23a. However, this isotropy is broken when including the trigonal warping parameter (labeled γ_3) of the SWM model in the band structure calculation of graphene. As a consequence, the rotational symmetry is restricted to momenta with rotations of 120° ($\pm 2\pi/3$), as seen in Figure 2.23b. As a result, the quantum number m_z, associated with the rotational symmetry, which could assume all integer values from $-\infty$ to $+\infty$ in the case of the continuous rotational symmetry, has only three distinct values for the threefold symmetry: all the m_z differing by a multiple of 3 become equivalent [160].

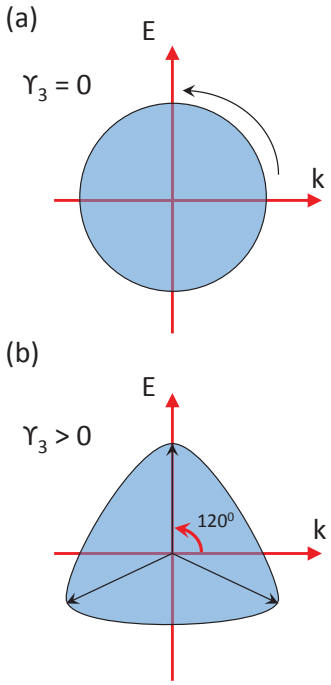

FIGURE 2.23: Effect of trigonal warping on the band structure of graphene. (a) Top view of the conical dispersion in the absence of trigonal dispersion. (b) Top view of the deformation induced by the trigonal warping. The scale is exaggerated for illustration.

Following these observations, the Raman-active inter-Landau level transitions can be further classified into two groups: (i) Transitions that are allowed even when the trigonal warping is ignored ($\gamma_3 = 0$), thus surviving the continuous rotational symmetry. We will refer to these excitations as *strongly allowed*. (ii) The second type of transitions need a non zero value of the trigonal warping to be activated. We refer to these excitations as *weakly allowed*. These two types of transitions can be probed using circularly polarized magneto-Raman scattering experiments.

The reason is that circularly polarized photons carry angular momentum $m_z = \pm 1$. In the co-circular polarization configuration, the incident and emitted photons have the same angular momentum, this results in angular momentum change equals to $\Delta m_z = 0$. However, in cross-circular polarization configuration, the incident and emitted photons have opposite polarization, which results in angular momentum change equals to $\Delta m_z = \pm 2$. An inter-Landau level transition $n^- \rightarrow (n + m_z)^+$ carries angular momentum m_z. This immediately designates the transitions with $\Delta|n| = 0$ and $\Delta|n| = \pm 2$, with the corresponding transition energies $L_{\Delta|n|=0} = 2\epsilon_{|n|}, L_{\Delta|n|=\pm 2} = (\epsilon_{|n|-1} + \epsilon_{|n|+1})$, as the strongly allowed processes in the co-circular and cross-circular polarization configurations, respectively [158–160].

Figure 2.24b shows non-polarized magneto-Raman spectra measured from a graphene monolayer flake on top of the surface of bulk graphite [169]. In these spectra, all Raman-active excitations are expected to be observed. However, it is clear from Figure 2.24 that the strongest contribution to the magneto-Raman spectrum originates from the

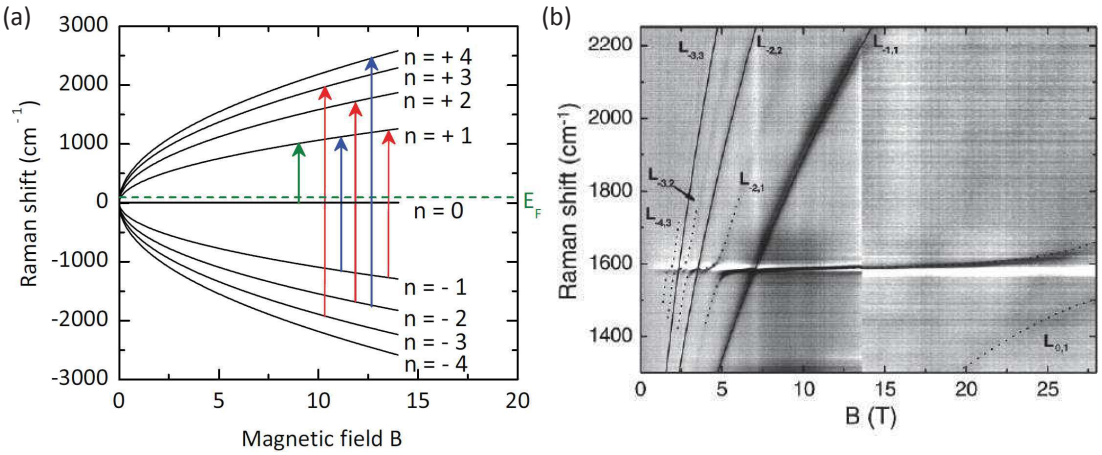

FIGURE 2.24: (a) Schematics of the Landau levels dispersion in graphene and the electronic excitations that are probed in magneto-Raman spectroscopy. The Fermi level is pinned near the zeroth Landau level. Red arrows indicate $\Delta|n| = 0$ inter-Landau level transitions, blue arrows $\Delta|n| = \pm 2$, and green arrow the intra-band transition $L_{0,1}$. (b) Micro-magneto Raman experiment revealing the observation of the inter-Landau level transitions in monolayer graphene on top of bulk graphite [169].

$\Delta|n| = 0$ transitions (red arrows in Figure 2.24a), which is in line with the theoretical predictions [158].

The optical-like excitations ($\Delta|n| = \pm 1$) are not expected to be Raman-active without trigonal warping [170]. Indeed, when γ_3 is included then these excitations are expected to be weakly allowed. To illustrate this, let us consider the excitation $L_{n^-,(n+1)^+}$ with $\Delta|n| = +1$. The trigonal warping induces mixing of the levels $n^-, (n+3)^-$, through the excitation $L_{(n+3)^-,(n+1)^+}$ which is strongly allowed in Raman scattering. Consequently, $\Delta|n| = \pm 1$ are expected to be observed in the same crossed-circular polarization as $\Delta|n| = \mp 2$ excitations. This effect has been confirmed experimentally by P. Kossacki *et al.* [160]. Their amplitude, however, is small compared to $\Delta|n| = 0$ excitations (see Figure 2.25a).

The $\Delta|n| = \pm 1$ transitions resemble the $\Delta|n| = \pm 1$ excitations observed in far infra-red magneto absorption experiments, but it is found that they belong to the E_2 symmetry class while the infra-red transitions belong to E_1 symmetry class [159]. The magnetic oscillations of the E_{2g} phonons (G band) are due to the coupling with the $\Delta|n| = \pm 1$ that have the same symmetry as the Γ point phonons (see Figure 2.25b). The detailed analysis of this resonant effect will be presented in the next section.

The polarization dependent selection rules in graphene have been confirmed by polarization resolved magneto-Raman scattering experiments, performed on high mobility graphene flakes on top of bulk natural graphite [164]. These results are shown in Figure 2.25. In the co-circular polarization configuration, strong features evolving like $\sqrt{B}$ were observed, and they correspond to $L_{-n\to n}$ excitations. While their intensities are much lower compared to $\Delta|n| = 0$, weak traces of $\Delta|n| = \pm 1$ inter-Landau level transitions

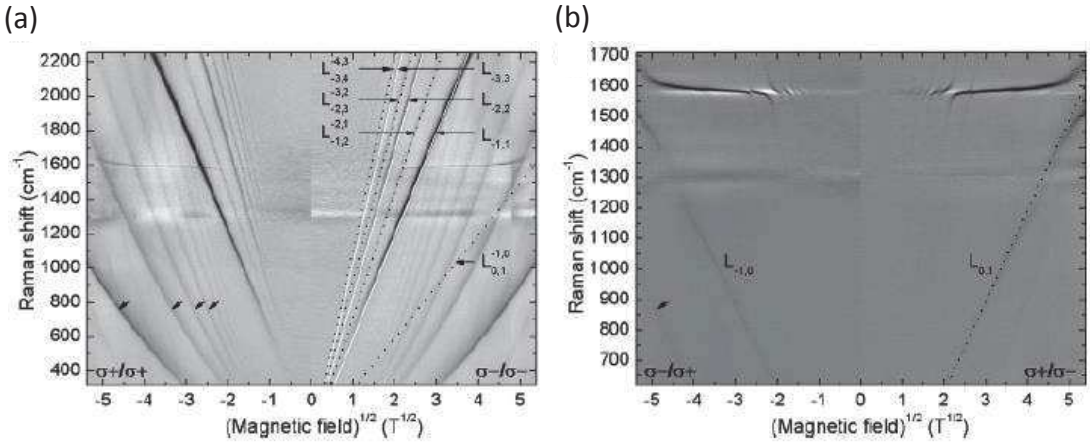

FIGURE 2.25: (a) Magneto-Raman scattering response of graphene on natural graphite measured in co-circular polarization configuration that selects $\Delta|n| = 0$ inter-Landau level transitions. (b) Cross-circular polarization configuration blocks the $\Delta|n| = 0$ transitions and allows the $\Delta|n| = \pm 1$ that are seen through their coupling to the E_{2g} phonon mode. Black (white) corresponds to high (low) intensity. From [164]

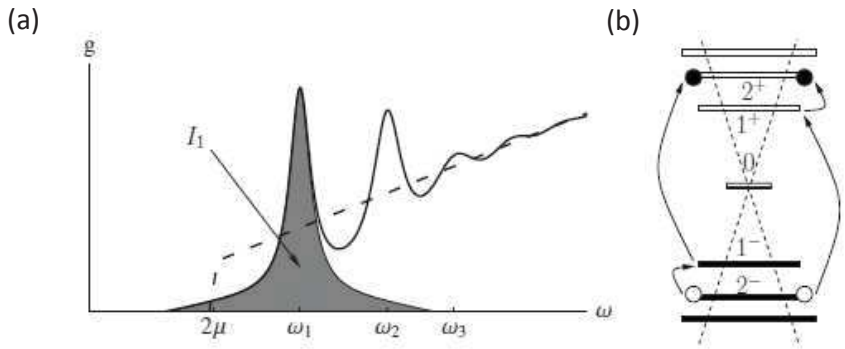

FIGURE 2.26: (a) Spectral density $g(\omega)$ of light inelastically scatterred from electronic excitations in graphene at under magnetic fields (solid line) and at zero magnetic field (dashed line). Here $\omega \ll \Omega$ is the Raman shift. (b) Sketch illustrates intermediate and final states of the electronic Raman process in monolayer graphene. Figures are taken from [158].

are also visible in the co-circular configuration. In the cross-circular polarization configuration, the intra-band transitions $L_{0\to 1}$ and $L_{-1\to 0}$ are clearly observed, while the inter-band transitions $L_{-n\to n+1}(L_{-(n+1)\to n})$ with E_2 symmetry are visible through their coupling to the E_{2g} optical phonons.

In magnetic fields, the Raman amplitude of the $\Delta|n| = 0$ excitations is given by [159]:

$$R_{n^-\to n^+} = \frac{1}{4}\frac{(ev\hbar)^2}{c^2\Omega} \sum_{\alpha=\pm}\left[\frac{(\mathbf{I}\mathbf{e}_+)(\tilde{\mathbf{I}}^*\mathbf{e}_-)}{\Omega-\varepsilon_n-\alpha\varepsilon_{n+1}} - \frac{(\mathbf{I}\mathbf{e}_+)(\tilde{\mathbf{I}}^*\mathbf{e}_-)}{\varepsilon_n-\Omega-\alpha\varepsilon_{n-1}} - \frac{(\mathbf{I}\mathbf{e}_-)(\tilde{\mathbf{I}}^*\mathbf{e}_+)}{\Omega-\varepsilon_n-\alpha\varepsilon_{n+1}} + \frac{(\mathbf{I}\mathbf{e}_-)(\tilde{\mathbf{I}}^*\mathbf{e}_+)}{\varepsilon_n-\Omega-\alpha\varepsilon_{n-1}}\right], \tag{2.31}$$

where the ($\mathbf{Ie}_{\pm}$) and ($\tilde{\mathbf{Ie}}^{*}_{\pm}$) describe the circular polarization of the incident/scattered photon, respectively. The spectral density of the angle-integrated Raman scattering signal, plotted in Figure 2.26a, can be obtained from 2.31 by integrating over all directions of propagation of the scattered photons:

$$g_{n^-\to n^+}(\omega) = \Xi_{A_1}\left(\frac{v^2}{c^2}\frac{e^2/\lambda_B}{\pi\Omega}\right)^2 \sum_{n\geq 1}\gamma_n(\omega - 2\varepsilon_n). \tag{2.32}$$

Were, $\pi^{-1}\Gamma_n/[x^2+\Gamma_n^2]$ is a normalized Lorentzian function, and Γ_n accounts for the Landau level broadening which increases with the Landau level index n.
It is important to note that from 2.32, the intensity of the Raman active inter-Landau level transitions decreases as $(1/\Omega)^2$, where Ω is the excitation energy. From the experimental point of view, the best configuration to observe these excitations will be to use long wavelengths laser sources [165].

2.3.3.2 Multilayer graphene and bulk graphite

Magneto-Raman scattering experiments have been conducted to search for inter-Landau level excitations in multilayer graphene with either Bernal stacking [31] or rhombohedral stacking [75]. Figure 2.27 shows non-polarized magneto-Raman spectra obtained from probing inter-Landau level transitions under strong magnetic fields. The effective bilayer model introduced in Chapter 1 is used to confront the experimental data to theory. Since monolayer and bilayer graphene are the building blocks for every stacking configuration of multilayer graphene, their magneto-Raman selection rules can be used for every number of layers [171]. The most pronounced features are those originating from the $\Delta|n| = 0$ electron-hole excitations, while $\Delta|n| = \pm 1$, $\Delta|n| = \pm 2$ are hardly seen in Raman spectroscopy. As we will show in the Chapter 5, both theory and experimental results confirm similar selection rules for inter-Landau transitions in ABC-stacked N-LG as in ABA-stacked N-LG [75].
Dirac fermions have been observed experimentally in graphene parent crystal, bulk graphite [172, 173]. Several experimental techniques have been used to probe

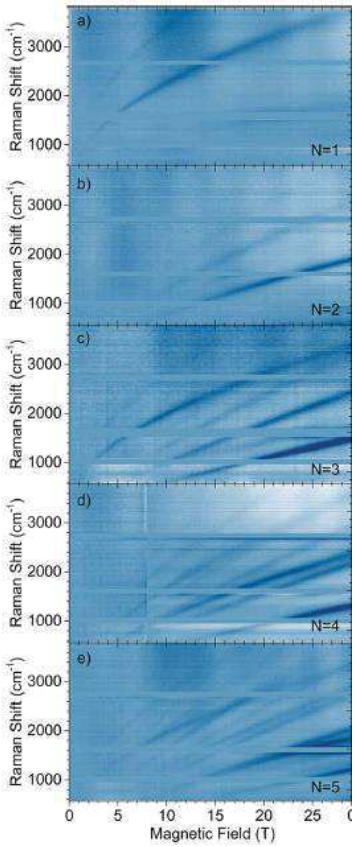

FIGURE 2.27: Micro-magneto-Raman scattering on suspended ABA-stacked multilayer graphene flakes with varying thickness [31].

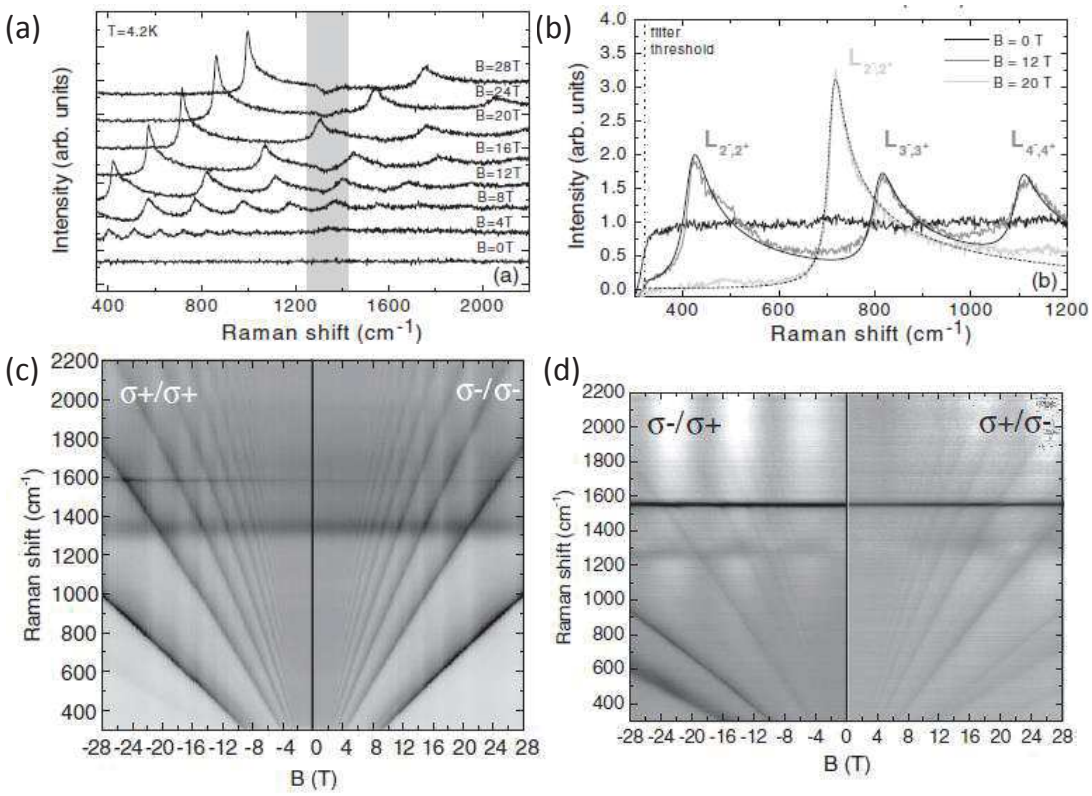

FIGURE 2.28: (a) Representative Raman scattering spectra with subtracted B = 0 T spectrum in the co-circular configuration showing many asymmetric magnetic field dependent features. (b) Zoom on the asymmetric features of the inter-band Landau level transitions for three different values of B. Solid lines are calculated dispersions using two parameters model as in [160]. (c,d) False color map of the polarized magneto-Raman intensity, both positive and negative fields are used to invert the polarization [160]. Co-circular configuration probes the $\Delta|n| = 0$ transitions (c), while the cross-circular configuration selects $\Delta|n| = \pm 1$ in (d).

the corresponding electronic excitations when graphite is under magnetic fields, using mainly magneto-Raman and infra-red spectroscopy techniques.

In contrast to discrete Landau levels in purely 2D systems such as graphene, graphite under the effect of magnetic fields will split into Landau bands. The joint density of states diverges at the K and H points, and the optical response of graphite is dominated by contributions from excitations at these two high symmetry points [174]. Observation of inter-Landau band transitions in bulk graphite has been reported in magneto- spectroscopy studies for massive Dirac fermions in the vicinity of the K point [44, 160, 175], but also for massless Dirac fermions at the H point [114]. In-line with the effective bilayer model introduced in Chapter 1, electrons in the vicinity of the K point behave as massive Dirac fermions with mass twice enhanced in comparison to a true graphene bilayer, while the holes around the H point have nearly linear dispersion and behave as massless Dirac fermions in graphene, but with an additional double degeneracy [46].

Figure 2.28 depicts a magneto Raman study of these Landau band transitions in Bernal-stacked bulk natural graphite [160], using co-circular and cross-circular polarization configurations. Similar to selection rules in bilayer graphene [171], the co-circular polarization configuration selects symmetric transitions with $\Delta|n| = 0$, while cross-circular polarization selects $\Delta|n| = \pm 1$.

2.4 Magneto-phonon resonance

2.4.1 Electron-phonon coupling

Electron-phonon coupling (EPC) plays a major role in understanding many physical phenomena in condensed matter physics. The microscopic theory of the Raman scattering effect, as we discussed in the beginning of this Chapter 2, depends entirely on the concept of EPC. For conventional superconductors (in which superconductivity occurs at relatively low critical temperatures), the EPC is responsible for the formation of the so-called *Cooper pairs*, as was proposed by Bardeen–Cooper–Schrieffer (BCS theory) in their microscopic theory of superconductivity [176].
In sp^2 carbon allotrope, the EPC determines both the phonons dispersion and their lifetime [177, 178]. For both metallic and semi-conducting single-walled carbon nanotubes (SWCNTs), numerous studies have shown that their transport properties are intimately related to the EPC involving acoustical and optical phonons [179–183], which can set the critical limit for the observation of ballistic transport on these systems. Plenty of other physical phenomena are related to the EPC: the dynamics of excited states, heat capacity of metals, formation of polarons (i.e., bounded states for the charge carriers that interacts with electromagnetic radiations) in quantum dots and quantum wells [184, 185].
As we will show in the following, theoretical and experimental studies of the physical properties of graphene have shown that the coupling between electrons and the vibrational modes in this material presents a concept of prime interest in understanding many experimentally observed phenomena.

2.4.2 The electron-phonon coupling in graphene

2.4.2.1 The Kohn anomaly

Lattice vibrations in metals are partly screened by conduction electrons. For certain phonon frequencies $\mathbf{q}$, this screening can change rapidly which leads to an abrupt change in the phonon energy $\hbar\omega_q$. Such effect is called a Kohn anomaly, as was first evidenced

theoretically by W. Kohn in 1959 [186]. In metals, the points at which Kohn anomalies occur are directly determined from the shape of their *Fermi surface*.

The Fermi surface is a concept that represents the energy boundaries of charge carriers in k-space for metals, semi-metals, and doped semi-conductors [187]. The determination of the Fermi surface is very useful in predicting the electronic properties of many materials, probed by transport and optical spectroscopy techniques. In condensed matter experiments, the Fermi surface of metals and related materials is determined by measuring the quantum oscillations of a given observable under strong magnetic fields, such as the *de Haas–van Alphen* effect for magnetization, and the *Shubnikov–de Haas* effect for resistivity. The cross-section $\mathbf{A}_\perp$ of the Fermi surface that is perpendicular to the applied magnetic field is then given by the Onsager relation [187]:

$$\mathbf{A}_\perp = \frac{2\pi e \Delta \mathbf{B}}{\hbar c}. \tag{2.33}$$

Kohn anomaly connects two electronic states $\mathbf{k}_1$ and $\mathbf{k}_2$, from the Fermi surface of the studied material, by a phonon with wave vector $\mathbf{q}$ such as [187]:

$$\mathbf{k}_2 = \mathbf{k}_1 \pm \mathbf{q}. \tag{2.34}$$

The Kohn anomaly has been predicted and observed for graphite and metallic carbon nanotubes [177, 178, 183, 188]. In graphene, there are two points in its BZ where the valence and conduction bands touch at the Dirac point (i.e., K and K′). The Fermi surface of neutral graphene can be viewed as a set of points distributed on the K and K′ valleys of its BZ. Thus, the Kohn anomaly in graphene occurs either at the Γ point, where two electronic states can be connected by a phonon with a wave vector $\mathbf{q} \sim 0$, or at the K and K′ points, where two electronic states are connected with a phonon with a wave vector $\mathbf{q} \sim \pm\mathbf{K}$ through an inter-valley electron-phonon scattering process [177, 189].

However, it is important to note that not all phonons at the Γ and K points will experience a Kohn anomaly. For symmetry reasons, the Kohn anomaly in graphene occurs only for the doubly degenerate E_{2g} optical phonons and only the phonons with the A_{1g} symmetry at the K point, while the other vibrational modes have no Kohn anomalies [189].

Figure 2.29 shows the phonon dispersion in graphene along the high symmetry axis Γ-M-K line. The red lines indicate where the Kohn anomaly occurs, in the form of two sharp kinks, at the Γ for the highest branches of the LO phonons, and at K point in the TO phonon branches. At these points, two effects are observed: (i) the phonon's energy becomes quasi-linear with momentum, (ii) the phonon's energy is lowered by an amount of 5% with respect to the unperturbed phonon energy (lower panel of Figure 2.29) and

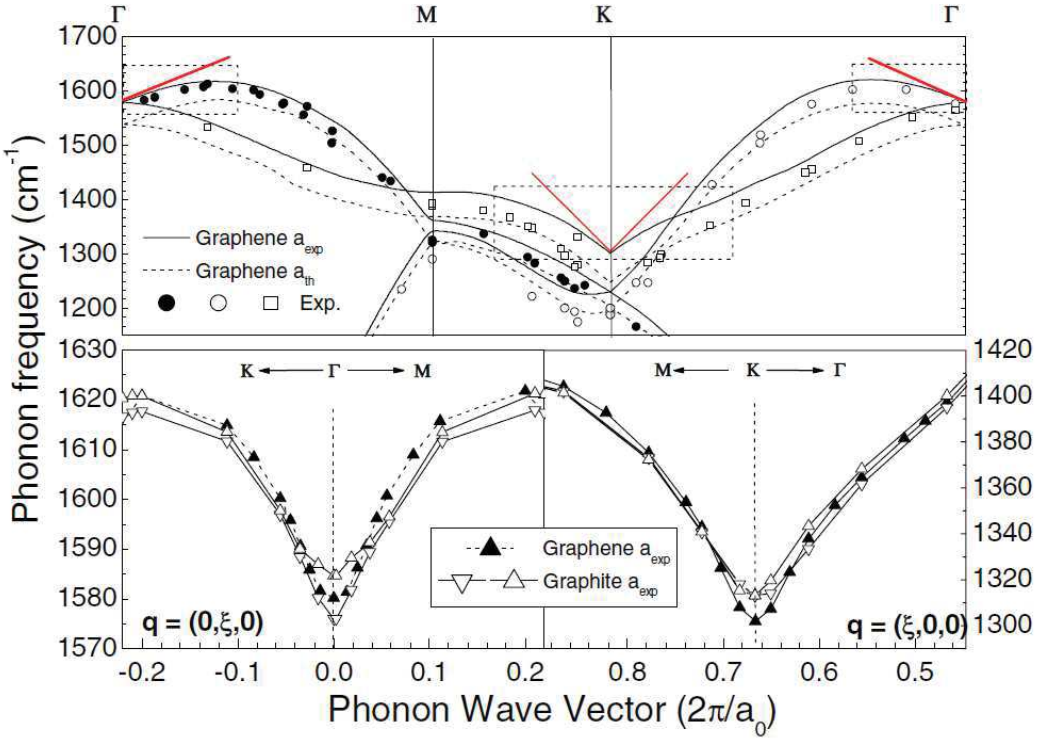

FIGURE 2.29: Phonon dispersion in graphene along the Γ-M-K line (upper panel). Dashed lines are calculated dispersions using a theoretical value of the lattice parameter, while solid lines are calculated dispersions using the experimental value of the lattice parameter. Energies of the highest optical branches at the Γ and K points are renormalized due to the Kohn anomaly, shown as cusps (lower panel) [177, 188]. The experimental points are the phonons dispersion determined using neutron or X-ray scattering techniques [86].

is representative of the EPC contribution to the phonon's energy.

In their study, Piscanec *et al.* [177] showed that the slope of these kinks is proportional to the square of the EPC. Thus, based on a mean field single particle formalism, such as DFT or Hartree-Fock, an analytical expression of the EPC can be derived for graphene at the points where the Kohn anomaly occurs. The linear dispersion of the phonon's energy in the vicinity of the Γ(K) points is given by:

$$E^{ph}_{\Gamma(K)}(q) = \hbar\omega_{\Gamma(K)} + S^{E_{2g}(A_{1g})}_{\Gamma(K)}|q|, \tag{2.35}$$

where $S^{E_{2g}(A_{1g})}$ refers to the slope of the $E_{2g}(A_{1g})$ phonon's energy near the Γ(K) points, which is directly related to the EPC [178]:

$$S^{E_{2g}(A_{1g})}_{\Gamma(K)} = \frac{\sqrt{3}\hbar a_0 \langle D^2_{\Gamma(K)}\rangle_F}{8M\hbar\omega^{\Gamma(K)}_{E_{2g}(A_{1g})} v_F}, \tag{2.36}$$

where M is the carbon atom rest mass, a_0 is the graphene lattice parameter, v_F is the Fermi velocity, and $\langle D^2_{\Gamma(K)}\rangle_F$ is the EPC averaged over the square of the Fermi surface. The above formula shows that it is possible to calculate the value of the EPC in graphene by measuring the phonon dispersion around the Γ and K points.
Following these observations, a large EPC is expected for the E_{2g} mode at the Γ point, and the A_{1g} mode at the K point. As we will show in the following, by tuning the electronic excitation spectrum we can tune the EPC in graphene. This is done in experiments by changing the electronic density (i.e., shifting the Fermi level ϵ_F) or under the effect of magnetic fields.

2.4.2.2 Tuning the EPC with an applied electrical field

Tuning the EPC in graphene-based systems using a gate voltage to shift the Fermi level away from the charge neutrality point by electrons or holes doping, was first studied theoretically by T. Ando, A. H. Castro Neto, and F. Guinea [190–192] for the case of monolayer and bilayer graphene. It was evidenced shortly after by Raman scattering experiments for both monolayer and bilayer graphene systems [152, 153, 155, 156] (see also the previous section about doping).
Figure 2.30 shows the results of such a study in the case of gated monolayer graphene by Yan *et al.* [156]. The G band (represented by Feynman diagrams in the insets of Figure 2.30a,d) interacts with virtual electron-hole pairs that cause a re-normalization of the phonon energy (Figure 2.30e), while a broadening of its linewidth shows that shorter phonon lifetimes are linked to higher particle or hole density (Figure 2.30b). This resonant coupling is Pauli-blocked when the Fermi level is far away from the charge neutrality, as seen in Figure 2.30c,f.

In his theoretical paper [190], T.Ando studied the dependence of the optical phonon energy and broadening as a function of the Fermi level. The energy shift and broadening of the E_{2g} phonon are given by the real and imaginary parts of the phonon's self energy. When the Fermi level is at $\epsilon_F = \hbar\omega_G/2$ (i.e. half the phonon energy), the energy shift diverges logarithmically to $-\infty$. However, when the Fermi energy is $\epsilon_F > \hbar\omega_G/2$, the phonon's energy increases in proportion to ϵ_F. In experiment, graphene samples are usually not ultra-clean, disorder and charged impurities trapped in the substrate will induce a departure from this ideal behavior, and the logarithmic divergence is not reached due to scattering of electrons by disorder (see Figure 2.30d). The shift in the E_{2g} energy as a function of the Fermi level is due to reduction in the screening of the phonon by inter-band electron-hole pair transitions. Indeed, when the Fermi level increases, Pauli blocking will not allow transitions below the Fermi level (see Figure 2.30e-f), so the screening of the phonon reduces leading to an increase in the phonon energy [156, 190].

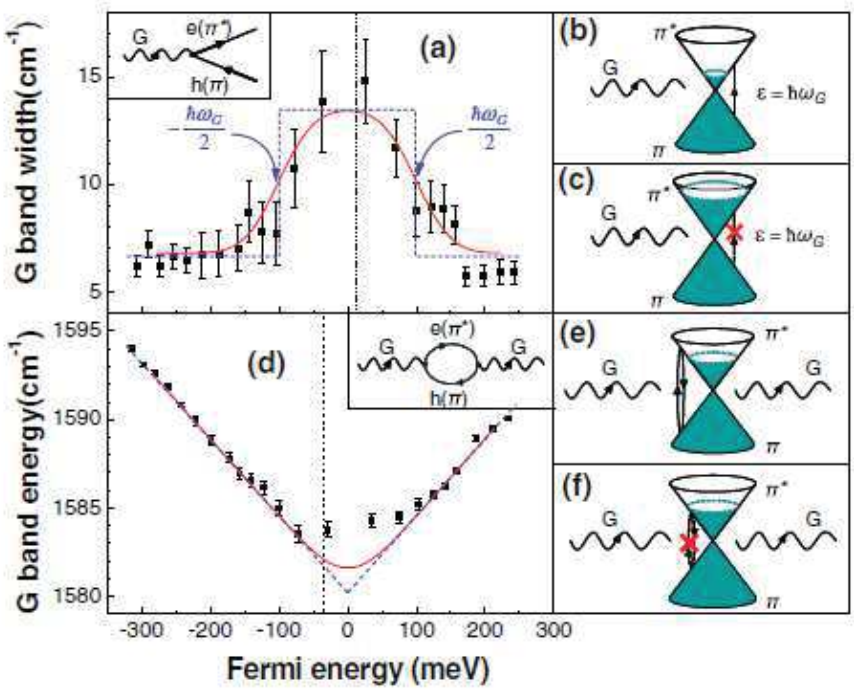

FIGURE 2.30: Graphene G band damping (a)-(c), and graphene G band renormalization (d)-(f) due to EPC. The dots are experimental results obtained from a Lorentzien fitting of the G band, while the lines are theoretical calculations based on time-dependent perturbation theory. Figure is taken from [156].

At high doping, the slope of the increase in the G band energy is directly proportional to the EPC.

For the phonon line-width, changes are predicted to occur when $-\hbar\omega_G < \epsilon_F < +\hbar\omega_G$ (see Figure 2.30a). Theoretically speaking [190], the change in the FWHM with ϵ_F should follow a step function with steps at $\pm\hbar\omega_G/2$ (blue dashed step function in Figure 2.30a), however disorder in the sample will induce a departure from this ideal picture. Pauli blocking of the electron-hole pairs induces a large phonon's life-time, and since the line-width and the life-time of an excitation are inversely proportional due to Heisenberg uncertainty principle, this will lead to a decrease in the phonon's linewidth at high electronic concentration [156].

It is important to note that the EPC in graphene as a function of the Fermi energy cannot be understood in the frame of the *adiabatic Born-Oppenheimer* approximation (ABO). This approximation has been intensively used to study the band structures of crystals. The ABO assumes that the lighter electrons adjust adiabatically to the motion of the heavier nuclei, remaining at any time in their instantaneous ground state. In this situation, the use of time-dependent perturbation theory is needed to fully understand the EPC in graphene and related systems when tuning the Fermi level [155, 156].

2.4.3 Magneto-phonon resonance in graphene, multilayer graphene, and bulk graphite

The application of magnetic fields to graphene, multilayer graphene, and bulk graphite will form discrete Landau levels on these materials. Consequently, instead of a continuous energy excitation spectrum, inter-Landau level excitations have a well-defined features that detach from the background in optical spectroscopy experiments. As we will be discussing in this section, the Landau quantization will have a strong effect on the EPC in graphene based systems. The energy of the n^{th} Landau level in graphene is given as [2, 193]:

$$E_n = sign(n) v_F \sqrt{2e\hbar B|n|} \tag{2.37}$$

where v_F is the Fermi velocity, and the energy of an inter-Landau level transition is given as $E_{m\to n} = |E_n| - |E_m|$. Indeed, the effect of EPC in graphene under magnetic fields happens to be observable in magneto-Raman scattering experiments, where it couples inter-Landau level transitions, that obey selection rules $\Delta|n| = \pm 1$ (n is the LL index), with the E_{2g} optical phonon at the Γ point. This series of resonant coupling between optical phonons and inter-Landau level excitations is known as a magneto-phonon resonance (MPR). Not only inter-band transitions participate in the electron-phonon coupling (blue arrows in Figure 2.31), but also intra-band transitions (green arrows in Figure 2.31), also known in literature as cyclotron resonance, that obey selection rules $\Delta|n| = \pm 1$ participate in the MPR coupling [194, 195].

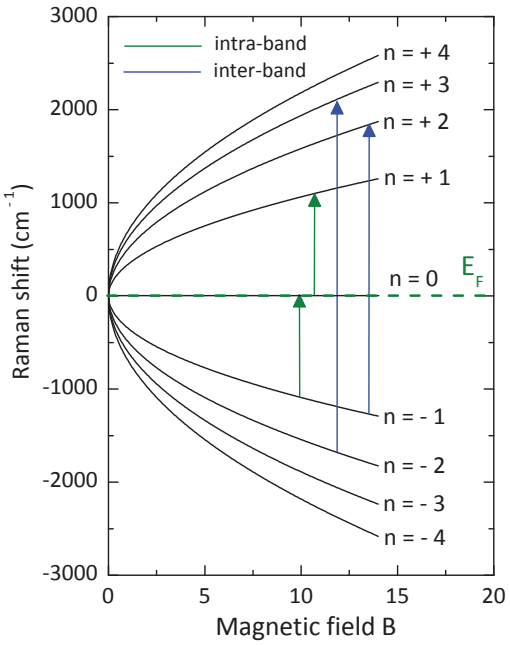

FIGURE 2.31: Landau level dispersion with magnetic field for monolayer graphene. The inter-Landau level transitions (blue arrows) and intra-band transitions (green arrows) with selection rules $\Delta|n| = \pm 1$ participate in the MPR for the E_{2g} optical phonons at the Γ point. The Fermi energy is pinned to the zeroth Landau level.

The MPR in monolayer graphene has been studied theoretically by T. Ando and by M. O. Goerbig *et al.* [194, 196], and also for bilayer graphene [192]. It has been extensively investigated experimentally in different graphene-based systems that were subjected to strong magnetic fields. Indeed, the MPR has been observed in multilayer epitaxial graphene on the

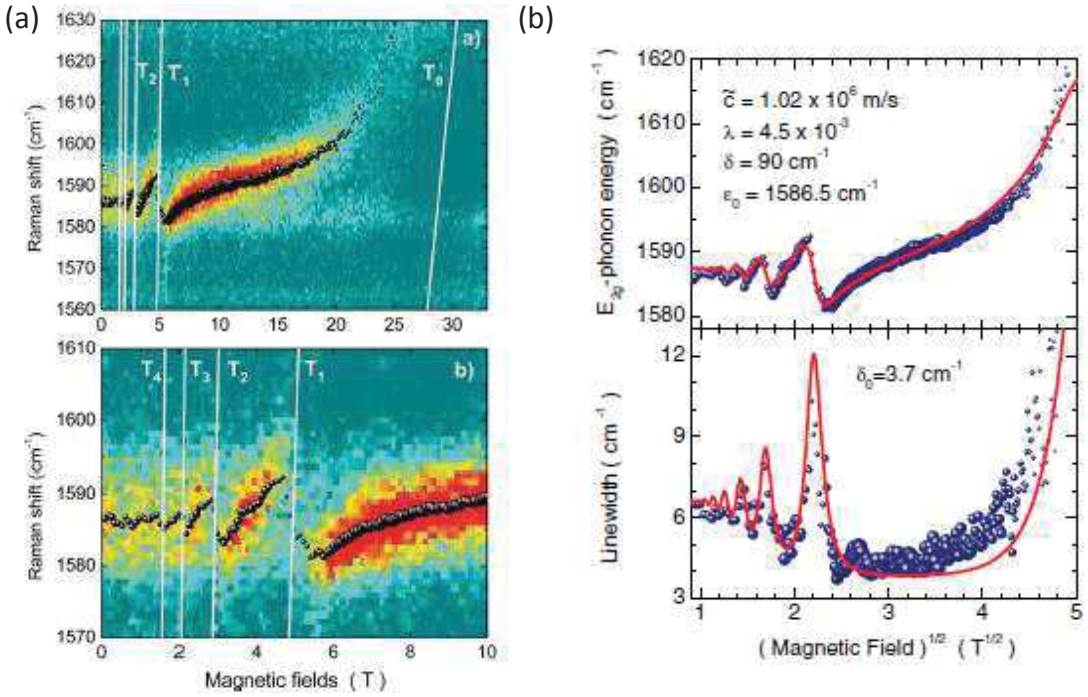

FIGURE 2.32: (a) Color map of the magneto-Raman scattered intensity for graphene on SiC. The MPR is conspicuous for the G band, seen as a series of avoided-crossing when it couples to $\Delta|n| = \pm 1$ inter-Landau level transition. (b) Data simulation (red lines) of the magnetic oscillations of the G band energy and linewidth, extracted from a Lorentzien fit (blue dots), based on the model from [194, 196]. Figures taken from [193].

surface of SiC [193], in graphene-like domains on the surface of bulk graphite [164, 169], in bulk natural graphite [118, 160] , in monolayer to penta-layer graphene suspended over the Si substrate [31], and also in graphene encapsulated on hBN [166, 197]. As we will discuss in Chapters 4 and 5, this effect is also observed for bilayer graphene on hBN, and for rhombohedral multilayer graphene.

Figure 2.32 shows the MPR in multilayer epitaxial graphene on SiC [193]. When varying the magnetic field, the G band exhibits a series of anti-crossing oscillations, shifts and broadening of its line-width each time the energy of a $\Delta|n| = \pm 1$ inter-Landau level transition is tuned with the G band energy. In order to reproduce the behavior of the G band under the effect of magnetic field, we follow the approach described in [194, 196]. Within an effective mass approximation, the Hamiltonian of monolayer graphene under a transverse magnetic field is written as:

$$\mathcal{H}_0 = \frac{\sqrt{3}a}{2}\gamma_0 \begin{pmatrix} 0 & k_x - ik_y \\ k_x + ik_y & 0 \end{pmatrix} = \frac{\sqrt{3}a}{2}\gamma_0(\boldsymbol{\sigma}.\boldsymbol{k}), \tag{2.38}$$

γ_0 is the intra-layer coupling in graphene, $\boldsymbol{\sigma} = (\sigma_x, \sigma_y)$ are Pauli matrices, and $\boldsymbol{k} = (k_x, k_y) = -i\Delta + e\boldsymbol{A}/\hbar c$ is the canonical momentum in the presence of a vector potential

$\boldsymbol{A} = (Bx, 0)$. Since we focus our study on the coupling of E_{2g} optical phonons with electron-hole pairs in graphene, only the limit of long wave-lengths (i.e., $|\mathbf{q}| \sim 0$) is considered. The anti-symmetric longitudinal or transverse displacements of the two in-equivalent sublattices A and B of the graphene honeycomb lattice, that are represented by the E_{2g} optical phonons, are given by [190, 194, 196]:

$$\mathbf{u}(\mathbf{r}) = \sum_{\mathbf{q},\mu} \sqrt{\frac{\hbar}{2NM\omega_0}} \left(b_{\mathbf{q},\mu} + b^{\dagger}_{-\mathbf{q},\mu}\right) \boldsymbol{e}_{\mu}(\mathbf{q}) e^{i\mathbf{q}.\mathbf{r}}, \tag{2.39}$$

where N is the number of unit cells, M is the carbon atom rest mass, ω_0 is the unperturbed optical phonon frequency at the Γ point, $\mathbf{q} = (q_x, q_y)$ is the phonon wave vector, μ denotes the vibrational modes (μ ='t' for transverse and 'l' for longitudinal), and $b^{\dagger}_{\mathbf{q},\mu}$ and $b_{\mathbf{q},\mu}$ are the creation and destruction operators, respectively. The corresponding phonon Hamiltonian is written as:

$$\mathcal{H}_{ph} = \sum_{\mathbf{q},\mu} \hbar\omega_0 \left(b^{\dagger}_{\mathbf{q},\mu} b_{\mathbf{q},\mu} + \frac{1}{2}\right), \tag{2.40}$$

where ω_0 is the unperturbed optical phonon's frequency at the Γ point. The E_{2g} optical phonon mode change the distance between neighboring carbon atoms, which modifies the band structure through a change in the overlap integral between the carbon atoms. The resulting change in Hamiltonian 2.38 describes the electron-phonon interaction in graphene. At the K point, the Hamiltonian of the electron-phonon coupling is given by:

$$\mathcal{H}_{int} = -\sqrt{2}\frac{\beta\gamma}{b^2}\boldsymbol{\sigma} \times \mathbf{u}(\mathbf{r}), \tag{2.41}$$

where $b = a/\sqrt{3}$ is the equilibrium bond length. The change in the wave-function overlap integral between electrons localized on the two nearest neighboring atoms, with respect to the change in inter-atomic distance is given by the dimensionless parameter β:

$$\beta = -\frac{\mathrm{d}\ln\gamma_0}{\mathrm{d}\ln b}. \tag{2.42}$$

The magnetic oscillations of the optical phonon's energy and linewidth can be calculated from the poles of its Green's function [194, 196], which describes the interaction of the phonon with electron-hole pairs, and is given by:

$$D_{\mu}(\mathbf{q}, \omega) = \frac{2\hbar\omega_0}{(\hbar\omega)^2 - (\hbar\omega_0)^2 - 2\hbar\omega_0\Pi_{\mu}(\mathbf{q}, \omega)}, \tag{2.43}$$

where ω denotes the re-normalized phonon's frequency due to interactions with $\Delta|n| = \pm 1$ excitations, and $\Pi_{\mu}(\mathbf{q}, \omega)$ is the phonon's self energy, which is given for the optical

phonons at the Γ point by:

$$\Pi(\mathbf{q},\omega) = -\frac{1}{4}\lambda\left(v_F\sqrt{2\hbar eB}\right)^2 \sum_{s,s'}\sum_{n=0}^{\infty}\left([f(s\epsilon_n) - f(s'\epsilon_{n+1})] \times \frac{2(s\epsilon_n - s'\epsilon_{n+1})}{(\hbar\omega + i\delta)^2 - (s\epsilon_n - s'\epsilon_{n+1})^2} - \frac{1 - ss'}{\epsilon_{n+1} + \epsilon_n}\right), \quad (2.44)$$

where λ is a dimensionless parameter that characterizes the electron-phonon coupling, $\hbar\omega$ is the phonon energy re-normalized due to the MPR, and δ is a phenomenological broadening parameter due to scattering of electrons by other mechanisms, such as disorder or acoustic phonons. The $(s\epsilon_n - s'\epsilon_{n+1})$ terms in Eq. 2.44 correspond to the $\Delta|n| = \pm 1$ inter-Landau level transitions that couples to the E_{2g} phonon. The Fermi-Dirac distribution $f(s\epsilon_n)$ represents the occupation factor of the n^{th} Landau level, with an energy ϵ_n, in the conduction band (s=+1) or the valence band (s=-1). The mode index μ has been omitted since the matrix elements squared do not depend on it. In order to avoid divergence of the series, the summation over the Landau level index n has a cutoff n_c that corresponds to an energy ϵ_c of the order of the graphene band width. Knowing the optical phonon self-energy, the poles of the phonon Green's function are given by [194]:

$$\left(\frac{\omega}{\omega_0}\right)^2 - 1 = \frac{2}{\hbar\omega_0}\ \mathrm{Re}\ \Pi_\mu(\mathbf{q},\omega). \quad (2.45)$$

Thus, the shift and broadening of the E_{2g} optical phonon (the G band) can be calculated self-consistently from the real and imaginary parts of its self-energy [194]:

$$\Delta\omega = \frac{1}{\hbar}\ \mathrm{Re}\ \Pi(\mathbf{q},\omega), \quad (2.46)$$

$$\Gamma = -\frac{1}{\hbar}\ \mathrm{Im}\ \Pi(\mathbf{q},\omega). \quad (2.47)$$

This model for the MPR was used to fit the magneto-Raman data in Figure 2.32b (red lines). Since the shift and broadening of the G band are extracted from experimental data, the only free parameter, which is the EPC parameter λ, can be tuned to best fit the experimental results. Thus, magneto-Raman spectroscopy is a method of choice to characterize the electron-phonon interaction in graphene, multilayer graphene, and other graphene-based structures. The value of the EPC is in the range $\lambda = 4 - 4.5 \times 10^{-3}$. These values have been extracted from different graphene-based systems that exhibit the MPR effect [160, 164, 193, 197].

Chapter 3

General description of experimental setups

3.1 Room temperature micro-Raman setup

Figure 3.1 is a schematic presentation for the micro-Raman setup used to characterize the graphene based samples, and to perform mapping at room temperature.
The excitation source is provided by a helium-neon (HeNe) gas laser, operating at a wavelength of 632.8 nm. The laser beam is coupled through a set of mirrors to an optical microscope equipped with a halogen lamp. A beam splitter inside the microscope is used to focalize either the laser or the light from the lamp, or both, depending on the work configuration desired. This configuration allows for high resolution imaging of the studied flakes, and to locate a specific region for Raman measurements.
The scattered light is then coupled to a single stage spectrometer equipped with a nitrogen cooled charge coupled device (CCD) camera for data analysis. The spectrometer is composed of different diffraction gratings. To get a clean Raman signal, we place in front of the spectrometer a steep long pass filter, optimized for 632.8 nm, in order to block the scattered light from entering the spectrometer.
The microscope is equipped with four different objective lenses (5X, 10X, 20X, 50X) to focalize the light and the laser beam on the sample. To adjust the focus on the sample, the microscope has been equipped with a knob that moves the sample holder up or down. For Raman measurements, the 50X is used. The laser spot is then focused on $\sim 1\mu$m diameter.
The sample is placed under the microscope objective, on top of X-Y piezoelectric stages. This system allows for the displacement of the sample relative to the laser spot with sub-micrometer accuracy. One can access a specific region of the sample, or perform

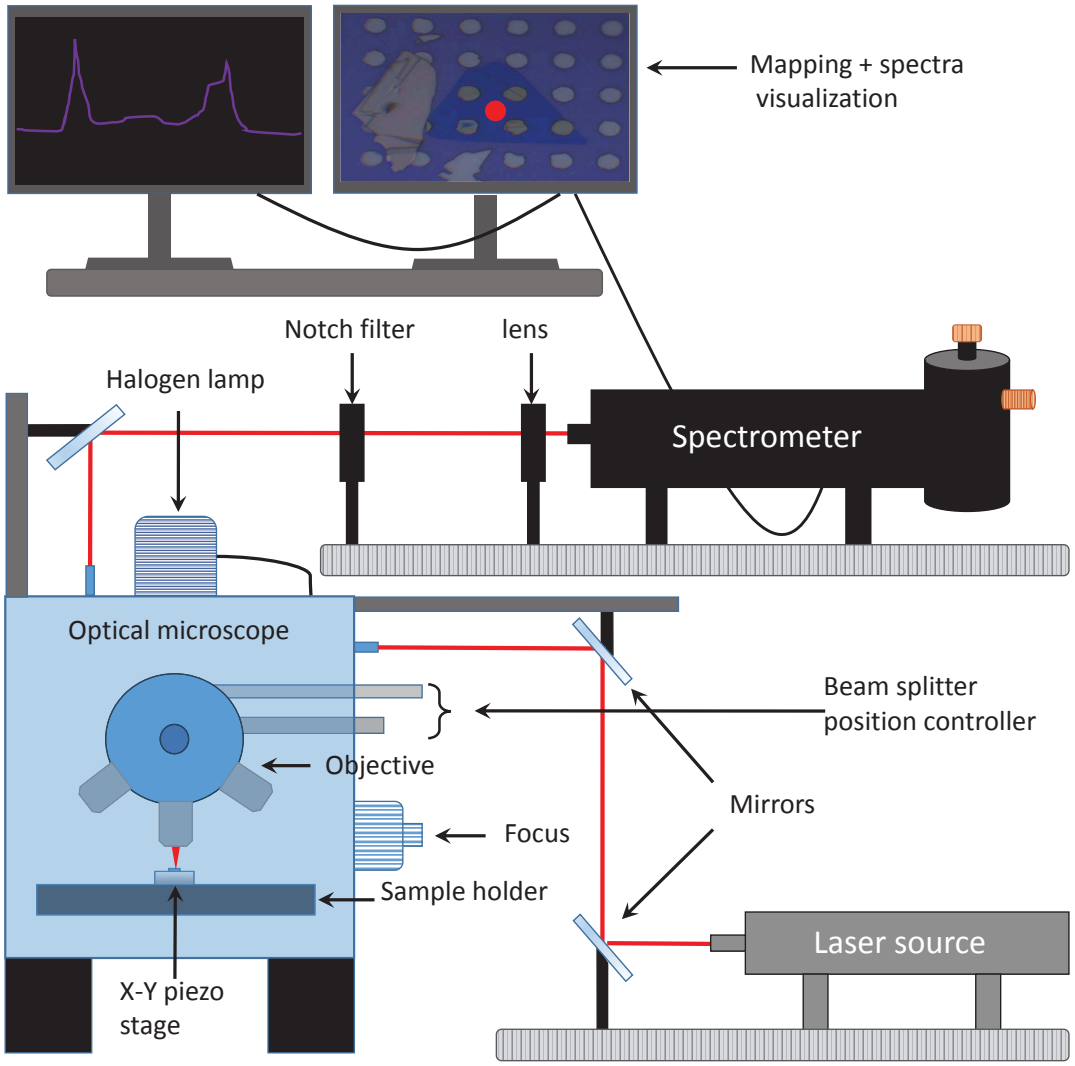

FIGURE 3.1: Schematics of the micro-Raman set up. This set up is used for sample characterization prior to magnetic field measurements.

high resolution mapping for a given flake by recording its Raman scattering response at the same time.

3.2 Fiber optics micro-magneto Raman setup

For Raman measurements under strong magnetic fields, we used the experimental set up depicted in Figure 3.2. The magneto-Raman set up is composed of three main components: *the excitation set up* (Laser + optical table + excitation fiber), the *micro magneto-Raman probe* (miniaturized optical table, Raman probe, cryostat+magnet), *the detection set up* (spectrometer with CCD camera, collection fiber, notch filter), and finally *the low temperature magneto-system* (magnet + cryostat). In the following, we

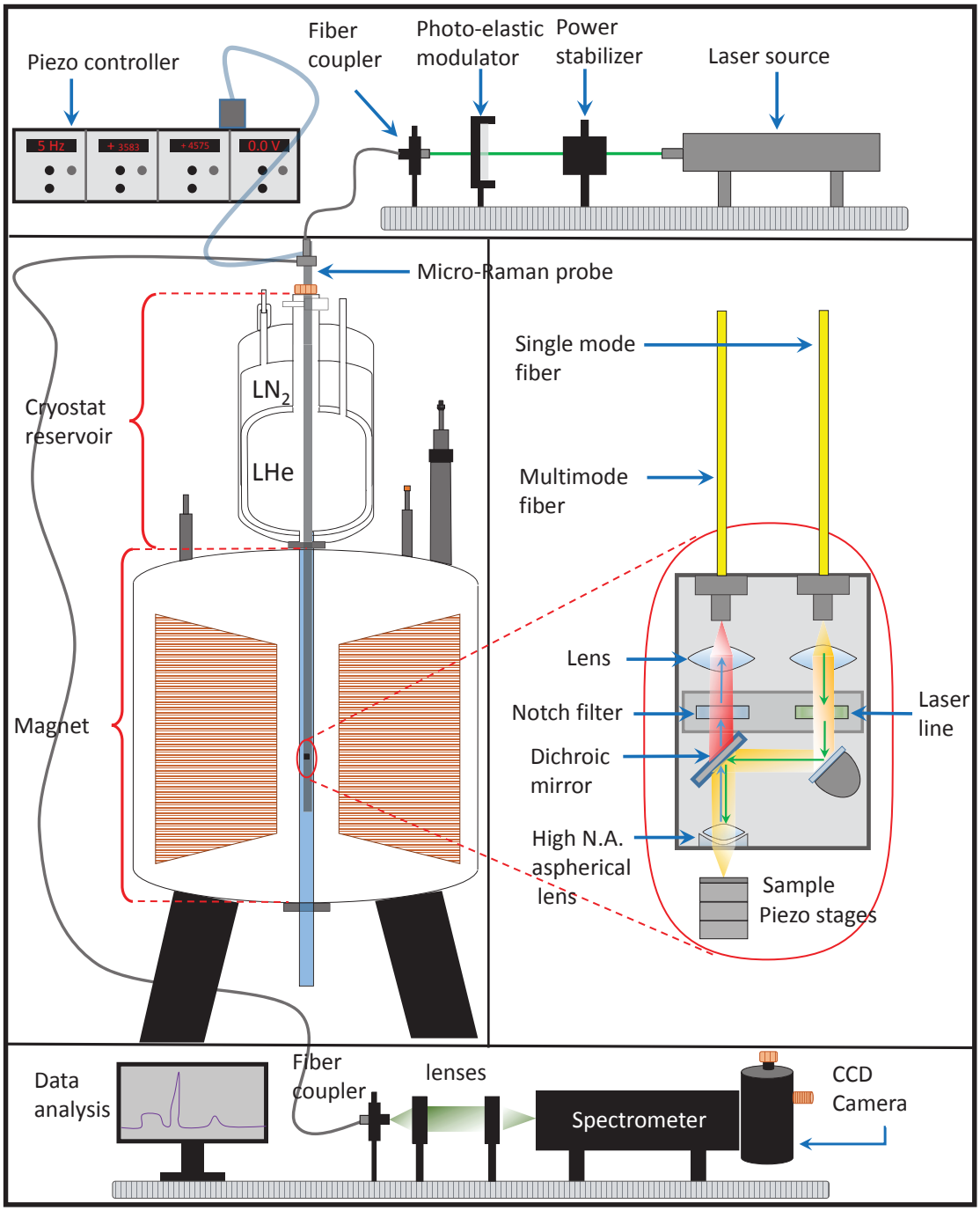

FIGURE 3.2: Schematic presentation of the micro-magneto Raman set up. The probe shown in this figure is equipped with optical fibers to bring the excitation wavelength to the sample, and to collect the scattered light for data analysis.

should give a detailed description of the different components that are making each part of the magneto-Raman setup. This experimental set up was used to study the structures that will be presented in Chapter 4 and Chapter 5.

3.2.1 The excitation setup

In general Raman scattering experiments are conducted by using coherent source of light, that are strong enough to allow for the observation of the Raman scattering in the studied systems (which is six orders of magnitude smaller than the Rayleigh scattering). This is done by using lasers as a source for the excitation. Our experiments were performed using two different laser sources. One excitation source was provided by an argon-ion (Ar^+) gas laser, operating at 514.5 nm wavelength (energy 2.43 eV). The other excitation source is provided by a solid state titanium doped sapphire (Ti:Al_2O_3 or Ti:sapph) laser. Ti:sapph is composed of two parts: one is presented as a pumping semi-conductor diode laser, operating at 532 nm, the second part contains a crystal of sapphire (Al_2O_3) doped with titanium ions. Ti:sapph can be tuned at excitation energies ranging from 690 to 1100 nm.

In order to get a spectrally clean laser beam, we used for the argon laser a dielectric filter that transmits in a very narrow range around the excitation wavelength. For the Ti:sapph laser, we used a prism-based monochromator table. The laser power is then stabilized using a liquid crystal based modulator, which acts as a laser power stabilizer. After the power stabilizer we placed a photo-elastic modulator. The purpose of the photo-elastic modulator is to depolarize the laser light. It contains a quartz crystal that vibrates at high frequency, resulting in a time shift in one component of the linearly polarized light, this will change the polarization of the laser light. The timescale of the polarization change is very short compared to the timescale used for spectra acquisition, resulting in a complete depolarized light for Raman measurements. This component plays an important role in magneto-Raman measurements, since a Faraday effect occurs in the filters and optical elements for linearly polarized light when changing the magnetic field. The Faraday effect causes a modulation in the excitation power and thus a change in the intensity of the scattered light.

The last element on the optical table is the fiber coupler. It consists of a threaded ceramic-based ferule connector (FC/PC). The fiber coupler is equipped with screws to displace the connector in X and Y directions, change the angle relative to the incident laser beam, and also to adjust the focal length of the fiber.

3.2.2 The micro magneto-Raman probe

The micro Raman probe is used to perform low temperature Raman spectroscopy on the sample under magnetic fields. The end of the probe hosts a miniaturized optical table (red encircled region in Figure 3.2) that comprises a set of filters and lenses to clean and focalize the laser spot on the sample, and to collect a clean Raman scattering response. The working configuration is the back-scattered geometry, this means that after hitting the sample the light will be scattered at an angle of 180°.

The excitation wavelength is brought to the miniaturized table by a single mode optical fiber with a core diameter of 5μm. After passing through a lens that collimates the beam, the laser passes a dielectric filter called laser line. This filter will be transparent only to wavelengths λ close to λ_{exc} of the excitation laser. This step is important since the electromagnetic wave will interact with the fiber's medium, resulting in a strong parasitic luminescence signal. A dichroic mirror, mounted at 45° (see the miniaturized table in Figure 3.1), acts as a mirror for λ_{exc} and is transparent for other λ. This allows the excitation light to be reflected while the back-scattered light is transmitted. The excitation light is then focused on a $\sim 1\mu$m spot on the sample by a high NA aspherical lens.

The sample is mounted on X-Y-Z piezoelectric stages, that operates at low and room temperatures. This system allows for moving the sample relative to the laser spot with an accuracy of 0.5 μm. X-Y directions are relevant for moving from a spot to the other, and performing Raman mapping of different regions on the sample, while the Z is used to move the sample in the direction parallel to the laser beam, thus tuning the focus on the sample.

After hitting the sample, the light is back scattered, passes the dichroic mirror, and goes through a sharp edge high-pass filter. The high-pass filter allows transmission of wavelengths above the laser wavelength, thus blocking the very intense elastically scattered laser light. The scattered light is then injected in a multi-mode optical fiber (also called collection fiber), with a core diameter of 50 μm, and passed to the spectrometer set up in order to be analyzed.

In order to perform low temperature measurements, the probe is air pumped, and then a helium exchange gas is injected inside the probe, with an inner pressure tuned to 100-200 mbar. The Raman probe is then inserted into the cryostat that is equipped with a reservoir of liquid helium at 4.2 Kelvin.

The cryostat is coupled to an electromagnet (see Figure 3.2) that delivers a static magnetic field from 0 to 30 Tesla. The sample is placed in the probe at the center of the magnetic field, where the magnetic lines are parallel to the light propagation direction. This configuration is called Faraday geometry.

The micro-Raman probe is made of non-magnetic elements. This will insure a stability of the set-up since our measurements are performed in high magnetic field conditions.

3.2.3 The detection setup

In the detecting part of our setup, the scattered light is brought to the spectrometer by the multi-mode fiber. In front of the spectrometer a set of two lenses are used to collimate the beam exiting the fiber holder and to focus it on the slit of the spectrometer. An additional notch filter may be added before the focusing lens if necessary, to block more of the elastically scattered light.
The spectrometer (from Princeton Instruments Inc.) has a focal length of 500 mm. It is equipped with a stage that contains three different gratings, each of them has a specific resolution. The use of a specific grating depends on the needs of the experiment. The light is then sent to a charged coupled device silicon array. The induces charges can be read by the electronics and turned into a digital copy of the light patterns falling on the device. The camera is constantly cooled with liquid nitrogen to improve its sensitivity. Silicon based CCD cameras are suitable for Raman spectroscopy in the visible range, since their quantum efficiency is high.

3.3 Free beam micro magneto Raman setup

In this section we will give a brief description of the experimental set up used for low frequency Raman spectroscopy measurements. The fiber optics micro-Raman set-up has a filtering system based on optical filters with high cut-off frequencies. This approach will not allow access to the low energy part of the spectrum.
The free beam Raman probe has no optical fibers, so rejection of light is based on the triple spectrometer, and the Bragg filters if needed. This allows to get rid of the luminescence caused by the interaction of light with the medium inside the fiber. Moreover, a very narrow line optical filter, called Bragg notch filter, is added in the optical table on top of the micro-Raman probe. The Bragg filter allows a very narrow transmission of the excitation light, and has a very narrow bandwidth (4 nm). This will allow the observation of Raman modes as close as 5 cm^{-1} to the laser line. Two types of Bragg filters are commercially available: The Bragg filters in reflection, where the incoming light is filtered and then reflected by the surface of the filter. The second type of Bragg filters is in transmission, where light is filtered and transmitted through the volume of the filter.

3.4 The magneto-Raman probe

The free beam magneto-Raman probe is depicted in Figure 3.3a. It has an optical table on its top, that comprises a set of lenses and mirrors, but also the 3D volume Bragg filter, used in reflection to clean the laser. The end of the probe is where the sample is placed, on top of X-Y-Z piezoelectric stages (see inset Figure 3.3a). A glass window separates the interior of the probe from the optical table, and acts as an isolating interface from the outer environment.
The excitation light is brought from the laser source to the optical table by a set of mirrors. It is then reflected by the Bragg filter at a given angle and reflected again by the beam splitter which is at an angle 45°. The light is then collimated to the end of the probe until the focusing lens in front of the sample. The back-scattered light goes through the beam splitter and is directed by a mirror to the detection set-up, and finally goes in the triple stage spectrometer (detailed description in the next section) to be analyzed.
All the elements of the probe are non-magnetic to insure a high stability of the magnetic field experiments.

3.5 Triple stage spectrometer

For the low frequency Raman experiments, the detection set-up is made of a triple stage spectrometer (TriVista: Acton/Princeton instruments). It is equipped with two CCD detectors : a CCD camera (Acton/Princeton Instruments) that is cooled with nitrogen and another CCD camera (PiXis/Princeton Instruments) Peltier cooled.
The TriVista spectrometer can be used in single, double and triple configurations. The light beam is passed sequentially through 2 or 3 stages and the gratings coherently move together with very high precision. The TriVista can operates in two different modes: *Additive mode*, which gives high spectral resolution and high linear dispersion. *Subtractive mode*, which gives high stray light rejection. The triple configuration (in the subtractive mode) is shown in Figure 3.3b. In the following we give a more detailed description of how these two modes operate.

3.5.1 Additive mode

In this mode (left panel of Figure 3.4), the gratings on all 3 stages contribute to the light dispersion. Polychromatic light enters the first stage of the instrument through the first slit. The first grating disperses the light. The second slit acts as a bandpass filter, as

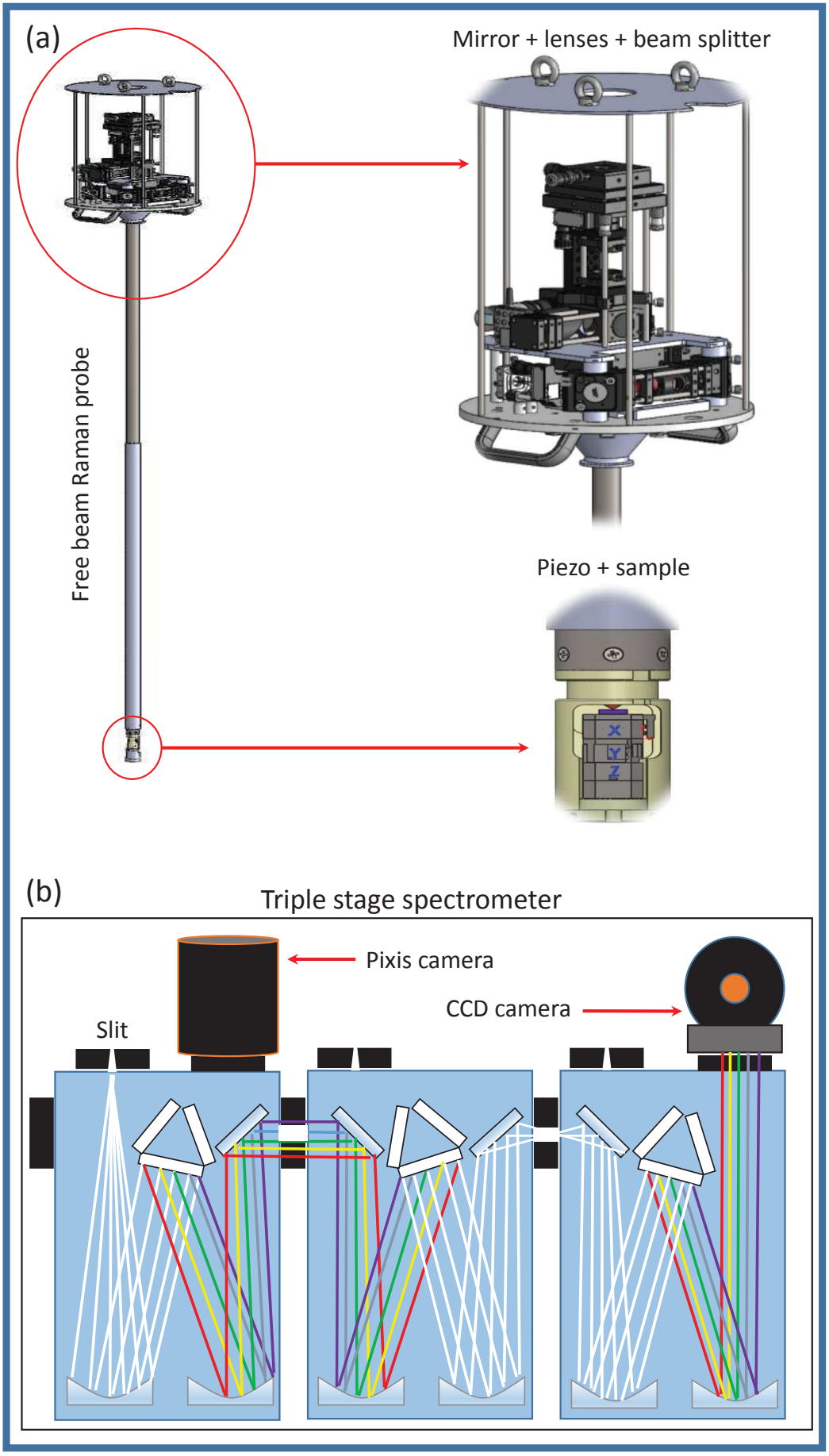

FIGURE 3.3: (a) Free beam probe used for low frequency magneto-Raman measurements. (b) Schematics of the triple stage spectrometer. The triple stagers are in the subtractive mode.

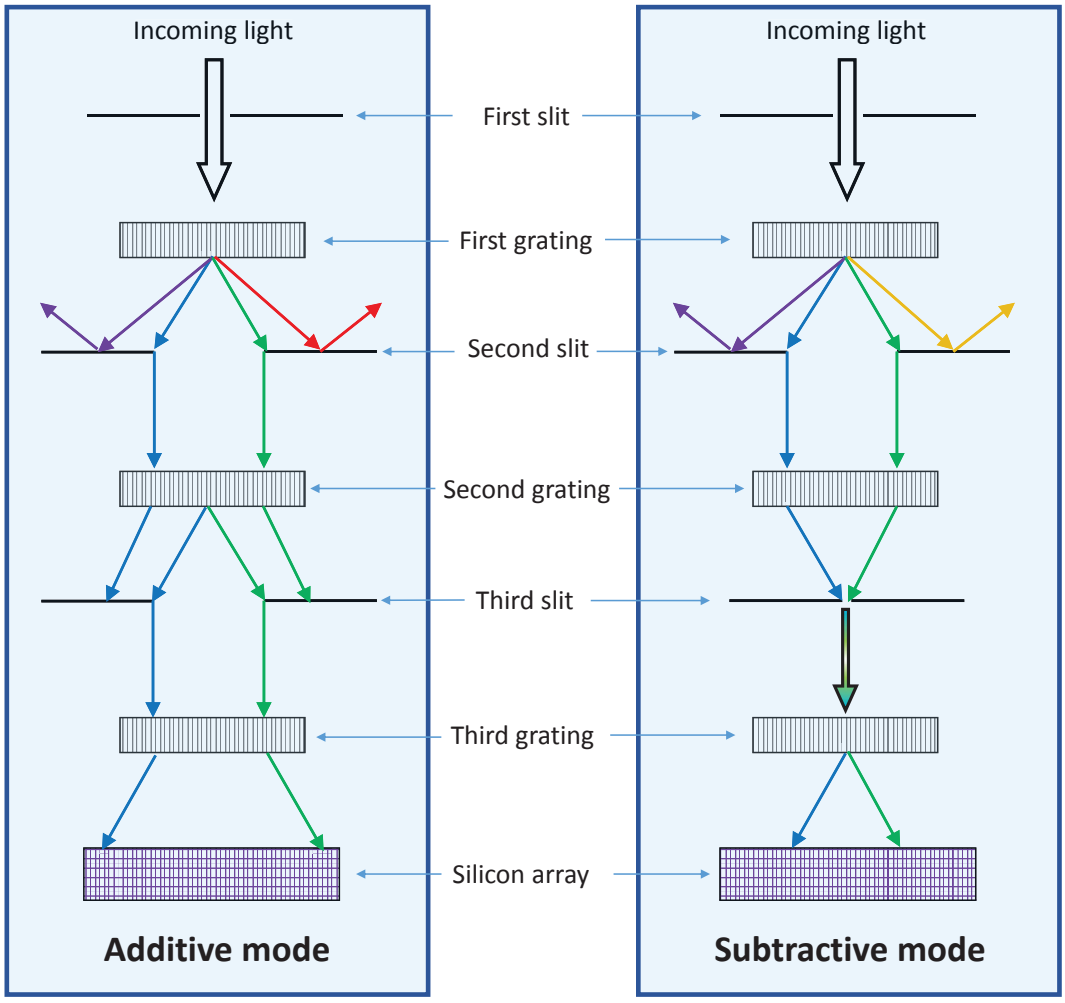

FIGURE 3.4: Schematics of the two working modes for the TriVista spectrometer.

it passes through only a narrow portion of the spectrum which is further dispersed on the second grating. Light passing through the third slit is dispersed for a third time on the third grating and is projected on the silicon detector. The dispersion of the TriVista in additive mode is defined by adding dispersions of each stage. If all three stages have the same gratings and focal lengths, the total dispersion simply equals the dispersion of any single stage. Let us consider as an example a TriVista where the focal length for all three stages equal 500 mm and 1200 g/mm gratings are used on each stage. A single 500 mm stage with 1200 g/mm grating has a nominal linear dispersion of 1.7 nm/mm. In the triple configuration, additive mode linear dispersion of the TriVista is approximately equal to 0.5 nm/mm for the center of the visible spectral range.

3.5.2 Subtractive mode

Excellent stray light rejection with a CCD detector can be achieved when subtractive mode is used. In this mode, the first and the second stages of spectrometer work as a tunable bandpass filter, cutting out a desirable portion of spectrum and projecting it onto the CCD (right panel of Figure 3.4). Poly-chromatic light enters the first stage through the entrance slit and is dispersed by the first grating. The second slit, as in the additive mode, acts as a bandpass filter passing only light with wavelengths between λ_1 and λ_2. However, this time, the second grating recombines all the dispersed light and focuses it into the middle of the third slit, reproducing the polychromatic light limited to the spectral range between wavelengths λ_1 and λ_2. The third grating disperses this light and projects it onto the silicon detector. The second slit in subtractive mode is usually relatively wide opened to allow a desirable spectral range $\lambda_1 - \lambda_2$ to pass through. But the third slit is normally very narrow to insure high spectral resolution. The first and second gratings in subtractive mode must match in groove density and therefore their dispersion actions totally cancel each other. They act as a very sharp bandpass filter allowing for Raman measurements very close to the laser line. In this sense, spectral resolution of the TriVista is entirely defined by the spectral resolution of the third stage depending on the third slit width, the third grating groove density and the third stage focal length.

Chapter 4

Experimental results: Graphene-hBN hetero-structures

4.1 Introduction

One of the recurring ideas in condensed matter physics is to investigate the role of electron-electron interactions, where the single particle picture breaks down, leading to the re-normalization of the electronic ground states. In condensed matter systems, most of the ground states are described in terms of collective excitations, and the single particle picture happens to be a good approximation to describe the electronic properties of some systems. However, this approximation usually fails to account for phenomena such as superconductivity and ferromagnetism.

Monolayer graphene is characterized by its Dirac cone with a vanishing density of states (DOS) when approaching the Dirac point [6]. This linear dispersion causes a breakdown of the insensitivity of the collective excitations to the electron-electron interactions, that holds for conventional semi-conductors with a parabolic dispersion according to Kohn's theorem [198–203]. Moreover, the effects of long range Coulomb interactions are most prominent at the charge neutrality, where the DOS tends to be zero, allowing for a very low screening of charged particles.

The observation of the FQHE in high correlated fermions in two dimensional electron gas systems [68, 204], such as conventional semiconductor hetero-junctions, became a fingerprint of highly correlated electronic states in condensed matter systems [205]. Recently, two groups reported on the experimental observation of the FQHE in high mobility, low doped, suspended graphene [206, 207] and bilayer graphene flakes [208, 209]. Other studies have reported the observation of broken symmetry interaction-induced states in

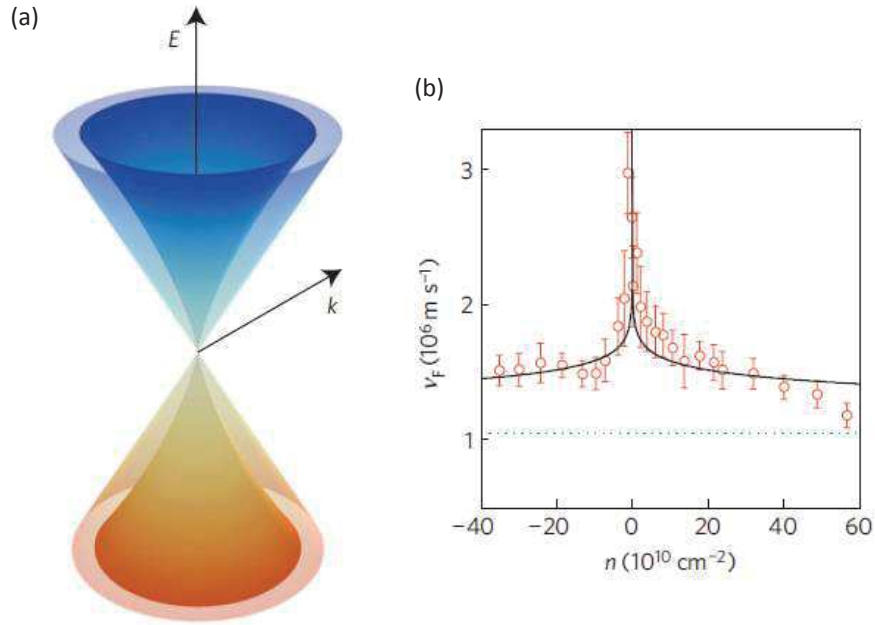

FIGURE 4.1: (a) Schematic illustration of the low energy band dispersion in monolayer graphene, renormalizated by the effect of electron-electron interactions. (b) Experimental data from transport measurements showing a Fermi velocity that peaks at the charge neutrality. Figures are taken from [215].

bilayer, trilayer, and quadri-layer [210–212]. These observations show that high correlation effects are prominent in graphene and multilayer graphene.

Our focus here will be on studying the effects of Coulomb interactions. A qualitative measure of the Coulomb strength in the low energy spectrum of graphene is given by an effective coupling constant that represents the ratio between the Coulomb and the kinetic energies. This latter is related to the dimensionless *fine structure constant* of quantum electrodynamics (QED), which characterizes the strength of the electromagnetic interaction between elementary charged particles in vacuum. While in QED the fine-structure constant has a negligible value $\alpha \sim 1/137$, the coupling strength related to pristine monolayer graphene is re-scaled to $(c/v)\alpha \sim 2$. Hence, in the absence of doping and substrate induced interaction, pristine monolayer graphene cannot be considered as a weakly interacting system [201, 202, 213, 214]. Thus, studying the effects of Coulomb interactions on the band structure of this material is of prime importance.

When graphene is placed on a dielectric medium, for instance on top of a substrate such as SiO_2 or hBN, the corresponding coupling strength is affected by the dielectric tensor of the medium ϵ. For high symmetry crystals, the dielectric tensor can be approximated by a scalar value, and the coupling strength of graphene is given by [201]:

$$\alpha_\epsilon = \left(\frac{c}{v}\right)\left(\frac{\alpha}{\epsilon}\right). \tag{4.1}$$

The experimental evidence for the Coulomb interactions has been challenging to observe. This is due to two main factors: (i) the dielectric screening by the substrate on top of which graphene is placed, (ii) and charge doping that shifts the Fermi level away from the charge neutrality, where the effects due to Coulomb interactions are the most pronounced. Suspended graphene, and graphene encapsulated on hBN offer the possibility to roll out these issues. Experiments performed on these structures show high crystal quality and high carrier mobility in the graphene flakes. The effect of electron-electron interactions in the band structure of graphene has been first evidenced in the absence of magnetic fields [215, 216], and later on in the presence of magnetic fields [126, 166, 217]. One way of estimating the carriers effective mass is to measure the temperature dependence of the quantum oscillations that are usually probed in transport experiments. Recent transport measurements, performed on a gated suspended graphene structure with extremely high mobility [215], show an effective mass for the charge carriers that evolves in a non-linear fashion with respect to $k_F = \sqrt{\pi n}$. This non-linear dependence of the effective mass on k_F can be translated to a dependence of the Fermi velocity on the carriers concentration n. Figure 4.1b, shows a plot of the Fermi velocity as a function of the carriers density n, where a diverging Fermi velocity around the charge neutrality point is observed, thus contradicting the linear dispersion that is usually assumed for graphene flakes on the substrate.

Gonzalez *et al.* studied theoretically the effects of Coulomb interactions in single layer graphene long before its experimental isolation [203]. Following their work, Elias *et al.* [215] considered a re-normalized band structure at low energies, such as the one plotted in Figure 4.1a, when the effects of electron-electron interactions are to be taken into account. The re-normalized bands have a logarithmic divergence of the band velocity at the Dirac point, consistent with the experimental data.

Transport measurements probe the physics of condensed matter systems at the Fermi level, so the re-normalization of the band structure is observable only at very low energies (of the order of $E_F \sim$ meV). However, as we will show in the following, the effects of electron-electron interactions are seen for a larger energy scale when probing the inter-Landau level transitions under strong magnetic fields using Raman scattering spectroscopy.

Suspended graphene structures present a disadvantage for practical applications. For the observation of high correlation effects, a proper choice of a substrate with low doping and high quality surface is of prime importance to study the intrinsic properties of graphene and multilayer graphene. Owing to similar crystal structure as graphene, hexagonal boron nitride (hBN) is a substrate of choice in the study of low energy excitations in graphene. High charge carriers mobility and the experimental observation of the FQHE on graphene deposited on hBN substrate [218, 219] are strong proofs to the superior quality of graphene-hBN hetero-structures with respect to conventional graphene

flakes on SiO_2/Si substrate. As we will show in the following, all studied samples in our experiments present very low doping (their Fermi energies correspond to $\sim$ 60 meV) which allows the observation of the band velocity re-normalization on the band structure of graphene (see Figure 4.1).
The investigation of many body effects in graphene based structures should not be limited to transport techniques. Notably, ARPES measurements, a well-adapted surface probe allowing to trace electronic bands in solids, is a method of choice to probe correlation effects such as electron-electron and to electron-phonon interactions [220–222]. On the other hand, this technique cannot be implemented with an applied magnetic field which makes it impossible to study graphene based systems in the QHE regime, and reveal interaction effects among highly degenerated Landau levels. To overcome this difficulty, we use magneto-Raman scattering techniques to study the effects of electron-electron interactions in graphene in the QHE regime.

4.2 Monolayer graphene/hexagonal boron nitride

First we will discuss the experimental results obtained from the magneto-Raman study of G-hBN hetero-structures. Two G-hBN samples have been investigated with magneto-Raman spectroscopy: One sample was provided by the group of *Prof. Andre Geim* from Manchester University (we will refer to this sample as A), while the second sample (labeled B) was provided by the group of *Prof. Philip Kim* from Columbia University. Magneto-Raman measurements were performed by using a superconducting coil up to 14 T (in the case of sample B), or a resistive magnet that delivers a continuous magnetic field up to 29 T (case of sample A).

4.2.1 Raman characterization in the absence of magnetic field

Figure 4.2(a,b) shows optical microscope images of samples A and B, respectively. A schematic presentation of sample A is shown in Figure 4.2c, where we have three different structures on: graphene directly on SiO_2, graphene on hBN (G-hBN), and graphene encapsulated in hBN (hBN-G-hBN).
We first characterize the two samples at low temperature in the absence of magnetic fields. Figure 4.2d shows a falsed color map of the Raman scattered intensity at the 2D band energy from sample A, where the 2D band is the most pronounced at the G-SiO_2 locations, is less intense at G-hBN locations, and very weak at hBN-G-hBN locations. This contrast in the intensity allows a Raman imaging of the three different structures on the sample. Three corresponding Raman scattering spectra from these locations are shown in Figure 4.3a, while Figure 4.3b shows a Raman spectrum from sample B. For

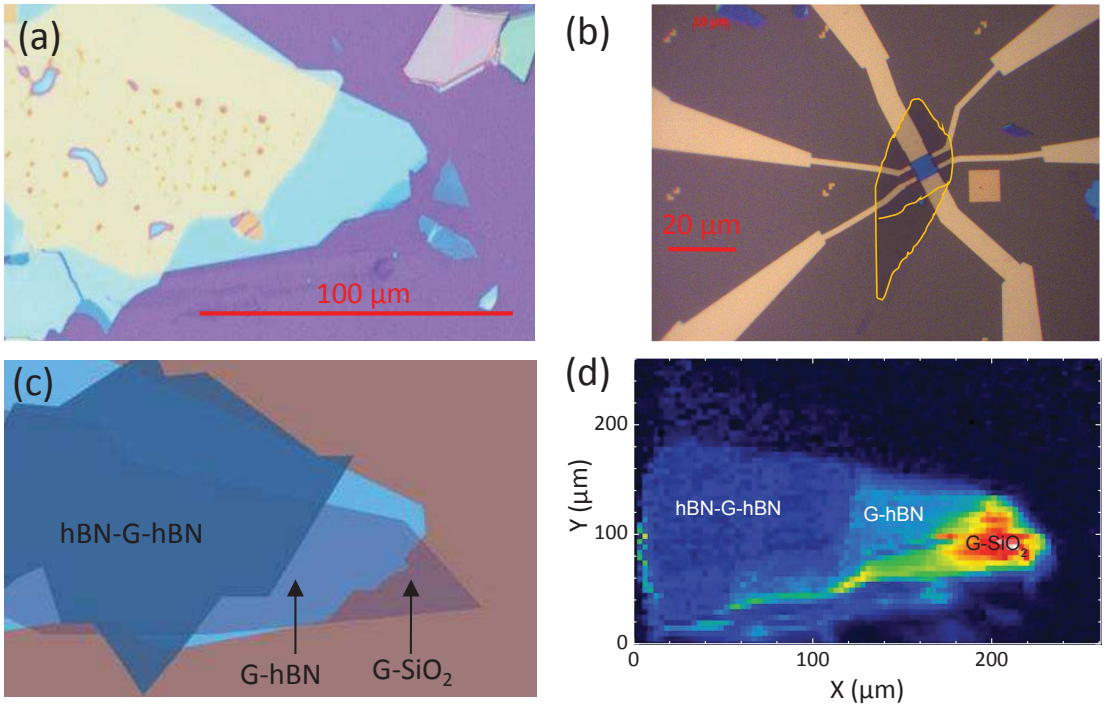

FIGURE 4.2: (a,b) Optical microscope image of sample A and B, respectively. (c) Schematics of sample A showing different locations with graphene on SiO_2, graphene on hBN and graphene encapsulated in hBN. (d) Falsed color spatial map of the scattered intensity at the 2D band energy from sample A.

both samples, a single Lorentzian peak is observed at 1370 cm^{-1}, which corresponds to the Raman-active E_{2g} mode in BN with a hexagonal symmetry [223]. The G band of graphene is observed at 1584 cm^{-1} with a full width at half maximum (FWHM) as large as 16 cm^{-1} in G-hBN locations. Such a FWHM for the G band is an indication of moderate doping for the graphene on hBN [152], hence the two samples are close to charge neutrality.

Figure 4.3c is a zoom on the 2D band of G-SiO_2 and G-hBN from sample A. On G-hBN location, the 2D band is observed at $\sim$ 2690 cm^{-1} with a FWHM of $\sim$ 20 cm^{-1}. As we discussed in Chapter 2, the 2D band has a FWHM which depends on the rotational angle of the graphene sheet with respect to the hBN substrate, or when on top of another graphene layer with a twist angle. The value of the FWHM, observed on our samples is representative of non-aligned G-hBN structures [134].

The comparison of the Raman spectra shows a clear background formation where the graphene layer lays are encapsulated on hBN. This fluctuating background is moderate on the G-hBN structure, but became 5 times higher in the encapsulated graphene regions on sample A (see Figure 4.3a). The origin of this background might be related to the wet transfer fabrication technique that gives such encapsulated hetero-structures (see Annex 7). Indeed, the polymer compound that is used to transfer each flake on top of the other is shown to contaminate the interfaces between the flakes. These contaminations have

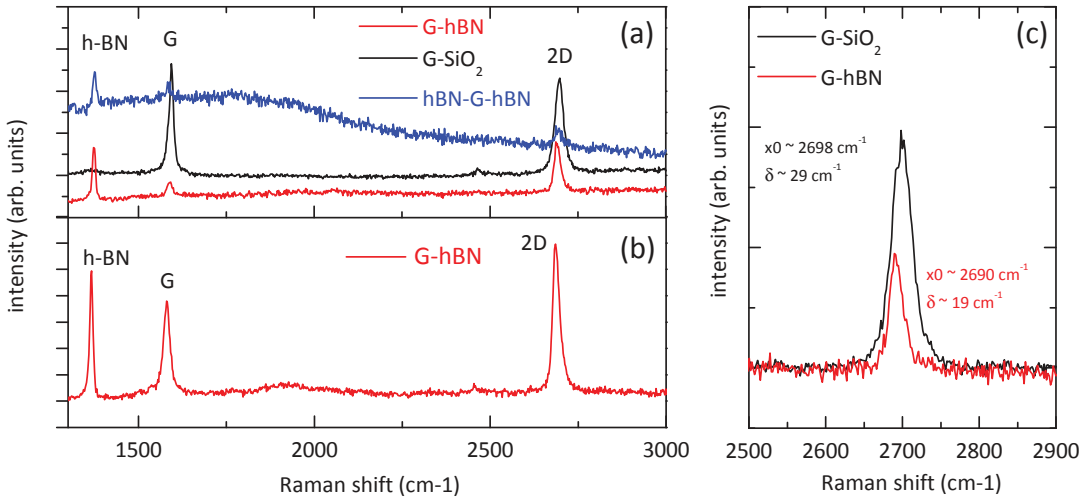

FIGURE 4.3: Representative Raman scattering spectra from sample A, measured on graphene on SiO_2 (black), on graphene on hBN (red spectrum) and on graphene encapsulated in hBN (blue). (b) Representative Raman scattering spectrum of graphene encapsulated in hBN from sample B. (c) 2D band from sample A on a G-SiO_2 location (black curve), and on G-hBN location (red curve)

tendency to group together to form bubbles, most of which have a sub-micron size (see dark spots in Figure 4.2a). Such background makes it very difficult to perform Raman scattering measurements on the encapsulated locations. In the following we will focus our studies on the graphene on top of hBN regions where the background is very moderate.

4.2.2 Experimental results: magneto-phonon resonance

The inter-Landau level transitions are hard to observe in graphene-based systems. Their observation in Raman scattering experiments strongly depends on the quality of the samples, the background in the Raman signal, and the mobility of the charge carriers. On the other hand, the chances to observe the magneto-phonon resonance (MPR) in graphene-based samples is higher. The study of the MPR in graphene is used as a tool to probe the Landau levels spectroscopy of the electronic excitations at the optical phonon energy. This approach allows the determination of the low energy band structure in the system and the number of graphene stacked layers [224]. In the following we start by presenting the experimental results of the MPR in our G-hBN samples, and then move to discuss the experimental results on the observed electronic excitations in the next section.

Figure 4.4a,b shows magneto-Raman scattering spectra from both samples. The energy scale is in the range of the G band, and spectra are shown for different values of

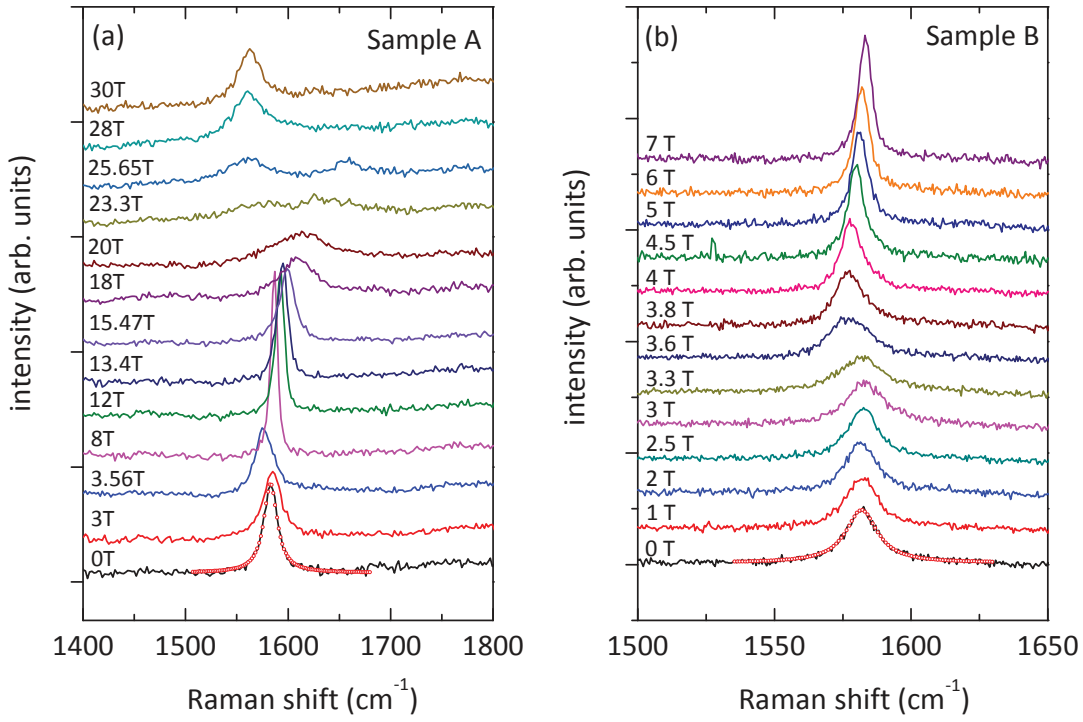

FIGURE 4.4: (a,b) Magneto-Raman scattering spectra in the G band energy range from sample A and B, respectively. In both samples, the G band exhibits strong MPR. The red dots indicate Lorentzian fits of the G band.

the magnetic field from 0 to 30 T. Notice how the G band undergoes strong shifts and broadening when the magnetic field changes.

In order to get a better visual of the observed behavior, the magnetic field evolution of the G band from the two samples A and B is presented in Figure 4.5(a,b) respectively, in the form of false color maps of the Raman scattered intensity in the optical phonon range of energy as a function of $\sqrt{B}$. In these two plots, one can appreciate the oscillations of the G band feature at particular values of the magnetic field (indicated by white arrows), which are characteristic of the MPR. As has been discussed in Chapter 2, the MPR is due to the resonant coupling between the E_{2g} phonon and the discrete $\Delta|n| = \pm 1$ inter-Landau level transitions in monolayer and N-LG [192, 194, 196], or the inter-Landau bands in bulk graphite [160].

In the single particle approximation, the energy dispersion of the Landau levels in monolayer graphene is given by (see Chapter 1 for further details)

$$E_n = \pm v\sqrt{2e\hbar B|n|}, \tag{4.2}$$

where +(-) labels the electron (hole) levels, and v is the band velocity, which represent the fitting parameter for the coupling of inter-Landau level transitions with the optical phonon. A transition from a filled m level to an empty n level has an energy: $L_{m,n} = E_n - E_m$. The $\Delta|n| = \pm 1$ transitions have the same symmetry as the E_{2g}

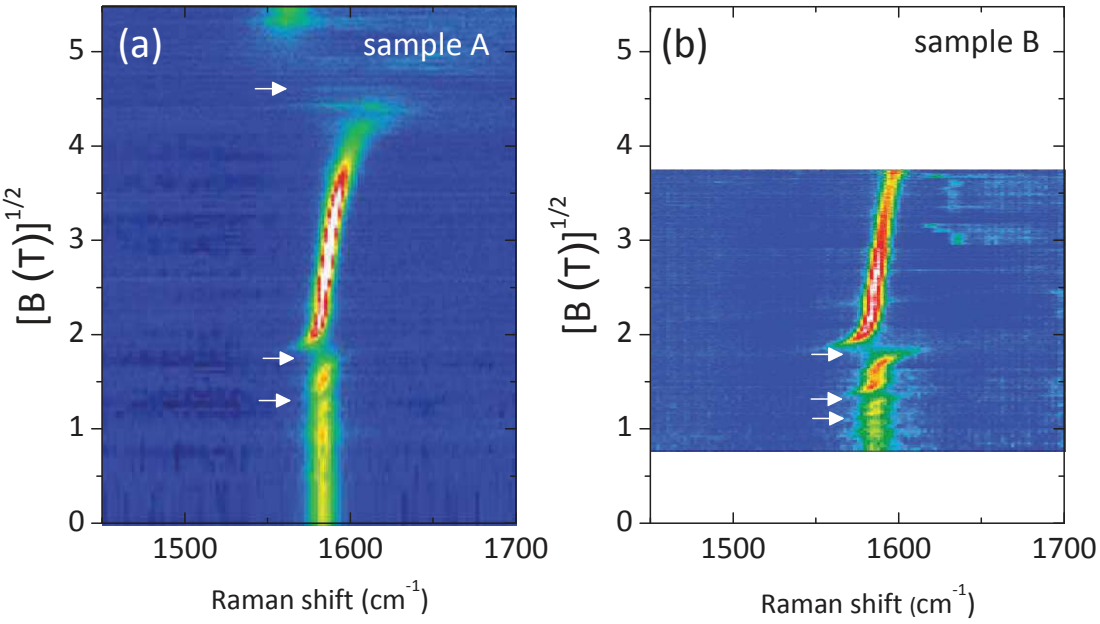

FIGURE 4.5: (a,b) False color maps of the Raman scattered intensity as a function of the square root of the magnetic field in the G band range of energy for the G-hBN locations from samples A and B, respectively.

optical phonon at the Γ point, they are known to be responsible of the observed MPR in graphene based systems [158].

Figure 4.6(a,b) shows the results of the MPR observed in our measurements. Single Lorentzian fits are used to extract the evolution of the G band position and its FWHM. These values are plotted as a function of the $\sqrt{B}$ for samples A and B, respectively. Starting from their unperturbed values ($\sim$ 1584 cm^{-1} for its energy and $\sim$ 18 cm^{-1} for its linewidth), the energy and line-width of the G band show clear oscillations when changing the magnetic field. These oscillations are observed for both samples, and their magnitude increases with increasing magnetic field. The most pronounced oscillation is observed for sample A around $\sim$ 22 T.

In a series of previous MPR studies on multilayer epitaxial graphene [193], and graphene locations on the surface of bulk graphite [164, 169, 225, 226], a single value of the band velocity has been used for $\Delta|n| = \pm 1$ inter-Landau level transitions at the phonon energy. In our study, this approach is no longer valid.

Figure 4.7 plots the Fermi velocity values for resonant transitions, that are well observed in both samples, as a function of the logarithm of the magnetic field normalized to B_0= 1 T. The choice of the logarithmic scale will become clearer afterwards. Indeed, our data for both G-hBN samples show resonant magnetic fields, with most pronounced resonances at: $B_0 \sim 22T, B_1$ (observed only in sample A), $\sim 3.3T$ and $B_3 \sim 1.8T$. In order to identify the inter-Landau level transitions that are responsible for the oscillations at these resonant magnetic fields, we use Eq. 4.2. At the G

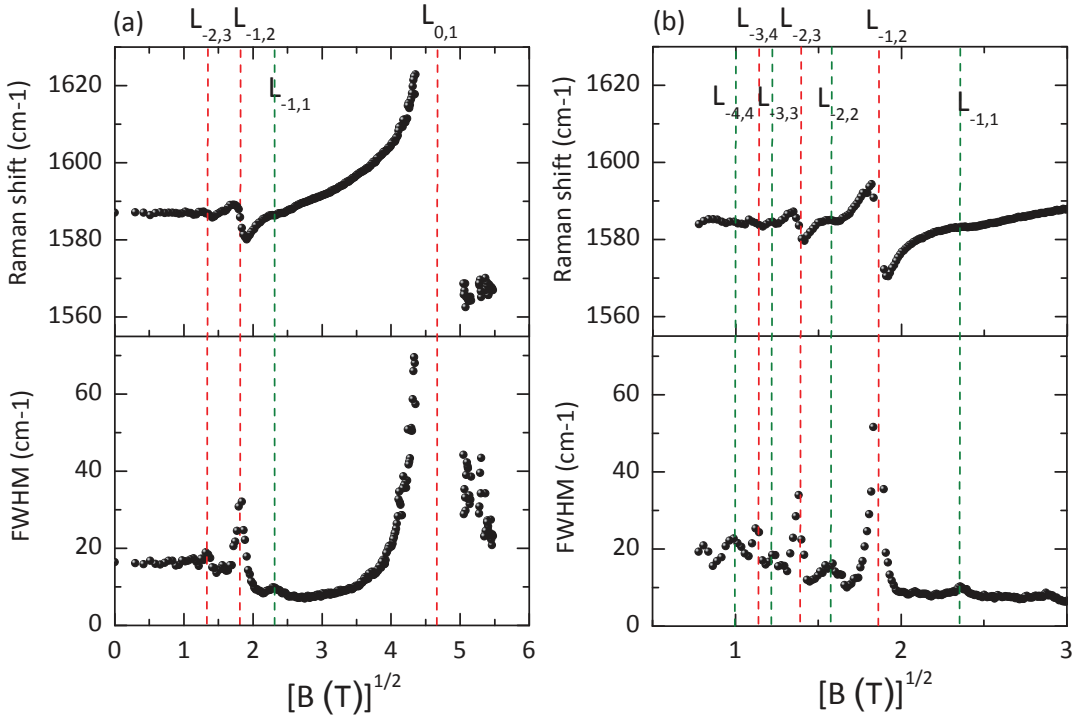

FIGURE 4.6: (a,b) Energy position (upper panels) and FWHM (lower panels) for samples A and B respectively, as a function of the square root of the magnetic field, obtained from a single Lorentzian fit of the G band feature. The vertical red dashed lines mark the observed resonant magnetic fields for the $\Delta|n| = \pm 1$ transitions, while the green dashed lines indicate the weak coupling of the $\Delta|n| = 0$ transitions with the G band.

band energy, these values of the magnetic field correspond to the resonance of the G band with $L_{0(-1),1(0)}, L_{-1(-2),2(1)}$ and $L_{-2(-3),3(2)}$, characterized by $v \sim 1.15 \times 10^6 m/s$, $v \sim 1.24 \times 10^6 m/s$, and $v \sim 1.28 \times 10^6 m/s$, respectively.

A key information is deduced from Figure 4.7: different band velocities are attributed to the $\Delta|n| = \pm 1$ transitions when tuned to the G band energy. This observation is in clear contrast with the Landau level dispersion in Eq.4.2, derived in the frame of the single particle picture. As we will show in the theoretical modeling section, such an effect stems from the strong electron-electron interactions in graphene.

The oscillations of the G band line-width are more pronounced compared to the oscillations of its energy. In Figure 4.6, a series of oscillations in the G band line-width in sample B and another oscillation in sample A do not correspond to the coupling with $\Delta|n| = \pm 1$ transitions. These oscillations have relatively weak magnitudes compared to the resonant coupling with $\Delta|n| = \pm 1$ transitions (green lines in Figure 4.6a,b). By matching their energies with the E_{2g} optical phonon, we attribute these oscillations to the G band coupling with inter-Landau level transitions that obey selection rules $\Delta|n| = 0$. In both samples, we identify the coupling of the G band with $L_{-1,1}$ transition at $B \sim 5.3T$ ($\sqrt{B} \sim 2.31T^{1/2}$), which correspond to a Fermi velocity $v \sim 1.18 \times 10^6 m/s$. Three additional couplings are observed in sample B at $B \sim 2.46T$, $B \sim 1.47T$, and

$B \sim 1T$. They correspond to transitions $L_{-2,2}$, $L_{-3,3}$, and $L_{-4,4}$, with Fermi velocities $v \sim 1.22 \times 10^6 m/s$, $v \sim 1.29 \times 10^6 m/s$, and $v \sim 1.35 \times 10^6 m/s$, respectively.

Thus, we reveal another surprising result in our studies, since this coupling is forbidden for symmetry reasons [159, 194], as has been discussed in Chapter 2. However, we note that previous magneto-Raman studies performed on graphene-like locations on the surface of bulk graphite [164, 169, 226], and low fields magneto-Raman study of high mobility graphene flake encapsulated on hBN [197] reported the observation of an unexpected coupling of the G band with the $\Delta|n| = 0$ inter-landau level transitions.

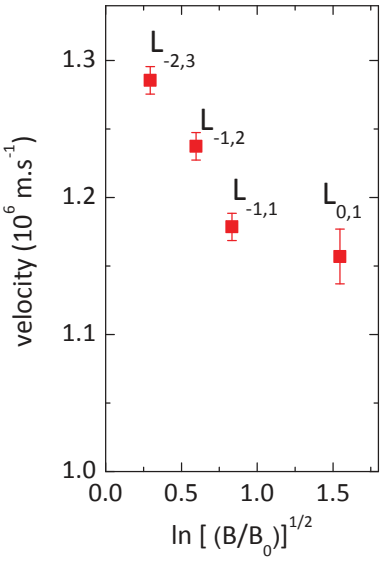

FIGURE 4.7: Values of the band velocity deduced from the analysis of MPR on G-hBN (red squares). The corresponding inter-Landau level transitions are indicated. We plot these values as a function of the magnetic field in logarithmic scale.

Magneto-Raman experiments on graphene domains on the surface of bulk graphite show a clear coupling of the E_{2g} phonon with the symmetric transitions $L_{-3,3}$, $L_{-2,2}$, and $L_{-1,1}$ [164]. Notably, unlike the MPR involving the $\Delta|n| = \pm 1$ transitions, this resonant coupling is less pronounced when the magnetic field is increased. Since the observation of this forbidden coupling is not limited to graphene flakes on the surface of graphite [197], we assume that this effect is an intrinsic behavior of electronic excitations in graphene. As long as the studied samples are of good quality, one might observe this forbidden resonance of the G band with the $\Delta|n| = 0$ inter-landau level transitions.

It is not clear why such a coupling is observed in graphene. However, the decrease in the coupling of the G band with the $\Delta|n| = 0$ transitions as a function of the strength of the magnetic field makes us speculate that the mechanism behind this resonance originates from the mixing of wave functions of neighboring Landau levels. Such mixing of Landau levels is lifted by strong applied magnetic fields [169, 197, 227].

4.2.3 Experimental results: inter-Landau level transitions in G-hBN

In order to favor the observation of the symmetric inter-Landau level transitions ($\Delta|n| = 0$) in the Raman scattering spectra of graphene, we performed co-circular polarized magneto-Raman scattering measurements on G-hBN (sample B) up to 14 Tesla, using

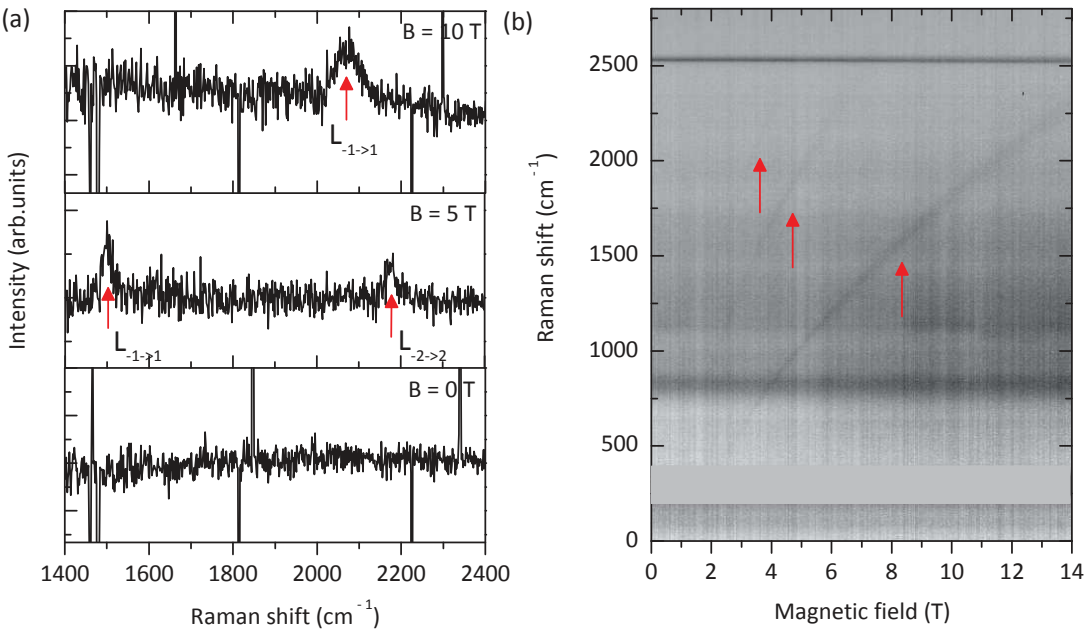

FIGURE 4.8: (a) Magneto-Raman spectra showing electronic excitations at different values of B. (b) Grey scale map showing the $L_{-1,1}$, $L_{-2,2}$, and $L_{-3,3}$ inter-Landau level transitions in the G-hBN sample B.

the superconducting coil. In this configuration, the G band is not active since it is cross-circularly polarized [160], as has been discussed in Chapter 2.

Figure 4.8a shows three different Raman spectra at 0T, 5T, and 10 T. Magnetic-dependent features, that we attribute to $L_{-1,1}$ and $L_{-2,2}$, are observed. The associated grey-scale map of the magneto-Raman scattered intensity (Figure 4.8b) shows the $\sqrt{B}$ dispersion of at least three excitations with the magnetic field, characteristic of massless Dirac Fermions. In our G-hBN sample and the two other comparative samples, the $L_{-1,1}$ transition starts to be visible at $B \sim 2.5$ T, corresponding to an onset energy $E_{ons} \sim 1000$ cm^{-1}. The upper limit for the Fermi energy is then pinned at $E_F = E_{ons}/2 \sim 60$meV, which confirms a relatively low charge doping in all these graphene-based systems, relevant to the observation of the band velocity re-normalization around the charge neutrality point [215].

Figure 4.9a shows the Landau level dispersion of monolayer graphene, plotted with a single value of the band velocity. The corresponding $\Delta|n| = 0$ transitions are plotted in Figure 4.9b. There is no chance to fit the observed transitions with a single value of the band velocity. This approach fails for two main reasons: first of all, and similar to the analysis of the MPR, the higher the value of the Landau level index, the higher the corresponding value of the band velocity associated with each transition. Then, for a fixed Landau level index, there is a clear deviation from the experimental points when changing the magnetic field for the associated band velocity of each transition. This is especially seen for the $L_{-1,1}$ transition, where a clear departure from the experimental

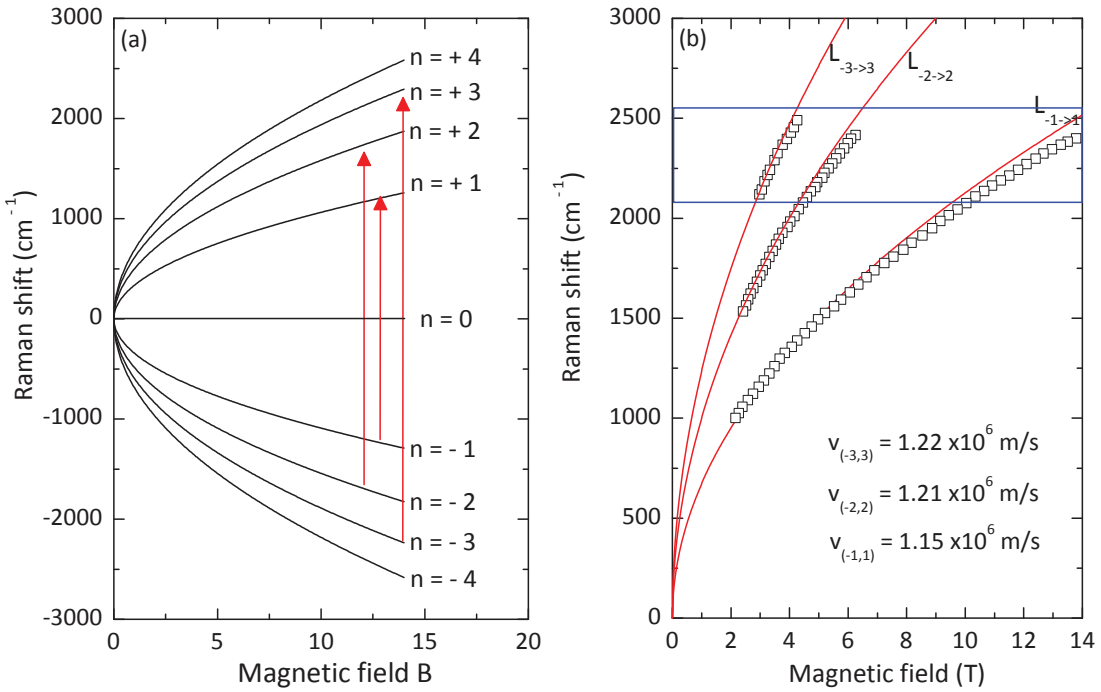

FIGURE 4.9: (a) Landau levels dispersion for monolayer graphene. The red vertical arrows indicate symmetric transitions that are Raman-active. (b) Plot of the $L_{-1,1}$, $L_{-2,2}$, and $L_{-3,3}$ inter-Landau level transitions using different values of the band velocity. The blue box indicate a strong deviation of the data from the single particle model.

curve is seen when the magnetic field increases (blue boxed region in Figure 4.9b). Two main conclusions are deduced from this analysis: (i) the band velocity is a function of the Landau level index. (ii) The band velocity associated with each Landau level index changes as a function of the magnetic field. These observations represent a clear deviation from the single particle picture, in which the band velocity is independent of the Landau level index and of the value of the magnetic field.

The coupling strength associated with the Coulomb interaction in graphene depends strongly on the dielectric function ϵ of the surrounding medium, as we discussed in the beginning of this section. The deviation from the single particle picture is expected to be more pronounced in the absence of screening, leading to enhanced Coulomb interactions. This has been evidenced from magneto-Raman scattering measurements on suspended monolayer graphene [31]. On the other hand, a strong screening from the surrounding medium (such as metallic substrates) where the dielectric constant is large, leads to weak Coulomb interactions (i.e., graphene locations on the surface of bulk graphite).

In order to show the effects of the substrate on the strength of the electron-electron interactions in graphene, and thus on the Landau level dispersion with magnetic fields, we compare our G-hBN results with two different sets of magneto-Raman scattering data. The first set of data are obtained from a suspended graphene flake (G-S) [31], while the second set of data is from graphene locations on the surface of bulk graphite

(G-Gr) [164, 165].

Figure 4.10 compares the inter-Landau level transitions observed on each graphene specimen. The $L_{-1,1}$, $L_{-2,2}$ are well observed in all systems. We note that G-Gr sample shows much richer spectra, a large number of symmetric $\Delta|n| = 0$ transitions (at least up to n = 5) are observed. The weakly allowed $\Delta|n| = \pm 1$ transitions [158, 159] are also well seen in G-Gr in a wide range of magnetic fields [164, 165]. However, since $L_{-1,1}$ and $L_{-2,2}$ are present in all studied systems, we will focus our analysis on these two transitions.

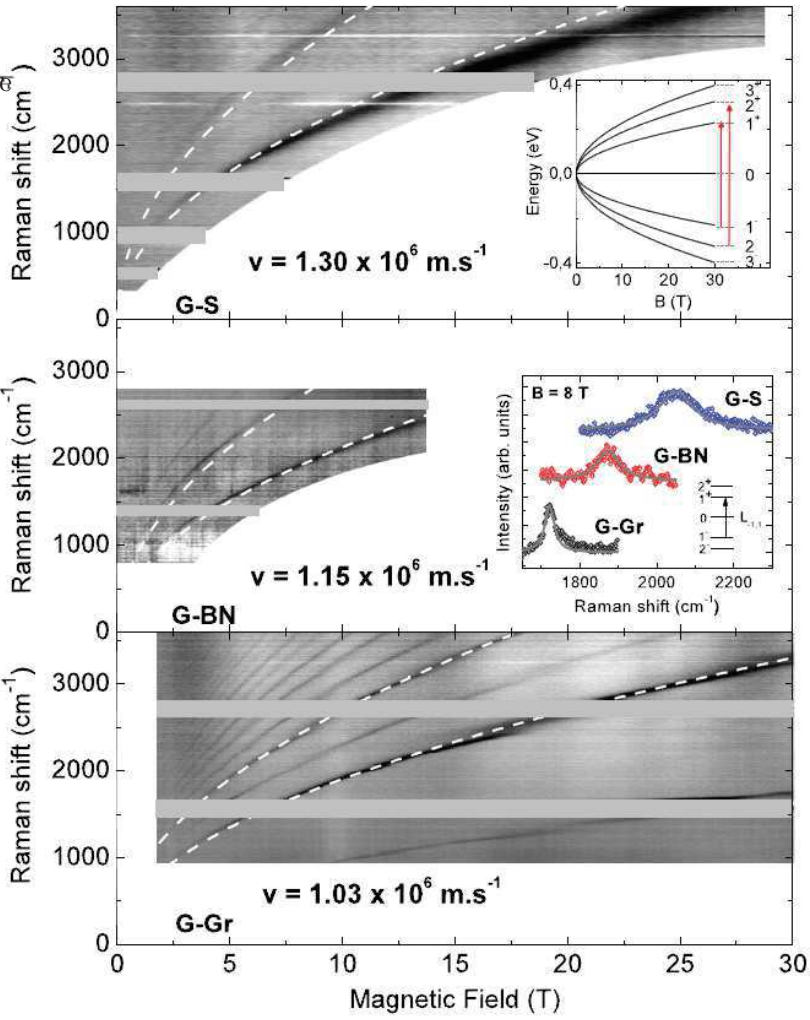

FIGURE 4.10: Landau levels spectroscopy of three different graphene based systems. Graphene suspended (upper panel), graphene on hBN (middle panel), and graphene on graphite (lower panel).

Keeping in mind that the band velocity possibly depends on both the magnetic field value and on the Landau level index, as was evidenced by our data analysis from the G-hBN sample, we proceed by assigning a mean value of the band velocity that best fits the $L_{-1,1}$ excitation in each graphene system. Surprisingly, in order to fit the same $L_{-1,1}$ transition for each graphene specimen, we were obliged to use completely different values of the band velocity. We used $v = 1.3 \times 10^6$m/s for G-S (upper panel), $v = 1.15 \times 10^6$m/s for G-hBN (middle panel), and $v = 1.03 \times 10^6$m/s for G-Gr (lower panel). Different mean values of the band velocities for each graphene specimen are directly visualized in

the inset of Figure 4.10, where at a fixed value of the magnetic field, the $L_{-1,1}$ transition appears at clearly different energies.
To summarize our results, we can say that the band velocity in monolayer graphene is strongly dependent on three major factors:

1 - The dielectric environment, characterized by its dielectric constant ϵ

2 - The strength of the magnetic field

3 - The Landau level index

4.2.4 Theoretical modeling: including electron-electron interactions in graphene

The theoretical calculations shown in this Chapter 4 have been done by *Dr. Denis Basko*. He calculated the corrections to the band velocity in monolayer graphene in the presence of magnetic fields [166]. In the single particle model, the band velocity should not depend on the parameters that we mentioned above. So in order to account for the observed discrepancies with the single particle model, one should consider the effects of many body interactions (i.e., electron-electron interactions).
To do so, we will adopt the approach of Gonzalez *et al.* [203], in which Coulomb interactions among electrons should cause a logarithmic divergent re-normalization of the band velocity in un-doped single layer graphene. We start with the case of zero magnetic field by considering a simple correction to the band velocity using perturbation theory. In this approach, we expand the band velocity at the first order in the effective fine-structure constant $\alpha_\epsilon = \left(\frac{c}{v}\right)\left(\frac{\alpha}{\epsilon}\right)$. The corrections to the band velocity are then:

$$\frac{v}{v_0} = 1 - \frac{\alpha_\epsilon}{4} \ln \frac{|E|}{W}, \quad v = v_0 - \frac{\alpha c}{4\epsilon} \ln \frac{|E|}{W}, \tag{4.3}$$

where E is the electron energy that is counted from the Dirac point. v_0 is the bare velocity for the non-interacting system, and W is the high energy cut-off that is of the order of the electronic bandwidth (i.e., few eV). The dielectric constant ϵ is that of the surrounding medium for the suspended and encapsulated graphene, while α is the fine-structure constant. Consequently, formula 4.3 tells us that the band velocity is decreasing logarithmically when the band energy increases.
Let us now consider the effect of magnetic field on the above formula. In the presence of a uniform magnetic field, the band structure of graphene is quantized into Landau levels, and this effect needs to be taken into account in computing the band velocity re-normalization by replacing the energy bands with the corresponding inter-Landau level transition $\hbar\omega_{-n,m}$ [200]. Following this procedure, it is legitimate to predict a band

velocity that decreases with higher energy inter-Landau level transitions (i.e., higher n). However, as we will show from our experimental observations, the opposite trend is observed. Transitions with higher Landau level index are associated with higher band velocities.

To account for this discrepancy between the results of Gonzalez *et al.* and our experimental results, we used first order perturbation theory (FOPT) to derive an expression for the band velocity re-normalization in the presence of magnetic fields [166].

If the energy of the n^{th} symmetric inter-Landau level transition is given as $\hbar\omega_{-n,n}$, we give the corrections to the band velocity by:

$$\upsilon_n = \frac{\omega_{-n,n} l_B}{\sqrt{8n}} = \upsilon_0 + \frac{\alpha c}{4\epsilon}\left(\mathcal{L} - \ln\frac{l_{B_0}}{l_B}\right) + \frac{\alpha c}{4\epsilon} C_n. \tag{4.4}$$

Formula 4.4 shows clearly that, in the presence of magnetic fields, the band velocity evolves as: $\ln\frac{l_B}{l_{B_0}} = \ln\sqrt{\frac{B_0}{B}}$. Here, l_B is the magnetic length. The quantity $\mathcal{L} = \ln\frac{W l_{B_0}}{\hbar\upsilon_0}$, together with the logarithmic term, represent the corrections to the self-energy due to interactions with states deep in the valence band, that are not sensitive to the Landau quantization (n independent). However, the $C_n = \{C_1 = -0.398, C_2 = -0.197\}$ are numerical coefficients that depends on the Landau level index. These coefficients originate from two contributions: (i) residual corrections to the self energy from interaction with states near the Fermi level, where the Landau quantization is relevant. (ii) Vertex corrections or the so-called excitonic effects between the excited electrons and the holes left in the initial Landau level.

In his seminal paper [198], W. Kohn studied the many body effects in conventional semiconductors with parabolic dispersion of their electronic bands. He derived a theorem in which he stated that the cyclotron resonance, which characterizes the optical transitions ($\Delta k \sim 0$) of quasi-particles in magnetic fields, has a frequency independent on the many body effects such as electron-electron interactions. In the corresponding Hamiltonian, the excitonic effects and the exchange interaction terms are shown to cancel each other. The Kohn's theorem, however, is violated in graphene, which has low energy linear dispersion of its electronic bands. The cyclotron resonance has a $\sqrt{B}$-dependence, this means that departure from the single particle picture is seen even for optical-like transitions with $\Delta k \sim 0$. Hence many body effects do contribute to its magneto-optical response [217].

The C_n in Eq. 4.4 are negative terms such as: $|C_1| > |C_2|$. They will invert the trend of Eq 4.3 which suggests that higher transition energies are associated with smaller band velocities. Consequently, $L_{-2,2}$ transition has bigger band velocity compared to $L_{-1,1}$ transition.

The formula in 4.4 shows a linear dependence of the band velocity on the quantity $\ln\frac{l_B}{l_{B_0}}$. In a non-interacting system, the band velocity displays a horizontal line as a function of

the magnetic field with a zero slope. In our case, the slopes of the re-normalized band velocities are given by the parameter $\alpha c/4\epsilon$. These slope vary according to the value of the dielectric constant of each surrounding medium ϵ.

Consequently, from equation 4.4 we are able to account, qualitatively, for the following: (i) When ϵ is large, the slope ($\propto 1/\epsilon$) is small. This means that the effects of Coulomb interactions are small for media with a large dielectric constant, and strong for media with small dielectric constant. This gives a large slope for band velocity for the G-S ($\epsilon = 1$), and a smaller slope for G-hBN ($\epsilon \approx 5$), G-Gr systems, respectively. Graphite on the other hand is a metallic substrate, thus can be viewed as medium with a large effective dielectric constant (slope close to zero), which gives an even smaller effect of the Coulomb interactions. (ii) For the same dielectric constant ϵ (graphene on top of a given substrate) and the same value of the magnetic field, the band velocity associated with the transition $L_{-2,2}$ (v_2) is bigger than the band velocity associated with the transition $L_{-1,1}$ (v_1) due to $C_2 > C_1$ in Eq. 4.4. (iii) According to equation 4.4, the difference in the values of the band velocities at a fixed magnetic field value is given as:

$$\delta v_{21} = v_2 - v_1 = \frac{\alpha c}{4\epsilon}(C_2 - C_1). \tag{4.5}$$

This means the bigger the dielectric constant ϵ, the smaller the dependence of the band velocity on the Landau level index n.

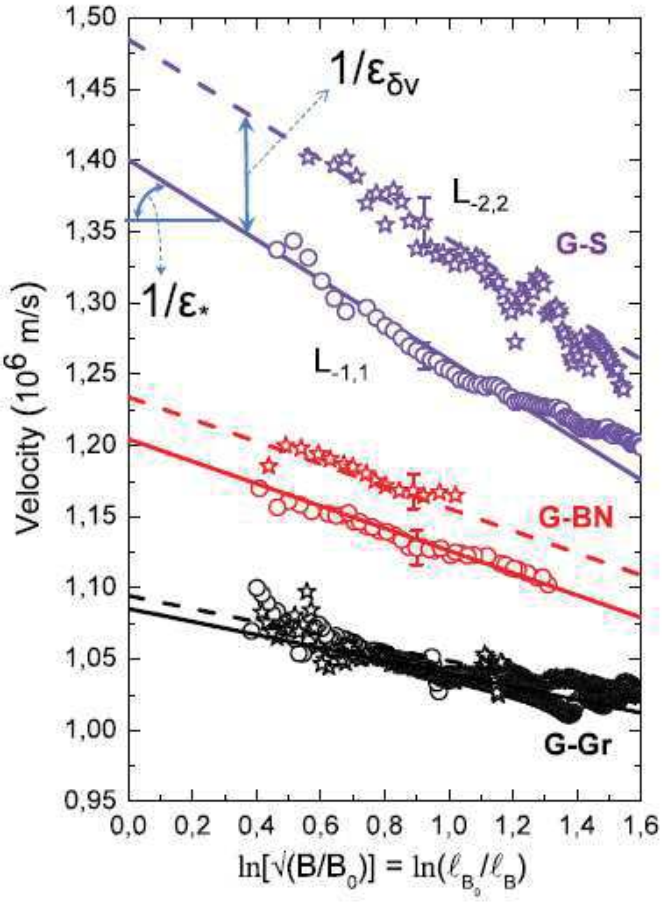

FIGURE 4.11: Band velocities evolution associated with $L_{-1,1}$ and $L_{-2,2}$. The experimental data (theoretical modeling) are shown for $L_{-1,1}$ as open circles (solid lines) and for $L_{-2,2}$ as open stars (dashed lines) for G-S, G-hBN, and G-Gr samples. The dielectric constants are ϵ=3.9, 7, 12 for G-S, G-hBN, and G-Gr, respectively. The figure is taken from [166]

Figure 4.11 summarizes the theoretical model, that is described by Eq. 4.4, along with

the experimental values of the band velocity, extracted from fitting the observed transitions using Lorentzian fits. For each graphene-based system, the evolution of the extracted band velocities v_n^{exp} is plotted as a function of $\ln\sqrt{\frac{B_0}{B}}$. Our model follows the experimental observations, since the slopes of the band velocities, and the dependence on the Landau level index, increase for smaller values of the dielectric constant.

Unfortunately, Eq. 4.3 and subsequently Eq. 4.4 fail to reproduce qualitatively the value of the slopes in Figure 4.11, and do not give the values of δv_{21} that are seen in our experiments. This is explained by the fact that FOPT works good for small values of the coupling strength, which is legitimate when considering charged particles interacting in vacuum (where the coupling strength is given by the fine structure constant $\alpha = 1/137 << 1$). However, FOPT is not a good approximation technique for a large effective coupling strength α_ϵ, as we discussed in the beginning of this section, its value is larger than 2 for suspended graphene.

In order to have a good estimation of the values of the slopes and the difference in velocities in the same graphene specimen, one should introduce an effective dielectric constant ϵ^* instead of ϵ that can be adjusted to match theory with experiment. A good match is found for:

$$\epsilon^*_{G-S} = 3.9, \quad \epsilon^*_{G-hBN} = 7, \quad \epsilon^*_{G-Gr} = 12, \tag{4.6}$$

which are quite different from the values of the dielectric constants for G-S ($\epsilon = 1$) and G-hBN ($\epsilon = 5$).

In order to obtain more realistic values for the dielectric constants, we will proceed differently. Graphene offers another expansion parameter that can control the perturbation theory even when α_ϵ is big. This parameter is identified as $1/\mathcal{O}$, where $\mathcal{O}$ is the number of electronic species, which is equal to 4 for monolayer graphene (the spin and the valley degeneracy) [166, 202]. Hofmann *et al.* used the random phase approximation (RPA) to expand the band velocity in the power of $1/\mathcal{O}$, resulting in an infinite number of terms for all the orders in α_ϵ, but with only the leading terms in $1/\mathcal{O}$ that are relevant [201]. In the absence of magnetic fields (B=0T), this new approach will induce a slight modification in equation 4.3, where the term in front of the logarithm became [166]:

$$\frac{\alpha c}{4\epsilon} \to \frac{\alpha c}{4(\epsilon + 1.28\alpha c/v_0)} = \frac{\alpha c}{4\epsilon_{1/\mathcal{O}}}, \tag{4.7}$$

where $\epsilon_{1/\mathcal{O}} = \epsilon + 1.28(\alpha c/v_0)$ is seen as an added screening capacity by the Dirac electrons themselves. By assuming that $v_0 = 0.88 \times 10^6 m/s$ the RPA give the following values of the dielectric constants:

$$\epsilon^{1/\mathcal{O}}_{G-S} = 4.16, \quad \text{for} \quad \epsilon = 1, \quad \epsilon^{1/\mathcal{O}}_{G-hBN} = 8.16, \quad \text{for} \quad \epsilon = 5, \tag{4.8}$$

which are quite close to the measured values of $\epsilon_* = 3.9$ for G-S, and $\epsilon_* = 7$ for G-hBN. For the results with $B > 0T$, the RPA can be used to apprehend the observed slopes on Figure 4.11. However, this approach fails to account for the values of δv_{21} observed for each graphene-based sample. Indeed, this replacement is valid only for the leading logarithmic term, while the sub-logarithmic terms should be calculated explicitly, and the simple combination C_n/ϵ is replaced by some more complicated one. The only way to give a full explanation for the whole experimental data is to adopt an empirical approach, by assuming the following band velocity re-normalization equation [166]:

$$v_n = v_0 + \frac{\alpha c}{4\epsilon_*}\left(\mathcal{L} - \ln\frac{l_{B_0}}{l_B}\right) + \frac{\alpha c}{4\epsilon_{\delta v}}C_n. \tag{4.9}$$

The above formula is similar to equation 4.4, but with slight changes. We kept the same values of the effective dielectric constants that we obtained from FOPT, and that are in close agreement with the $1/\mathcal{O}$. C_n is the same coefficient as in equation 4.4, and $\epsilon_{\delta v}$ is chosen to reproduce the experimental values of δv_{21}. By setting $\epsilon_{\delta v} = 1.3, 3.7, 12$, only two adjustable parameters remain: the bare velocity v_0, and $\mathcal{L}$. All experimental lines in Figure 4.11 are fitted by setting $v_0 = 0.88 \times 10^6$m/s, and $\mathcal{L} = 4.9$, which gives a cut-off energy of the order $W = (\hbar v_0/l_{B_0})e^{\mathcal{L}}$=3.1 eV. These values of the bare velocity and the bandwidth are in good agreement with what is expected in monolayer graphene [228].

4.3 Bilayer graphene/ hexagonal boron nitride

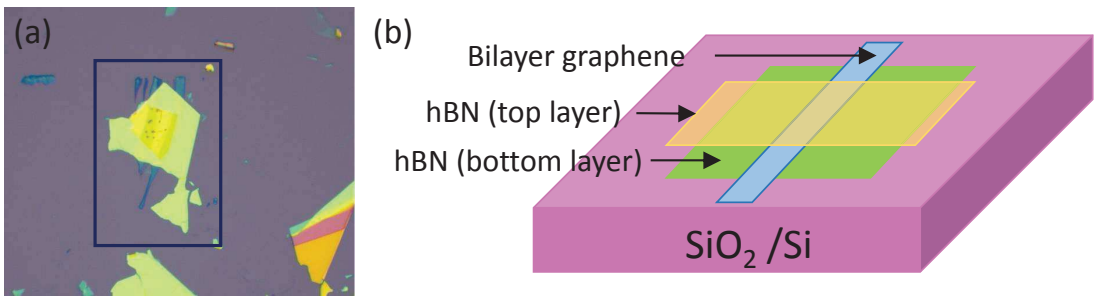

FIGURE 4.12: (a) Optical microscope image, where the sample of interest is boxed in blue. (b) Schematics of the sample showing different locations with bilayer graphene on SiO_2, graphene on hBN and graphene encapsulated in hBN.

The bilayer graphene sample was provided by the group of Prof. *A. Geim* from Manchester University. This bilayer graphene-hBN hetero-structure was produced following the same approach as the G-hBN samples (see Annex 7). Figure 4.12a presents an optical microscope image of the sample. To get a better idea about the structure, Figure 4.12b presents a schematic presentation of the sample's structure. There exist three different configurations, similar to the G-hBN samples: BG-SiO_2, BG-hBN, and hBN-BG-hBN.

These locations are large enough to be probed specifically by micro-Raman scattering spectroscopy.

4.3.1 Raman characterization in the absence of magnetic field

Raman scattering spectra taken in the absence of the magnetic field are shown in Figure 4.13a. The red and black curves are taken from BG-hBN and BG-SiO_2 respectively. One can also recognize the four components 2D band of AB-stacked bilayer graphene [91] as compared with the 2D band few layer graphene (blue curve in Figure 4.13a). There is no observable changes in the 2D band feature from BG-SiO_2 and BG-hBN, as can be appreciated from Figure 4.13b. The G band has a FWHM of about 13 cm^{-1} when measured on the location BG-hBN. This excludes any significant doping from the hBN [152]. Prior to magnetic field measurements, we performed Raman scattering

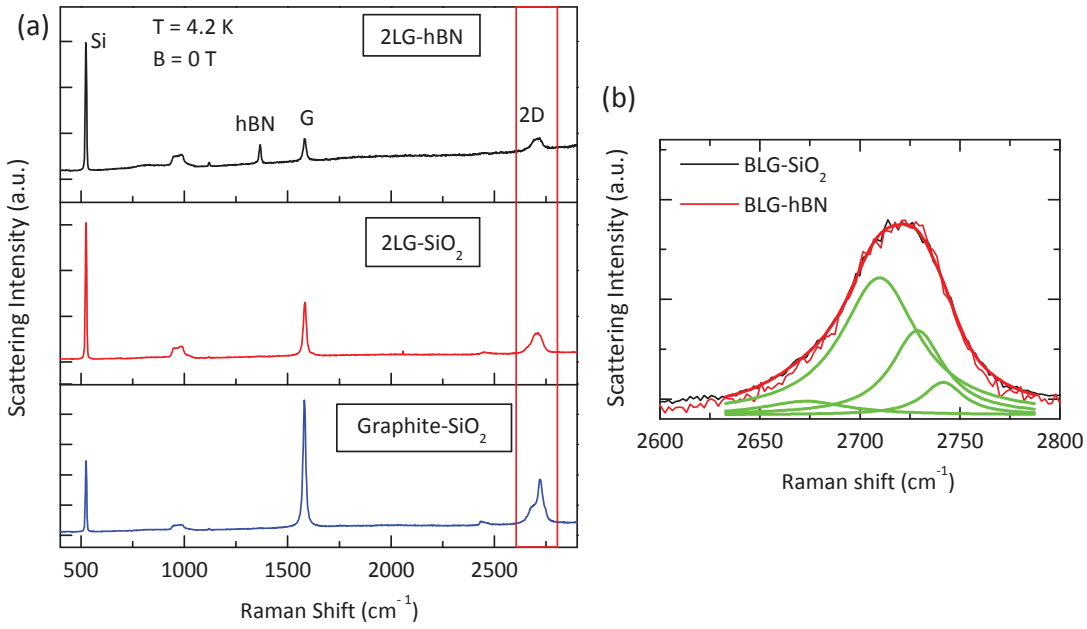

FIGURE 4.13: (a) Representative Raman scattering spectra measured on bilayer graphene on hBN (black), bilayer graphene on SiO_2 (red), and bulk graphite on SiO_2 (blue). (b) 2D band from bilayer graphene on SiO_2 (black curve) and from bilayer graphene on hBN (red curve).

investigation of the flake by mapping its surface using X-Y-Z piezoelectric stages. Figure 4.14a shows Raman scattered intensity at the Si peak energy. The features of the flake are seen, where the Si peak is screened by the layers of the graphene and hBN. The dark regions show the graphene that is enclosed in hBN. To localize the regions where the graphene flake is, we plot in Figure 4.14b the Raman scattered intensity from the G

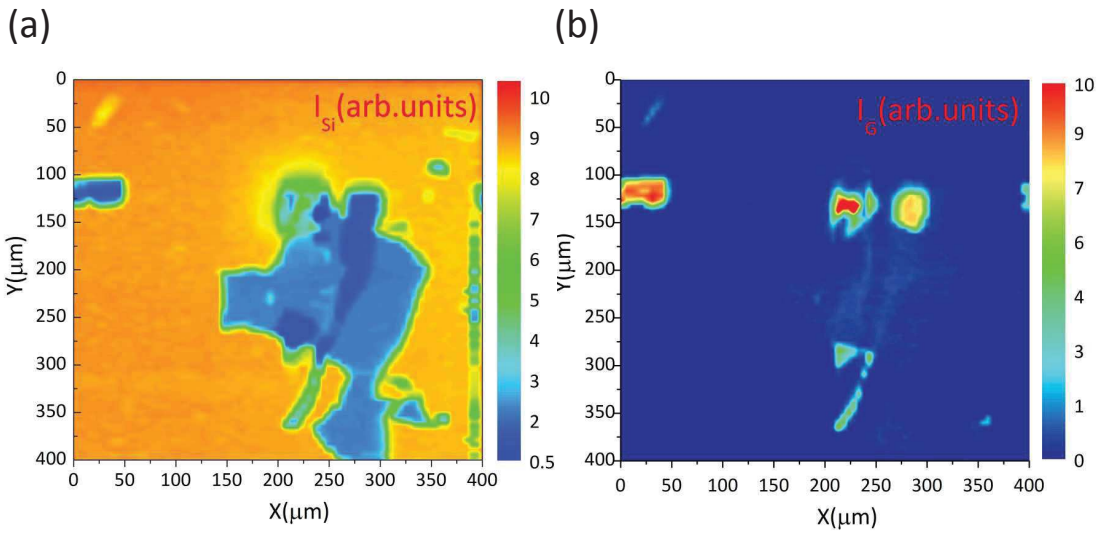

FIGURE 4.14: (a,b) False color maps of the Raman scattered intensity at the Si band energy and the G band energy, respectively. These maps reveal the locations of the graphene encapsulated on hBN or on top of SiO_2.

band, and reveal the features of the graphene encapsulated on hBN (light blue) or the graphene on SiO_2/Si (warmer colors).

4.3.2 Magneto-Raman scattering measurements

Similar to the case of G-hBN, magneto-Raman scattering experiments on the BG-hBN location reveal the presence of the MPR for the optical phonons (however is less pronounced than the case of monolayer graphene). Figure 4.15a shows the G band feature for different values of the magnetic field. Its energy undergoes a shift and we see a broadening of its line-width when changing the magnetic field. The MPR is presented as a false color map of the magneto-Raman scattered intensity in Figure 4.15b, in the G band energy range. The white arrows indicate magnetic field regions where the resonant effect is very pronounced.

At low energies, bilayer graphene presents two parabolic bands, touching at K and K′ points of the Brillouin zone (see Figure 4.16a). As shown in Figure 4.16b, the parabolic bands touching at zero energy split into Landau Levels with a quasi-linear evolution with magnetic fields. Their dispersion, as seen in Chapter 1, is given by [74]:

$$E_n^{BG} = \pm \left[\frac{\gamma_1^2}{2} + (|n| + \frac{1}{2})E_1^2 - \sqrt{\frac{\gamma_1^4}{4} + (|n| + \frac{1}{2})E_1^2\gamma_1^2 + \frac{E_1^4}{4}} \right]^{1/2}, \tag{4.10}$$

where γ_1 is the nearest neighbor inter-layer coupling parameter and +(-) holds for electron (hole) Landau levels. The transition from the filled m level to the empty n level is

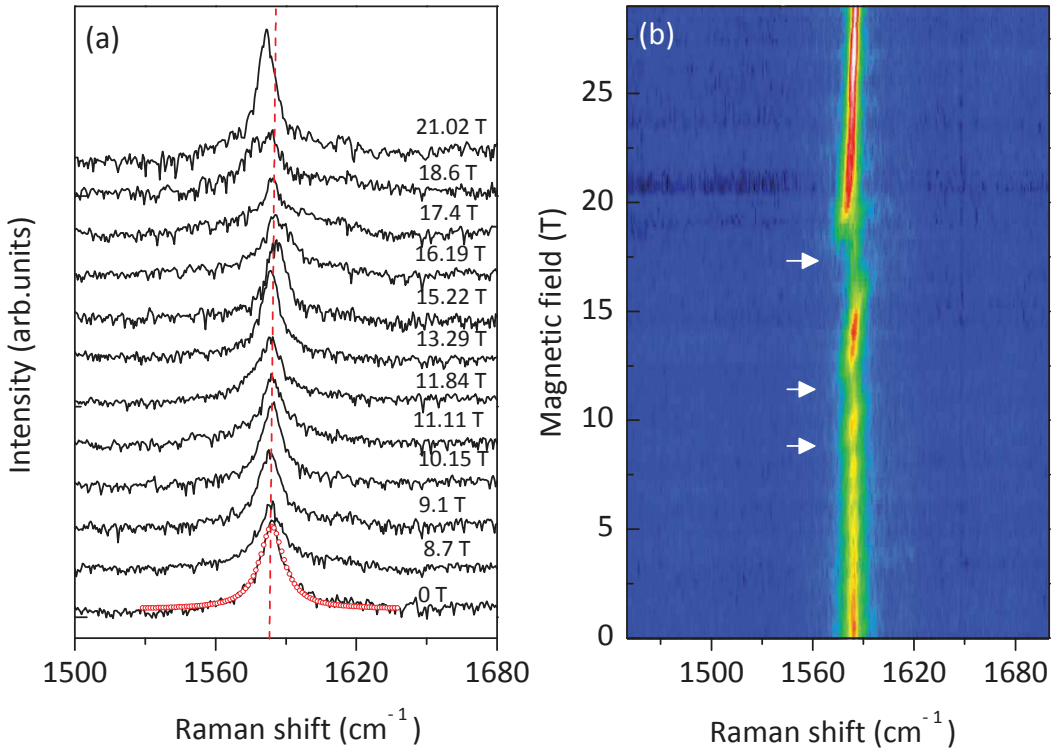

FIGURE 4.15: (a) Raman spectra of the G band for different values of the magnetic field. The G band is fitted with a single Lorentzian as indicated by red open circles in the first spectrum. (b) False color map of the magneto-Raman scattered intensity as a function of the magnetic field for the BG-hBN.

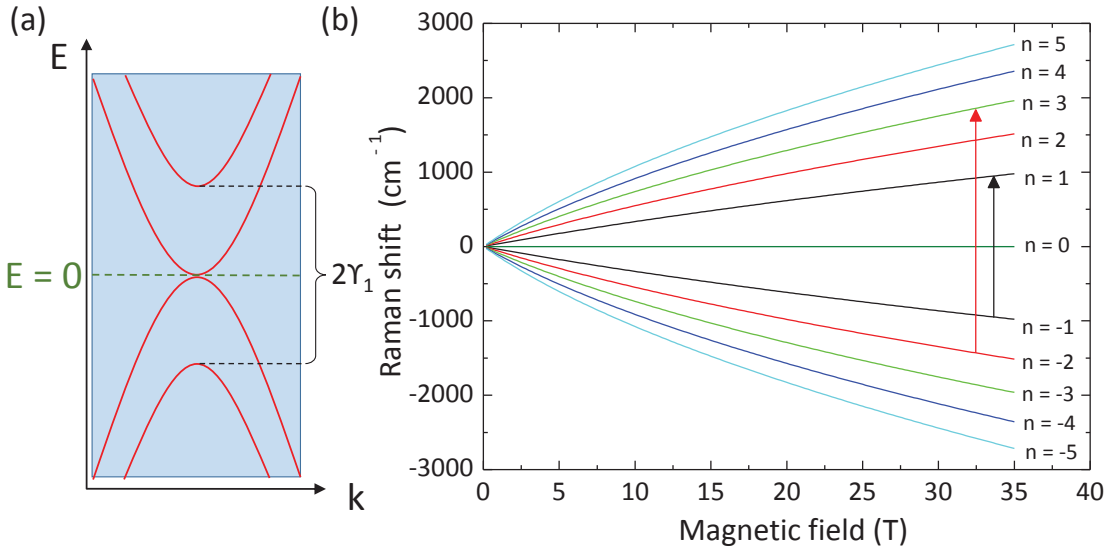

FIGURE 4.16: (a) Low energy parabolic dispersion in AB-stacked bilayer graphene. The gapped bands are separated by twice the value of the inter-layer coupling ($\gamma_1 = 0.39$ eV). (b) Landau levels dispersion in magnetic field for the touching bands in (a). The energy scale is shown in cm^{-1}. The black arrow is a $\Delta|n| = 0$ transition, while the red arrow is a $\Delta|n| = \pm 1$ transition.

given by:

$$L_{m,n} = E_n - E_m. \tag{4.11}$$

In order to reproduce the behavior of the G band under the effect of magnetic fields, we follow the same approach as T. Ando [192] in his theoretical model of the MPR in bilayer graphene. This model consists on calculating the shift and broadening of the E_{2g} phonon from the real and imaginary parts of the corresponding phonon's self energy $\Pi(\mathbf{q}, \omega)$ [192], also known as the *polarization operator*:

$$\begin{cases} \Delta\omega = \frac{1}{\hbar}\mathrm{Re}[\Pi(\mathbf{q}, \omega)], \\ \Gamma = -\frac{1}{\hbar}\mathrm{Im}[\Pi(\mathbf{q}, \omega)]. \end{cases} \tag{4.12}$$

To calculate the energy and broadening of the G band as a function of the magnetic field, we need the values of four parameters: the Fermi velocity, the phonon energy at zero magnetic field, the value of the dimensionless electron-phonon coupling strength [194], and finally the phenomenological broadening of the inter-Landau level transitions δ.

Figure 4.17 shows the magnetic-oscillations of the G band energy and its FWHM (blue dots), obtained from Lorentzian fits of the G band feature. These results are confronted to our calculations (red curves) following the model discussed above. There is a very good match between the experimental results and theory for a value of the dimensionless electron-phonon coupling strength of $\lambda = 4 \times 10^{-3}$, in agreement with other studies of the MPR in graphene based systems [160, 193], and a phenomenological broadening of 150 cm^{-1} to account for the broadening of the inter-Landau level transitions and the E_{2g} phonon.

In contrast to G-hBN, we used a single value of the band velocity ($\upsilon = 1.05 \times 10^6 m/s$) in Figure 4.17. We calculated, using this single value, the $\Delta|n| = \pm 1$ Landau level transitions that couple to the E_{2g} phonon (red dashed lines in Figure 4.17). The MPR is clearly observed for three resonant magnetic fields: the $L_{-1,2}$ transition couples at $B = 17.8T$, the $L_{-2,3}$ transition couples at $B = 11.6T$, and for $L_{-3,4}$ the coupling occurs at $B = 8.4T$. This single particle approximation for bilayer graphene is consistent with other magneto-Raman measurements performed on suspended graphene and N-LG structures [31], where a single value of the band velocity is used to fit the observed transitions for bilayer graphene and thicker flakes. While similar to our results on G-hBN samples, a clear deviation from the single value of the Fermi velocity has been observed in the case of suspended monolayer graphene [31, 166]. These two different behaviors could be related to the vanishing density of states at low energy for monolayer graphene with linear electronic dispersion, while bilayer graphene with a parabolic dispersion shows a constant density of states. This leads to rather different screening possibilities. Under

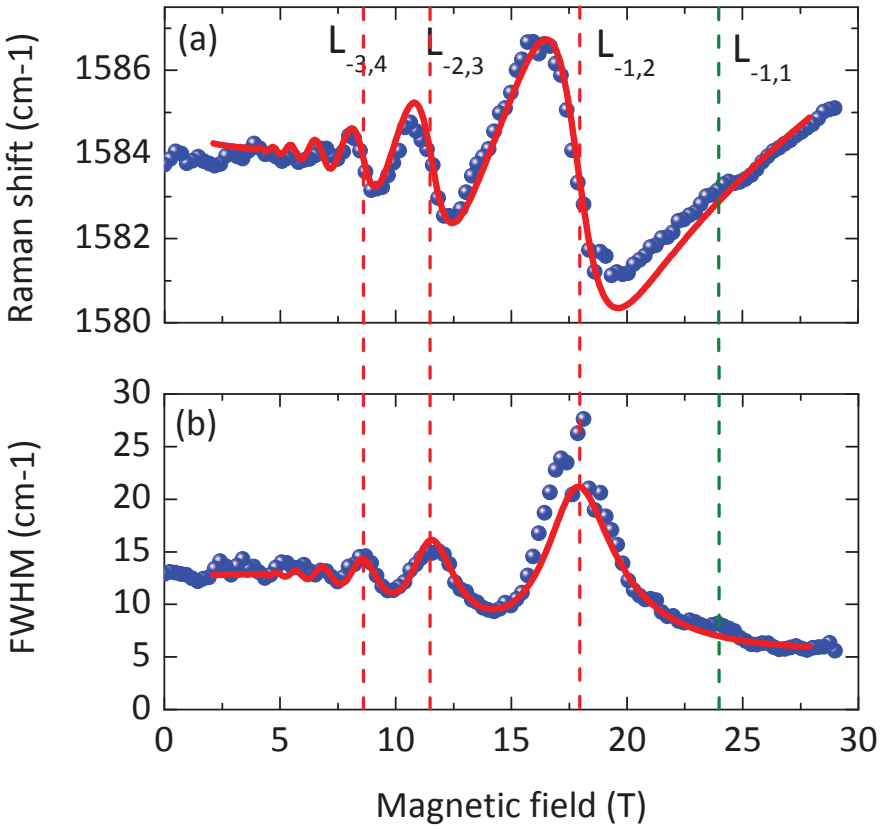

FIGURE 4.17: (a,b) Energy position and FWHM respectively obtained from a single Lorentzian fit of the G band feature as a function of the magnetic field for BG-hBN. The vertical red dashed lines mark the observed resonant magnetic fields for the $\Delta|n| = \pm 1$ excitations while the green dashed line indicates the $L_{-1,1}$ excitation. The red solid lines are the result of the calculation of the MPR in BG, without considering the $L_{-1,1}$ excitation.

the effect of magnetic fields, this difference somehow persists with the existence of a 4-fold and of a 8-fold degenerate n = 0 Landau level in monolayer and bilayer graphene, respectively. For low doped graphene monolayer or N-LG systems, the Fermi level is pinned on the n = 0 Landau level and the screening efficiency will be directly related to its degeneracy.

Unexpectedly, we also observe an increase of the FWHM together with a change of the phonon energy close to the value B = 24.2 T. These changes in the FWHM and phonon energy are small compared to the expected resonant values of the magnetic field for $\Delta|n| = \pm 1$ transitions. For the same value of the band velocity, this value corresponds to the resonant magnetic field for the $L_{-1,1}$ transition (green dashed line in Figure 4.17), which confirms the observation of the coupling of the E_{2g} phonon with the symmetric $\Delta|n| = 0$ inter-Landau level transitions for bilayer graphene, as was evidenced for previous studies on monolayer graphene systems [164, 169, 197], and in our MPR results on G-hBN samples.

4.4 Conclusions

Using magneto-Raman spectroscopy, we investigated the electronic properties of graphene and bilayer graphene deposited on top of hBN. This substrate presents a clear advantage with respect to SiO_2/Si. This is evidenced by the observation of inter-Landau level excitations in some G-hBN samples, as well as the magneto-phonon resonance in both monolayer and bilayer systems (G-hBN, BG-hBN). These observations attest the high quality of the substrate that prevents high doping on graphene.

The MPR for both G-hBN and BG-hBN shows coupling of the $\Delta|n| = \pm 1$ inter-Landau level transitions with the E_{2g} optical phonon at the Γ point. However, a series of anti-crossing of the G band energy and an increase on its FWHM indicate a coupling of the E_{2g} optical phonon with the symmetric $\Delta|n| = 0$ inter-Landau level transitions. The band velocity associated with each symmetric transitions is different, and has a value that increases with the Landau level index.
We attribute this band velocity re-normalization to the effects of electron-electron interactions inducing a mixing in the electronic wave functions of the Landau levels. The Coulomb interactions are to be less pronounced in the case of bilayer graphene, due to its finite density of states around the charge neutrality point that allows a more efficient screening of electron-electron interactions. This is evidenced by its MPR where all the values of the resonant fields can be well described by a single value for the band velocity.

Afterwards, we moved to the the analysis of the Raman-active inter-Landau level excitations, observed in our Raman scattering experiments on G-hBN samples. We compare these results to previous studies on graphene placed on different dielectric environments: graphene suspended, and graphene on the surface of bulk graphite.
Signatures of electron-electron interactions are seen through three main observations : (i) The band velocity strongly depends on the dielectric constant ϵ of the surrounding medium. We confirm that the electronic properties of graphene on insulating substrates (weak dielectric screening) are strongly affected by electron-electron interactions (graphene suspended, and G-hBN), whereas conducting substrates favor the single- particle behavior, such as graphene on graphite, and graphene on metals. (ii) At a given magnetic field value, the band velocity associated with each transition is different. Transitions with higher Landau level index are associated with higher band velocity. (iii) The band velocity associated with each transition decreases significantly when increasing the magnetic field.

The experimental results we obtain in this Chapter 4, and the concluding remarks, suggest that low energy carriers in graphene and bilayer graphene are sensitive to Coulomb interactions. The simple $\sqrt{Bn}$ scaling expected for strictly linear electronic bands in

monolayer graphene, characterized by a single band velocity, is not sufficient to account for our observations. Thus, Kohn's theorem for optical-like transitions in graphene ($\Delta k \sim 0$) is violated, and a full understanding of the excitation spectra falls beyond the frame of the single particle picture.

Chapter 5

Experimental results: Rhombohedral multilayer graphene

5.1 Introduction

Motivation and content:

We have shown in Chapter 1 that the electronic properties of multilayer graphene are intimately related to the way the graphene layers are stacked on top of each other. This possibility that is offered by the physics of 2D materials has encouraged a strong interest in studying the evolution and changes in N-LG band structure for different stacking configurations.

In this Chapter 5, we will present the results obtained in studying the magneto-Raman response of rhombohedral ABC multilayer graphene. Many years ago it has been shown theoretically that the electronic properties of this stacking order are quite different with respect to Bernal N-LG [229].

A series of recent experiments performed on exfoliated ABC tri-layer graphene have shown the possibility of opening a band gap in the structure of this stacking [32, 38], as well as the observation of an unconventional quantum Hall effect of chiral quasiparticles [37]. Nevertheless, little has been done to experimentally investigate the electronic properties of N-LG with large ABC stacking sequences. This is mainly due to naturally small amount of ABC sequence found within exfoliated N-LG flakes.

We present the first magneto optical study of large ABC domains in thin graphite flakes, with ABC sequences exceeding 17 monolayers. We show that the number of the ABC-stacked layers can be estimated from a unique electronic Raman scattering (ERS) feature

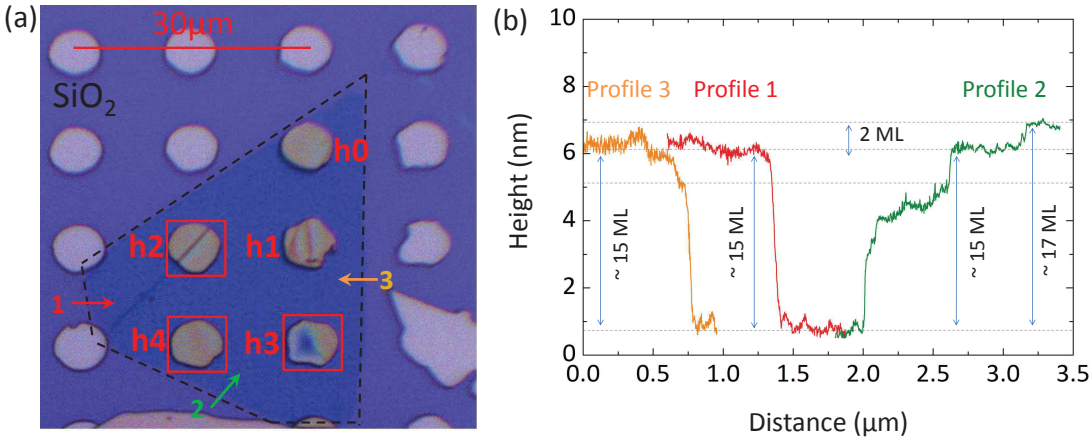

FIGURE 5.1: (a) Optical microscope image of the flake, the colored arrows indicate the sections where AFM measurements were performed. (b), Plot of the edges profile (a) obtained from the AFM scans. The thickness varies from 15 to 17 graphene monolayers.

at zero magnetic field, observed even at room temperature. At low temperatures, we trace the magnetic field evolution of the Raman-active inter-Landau level transitions from the ABC-stacked domain of the flake.

The tight binding model for ABC N-LG, presented in Chapter 1, is used to fit the excitation spectra observed in our experiment. The importance of our results point toward the investigation of high correlation effects on rhombohedral N-LG, such as ferromagnetism or superconductivity, that is offered by the highly degenerate flat bands.

Experimental details:

In order to investigate the Raman response of our flake, we used three different excitation wavelengths. For the room temperature Raman measurements, we used the micro-Raman set up with the excitation wavelength at 632.8 nm. For the low temperature magneto-Raman measurements, we used the fiber optics micro-Raman probe with either the argon-ion laser at 514.5 nm, or the Ti:sapph at 785 nm (see Chapter 3 for a detailed description of the experimental set up).

Atomic force microscopy measurements:

For the sake of completeness ,the thickness of the flake is investigated using atomic force microscopy (AFM). By scanning three different edges of the N-LG flake as seen in Figure 5.1a. The number of layers was estimated from the edges by assuming a thickness of the first monolayer sheet on top of SiO_2 equal to 0.529 ± 0.1 nm (as measured under nominally the same conditions for a reference graphene flake). The atomic interlayer distance in graphite is taken to be 0.335 nm [18], which gives a thickness that varies from 15 to 17 monolayers.

5.2 Raman characterization at room temperature

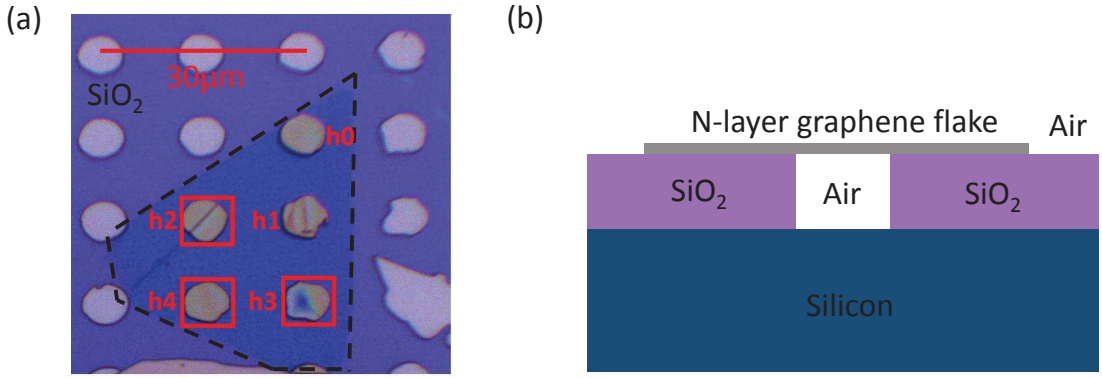

FIGURE 5.2: (a) Optical microscope image of the flake on interest. The flake, larger than 30 μm is suspended over five different holes labeled from h0 to h4. (b) Schematics of the suspended parts over the substrate, where magnetic field measurements have been performed.

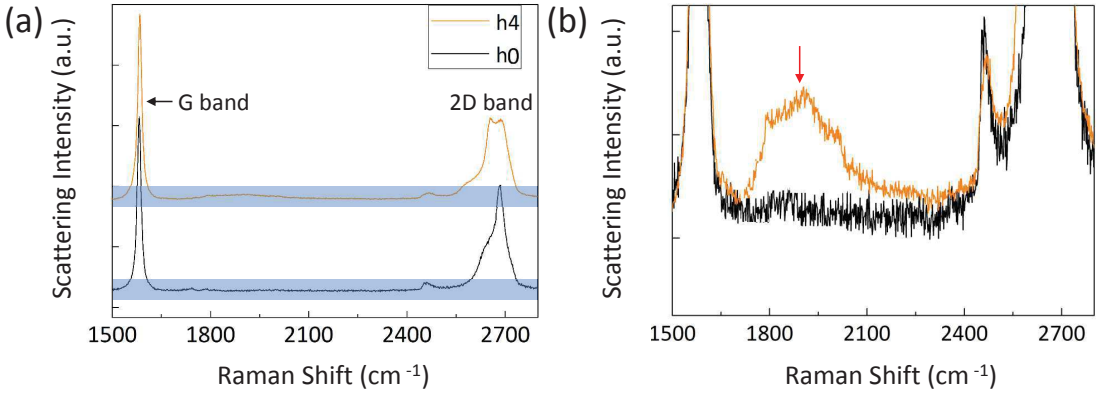

FIGURE 5.3: (a) Raman spectra from h0 (ABA N-LG) and h4 (ABC N-LG) respectively. (b) Zoom on the blue strip regions in (a), where the broad feature is observed on h4 and not seen on h0.

An optical photograph of the investigated flake, obtained by mechanical exfoliation and transferred on Si/SiO_2 with holes pattern as described in the Annex 7, is presented in Figure 5.2a. The holes of interest, covered by our N-LG flake, are labeled h0 to h4. As seen in the schematic (Figure 5.2b), the flake suspended over the holes do not suffer interaction with the substrate.

We start by investigating the room temperature response of our sample in the absence of magnetic fields. Characteristic room temperature Raman scattering spectra, measured on suspended parts at h0 and h4 using 632,8 nm excitation, are presented in Figure 5.3. In all spectra, one can recognize the Raman active G band around 1580 cm^{-1}, characteristic of sp^2 bonded carbon atoms, and the 2D band that is observed around 2700 cm^{-1} when measured with 632.8 nm excitation. Besides these well-known Raman scattering features, an additional puzzling broad feature is observed on h3 and h4 around

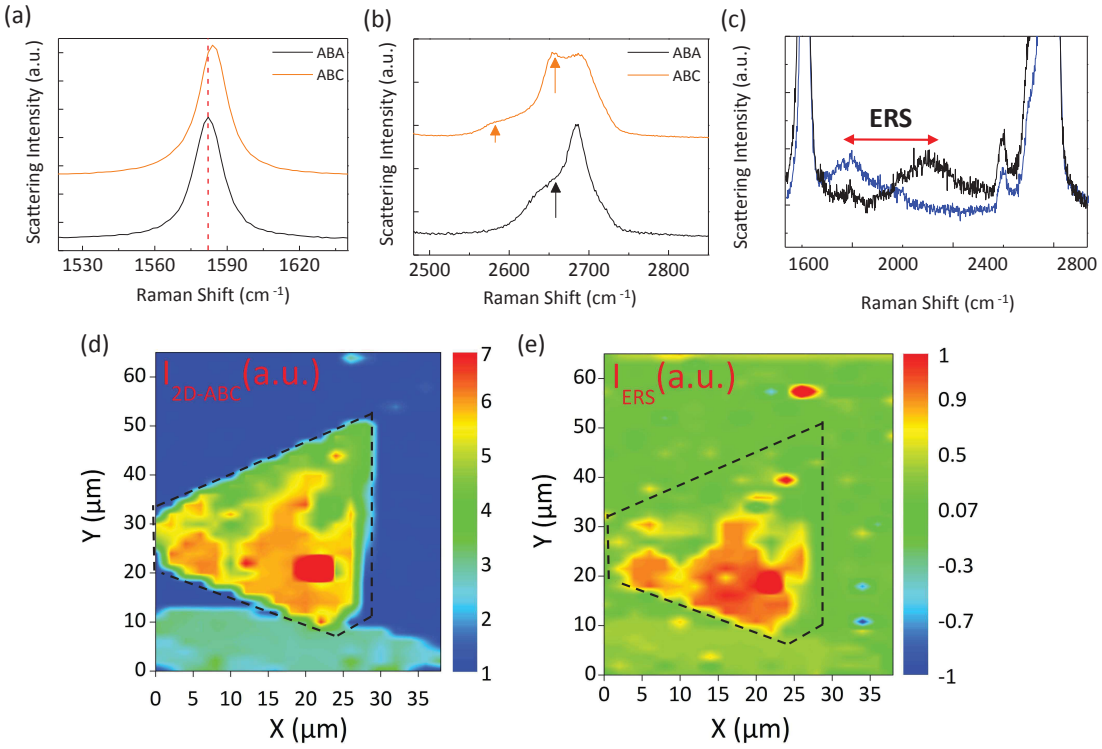

FIGURE 5.4: (a,b) Zoom on the G and the 2D modes lineshape from h0 and h4 (black and orange lines, respectively). (c) Raman spectra taken from two different locations within the same ABC domain but with different number of ABC stacked layers as evidenced by the change in energy of the corresponding ERS. (d,e) False color maps of the micro-Raman scattering intensity from: the ABC N-LG 2D mode subcomponent indicated by and arrow in (b), and an ERS corresponding to a thickness of 15 layers.

1904 cm^{-1} and 1805 cm^{-1} respectively, with a full width at half maximum (FWHM) of $\sim$ 180 cm^{-1}. This broad feature seems to be absent on the Raman scattering spectra of h0, h1 and h2. At the same locations where the broad feature is observed, the line shape of the 2D band feature does not correspond to Bernal AB-stacked thin graphite layers [83, 91] (see fits in Figure 5.5). To better illustrate these differences, we show in Figure 5.4a-b a comparison between the Raman spectra of h1 and h4 with a zoom on the phonon G and 2D modes. The G mode blue shifts, while we observe a drastic change in the 2D band feature. As we will discuss in more details in the following, these three changes (blue shift of the G band, shape of 2D band, and the presence of the broad feature) present the main Raman scattering signatures of ABC-stacked multilayer graphene.

In order to investigate these changes more properly, we have performed spatial mapping of the Raman scattering intensity of the whole N-LG flake, by moving the flake relative to the laser spot with 2μm steps using X-Y piezo electric stages. When comparing different locations, it appears that the broad Raman scattering feature presented on h4 is also observed at different locations on the flake, but that its central position is changing from one location to another (see Figure 5.4c). As will be clarified in the next

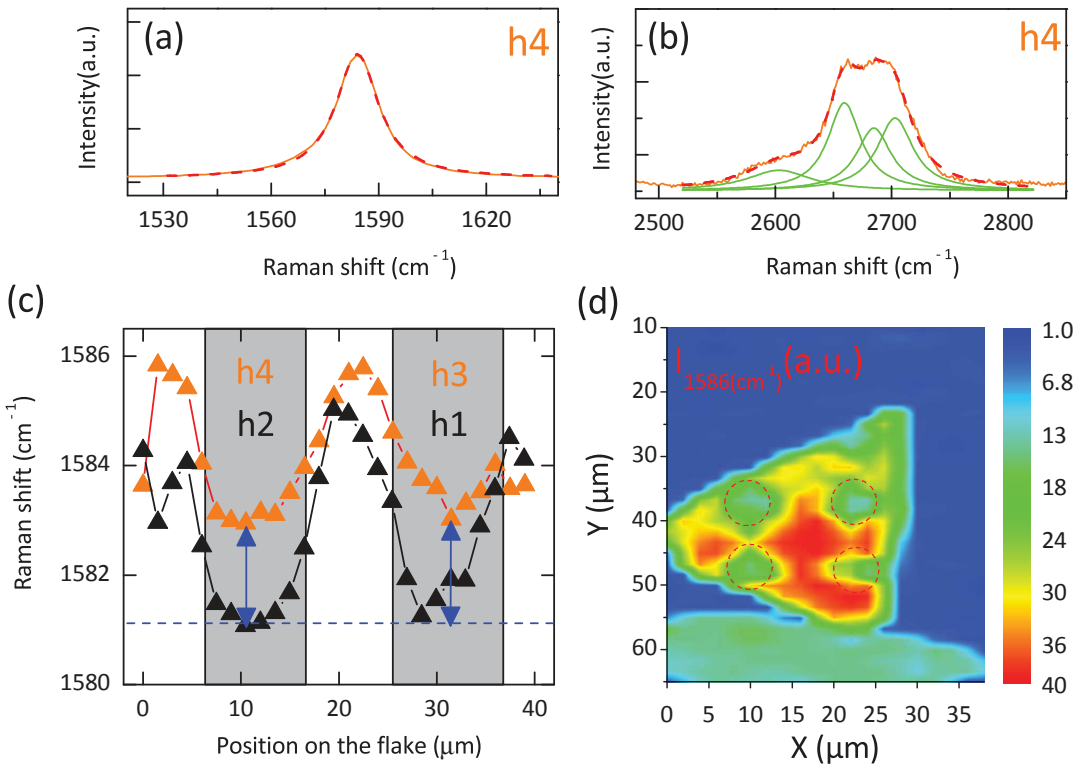

FIGURE 5.5: Single Lorentzian fit of the G band (a) and four Lorentzian fit of the 2D band (b) from the suspended part on h4. (c) Evolution of the G band frequency extracted from scanning the surface of the flake from h1 to h4. The symbols size indicate the uncertainty of the fits. (d) False color map of the Raman scattered intensity of the G band at 1586 cm^{-1}. The suspended parts are shown in dashed red circles.

section by the evolution with magnetic field, we interpret this feature as arising from an electronic Raman scattering (ERS) at zero magnetic field between the lowest gapped bands in the band structure of ABC N-LG. Similar to metallic carbon nanotubes [161], graphene [163], and bulk graphite [160, 162], electronic excitations do contribute to the room temperature Raman scattering response of ABC stacked N-LG. The different locations on the flake where this ERS signal is observed are presented in a false color spatial map in Figure 5.4e. The modified line shape of the 2D mode is also observed at different locations on our flake, shown in Figure 5.4d. The correlation between these two false color maps is a strong indication that the observation of the broad ERS feature and of the modified 2D mode line-shape are signatures of the same, ABC stacking. Our flake is hence composed of two distinct regions: an ABA-stacked domain extending over h0, h1 and h2, and an ABC-stacked domain extending over h3 and h4.

A comparison between the Raman G and 2D bands of the two domains is done by fitting these two bands with Lorentzian functions. The Lorentzian function is defined such as:

$$\mathcal{L}(x) = \frac{A}{2\pi} \frac{\Gamma}{(x - x_0)^2 + (\Gamma/2)^2} + \mathcal{C}, \tag{5.1}$$

where A is the integrated amplitude, Γ is the FWHM of the feature, and x_0 is the position of the maximum. We account for the homogeneous background in the signal by adding a constant $\mathcal{C}$. The G band is fitted using a single Lorentzian (see Figure 5.5a), while the best fit of the 2D band feature is achieved using four Lorentzian functions (Figure 5.5b), similar to the 2D band in bilayer graphene but in clear contrast to the two Lorentzian feature of the 2D band of Bernal-stacked N-LG (see the black curve in Figure 5.4b). Previous studies have shown less pronounced differences in the 2D band features of ABC and ABA tri-layers, with the 2D band in ABC tri-layer presenting a slightly asymmetric feature with an enhanced peak and shoulder compared to the 2D band feature seen in ABA tri-layer [32, 104]. However, these studies have been limited to the case of thin flakes (3 or 4 monolayers) and these differences are less pronounced compared to our observations.

In order to present the energy shift of the G band in the different stacking domains from the flake, we proceed in two different approaches. First, we plotted in Figure 5.5c the Raman scattered intensity at a given energy (1586 cm^{-1}). Regardless of the stacking configuration, the G band energy red shifts (i.e., decrease in energy) on the suspended parts compared to its energy on the SiO_2. We attribute this change on the G band energy to interactions with the substrate that induces charge doping of the graphene layers [152].

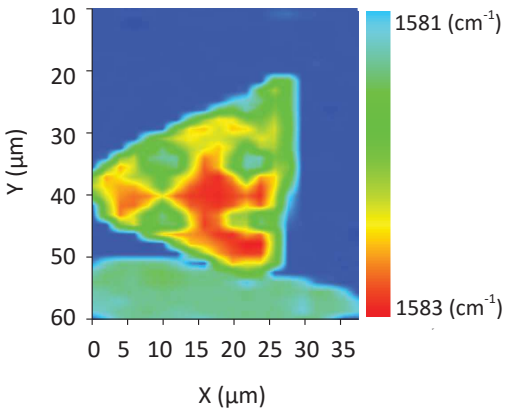

FIGURE 5.6: False color map of the G band Raman shift from the flake. The energy of the G band is plotted from 1581 to 1583 cm^{-1}

While suspended parts do not suffer from interactions with the SiO_2, differences in the G band energy are conspicuous between the two stacking domains. In h1 and h2 (i.e., Bernal stacked domain) the G band energy peaks around $\sim$ 1581 cm^{-1}, while it blue shifts by $\sim$ 3 cm^{-1} on h3 and h4, where the ABC domain is located (see Figure 5.5c). Figure 5.6 is different from Figure 5.5c, in the sense that it plots the G band energy in the range 1581 cm^{-1} to 1583 cm^{-1}. This procedure yields similar results and we reveal again the two domains with different stacking configurations.

The red shift observed in our study is higher compared to the Raman scattering study of ABC and ABA tri-layers by Lui *et al.* [32], where they reported a red shift in the G band energy of $\sim$ 1 cm^{-1} between the two stacking configurations. Based on the theoretical work by Yan *et al.* [230], in which they used DFT calculations to compute the phonon dispersion of ABA and ABC tri-layers, they ascribe the red shift of the G

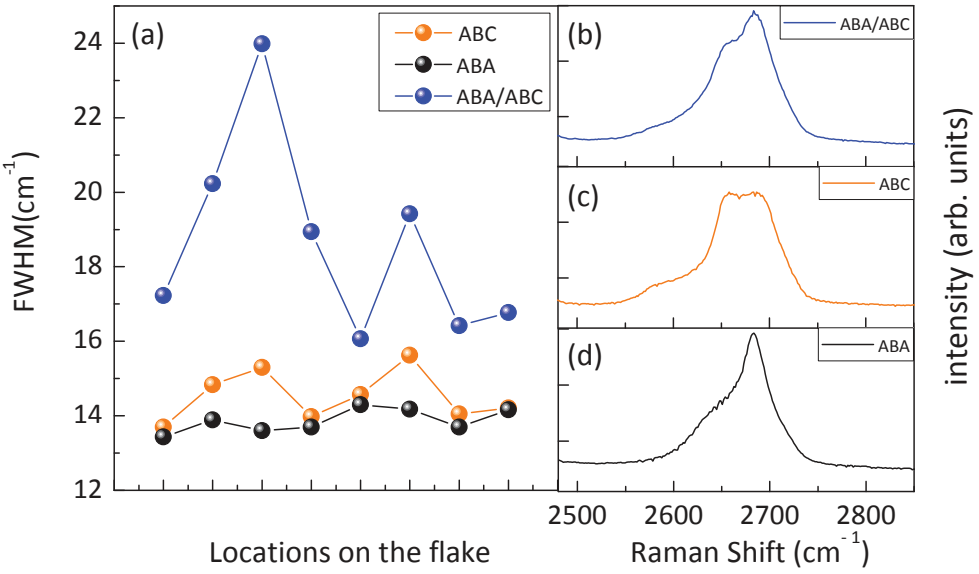

FIGURE 5.7: (a) FWHM of the G band extracted from different locations on the ABA domain (black circles), ABC domain (orange circles), and where both stacking configurations co-exist (blue circles). The symbols size indicate the uncertainty of the fits. (b-d) The corresponding 2D band features of each stacking configuration.

band energy to the slight difference in the ABA and ABC phonon band structures. The shift in the G band energy is summarized in Figure 5.5d which displays a false color map of the Raman scattered intensity of the G band energy at 1586 cm^{-1}. The color bar goes from red (small shift) to blue (big shift). The shift in the G band energy is bigger in the upper part of the flake (green and yellow colors) where the ABA stacking dominates, while the lower ABC part (red color) presents a smaller shift.

We also investigate the FWHM of the G band, extracted from our fits and presented in Figure 5.7a, with their corresponding 2D band features in Figure 5.7b-d. The values of the G band FWHM in ABA and ABC-stacked N-LG oscillate between 13 and 16 cm^{-1}, similar to the values reported in literature for bulk graphite [160], and multilayer graphene [104]. However, some locations on the flake present a significantly increased value of the FWHM (blue circles in Figure 5.7a) ranging from 17 to 24 cm^{-1}. The 2D band feature at these locations is also different from the Bernal and rhombohedral 2D band features (see Figure 5.7b), with one sub-component that increases in intensity compared to the 2D feature of ABC N-LG. This increase in the G band FWHM, as well as the change in the 2D band feature, can be explained by considering regions on the flake with mixed ABA/ABC-stacking configurations. Each stacking configuration will contribute a G band with slightly different energies, resulting in a G band that is a sum of the two peaks hence the increased FWHM.

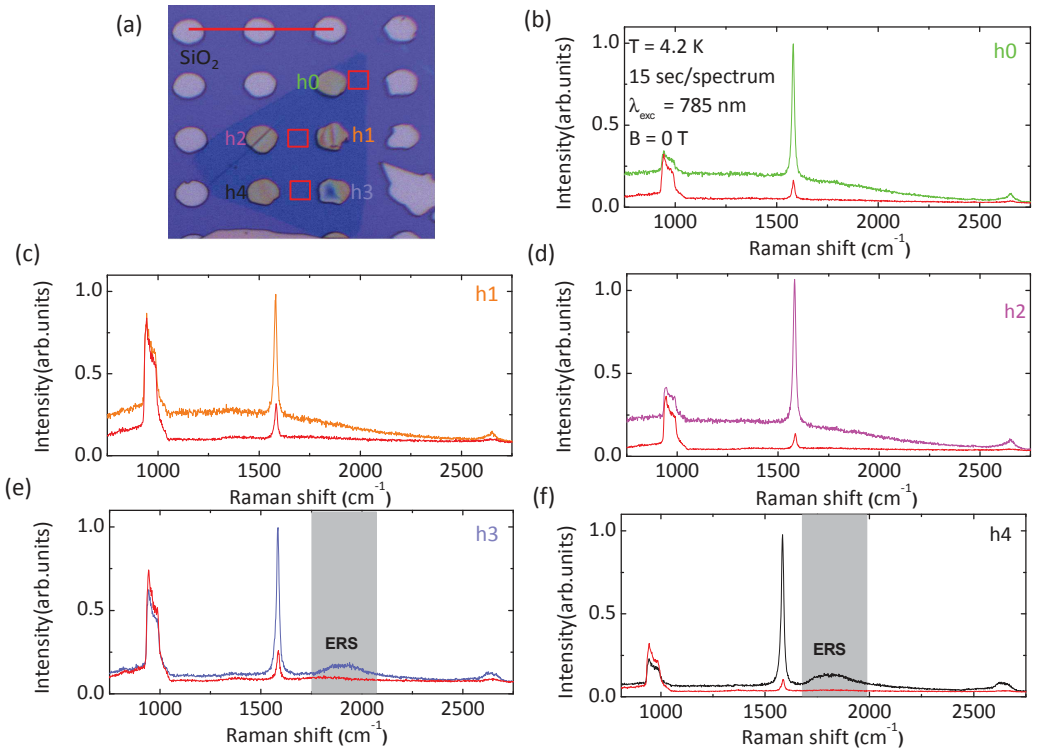

FIGURE 5.8: Raman characterization at low temperature: (a) Optical image of the flake with the suspended regions labeled h0 to h4. (b-f) Raman scattering spectra, measured with each 15 seconds with the same laser power, from the suspended parts h0 to h4 respectively, as well as from supported regions in the vicinity of the suspended parts in red (red boxes in a). The colors of spectra in (b-f) follow the color code in (a).

5.3 Magneto-Raman scattering study at low temperatures

When a transverse magnetic field is applied to the crystal plane, Landau levels are formed and their evolution with increasing magnetic field directly reflects the zero field electronic band structure of the crystal. Here, we use Raman spectroscopy to probe the evolution of the inter-Landau level transitions in our N-LG flake. The difference in the band structure between ABA and ABC-stacked domains is observed in their corresponding inter-Landau levels dispersion with magnetic field.

5.3.1 Raman characterization at zero magnetic field

The sample is now inside the end of the micro-Raman probe, which is submerged in the cryostat at liquid helium temperature (4.2 K). The excitation wavelength has been changed to 785 nm, to get the best configuration for observing the Raman-active inter-Landau level transitions [158]. In order to avoid heating the sample that could significantly shift the observed Raman scattering features [231–233], the excitation laser power

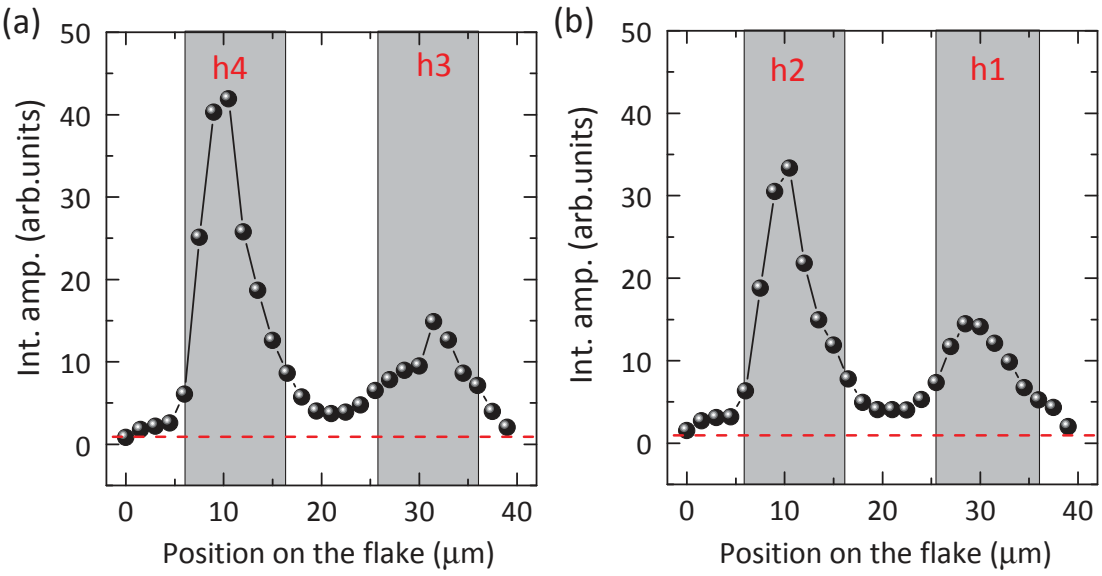

FIGURE 5.9: (a,b) Integrated amplitude of the Raman G band as function of the position on the flake, obtained from the Lorentzian fits. The suspended parts on h1 → h4 (inside the grey rectangles) present a significantly enhanced intensity with respect to the supported region.

has been limited to $\sim$ 1 mW, and focused onto $\sim$ 1μm diameter spot, similar to previous Raman scattering studies of N-LG systems [31].

Figure 5.8b-f shows Raman spectra measured at different suspended regions on the flake (boxed in colored squares in Figure 5.8a) as well as at the supported regions in the immediate vicinity of the holes (indicated by smaller red squares in Figure 5.8a).

At this excitation wavelength, the Raman scattered intensity of the G, the ERS, and 2D bands increases significantly on the suspended regions of the flake, where the SiO_2 thickness has been removed during the etching process (see the details in the Annex 7 describing the fabrication process).

As will be discussed in the Annex 7, this effect is due to multiple reflection interference of the Raman scattered light that occurs in our (N-LG/air/Si) system [36, 234, 235]. The enhancement of the Raman signal on the suspended regions is also reflected on the broad ERS feature, as can be seen on the Raman spectra of h3 and h4 in Figure 5.8e-f, respectively.

In order to quantitatively estimate this enhancement of the Raman modes on the suspended parts, we extract the intensity of the G band from Lorentzian fits of its feature using Eq.5.1. Figure 5.9a,b plots the results of the extracted values of the integrated intensity of the G band. The enhancement of the Raman intensity is not homogeneous from one suspended location to the other, which might indicate a residual thin layer of SiO_2 that has been left after the etching process on some of these holes. By taking the ratio between the G band intensity on each suspended part (where SiO_2 is etched) and

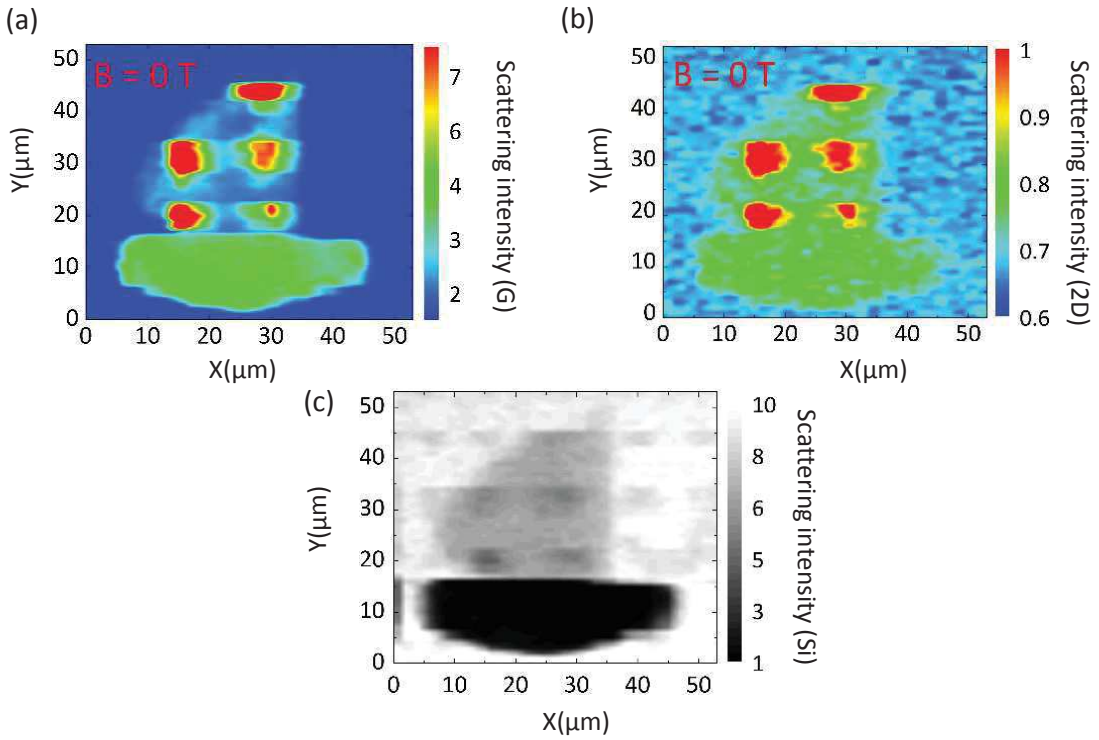

FIGURE 5.10: False colored maps of the micro-Raman scattering intensity at low temperatures: the scattered intensities are shown with respect to the: G Raman mode (a), 2D Raman mode (b), and the silicon Raman mode (c). The contrast in intensity between the suspended and supported regions makes it easy to identify the suspended parts.

the supported regions (SiO_2 not etched) and computing the mean value of this enhancement, we estimate the enhancement to be around ~ 6 for the excitation wavelength 785 nm. In order to visualize the contrast in the Raman scattered intensity, we performed a spatial mapping of our N-LG flake using the X-Y-Z piezoelectric stages and moving with 1.5 μm steps. The flake has been scanned using the same laser power ($\sim$ 1 mW) and acquisition time of 15 seconds for each spectrum. The obtained maps are presented in Figure 5.10a-c in the form of false color maps of the Raman scattered intensity at the G, 2D, and Si bands energies, respectively. Since our experimental set up does not comprise an optical microscope that allows a direct visualization of the flake, the identification of the suspended parts is made easier due to the strong contrast in the Raman scattered intensity between the suspended and supported parts for the G and 2D bands.

5.3.2 Electronic inter-Landau level excitations

We now focus our magneto-Raman studies on three different suspended locations: h2, h3, and h4. To perform the micro-magneto-Raman scattering (MMRS) measurements, we fix a position of interest and make a slow sweep of the magnetic field from 0 up to

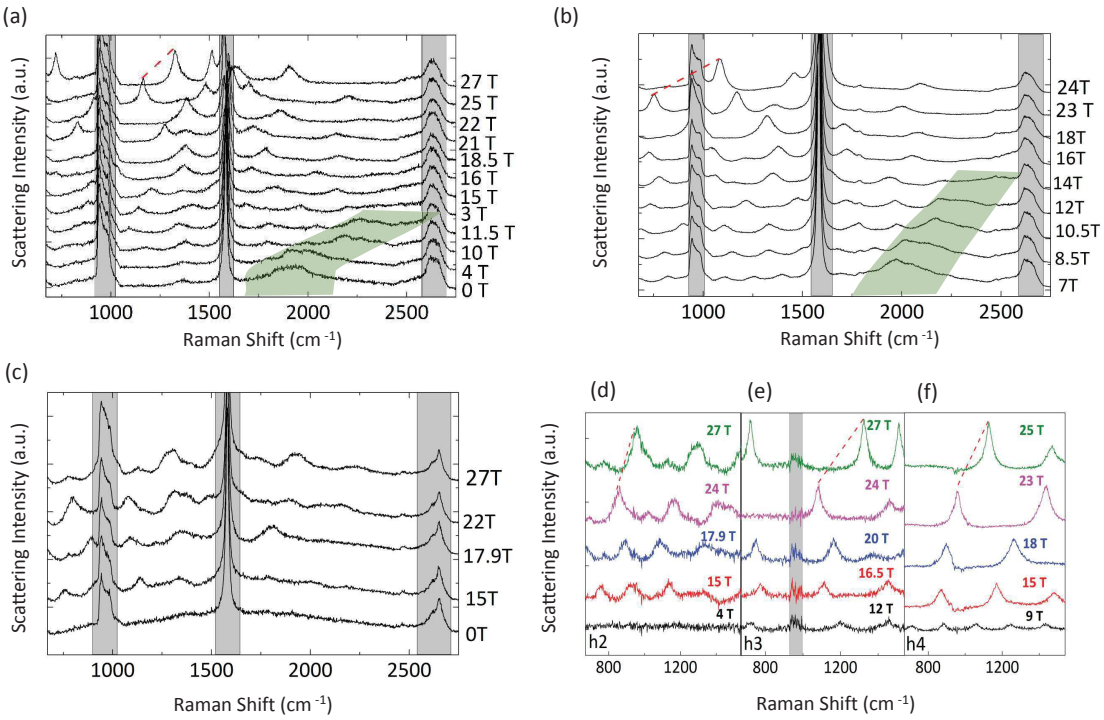

FIGURE 5.11: (a-c) Raw magneto-Raman spectra from h3, h4, and h2 for different values of B, showing inter-band electronic excitations (red dashed lines are guide to the eye). Notice the magnetic evolution of the ERS (the blurred green zones in a,b). The grey vertical bars in (a-c) mask the phonon contributions from the silicon, G and 2D mode features. (d-f) Raman spectra from h2, h3, and h4 respectively, after subtraction of the $B = 0$ corresponding spectra. Notice the highly symmetric features in h3 and h4 where the ABC stacked domain is located.

29 T. The change in magnetic field for each recorded spectrum should be small enough to avoid any significant broadening of the magnetic field-dependent features.

Raw MMRS spectra measured at h3, h4 and h2 are presented in Figure 5.11a-c respectively, for different values of the magnetic field, and after subtraction of the background. Above B > 5 T a series of sharp features, dispersing with the magnetic field, appears in the Raman scattering response. The central position of the broad ERS (highlighted by the green zones in Figure 5.11a-b) feature, observed in h3 and h4, seems to increase with increasing magnetic field and then it disappears for B > 15 T. The fact that magnetic fields can influence so much the energy and amplitude of this feature is in line with an electronic origin for this excitation.

A standard procedure is to subtract the $B = 0$ spectrum from the different magneto-Raman color maps obtained in our experiment. Such a procedure will ensure a better visualization of the magnetic field-dependent features. Figure 5.11d-f shows the result of B =0 subtraction on the spectra of h2, h3 and h4, respectively. The shape of the electronic excitations observed at h2 are characteristic of Bernal stacked graphene multilayers [31], which acquire an asymmetric line-shape at the bulk limit for AB-stacked natural graphite [160]. On the other hand, the electronic excitations observed at h3 and

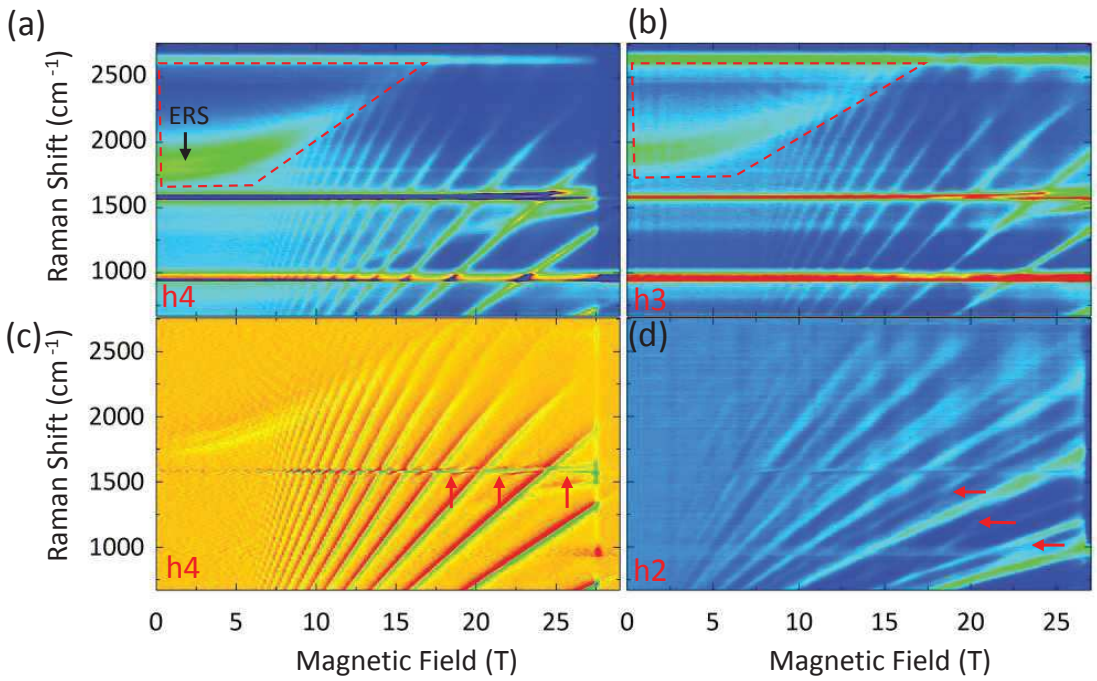

FIGURE 5.12: (a,b) Falsed color maps of the micro-Raman scattering intensity spectra from h4 and h3 that shows electronic excitations from the flat bands and the lowest in energy bulk subbands in the band structure of ABC N-LG. (c) False color map obtained from the B-differentiation of the color map in (a). A dense MPR of the G mode is seen in (c), due to its coupling with the non-Raman active $\Delta|n| = \pm 1$ optical-like transitions. (d) False color map of the micro-Raman scattering intensity from h2, where the ABA stacking dominates. The red arrows indicate the presence of three electronic excitations that disperse in similar way as in h3 and h4.

h4 have symmetric line-shape, and their magnetic field evolution are different. False color maps of the magnetic field evolution measured at h3 and h4 are presented in Figure 5.12a-b respectively, and a false color map of the differentiated with respect to B evolution at h4 is presented in Figure 5.12c. At these two locations, the observed electronic excitation spectrum as a function of magnetic field is composed of a series of features, well separated in energy and seems to have an almost linear dispersion with increasing magnetic field. Surprisingly, a linear extrapolation of these excitations shows that they differ from the usually observed electronic excitations in AB-stacked N-LG by a negative energy onset at $B = 0$. Of much weaker intensity, Raman scattering features with a negative energy dispersion when increasing the magnetic field are also observed on h4 and h3 (red marked regions in Figure 5.12a-b). These features are better seen in the differentiated false color map in Figure 5.12c.

The electronic excitation spectrum at h2 is shown in Figure 5.12d as a false color map of the Raman scattering intensity as a function of the magnetic field. Different electronic excitations are observed, with a quasi-linear evolution with increasing magnetic field. The large majority of these excitations converge to $B = 0$ when their energy tends to zero, characteristic of AB-stacked N-LG. However, three of them (indicated by red

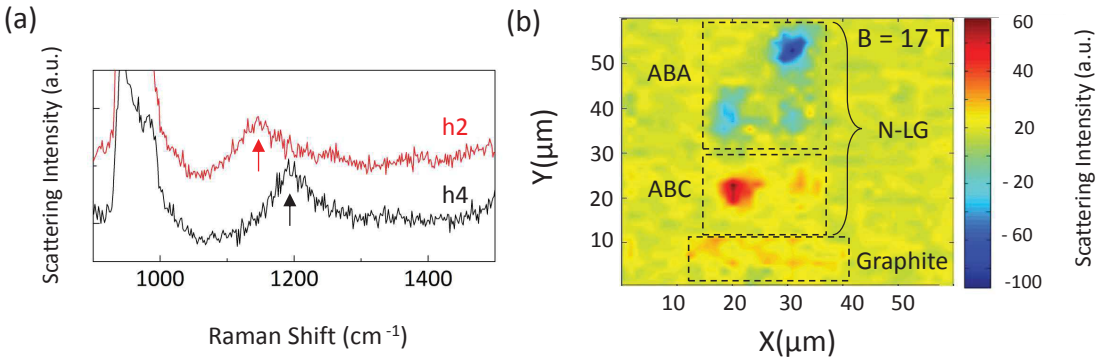

FIGURE 5.13: (a) Raman spectra recorded at B = 17 T from h2 (red curve) and h4 (black curve) showing two electronic excitations at 1136 cm^{-1} and 1192 cm^{-1}, respectively. The contrast in the scattering intensity between the two domains is shown in (b) in the form of a false color map of the micro-Raman scattering intensity from the N-LG flake at B = 17 T, obtained from the subtraction of the two spectra in (a).

arrows in Figure 5.12d), extrapolate to a finite B in a similar way to the excitations observed in h3 and h4.

While symmetric ($\Delta|n| = 0$) inter-Landau level excitations are directly observable in the spectra (see Section theoretical modeling of electronic excitations), optical-like excitations with $\Delta|n| = \pm 1$ are not directly seen but effectively couple to the G mode to give rise to the magneto-phonon resonance and the associated anti-crossings when they are tuned in resonance with the G mode energy [192, 194]. Such anti-crossings are indicated by red arrows in the differentiated magnetic field evolution presented in Figure 5.12d. In order to observe the difference in the electronic excitation spectra from one stacking domain to the other, we performed a spatial mapping of the magneto-Raman response at a constant value of the magnetic field (B = 17 T). Figure 5.13a shows two spectra from this map at h2 (red curve) and h4 (black curve) showing two electronic excitations at different energies: 1136 cm^{-1} (red spectrum) and 1192 cm^{-1} (black spectrum).

To reveal the energy difference between the electronic excitations in the suspended parts, we proceed as the following: we construct two false color maps of the magneto-Raman scattered intensity at B = 17 T. The first color map corresponds to the scattered intensity at the electronic excitation energy at h2 (1136 cm^{-1}), while the second color map plots the Raman scattered intensity at the electronic excitation energy at h4 (1192 cm^{-1}). After that, we subtract the two previous color maps from each other (h4-h2, in that order) and plot another color map of the magneto-Raman scattered intensity at the energy 1192 cm^{-1} of the electronic excitation at h4. The result of this procedure is shown in Figure 5.13b. Red colors show maxima of the scattered intensity that represent electronic excitations at energies 1192 cm^{-1}, located at the suspended parts h3 and h4, while blue colors represent minima of the scattered intensity that corresponds to electronic excitations at 1136 cm^{-1}, present at h0, h1, and h2.

Hence, we reveal again, using magneto-Raman spectroscopy, two distinct domains corresponding to locations with different excitations spectra (boxed in dashed lines squares in Figure 5.13b).

5.4 Theoretical modeling of the magneto-Raman scattering spectra

In this section, we use the tight binding model for the band structure of N-LG, introduced in Chapter 1. By including the effect of magnetic fields on the ABC Hamiltonian, we can reproduce the evolution of the electronic excitations observed on our magneto-Raman experiment. The magneto-Raman spectra of h3 and h4 are the $\Delta|n| = 0$ inter-Landau level transitions within the flat bands at the zero energy, and the lowest in energy gapped bands in the band structure of ABC N-LG. The case of the electronic excitation spectrum for h2 is also discussed, where the rich magneto-Raman spectra, observed for this suspended part, are modeled by considering a Hamiltonian that contains both ABC and ABA stacking configurations. For the high intensity electronic excitations observed

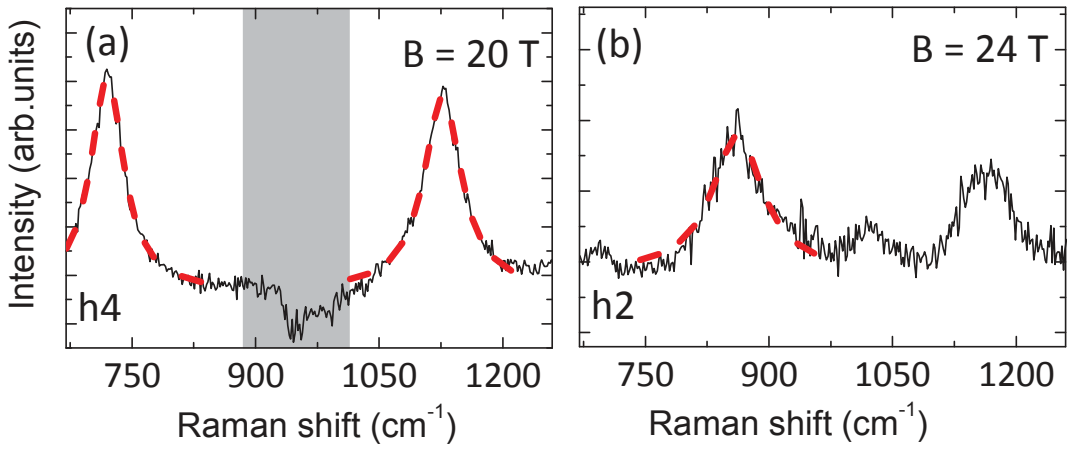

FIGURE 5.14: Lorentzian fits are favored in order to extract the frequencies and linewidths of the electronic excitations observed in our magneto-Raman scattering experiment.

in our magneto-Raman spectra, we extract the central positions and line-widths using Lorentzian fittings, as seen in Figure 5.14a-b. Concerning the low intensity electronic excitations observed in h3 and h4 that have negative dispersion with magnetic field, no fitting is possible. Thus, the frequencies of these excitations are taken directly from the false color maps of the magneto-Raman scattering intensity.

Here, I should clarify that the following sections in which I discuss the inelastic scattering of light at zero magnetic field, as well as the Landau levels spectrum with the selection

rules, have been done by the help of our collaborators: H.P. Ojeda Collado, G. Usaj, and C. Balseiro.

5.4.1 Case of the ABC stacked graphene layers in h3 and h4

The electronic band structure:

As we discussed in details in Chapter 1, by taking into account only the nearest neighbor intra-layer ($\gamma_0 = 3.08$eV) and inter-layer ($\gamma_1 = 0.39$eV) hopping terms, the low energy Hamiltonian for ABC-stacked N-LG graphene (around the K point) is given by:

$$H_{ABC} = \begin{pmatrix} 0 & v_F p_- & & & & & \\ v_F p_+ & 0 & \gamma_1 & & & & \\ & \gamma_1 & 0 & v_F p_- & & & \\ & & v_F p_+ & 0 & \gamma_1 & & \\ & & & \gamma_1 & \ddots & \ddots & \\ & & & & \ddots & \ddots & \end{pmatrix}_{2N\times 2N} , \tag{5.2}$$

where we used the basis $[\phi_{A_1}, \phi_{B_1}, \phi_{A_2}, \phi_{B_2}, \ldots, \phi_{B_N}]^T$. Here, $p_\pm = p_x \pm i p_y$ with $\boldsymbol{p} = (p_x, p_y)$ is the two-dimensional momentum operator, and $v = 3a\gamma_0/2\hbar$ is the band velocity, $a = 0.142$ nm being the carbon-carbon distance.

Inelastic light scattering at zero magnetic field

In order to derive the Landau level spectrum of ABC stacked N-LG, we follow a similar approach as in [159] to briefly present the theoretical description of the electronic Raman process. The interaction of the electrons with photons is included in the Hamiltonian (5.2) by replacing $\boldsymbol{p}$ by the canonical momentum $\boldsymbol{\Pi} = \boldsymbol{p} + \frac{e}{c}\boldsymbol{A}(\boldsymbol{r})$ where $\boldsymbol{A}$ is the vector potential associated with the light field and it is given by:

$$\boldsymbol{A} = \sum_{\boldsymbol{l},\boldsymbol{q},q_z} \frac{\hbar c}{\sqrt{2\Omega}} \left(\boldsymbol{l} e^{i(\boldsymbol{qr}-\boldsymbol{\Omega t})/\hbar} b_{\boldsymbol{l}\boldsymbol{q}q_z} + h.c. \right) . \tag{5.3}$$

The latter includes the annihilation operator $b_{\boldsymbol{l}\boldsymbol{q}q_z}$ for a photon with in-plane momentum $\boldsymbol{q}$, energy Ω (which determines its out-of-plane momentum component $q_z = \sqrt{\Omega^2/c^2 - \boldsymbol{q}^2}$) and polarization $\boldsymbol{l}$. Expanding the Hamiltonian up to the second order in the vector potential, we obtain the interaction part:

$$H_{int} = \frac{e v_F}{c} \boldsymbol{J} \cdot \boldsymbol{A} + \frac{e^2}{2c^2} \sum_{i,j} \left(\partial^2_{p_i p_j} H \right) A_i A_j , \tag{5.4}$$

where $v_F \boldsymbol{J} = \boldsymbol{\nabla}_{\boldsymbol{p}} H$ is the current vertex and $\frac{e^2}{2c^2}\left(\partial^2_{p_i p_j} H\right)$, with $i = \{x, y, z\}$, is the two photon contact interaction tensor [159]. Thus, there are two contributions to the

inelastic light scattering amplitude: a one-step process R_ω (contact interaction) and a two-step process R_D involving an intermediate virtual state. The latter consists of an absorption (emission) of a photon with energy $\Omega(\tilde{\Omega})$ transferring an electron with momentum $\boldsymbol{p}$ from an occupied state in the valence band into a virtual intermediate state, followed by another electron emission (absorption) of the second photon with energy $\tilde{\Omega}(\Omega)$, which moves the electron to the final state with momentum $\boldsymbol{p}+\boldsymbol{q}-\tilde{\boldsymbol{q}}$ and given by [158, 159, 236]:

$$R_D = \frac{(e\hbar v_F)^2}{2\sqrt{\Omega\tilde{\Omega}}}\left[(\boldsymbol{J_q}\cdot\boldsymbol{l})\,G^A_{\Omega+\epsilon_i}\left(\boldsymbol{J}_{-\tilde{\boldsymbol{q}}}\cdot\tilde{\boldsymbol{l}}^\star\right)+\left(\boldsymbol{J}_{-\tilde{\boldsymbol{q}}}\cdot\tilde{\boldsymbol{l}}^\star\right)G^A_{-\Omega+\epsilon_f}\,(\boldsymbol{J_q}\cdot\boldsymbol{l})\right]. \tag{5.5}$$

Here $\boldsymbol{J_q}$ denotes $\boldsymbol{J}(\boldsymbol{q})$ and $G^A_{\Omega+\epsilon_{i(f)}}$ is the advanced Green function for electrons with energy $\Omega+\epsilon_{i(f)}$ where $\epsilon_{i(f)}$ correspond to the energy of initial (final) electronic state. The energy difference $\omega=\Omega-\tilde{\Omega}=\varepsilon_f-\varepsilon_i$ is the Raman shift.

The contact interaction process, due to the terms quadratic in the electron momentum $\boldsymbol{p}$, is

$$R_\omega = \frac{(e\hbar)^2}{2\sqrt{\Omega\tilde{\Omega}}}\left(\partial^2_{p_ip_j}H\right)l_i\tilde{l}^\star_j\delta_{\boldsymbol{p},\boldsymbol{p}+\boldsymbol{q}-\tilde{\boldsymbol{q}}}. \tag{5.6}$$

In our case, $\boldsymbol{J}=(\sigma_x\otimes\mathbb{I},\sigma_y\otimes\mathbb{I},\sigma_z\otimes\mathbb{I})$ with $\mathbb{I}$ the $N\times N$ identity matrix and σ_i the 2×2 Pauli matrices. Considering $v_Fp\ll\Omega$ ($G^A_{\Omega+\epsilon_i}=1/\Omega$ and $G^A_{-\Omega+\epsilon_f}=-1/\Omega$) the dominant contributions to the Raman scattering amplitude is:

$$R_D = \frac{(e\hbar v)^2}{\Omega^2}\left(-i\left(\boldsymbol{l}\times\tilde{\boldsymbol{l}}^\star\right)_z J_z\right) \tag{5.7}$$

whereas the contact interaction takes the form:

$$R_\omega = \frac{(e\hbar v)^2}{6\Omega\gamma_0}\,(\hat{e_z}\times\boldsymbol{J})\cdot\boldsymbol{d} \tag{5.8}$$

with $\boldsymbol{d}=(l_x\tilde{l}^\star_y+l_y\tilde{l}^\star_x, l_x\tilde{l}^\star_x-l_y\tilde{l}^\star_y)$. The transition amplitude $R=R_D+R_\omega$ is analogous to what was obtained for monolayer graphene [158].

The Landau level spectrum and Raman active electronic excitations

In the presence of an external magnetic field $\boldsymbol{B}$ the Hamiltonian takes the form (see Chapter 1 for a detailed derivation of this Hamiltonian):

$$\begin{pmatrix}
0 & \epsilon_0\sqrt{n} & & & & \\
\epsilon_0\sqrt{n} & 0 & \gamma_1 & & & \\
 & \gamma_1 & 0 & \epsilon_0\sqrt{n+1} & & \\
 & & \epsilon_0\sqrt{n+1} & 0 & \gamma_1 & \\
 & & & \gamma_1 & \ddots & \ddots \\
 & & & & \ddots & \ddots
\end{pmatrix}_{2N\times 2N}. \tag{5.9}$$

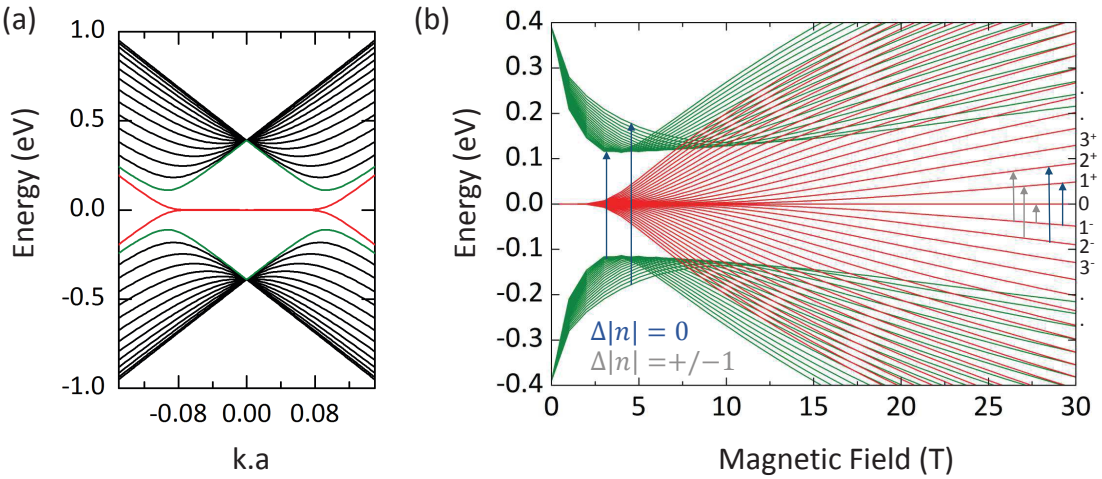

FIGURE 5.15: (a) Low energy band dispersion for ABC stacked graphene multilayers (total number of layers 15) in the absence of magnetic field. (b) The corresponding Landau level dispersions for (a) up to n = 20 Landau level index for the flat bands (red) and the lowest in energy gapped bands (green). The blue arrows indicate symmetric inter-band Landau level transitions (i.e., $\Delta|n| = 0$), known to be active in Raman spectroscopy. The grey arrows are electronic excitations that obeys $\Delta|n| = \pm 1$, seen through their coupling to the G band.

We use a computer program to numerically solve the eigenvalue equation and obtain the electronic dispersion with the corresponding Landau level as a function of the magnetic field. Figure 5.15a shows a plot of the low energy electronic band structure for ABC stacked 15-LG, obtained by diagonalizing the corresponding 30×30 Hamiltonian. The spectrum consists of a set of $2N$ bands, two of them touching each other at the Dirac point K with a flat dispersion, while the other branches are touching at an energy $\pm\gamma_1$ at $k = 0$. The corresponding Landau level spectrum is shown in Figure 5.15b, for the flat bands (red bands in Figure 5.15a) and the lowest in energy gapped bands (green bands in Figure 5.15b). To find the electronic Raman spectrum in the presence of an external magnetic field, we calculate the transition amplitude probability (matrix elements of the operator $R = R_D + R_\omega$) between the initial $|\psi_n^\alpha\rangle$ and final $|\psi_m^\beta\rangle$ states. This procedure leads to the selection rules $|n| = |m|$ and $\alpha = \beta$ for the R_D process as in monolayer graphene where the ones allowed by R_D correspond to symmetric optically active inter-LL excitations (transitions with $\Delta|n| = 0$ indicated by blue arrows in Figure 5.15b). Transitions with $|m| \neq |n|$ are also possible, due to processes represented by R_ω, but in this case with intensities considerably lower. From this modeling, we can extract $N = 14$ and $N = 15$ for h3 and h4, respectively (Figure 5.16a-b), while we set $\gamma_0 = 3.08$eV and $\gamma_1 = 0.39$eV, as observed in bulk graphite [159, 160, 236]. The fitting of the experimentally observed electronic excitations with our model reveals only transitions with $\Delta|n| = 0$.

In order to compare our theoretical calculations with the experimental magneto-Raman

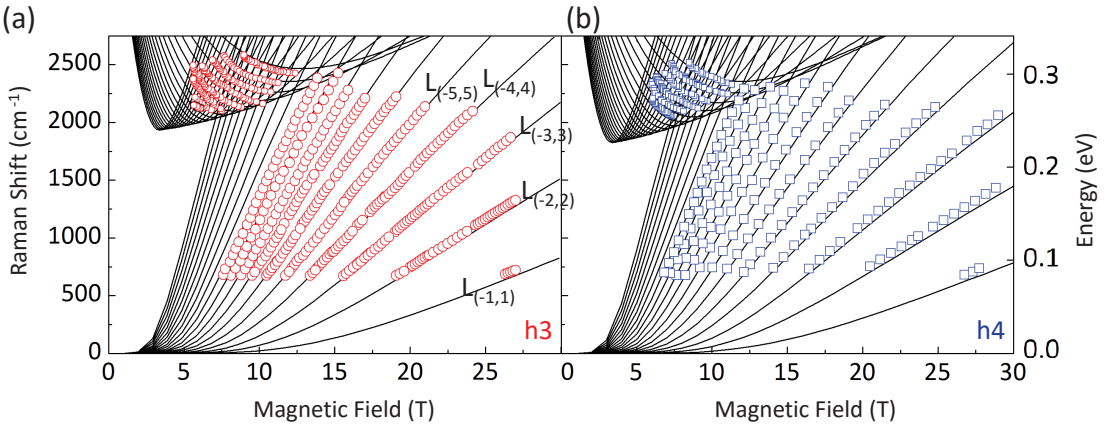

FIGURE 5.16: Modeling of the data from the magneto-Raman experiments from h3 and h4: (a,b) Experimental points were obtained using Lorentzian fits in order to extract the corresponding frequencies of the electronic Raman features with an experimental error that is smaller than the symbol size. The theoretical transition lines for $\Delta|n| = 0$ were calculated using the low energy Hamiltonian for ABC stacked 14LG (a) and 15-LG (b), respectively.

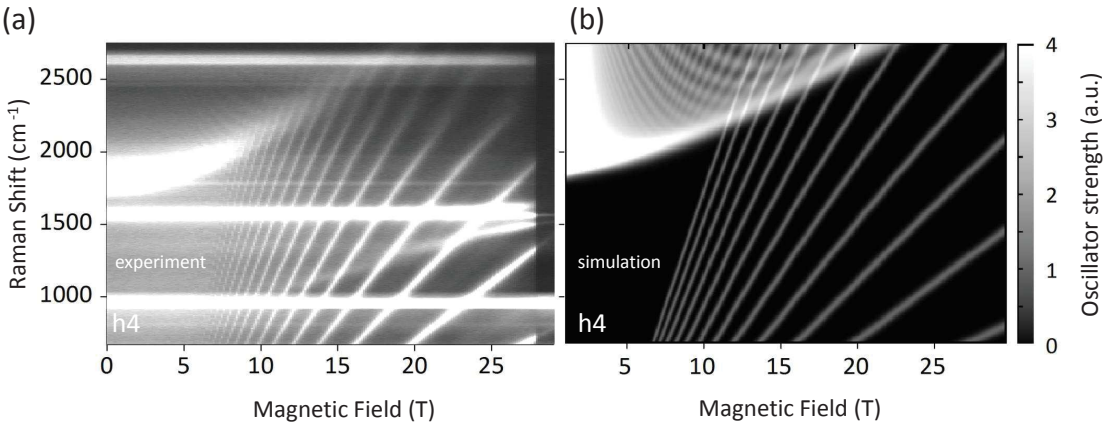

FIGURE 5.17: Considering the amplitude of the Raman scattering intensity of the electronic excitations for the ABC N-LG, a comparison between the experimental results and the theoretical calculations for h4 is shown in (a,b).

scattered spectra for ABC N-LG, we assign a Gaussian function to each possible transition line with height equal to $\left|\langle\psi_m^\beta|R|\psi_n^\alpha\rangle\right|^2$ and standard deviation $\sim$ 32 cm^{-1} to simulate a possible Landau level broadening in the real sample. Such comparison is presented in Figure 5.17a-b for h4. The model reproduces the main observed features, in particular, the broad ERS observed at $B = 0$ is reproduced and arises from inter band electronic excitation that loses its spectral weight when the magnetic field is increased, transforming into inter-Landau level transitions with their characteristic negative energy onset dispersion. However, our theoretical model is simplified since the oscillator strength (i.e., the transition rate between Landau levels) of $\left|\langle\psi_m^\beta|R|\psi_n^\alpha\rangle\right|^2$ depends on the magnetic field, which is assumed to be constant in our simulations.

Analysis of the line-widths of the inter-Landau level transitions

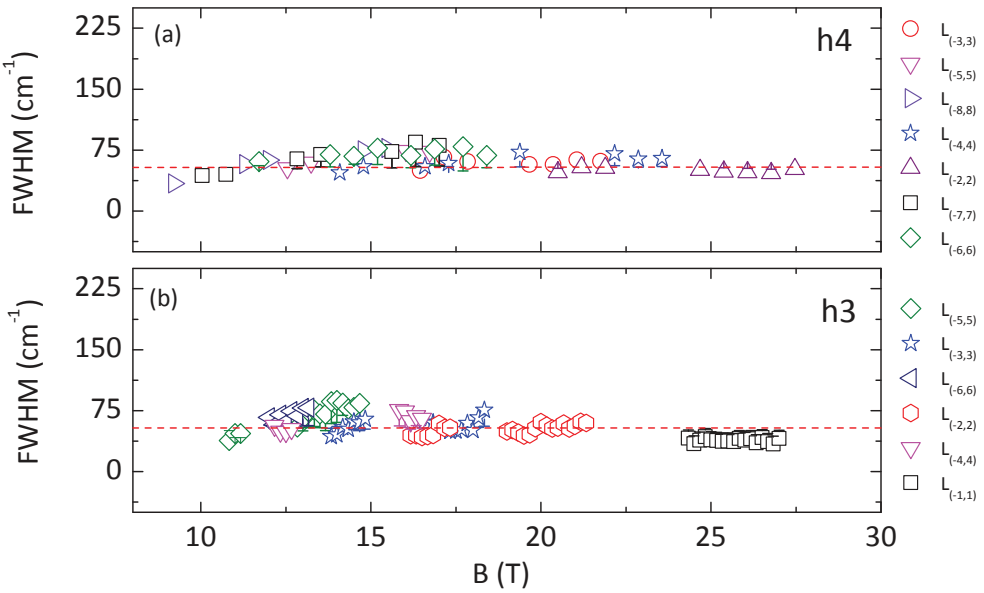

FIGURE 5.18: (a,b) FWHM of the $\Delta|n| = 0$ inter-Landau level transitions, obtained from Lorentzian fits of the magneto-Raman excitations on h3 and h4, respectively. The uncertainty of the fits is higher at values of the magnetic field where the transition lines cross the Si and G bands.

We analyze the line-widths of the inter-Landau level transitions from our magneto-Raman scattering results obtained from the ABC-stacked suspended parts on h3 and h4. This analysis is limited to the transition lines from the flat bands, since no fitting of the inter-Landau level transitions for the gaped bands is possible. Figure 5.18a,b plots the the evolution of FWHM for different inter-Landau level transitions $L_{-n,n}$ as a function of the magnetic field for the transition lines on h3 and h4, respectively. While Figure 5.19 presents the evolution of the FWHM for the inter-Landau level transitions as a function of the Landau level index n at fixed values of the magnetic field.

In the range $B = 10 - 25$ T, we considered the B-dependence of the FWHM for the transitions $L_{-1,1} \rightarrow L_{-8,8}$. For both suspended parts, the values of the line-widths when increasing the magnetic field are in the range 45-85 cm^{-1}, while no increase in the FWHM is observed as a function of the Landau level index (see Figure 5.19c,d). These transition lines are much narrower compared to values reported for high mobility suspended graphene [217, 237], and suspended Bernal-stacked N-LG [31]. Therefore, by a linear interpolation of the set of data we can extract a mean value of the line-width for the transition lines ~ 55 cm^{-1} as well as a mean value of the quasi-particles lifetime ~ 100 fs.

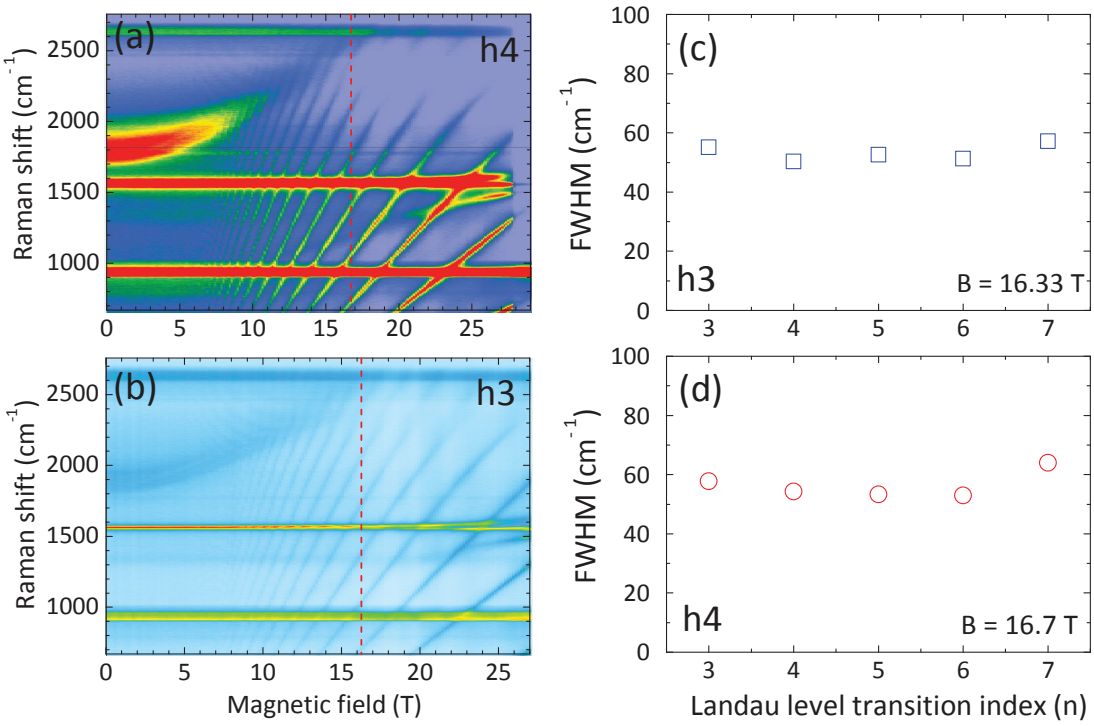

FIGURE 5.19: FWHM from the suspended parts h3 and h4 (c,d) for different inter-Landau transitions at fixed values of the magnetic field, indicated by dashed red lines in the false color maps of the magneto-Raman scattered intensity (a,b).

5.4.2 Case of the mixed stacking of graphene layers in h2

Three excitations observed at h2, that extrapolate at finite negative energy when B goes to zero, are shown in green open circles in Figure 5.20b. The remaining complex electronic excitation spectrum observed in the magneto-Raman at h2 are shown by open blue triangles in Figure 5.20c.

The evolution with magnetic field of the electronic excitations in h2 can be understood by considering a tight binding model for N-LG system, but this time with a mixed stacking of its graphene layers. In order to fit the magneto-Raman spectrum, we considered a Hamiltonian that contains an ABA-stacked 8-LG coupled to 7-LG with an ABC sequence. The low energy electronic band structure corresponding to the ABABABAB-ABCABCA stacked 15-LG is shown in Figure 5.20a. Under the effect of magnetic fields, the band structure in Figure 5.20a is Landau quantized. By considering the symmetric $\Delta|n| = 0$, the best fit for h2 yields N = 15, $\gamma_0 = 3.15$ eV and $\gamma_1 = 0.4$ eV (see black curves in Figure 5.20b-c).

The main conclusion is that while the suspended parts h3 and h4 have a pure ABC stacking, h2 on the other hand is interpreted as being inhomogeneous and exhibits both ABA and ABC stacking configurations. It is interesting to emphasize the striking difference in complexity that both cases present. While the mixed stacking in h2 presents

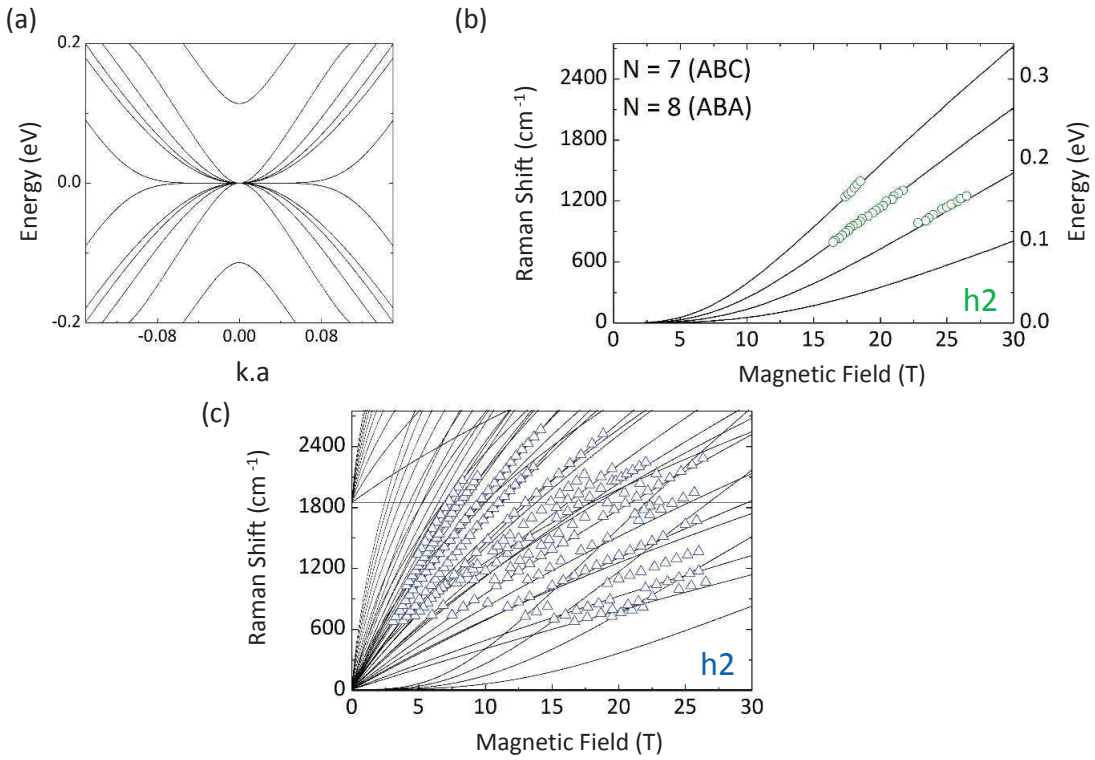

FIGURE 5.20: Modeling of the data from the magneto-Raman experiments corresponding to h2: By considering a single tight-binding Hamiltonian that contains the stacking configuration ABABABAB-ABCABCA, we plot its low energy band structure in (a). The fitting of the electronic excitations in the case of h2 is then obtained by considering ABA stacked 8-layer graphene (data indicated by blue triangles in b) coupled with ABC stacked 7-layer graphene (data indicated by green dots in b). The corresponding Landau level transitions reproduce well the observed electronic excitations from h2 (b).

a rather complicated magneto-Raman spectrum, the pure ABC stacking situations in h3 and h4 show a clean and simple one.

5.5 Conclusions

In this Chapter 5 of the thesis work, we have reported on the observation of electronic excitations in N-LG system, which comprises a pure rhombohedral ABC-stacking of its graphene sheets up to 15 layers. The analysis of its low energy electronic excitations and of their evolution for increasing magnetic fields can be understood in the frame of a tight-binding model with three parameters, the number of ABC stacked layers and the intra and inter-layer nearest neighbors hopping integrals γ_0 and γ_1. Such stacking has a unique signature in the $B = 0$ Raman spectra, in the form of low energy electronic excitations across the band gap. Surprisingly, the $B = 0$ ERS response is observed even at room temperature, and its central position can be related to the number of ABC-stacked layers within N-LG flakes. Thus, it can be used as a tool to estimate the length

of the ABC sequence using simple Raman spectroscopy. Our findings underscore the rich physics hidden in this stacking order, namely the existence of an electronic band with a flat dispersion (diverging density of states), theoretically predicted to be localized on the surface, and of electronic gaped bands, seen as bulk states, with a number of layer dependent energy gap. These results represent an impetus for other studies targeting the predicted highly correlated surface states, observed for a large number of ABC-stacked layers, which may lead to emergent exotic electronic ground states in multilayer graphene and similar 2D materials with ABC stacking.

Chapter 6

Summary

6.1 Summary (English)

Since its first experimental isolation, graphene offered the possibility to observe many novel physical phenomena. It has been twelve years since the first published papers about the properties of this material, and yet it continuous to be the subject of intense scientific research, with more studies nowadays that are oriented toward its potential applications in engineering future electronic devices.
Throughout this doctoral thesis, we addressed two fundamental issues on the physics of graphene:
(i) The effects of interaction with its surrounding medium on the physical properties of graphene.
(ii) The difference in the electronic properties of many layer graphene as a function of their crystallographic stacking configuration.
These issues have been addressed by measuring all the studied samples under strong continuous magnetic fields, available at the " Laboratoire National des Champs Magnetiques Intenses, LNCMI-CNRS ", at Grenoble. We used exclusively micro-Raman scattering spectroscopy to probe the response of the studied systems under the effect of magnetic fields.

The original results obtained in this doctoral thesis have been presented in full details in Chapter 4 and Chapter 5.

The effective coupling strength of charged particles, given by the fine structure constant of quantum electrodynamics, is re-scaled to a value around 2 in graphene. Knowing this, the strength of the Coulomb interactions cannot be ignored when treating charge carriers in graphene. Moreover, the optical-like transitions in conventional 2DES with parabolic bands are insensitive to many body effects, as stated by Kohn's theorem [198]. Graphene, however, has a linear dispersion around the charge neutrality. Consequently, its relativistic charge carriers escape Kohn's theorem and many body effects do contribute to its magneto-optical response [227]. Moreover, the effective coupling strength can be modulated by the dielectric function of the medium in which graphene is placed, allowing to different magnitudes of the Coulomb interactions between its charge carriers.

To address these issues, we demonstrated the effects of Coulomb interactions on the band structure of graphene in Chapter 4 throughout the investigation of its magneto-Raman scattering response in three different systems: suspended graphene, graphene on the surface of bulk graphite, and graphene encapsulated in hBN. We note that in the course of this work, our contribution has been the magneto-Raman measurements of graphene encapsulated in hBN samples, while the results obtained on suspended graphene, and graphene on the surface of graphite have been used as comparative results to our experimental data.

Our work was motivated by some experimental results reporting signatures of many body effects in graphene samples. In their Infrared spectroscopy study of Landau levels in high quality graphene samples [217], Jiang *et al.* showed that the band velocities associated with the observed transitions are different. A transport measurements study conducted by Elias *et al.* [215] demonstrated the effect of Coulomb interactions in re-shaping the low energy band dispersion in graphene through a re-normalization of its band velocity with a logarithmic divergence around the charge neutrality point.

Thus, it is interesting to investigate the role of many body effects in the presence of magnetic fields, where the excitation spectra are dominated by inter-band transitions between Landau level states. We had the possibility to understand how the dielectric function of the medium surrounding graphene will affect the strength of the Coulomb interactions, and thus the energy dispersion in graphene. We combined two different analyses. First, we studied the magneto-phonon resonance, which is the coupling of the E_{2g} optical phonon at the Γ point with the inter-Landau level transitions that obeys selection rules $\Delta|n| = \pm 1$. The Coulomb interactions induce a mixing of the electronic wave functions of the Landau levels. This Landau levels mixing is seen as the coupling of the E_{2g} optical phonon with the symmetric inter-Landau level transitions $\Delta|n| = 0$, supposed to be forbidden for symmetry reasons. Secondly, the Raman-active inter-Landau level transitions have been studied. The analysis of their dispersion in magnetic

fields reveals an associated band velocity that depends on the dielectric function of the surrounding medium, decreases in a logarithmic fashion with the magnetic field value, and increases with the Landau level index.

A straightforward conclusion follows the experimental results of Chapter 4, that is optical-like transitions (i.e., $\Delta k \sim 0$) are a probe to electron-electron interactions in graphene. Such results show a breakdown of the single particle picture that has been used so far to understand the electronic properties of graphene on SiO_2/Si substrates and strengthen the evidence for boron nitride to replace silicon as a substrate of choice to study graphene properties.

Shortly after the discovery of graphene, its peculiar band structure has been shown to change continuously when adding more layers of graphene on top of each other. Not only the number of layers, but also the way the graphene sheets are stacked implies changes in its band structure and thus its electronic properties. This degree of freedom not only present an interesting case to address many questions in fundamental physics, but it also points toward serious technological applications upon tailoring the electronic properties in the 2D materials.

The role that plays the stacking order in changing the electronic properties of multilayer graphene has been addressed in Chapter 5. We reported the first experimental observation of inter-Landau level excitations in multilayer graphene sample with a rhombohedral stacking of its graphene layers. This stacking is found in significant amount in flakes obtained from the mechanical exfoliation of kish graphite. However, this stacking order usually escapes characterization due to its lower abundance compared to the more stable Bernal stacking.
Several theoretical papers have stressed on the topological nature of the electronic states in N-LG with a rhombohedral stacking of its graphene sheets [55, 56, 59]. The nearly flat bands at the charge neutrality have a diverging density of states that can favor the observation of ferromagnetism or surface superconductivity in this material [39–41]. All these predictions made rhombohedral multilayer graphene an appealing system to study. On the other hand, the abundance of large ABC sequences in exfoliated flakes is limited, and it has been hard to present, until now, a comprehensive experimental study of the band structure of rhombohedral N-LG for $N > 5$.
Prior to this work, few experimental studies have been conducted on ABC tri-layers, and up to 5-layers. A tunable band gap [32, 38], a spontaneous band gap [54], and an anomalous QHE [34, 37] have been reported in this system.

In our magneto-Raman experiments, we reveal the nature of the rhombohedral stacking order in our N-LG sample from the observed electronic excitations. Two families of inter-Landau level transitions are observed. The first family consists of well-resolved

excitations that have an almost linear dependence with the magnetic field, however their slopes are strangely inclined toward negative energies onset. This unusual dispersion is in clear contrast to the Landau level dispersion of Bernal-stacked multilayer graphene. The second family of transitions are even more surprising. They have a dispersion that decreases with magnetic fields and then inverts tendency to grow almost linearly. At zero magnetic field, they condense at a finite energy to form a broad feature that is seen in Raman scattering. The location of this zero-field feature is found to be very sensitive to the thickness of the rhombohedral sequence. The analysis of these transitions with magnetic fields reveal the existence of rhombohedral sequences as long as 17 monolayers. Despite the rich excitation spectra observed in our experiment, we can account for all the transitions with our tight binding model. Only the inter-layer and intra-layer coupling constants are needed to fully understand the observed features. Under the effect of magnetic fields, the nearly flat bands at zero energy contribute the first family of inter-Landau level transitions, while the second family of transitions is associated with the lowest in energy gaped bands in the band structure of rhombohedral N-LG. The results of Chapter 5 open the route to a simple Raman characterization of rhombohedral multilayer graphene flakes.

Still, more studies are needed to fully understand the physical properties of rhombohedral graphite. It is still unknown if such a material can host superconductivity or ferromagnetism, especially that several papers have reported measuring these properties on different graphite specimens without giving a convincing explanation to the origin of their results [60, 62, 63]. Another point is the presence or not of an intrinsic band gap in this stacking order and what are the experimental conditions that allow its observation.

Finally, part of the work presented on Chapter 4 resulted in the publication of a peer review article in the journal **Physical Review Letters**, of *the American Physical society*. While another part of the work presented in Chapter 4 is in preparation for submission to publication. The results obtained in Chapter 5 resulted in the publication of another peer review article in the journal **Nano Letters**, of *the American Chemical Society*. The links to these publications are given below.

(a) Landau Level Spectroscopy of Electron-Electron Interactions in Graphene:
PRL 114, 126804 (2015)
DOI: 10.1103/PhysRevLett.114.126804

(b) Rhombohedral Multilayer Graphene: A Magneto-Raman Scattering Study:
Nano Lett. 2016, 16, 3710-3716.
DOI: 10.1021/acs.nanolett.6b01041.

6.2 Conclusions (Français)

Depuis son premier isolement expérimental, le graphène a offert la possibilité à l'observation de nombreux effets inhabituels. Douze ans se sont écoulés depuis les premiers articles publiés sur les propriétés de ce matériau, et pourtant il continue à faire l'objet d'intenses recherches scientifiques, avec plus d'études de nos jours qui sont orientées vers ses applications potentielles dans l'ingénierie futurs et dispositifs électroniques.
Tout au long de cette thèse de doctorat, nous avons abordé deux questions fondamentales sur la physique du graphène:
(i) Les effets de l'interaction avec son milieu environnant sur les propriétés physiques du graphène.
(ii) La différence dans les propriétés électroniques de plusieurs couches de graphène en fonction de leur configuration d'empilement cristallographique.
Ces questions ont été abordées par la mesure de tous les échantillons étudiés sous champs magnétiques intenses et continus, disponibles au " Laboratoire National des Champs Magnétiques Intenses, LNCMI-CNRS ", à Grenoble. Nous avons utilisé exclusivement la spectroscopie micro-Raman pour sonder la réaction des systèmes étudiés sous l'effet des champs magnétiques. Les résultats originaux obtenus dans cette thèse de doctorat ont été présentés dans tous leurs détails dans le Chapitre 4 et le Chapitre 5.

La force du couplage effective des particules chargées, donné par la constante de structure fine de l'électrodynamique quantique, est redimensionné à une valeur d'environ 2 dans le graphène. Sachant cela, la force de l'interaction de Coulomb ne peut être ignorée lorsqu'on étudie la dynamique des porteurs de charge dans le graphène. De plus, les transitions optiques comme dans les systems de gaz bidimensionnel classiques avec des bandes paraboliques sont insensibles aux effets à N corps, comme indiqué par le théorème de Kohn [198]. Le graphène, cependant, a une dispersion linéaire autour de la neutralité de charge. Par conséquent, ses porteurs de charge relativistes échappent à ce théorème et les effets à N corps contribuent donc à sa réponse magnéto-optique [227]. En plus, la force du couplage effective peut être modulée en fonction de l'environnement dans lequel le graphène est immergé, donnant lieu à des forces d'interactions Coulombiennes différentes.

Pour adresser ces problématiques, nous avons démontré les effets des interactions de Coulomb sur la structure de la bande du graphène dans le Chapitre 4. Nous avons étudié la réponse magnéto-Raman du graphène dans trois systèmes différents : le graphène suspendu, le graphène sur la surface de graphite en vrac et graphène encapsulé dans hBN. Nous notons que dans le cadre de ce travail, notre contribution a été les mesures magnéto-Raman du graphène encapsulé dans des couches de hBN ou deposé sur leurs surfaces, tandis que les résultats obtenus sur le graphène suspendu, et le graphène sur

la surface de graphite ont été utilisés comme des résultats comparatifs à nos données expérimentales. Notre travail a été motivé par des résultats expérimentaux rapportant les signatures des effets à N corps dans des échantillons de graphène. Dans leur étude de la spectroscopie infrarouge des niveaux de Landau dans des échantillons de graphène de haute qualité [217], Jiang *et al.* ont montré que les vitesses de bande associées aux transitions observées sont différentes. Une étude des mesures de transport menée par Elias *et al.* [215] a démontré l'effet des interactions de Coulomb dans le remodelage de la dispersion de bande à faible énergie dans le graphène par une re-normalisation de sa vitesse de bande avec une divergence logarithmique autour du point de neutralité de charge.

Ainsi, il est intéressant d'étudier le rôle des interactions à N corps en présence d'un champ magnétique, où les spectres d'excitation sont dominés par des transitions inter-bandes entre niveaux de Landau. Pour ce faire, la réponse magnéto-Raman du graphène dans des environnements différents a été sondé. Nous avons eu la possibilité de comprendre comment la fonction diélectrique du milieu environnant le graphène a une incidence sur la force des interactions de Coulomb, et donc la dispersion de l'énergie dans le graphène. Nous avons combiné deux analyses différentes. Tout d'abord, nous avons étudié la résonance magnéto-phonon, qui est le couplage du E_{2g} phonon optique au point Γ avec les transitions inter-Landau niveau qui obéit à des règles de sélection $\Delta|n| = \pm 1$. Les interactions de Coulomb induisent un mélange des fonctions d'onde électroniques des niveaux de Landau. Ce mélange des niveaux de Landau est considéré comme le couplage du E_{2g} phonon optique avec les transitions symétrique inter-niveau de Landau $\Delta|n| = 0$, censés être interdites pour des raisons de symétrie. Deuxièmement, les transitions symétriques inter-niveau de Landau qui sont actives dans les spectres Raman ont été étudiés. L'analyse de leur dispersion dans des champs magnétiques révèle une vitesse de bande associée qui dépend de la fonction diélectrique du milieu environnant, diminue de façon logarithmique avec la valeur du champ magnétique, et augmente avec l'indice de niveau de Landau.

Une conclusion simple suit les résultats expérimentaux du Chapitre 4, les transitions optiques ($\Delta k \sim 0$) sont une sonde à l'interaction électrons-électrons dans le graphène. Ces résultats montrent une brisure du model de la particule unique qui a été utilisé jusqu'à présent pour comprendre les propriétés électroniques du graphène sur les substrats SiO_2 /Si et de renforcer les preuves selon lesquels le nitrure de bore peut remplacer le silicium comme un substrat de choix pour étudier les propriétés du graphène.

Peu de temps après la découverte du graphène, sa structure de bande particulière a été démontré comme modulable par l'ajout de plusieurs couches de graphène au-dessus de l'autre. Non seulement le nombre de couches, mais aussi la façon dont les feuilles

du graphène sont empilées implique des changements dans sa structure de bande et donc ses propriétés électroniques. Ce degré de liberté ne présente pas seulement un cas intéressant à aborder en physique fondamentale, mais il pointe aussi vers des applications technologiques intéressantes autour des propriétés électroniques des matériaux 2D.

Le rôle que joue l'ordre d'empilement dans la modification des propriétés électroniques du graphène multicouche a été abordée dans le chapitre 5. Nous avons signalé la première observation expérimentale des excitations électronique dans l'échantillon de graphène multicouche avec un empilement rhomboédrique de ses couches de graphène. Cet empilement se trouve dans une quantité significative de flocons obtenus à partir de l'exfoliation mécanique du kish graphite. Cependant, cet ordre d'empilement échappe habituellement à la caractérisation en raison de sa faible abondance par rapport à l'empilement Bernal qui est plus stable.
Plusieurs articles théoriques ont souligné la nature topologique des états électroniques dans le graphène multicouche avec un empilement rhomboédrique de ses feuilles de graphène [55, 56, 59]. Les bandes presque plates au point de la neutralité de charge ont une densité électronique divergente qui peuvent favoriser l'observation de ferromagnétisme ou de la supraconductivité de surface dans ce matériau [39–41]. Toutes ces prédictions font du graphène multicouche rhomboédrique un système attrayant pour étudier. D'autre part, l'abondance de grandes séquences ABC en flocons exfoliées est limité, et il a été difficile de présenter, jusqu'à présent, une étude expérimentale approfondie de la structure de bande de ce matériau pour un nombre de couches $N > 5$.
Avant ces travaux, quelques études expérimentales ont été menées sur le ABC tri-couches, et jusqu'à 5 couches. Un gap de bande modulable [32, 38], un gap de bande spontanée [54], et une anomalie dans l'effet Hall quantique [34, 37] ont été rapportés dans ce système.

Dans nos expériences de magnéto-Raman, nous révélons la nature de l'ordre d'empilement rhomboédrique dans notre échantillon N-LG à partir des excitations électroniques observées. Deux familles de transitions entre niveaux de Landau sont observées. La première famille est constituée des excitations bien résolus qui ont une dépendance quasi linéaire avec le champ magnétique, mais leurs pentes sont étrangement inclinées vers les énergies négatives à champ nul. Cette dispersion inhabituelle est en net contraste avec la dispersion des niveaux de Landau du Bernal empilés dans le graphène multicouche. La deuxième famille de transitions est encore plus surprenante. Ils ont une dispersion qui est au debut négative avec le champ magnétique, mais qui inverse de tendence pour augmenter avec le champ. A champ nul, il se condensent à énergie finie sous forme du bande large qui est observable dans les spectres Raman. La localisation de leur forme en champ nul se trouve être très sensible à la longueur de la séquence rhomboédrique. L'analyse de ces transitions avec des champs magnétiques révèlent l'existence

de séquences rhomboédriques aussi longue que 17 monocouches.
Malgré les riches spectres d'excitation observée dans notre expérience, nous pouvons tenir compte de toutes les transitions avec notre modèle de liaison étanche. Seules les constantes inter-couche et de couplage intra-couche sont nécessaires pour bien comprendre les caractéristiques observées. Sous l'effet des champs magnétiques, les bandes presque plates à zéro énergie contribuent la première famille de transitions inter- niveau de Landau, tandis que la deuxième famille de transitions est associée à la plus faible dans l'énergie des bandes séparées dans la structure de bande du graphène multicouche rhomboédrique. Les résultats du Chapitre 5 ouvrent la voie à une caractérisation Raman simple des flocons de graphène multicouches rhomboédriques.

Pourtant, d'autres études sont nécessaires pour mieux comprendre les propriétés physiques du graphite rhomboédrique. On ignore encore si un tel matériau est un hôte pour la supraconductivité ou le ferromagnétisme, surtout que plusieurs travaux ont rapporté la mesure de ces propriétés sur différents échantillons de graphite sans donner une explication convaincante quant à l'origine de leurs résultats [60, 62, 63]. Un autre point est la présence ou non d'un gap de bande intrinsèque dans cet ordre d'empilement et quelles sont les conditions expérimentales qui permettent son observation. Enfin, une partie des travaux présentés sur le Chapitre 4 ont abouti à la publication d'un papier dans la revue **Physical Review Letters**, de *The American Physical Society*. Tandis qu'une autre partie du travail présenté dans le chapitre 4 est en préparation pour la soumission à la publication. Les résultats obtenus dans le Chapitre 5 ont abouti à la publication d'un autre article de revue dans le journal **Nano Letters**, de *The American Chemical Society*. Les liens vers ces publications sont donnés ci-dessous.

(a) Landau Level Spectroscopy of Electron-Electron Interactions in Graphene:
PRL 114, 126804 (2015)
DOI: 10.1103/PhysRevLett.114.126804

(b) Rhombohedral Multilayer Graphene: A Magneto-Raman Scattering Study:
Nano Lett. 2016, 16, 3710-3716.
DOI: 10.1021/acs.nanolett.6b01041.

Chapter 7

Annex

7.1 Graphene and bilayer graphene encapsulated on hBN

7.1.1 Advantage of using hBN as a substitute substrate to silicon

In this section we should give a brief description of the investigated samples in Chapter 4, as well as the process that allows the fabrication of these hetero-structures. The samples investigated are exfoliated flakes of graphene and bilayer graphene transferred on a thin layer of hBN with a thickness of 30 nm. The orientation of the graphene layer with respect to the hBN is random. Another thin hBN layer is then transferred on top of the structure to encapsulate the graphene or bilayer graphene layers. We preformed magneto-Raman experiments on a G-hBN sample that was provided by the group of Prof. *Philip Kim* from Columbia University, and BG-hBN sample that was provided by the group of Prof. *Andre Geim* from Manchester University. The details of the fabrication process has been explained in details in the literature [218, 219, 238].
Such graphene based hetero-structures significantly increase the quality of graphene flakes compared to those deposited on Si/SiO_2 substrate. Indeed, hBN is relatively inert and is expected to be free of dangling bonds or surface charge traps. The hBN crystal is an insulating isomorph of graphite (i.e., hexagonal lattice) with boron and nitrogen atoms occupying the in-equivalent A and B sub-lattices in a Bernal stacking configuration, but with a small lattice mismatch (1.7%) compared to graphite. Furthermore, the atomically planar surface should suppress rippling in graphene, which has been shown to mechanically conform to both corrugated and flat substrates [239, 240]. The dielectric

properties of h-BN ($\epsilon \sim 3-4$ and $V_{breakdown} \sim 0.7$ V nm^{-1}) compare favorably with those of SiO_2, allowing the use of hBN as an alternative gate dielectric with no loss of functionality [218, 241].

While on SiO_2 and similar oxide-based substrates, graphene carriers mobility is limited by scattering from charged surface states and impurities [242–246], hBN seems to present an ideal substrate for high quality graphene electronics due to the qualities mentioned above. This was first demonstrated by Dean *et al.* [218] in their transport experiments on G-hBN gated structures, where the field effect mobility can reach $\mu_{FE} \sim 140,000$ cm $^{-1}$ V $^{-1}$ s $^{-1}$ near the charge neutrality. When deterministically aligning graphene on hBN, novel quantum phenomena emerge thanks to the interplay potential between graphene and hBN layers. Most notable effects are the observation of an intrinsic band gap in aligned graphene-hBN structures [126] by means of magneto-infrared spectroscopy measurements, as well as the FQHM [219]. These observations lead to an increasing interest on graphene-hBN hetero-structures. The detailed magneto-Raman spectroscopy study performed on such structures will be presented in Chapter **??**.

7.1.2 Fabrication process

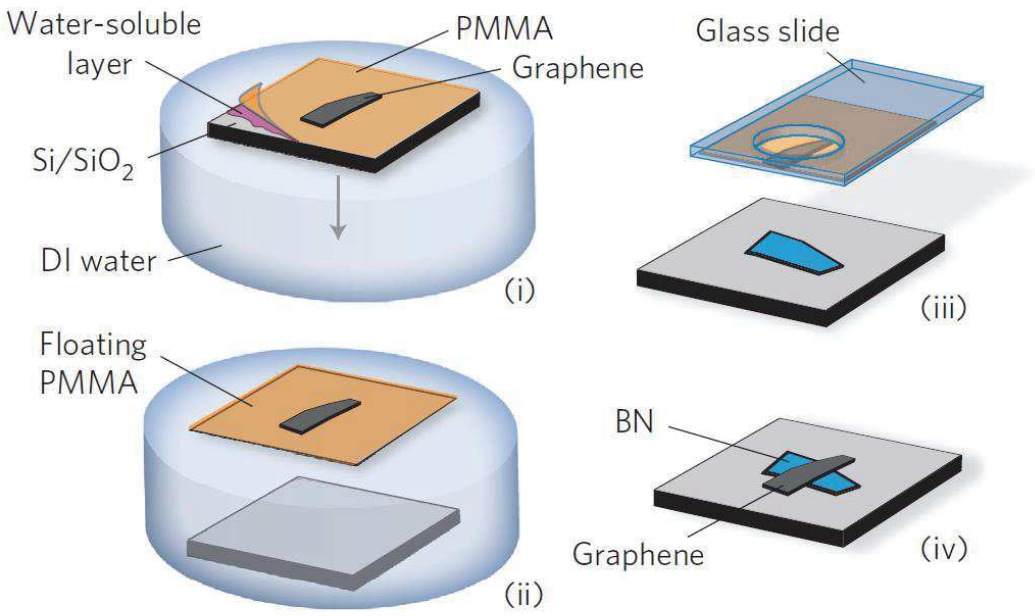

FIGURE 7.1: Four steps process that has been used to fabricate graphene-hBN hetero-structures. Figure taken from [219].

Graphene-hBN devices were fabricated according to the procedure illustrated in Figure 7.1. First of all, the fabrication began with the mechanical exfoliation of hBN single crystals and transferring them onto a silicon substrate with a SiO_2 layer of 285 nm.

Graphene was exfoliated separately onto a polymer stack consisting of: a water-soluble layer (PMGI), and hydrophobic polymethyl-methacrylate layer (PMMA), and the substrate was floated on the surface of a de-ionized (DI) water bath (Figure 7.1(i)). The PMMA thickness was precisely tuned to allow identification of monolayer graphene by optical means. Once the water soluble polymer had dissolved, the Si substrate sank to the bottom of the bath (Figure 7.1(ii)), leaving the extremely hydrophobic PMMA floating on top.
The PMMA membrane (with the graphene flake on top) was adhered to a glass transfer slide (Figure 7.1(iii)), which was clamped onto the arm of a micro-manipulator mounted on an optical microscope. Using the microscope to optically locate the position of the graphene flake on the suspended polymer film, the graphene was precisely aligned to the target hBN and the two brought into contact. With this technique, the graphene could be positioned to within a few micrometers of the target position. During transfer, the target substrate was heated to 110 C° in order to drive off any water adsorbed on the surface of the graphene or h-BN flakes, as well as to promote good adhesion of the PMMA to the target substrate. Once transferred, the PMMA was dissolved in acetone (Figure 7.1(iv)) leaving graphene on top of the hBN.

7.2 Rhombohedral multilayer graphene

7.2.1 Optical contrast as an approach to identify graphene flakes

Here, we will discuss the fabrication process to obtain N-LG flakes as the one studied in Chapter5. Graphite crystal is the most stable allotrope of carbon atoms. To make graphene flakes, we exfoliate graphite crystals using the scotch-tape technique as pioneered by K. Novoselov and A. K. Geim. By performing AFM scanning measurements, a technique which is sensitive down to monolayer graphene (i.e., 0.34 nm), one can measure the thickness of the exfoliated flakes. In the case of Bernal-stacked N-LG, performing Raman characterization of the 2D band feature allow us to estimate the thickness of the flakes up to $\sim 4-5$ layers [91].
The first studied graphene flakes were transferred on top of SiO_2/Si substrate in order to perform transport measurements [6, 9, 15]. The advantage of placing thin graphite flakes on top of SiO_2/Si substrates stems from the fact that multiple reflections of light from thin metallic films on top of a dielectric substrate will induce a contrast in the reflected light from the metallic film with respect to the oxide layer [247]. This contrast, which strongly depends on the wave-length of the light illuminating the sample and on the thickness of the SiO_2 layer, enables the observation of monolayer graphene by the naked eye using simple optical microscope set-up [248–252]. The optical contrast of graphene

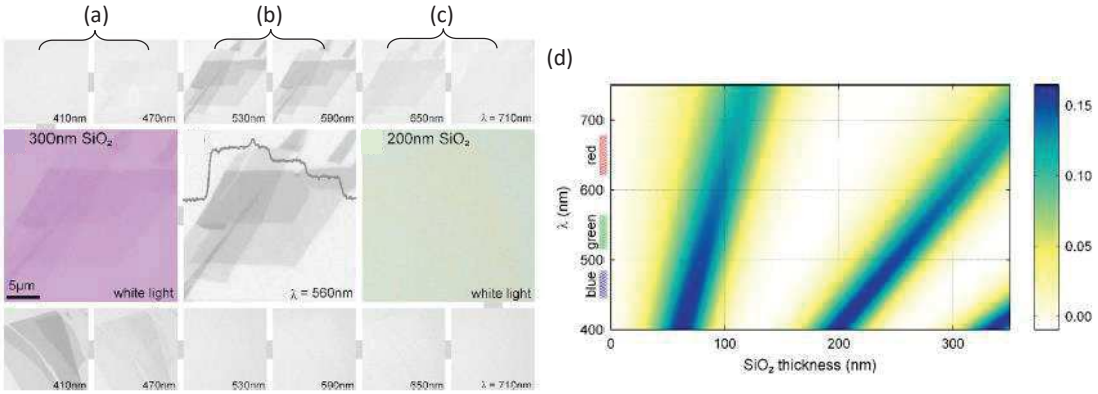

FIGURE 7.2: Optical microscope imaging of graphene flakes. The flakes contain areas of different thickness so that one can see changes in a flake's visibility with increasing numbers of layers. White light illumination on a 300 nm SiO_2 layer in (a), and green light (560 nm) illumination on a 300 nm SiO_2 layer in (b). (c) White light illumination on a 200 nm thick SiO_2 layer. Top and bottom panels in (a-c) show the same flakes but illuminated through various narrow band-pass filters. (d) False color map of the contrast from monolayer graphene as a function of the oxide thickness and the excitation wave-length. Figures were taken from [248].

on top of SiO_2/Si substrate also depends on the thickness of the flakes. Consequently, not only graphene can be visualized using simple optical microscope set-up, but one can also estimate the thickness of these exfoliated flakes from their apparent contrast using the classical laws of optics.

Figure 7.2 shows optical microscope images of the contrast from different graphene flakes as a function of the wave-length of the illuminating light, as well as the thickness of the SiO_2 layer [248]. While graphene flakes, when illuminated with white light, are clearly visible on top of SiO_2/Si wafer with an oxide thickness of 300 nm (Figure 7.2a), the transferred flakes on top of Si/ SiO_2 with an oxide thickness of 200 nm (Figure 7.2c) are completely invisible under white light illumination, and their invisibility holds until they reach a thickness of more than 10 layers. Figure 7.2b shows a maximum visibility of the flakes under green light illumination, and the traces are step-like changes in the contrast for 1, 2, and 3 layers. This proves that the contrast can also be used as a quantitative tool for defining the number of graphene layers on the silicon substrate.
The result of these observations in the case of monolayer graphene are summarized in Figure 7.2d, that shows a false color map of the contrast between the graphene flake and the SiO_2 layer for different excitation wave-lengths and different oxide thickness. Consequently, optical microscope imaging became a standard procedure to visualize exfoliated graphene flakes and other 2D materials when placed on Si/SiO_2 substrate, and to estimate their thickness in the limit of few layers (< 20 layers).

7.2.2 Mechanical exfoliation

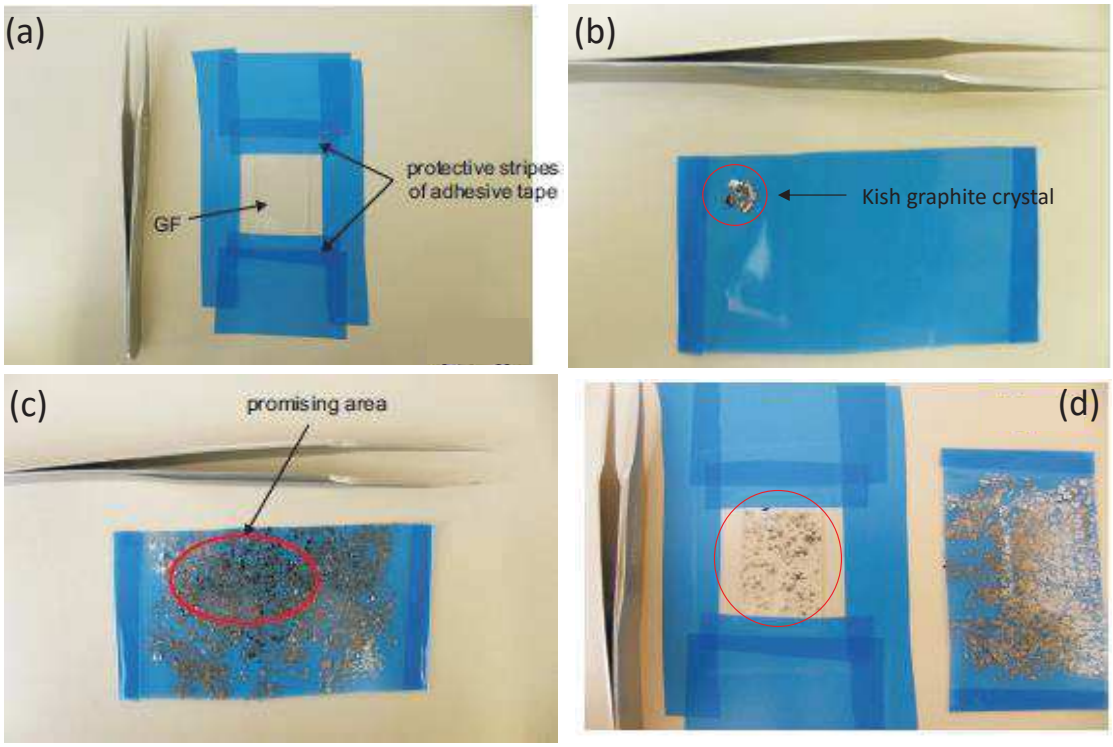

FIGURE 7.3: (a) GF placed on the table using blue adhesive scotch-tape. (b) A piece of kish graphite crystal is placed on the corner of a blue adhesive tape (F08xx). (c) Results of sticking and unfolding the kish graphite on the surface of the blue tape. An area which is uniformly covered with thick flakes is selected to be transferred on the GF (red circle).(d) The region of interest is transferred to the GF (encircled in red).

Most of the exfoliated N-LG flakes exhibit the Bernal (ABA) stacking, which is the most thermodynamically stable crystallographic order of graphite [23]. However, as we will discuss in Chapter 5, kish graphite allows to obtain a large amount of multilayer graphene flakes with rhombohedral (ABC) stacking compared to natural graphite [75]. The fact that rhombohedral N-LG flakes are easily found from the exfoliation of kish graphite seems to be related to the way kish graphite is produced. Indeed, kish graphite is a byproduct of steel-making. It is obtained when carbon crystallizes from molten steel during the steel manufacturing process. Thus, we might expect that during the process of steel-making many areas from the graphite crystals did not relax to the Bernal stacking during the cooling process, and instead exhibit less stable configurations, such as the rhombohedral stacking or a mixture of Bernal and rhombohedral.

In the following, we should present a standard approach to obtain multilayer graphene flakes from the mechanical exfoliation of bulk graphite using polymer-based adhesive tapes. The process of exfoliation can be divided in two major steps: (i) Producing thin graphite crystals on the surface of a polymer substrate, referred to as 'poly-dimethyl-siloxane', or 'PDMS gel film'. (ii) Transferring the graphene flakes from the gel film to

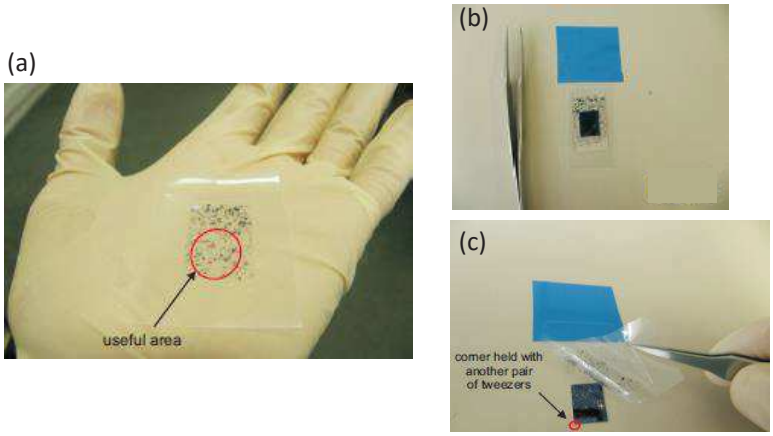

FIGURE 7.4: (a) The red circle shows the region of interest we will transfer in the silicon substrate. It is chosen based on the uniformity of thickness of the flakes and the density of coverage. (b) The GF is brought in contact with the silicon substrate. (c) The GF is slowly removed from its contact with the substrate starting from a corner (small red circle). This slow removal allows to transfer maximum of matter from the GF to the silicon substrate.

the top of a silicon substrate.

The blue adhesive tape, that we use to exfoliate graphite, came with different adhesive strengths that are specified by the manufacturer: F07xx (high,used to stuck the GF on the table), F08xx (medium, will be used for exfoliation), and F09xx (low, is not used in this process).

The GF is a material of choice in producing graphene flakes on top of silicon substrate. Indeed, its top and bottom surfaces are covered with two protective foils, one of them is of high transparency and strong adhesion strength, while the other is of reduced transparency and weak adhesion strength. Both of these foils can be used for different purposes, but more importantly the GF placed in between present an ultra clean surface, relevant to obtain graphene flakes on silicon substrate with no significant contamination. This is not the case when using standard adhesive tapes to transfer graphite flakes on top of the silicon substrate, where the acrylic glue residues, a substance usually present in commercial adhesive tapes, can induce a highly contaminated samples. The acrylic glue interacts strongly with coherent lights (i.e., lasers) which induces a strong luminescence that renders optical measurements complicated. Hence the choice of the GF seems to be an ideal approach to produce very clean graphene samples.

The gel film (GF) is first placed on a clean table, it is then stuck to the table using several stripes cut from a very adhesive blue tape (Figure 7.3a). Meanwhile, another strip of the F08xx blue tape is prepared, on top of which a small piece of kish graphite crystal is placed at the corner as seen in Figure 7.3b. The exfoliation is performed by folding and sticking two parts of the tape together in a way that avoids overlaps and maximizes the coverage with flakes on all the tape's surface. Figure 7.3c shows the

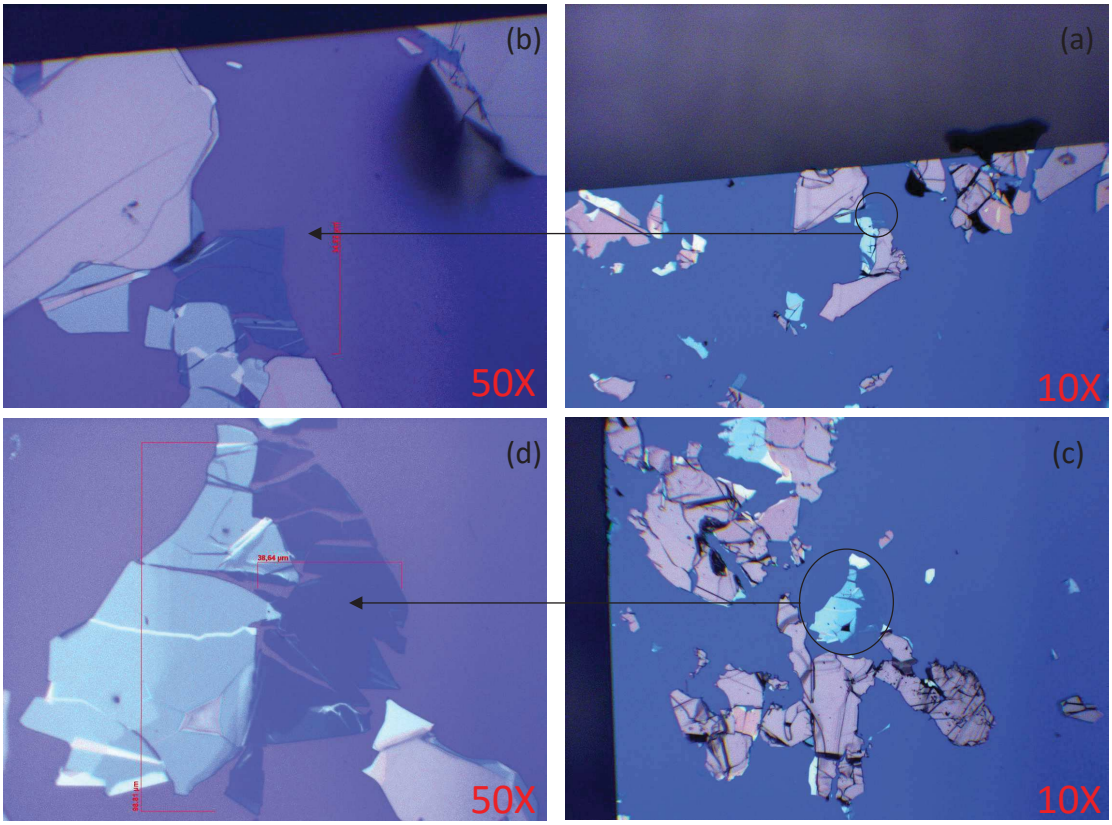

FIGURE 7.5: Optical microscope images of the flakes transferred on the silicon substrate. Right panels show 10X magnification images of two regions that contain multilayer graphene flakes (a,c). (b,d) 50X magnification of the multilayer graphene flakes.

resulting coverage from the exfoliation process, which should be dense and with relatively thick flakes. The next step consists of transferring the flakes from the tape to the GF placed on the table, after selecting a promising area covered with flakes of similar thickness (i.e., without big and thick crystallites), we stick the part of interest to the exposed surface of the GF in order to transfer maximum of flakes on the surface of the GF (Figure 7.3d).

The second part consists of transferring the flakes from the GF to the SiO_2/Si substrate. The target substrate is first placed on the table, and then we bring an area of interest from the GF (uniform coverage and thickness, as seen in Figure 7.4a in contact with the substrate by applying a delicate pressure using a thumb (see Figure 7.4b). The last step consists of stabilizing the substrate by holding it with tweezers on one of its corners, and using another pair of tweezers we start to peel off the GF. The detachment should be very slow to completely remove the GF, in order to transfer maximum of matter from the GF to the silicon substrate. For an ideal approach, the peel-off angle should be larger than 120; a good idea is to move along the substrate's diagonal when peeling-off the GF as illustrated in Figure 7.4c.

Figure 7.5 shows the results of the exfoliation process, after the kish graphite flakes

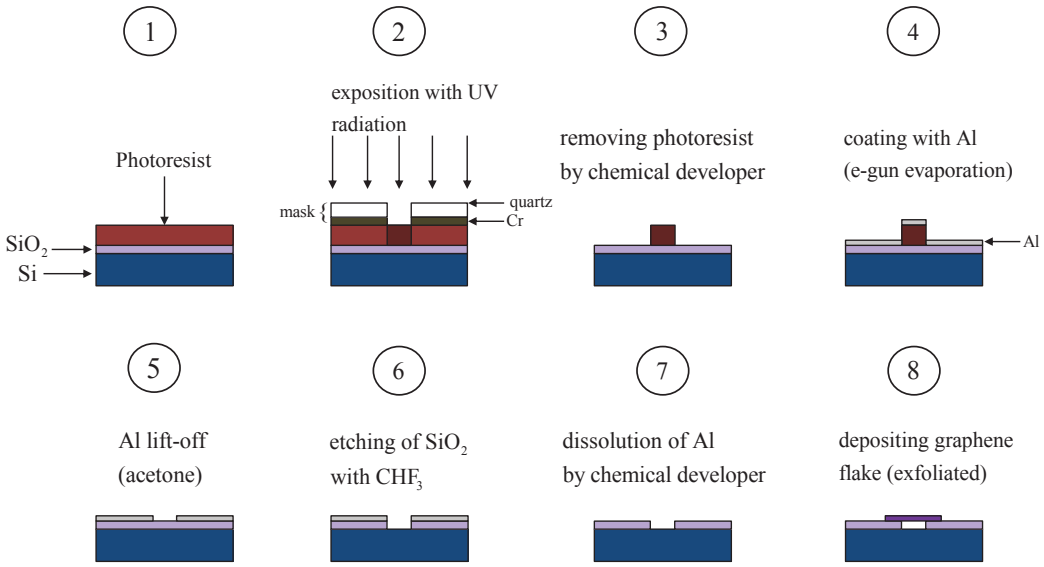

FIGURE 7.6: Schematic presentation of the 8 steps process to obtain suspended flakes of graphene over the silicon substrate.

has been transferred on the silicon substrate. Experiments using magneto-Raman spectroscopy (refer to Chapter5) show that these flakes exhibit rhombohedral stacking domains, with large sequence. Their signature is conspicuous in Raman spectroscopy even at room temperature.

7.2.3 Suspended flakes by means of optical lithography

In this section we will present the approach we used to make a suspended multilayer graphene flakes for magneto-Raman spectroscopy measurements.
Indeed, suspended flakes do not suffer interaction with the substrate. Such interaction causes changes in the properties of graphene, such as charge doping, impurities scattering, dangling of graphene surface due to the rough SiO_2 surface. From Raman spectroscopy point of view, placing graphene on silicon substrate makes the observation of electronic Raman scattering, with or without magnetic fields, highly un-likely. The main reasons are the non-neutrality of the system, the presence of disorder, and charge trapping. Thus, making suspended graphene flakes over the substrate is crucial to get the best Raman response from the suspended regions, and to probe the intrinsic properties of this material.

The process of making suspended graphene flakes over the substrate is performed in a clean-room facility. The whole process can be summarized as the following: the Si substrate needs to get pre-patterned with equidistant circular holes on its oxide layer,

so then we can transfer an exfoliated flake on its surface, where parts of the flake will be suspended on top of the holes. The holes diameter needs to be bigger than the laser spot diameter in order to investigate the suspended regions individually. But not that big in order to suspended graphene flakes on its surface.
This process is performed following an 8 steps procedure, as seen in Figure 7.6. The first three steps are performed using the so-called optical lithography technique. This technique, which used intensively for fabricating micro-structures, consists of printing a pattern of a polymer-based substance, called photo-resist (PR), on top of the Si substrate by exposing it to electromagnetic radiation. The PR, as its name suggests, is either weakened or strengthened by exposure to specific ranges of wave-lengths from the electromagnetic spectrum.

After cleaning the Si substrate with acetone and DI water, we proceed to deposit the PR by placing a drop of it on top of the substrate and spin-coating it at high speed. The centrifugal force will cause the PR to expand on the whole surface of the Si substrate. After baking the (PR+Si) at high temperatures (80 to 100 C°, depending on the nature of the PR), the PR will solidify on the Si substrate. The next step consist of printing the pattern on the PR. This is done by placing a quartz-chromium mask, with well-defined patterns, on top of the (Si+PR) sample (see Figure 7.6, step 2). The exposition of the (mask+PR+Si) system to ultraviolet (UV) light will strengthen the exposed PR that is not masked by the quartz-chromium mask, while the rest of the PR is screened from the UV radiation. Consequently, after placing the sample on a chemical developer, the unexposed PR will dissolve leaving only the exposed PR on the Si substrate (Figure 7.6, step 3).

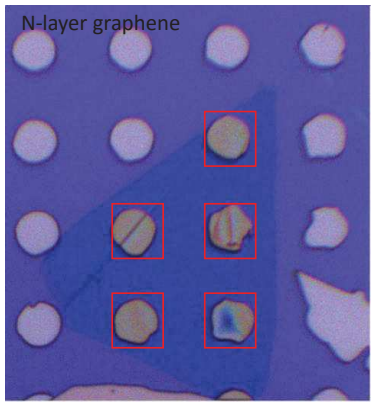

FIGURE 7.7: N-LG on top of the Si substrate, with holes pattern obtained from the procedure described in the main text.

Now that we produced a Si/SiO_2 substrate with patterns of PR on its top, we proceed to etch patterned holes on the oxide layer. To do so, we deposit a hard layer of aluminum (Al) using an evaporation set-up (MEB EVAP Plassys 550S) available in the clean room. The results of Al deposition, with a thickness 100-120 nm, are shown in the step 4 of Figure 7.6 where the Al layer tops the Si substrate and also the PR. The sample is then placed on an acetone solution that dissolves the PR. Consequently, only the Al in direct contact with the Si substrate will remain (Figure 7.6, step 5). We end up having a pre-patterned substrate with parts of SiO_2 exposed to air, while the remaining surface is under a hard Al layer. Afterwards, the exposed regions of SiO_2 are removed by placing the sample on a vacuum chamber and using a fluorocarbon plasma (CHF_3). The set-up

is called reactive ion etching (RIE), and is available at the clean room. The RIE plasma will etch the surface of the sample, leaving a thin layer of Al and a highly reduced or in-existent SiO_2 layer on the regions that were not primary covered with the Al layer (Figure 7.6, step 6). A chemical developer is used to completely remove the Al layer from the surface of the substrate, leaving a clean Si/SiO_2 substrate with holes pattern on the surface of the oxide layer, as seen in step 7 of Figure 7.6. This substrate will be used in the process of exfoliation to produce partially suspended flakes of N-LG.
The results of such a procedure are shown in Figure 7.7, where an N-LG flake has been exfoliated non-deterministically on top of the pre-patterned Si substrate. The flake is suspended over five different holes of 6 μm diameter each, which allows to perform Raman scattering measurements selectively on these regions. The results of the magneto-Raman scattering measurements performed on this suspended N-LG flake will be discussed in details in Chapter 5.

7.3 Interference effect on the Raman spectrum of multi-layer graphene

In this section, we will explain how the Raman signal, measured on the N-LG flake from Chapter 5, is greatly enhanced on the suspended parts. The enhancement of the Raman intensity for the G and 2D modes can be modeled using the multiple interference effect of the Raman scattered light on the graphene layer and the layer of air between graphene and the Si substrate. To do so, we start by computing the enhancement factor for the configuration graphene/SiO_2/Si, as was done in the literature [36, 234, 235], using the Fresnel equations for transmission and reflection of electromagnetic radiation by the thin layers of graphene and SiO_2, deposited on the Si substrate. The Fresnel transmittance and reflection coefficients for the interfaces involving air (0), graphene (1), SiO_2 (2), and Si (3) are given by:

$$t_1 = \left(\frac{2n_0}{\tilde{n}_1 + n_0}\right), \quad r_1 = \left(\frac{n_0 - \tilde{n}_1}{n_0 + \tilde{n}_1}\right), \quad r_2 = \left(\frac{\tilde{n}_1 - \tilde{n}_2}{\tilde{n}_1 + \tilde{n}_2}\right), \quad r_3 = \left(\frac{\tilde{n}_2 - \tilde{n}_3}{\tilde{n}_2 + \tilde{n}_3}\right), \tag{7.1}$$

$n_0 = 1$ is the refractive index of air, and $\tilde{n}_1$, $\tilde{n}_2$, and $\tilde{n}_3$ are the refractive indexes for graphene, SiO_2, and Si, respectively.
Figure 7.8 shows a schematic presentations of the multiple interference effect on layers of graphene and SiO_2 over the Si substrate. The color of the SiO_2 layer is caused by the interference of light reflected off the Si (below the oxide) and the light reflected off the top of the oxide layer. As the SiO_2 thickness changes, so does the interference and the SiO_2 seen color, hence the rainbow color chart in Figure 7.8.
In the multiple interference effect model, the absorption and scattering terms are treated

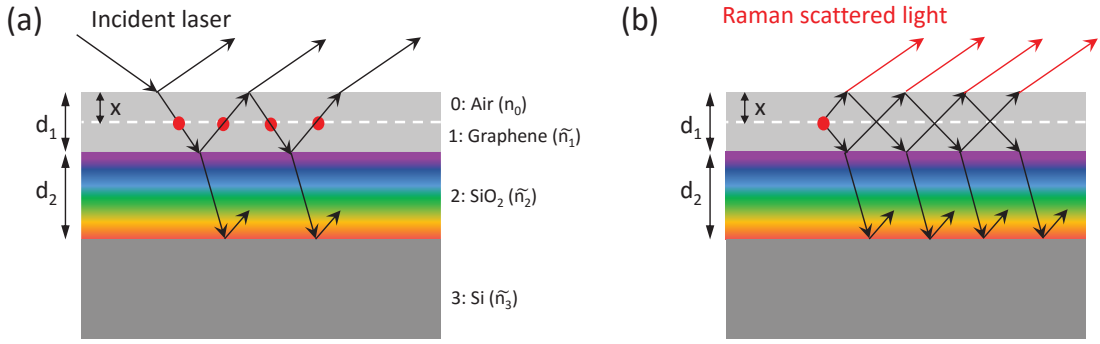

FIGURE 7.8: Schematic diagrams of multiple reflection interference in the (a) absorption and (b) scattering processes. n_0, $\tilde{n}_1$, $\tilde{n}_2$, and $\tilde{n}_3$ are the refractive indexes of air, graphene, SiO_2, and Si, respectively. d_1 and d_2 are the thickness of graphene and SiO2 layer, respectively, and x is the depth in the graphene layer. The dots are the points of interaction between the laser beam and the π electrons of graphene.

separately, since the differences between the wavelengths of the excitation laser, the G band and the 2D band are quite large. As shown in Figure 7.8a, the laser beam is absorbed by the π electrons of graphene while passing through the graphene layer. However, the laser beam goes through multiple reflections inside the graphene layer as well as in the SiO_2 layer. Due to these multiple reflections, there are multiple chances for the beam to be absorbed by the π electrons. Upon this, we can define the net absorption term (F_{ab}) as the sum of the dots in Figure 7.8a:

$$F_{ab} = t_1 \frac{[1 + r_2 r_3 e^{-2i\beta_2}]e^{-i\beta_x} + [r_2 + r_3 e^{-2i\beta_2}]e^{-i(2\beta_1 - \beta_x)}}{1 + r_2 r_3 e^{-2i\beta_2} + (r_2 + r_3 e^{-2i\beta_2}) r_1 e^{-2i\beta_1}}. \tag{7.2}$$

Similarly, the net scattering term (F_{sc}) could be represented by the sum of the red arrow lines in Figure 7.8b:

$$F_{sc} = t_1' \frac{[1 + r_2 r_3 e^{-2i\gamma_2}]e^{-i\gamma_x} + [r_2 + r_3 e^{-2i\gamma_2}]e^{-i(2\gamma_1 - \gamma_x)}}{1 + r_2 r_3 e^{-2i\gamma_2} + (r_2 + r_3 e^{-2i\gamma_2}) r_1 e^{-2i\gamma_1}}. \tag{7.3}$$

Here: $t_1' = \left(\frac{\tilde{n}_1}{\tilde{n}_1 + n_0}\right)$, and the following abbreviations for the absorption term has been used:

$$\beta_x = 2\pi \left(\frac{x\tilde{n}_1}{\lambda_{ex}}\right), \quad \beta_1 = 2\pi \left(\frac{d_1\tilde{n}_1}{\lambda_{ex}}\right), \quad \beta_2 = 2\pi \left(\frac{d_2\tilde{n}_2}{\lambda_{ex}}\right), \tag{7.4}$$

where x is the depth of the point where the interaction occurs in the graphene layer, d_1 and d_2 are respectively the thickness of the graphene and SiO_2 layers, and λ_{ex} is the wavelength of excitation. For the net scattering term, the excitation wavelength is replaced by either the scattered wavelength of the G band or the 2D band such as:

$$\gamma_x = 2\pi \left(\frac{x\tilde{n}_1}{\lambda_{sc}}\right), \quad \gamma_1 = 2\pi \left(\frac{d_1\tilde{n}_1}{\lambda_{sc}}\right), \quad \gamma_2 = 2\pi \left(\frac{d_2\tilde{n}_2}{\lambda_{sc}}\right). \tag{7.5}$$

The scattered wavelength (in meters) is given by:

$$\lambda_{G(2D)} = \frac{\lambda_{ex}}{1 - 10^{-7}(\omega_{G(2D)}\lambda_{ex}10^{9})}, \tag{7.6}$$

where $\omega_G \approx 1581$ cm^{-1} is the frequency of the G band in graphene. While for the 2D band, its energy disperses as a function of the excitation wavelength [84]. This dispersion can be given as a linear function [253]: $\omega_{2D} = 2444.24 + 99.06E_{laser}$cm^{-1}, where E_{laser} is the excitation laser energy given in eV.

The *total enhancement factor* of the Raman intensity is then calculated with respect to the total enhancement factor of the Raman intensity of a free standing multilayer graphene sheet. It is given by:

$$F = N \int_0^{d_1} |F_{ab}F_{sc}|^2 dx, \tag{7.7}$$

where N is the constant that represents the total enhancement factor for the free-standing multilayer graphene without the substrate:

$$F_{free} = \int_0^{d_1} |F_{ab}^{free}F_{sc}^{free}|^2 dx, \tag{7.8}$$

which is obtained by replacing the Si and SiO_2 layers by air.

The integral in 7.7 is calculated numerically. The enhancement in the Raman intensity is then given as:

$$I = I_i.F, \tag{7.9}$$

where I_i is the intrinsic Raman intensity playing the role of a single fitting parameter in the subsequent calculations.

In our analysis, we assumed a normal incidence of the wavelength of the excitation laser because our micro-Raman scattering measurements are performed in quasi back-scattering geometry.

In our experiments, the suspended N-LG over the Si substrate has no layer of SiO_2 below its surface, instead the etched hole on the oxide layer is assumed to be filled with air. The total enhancement factor for the G band, in this case of suspended N-LG over the substrate, is then calculated by replacing the refractive index of the SiO_2 layer by the refractive index of air (i.e., n_0=1) and making the same calculations for the net scattering and absorption terms for a thickness of N-LG that corresponds to 15 monolayers ($\sim$ 5.1 nm). Figure 7.9a,b shows false color maps of the calculated enhancement factor for graphene on SiO_2 and suspended N-LG over the Si substrate respectively. By assuming a hole depth that varies from 0 to 300 nm (i.e., when all the SiO_2 layer has been removed), we plotted the enhancement factor for the excitation wavelength 785 nm (see Figure 7.9c). For a depth of 300 nm (i.e., SiO_2 completely etched) the total enhancement

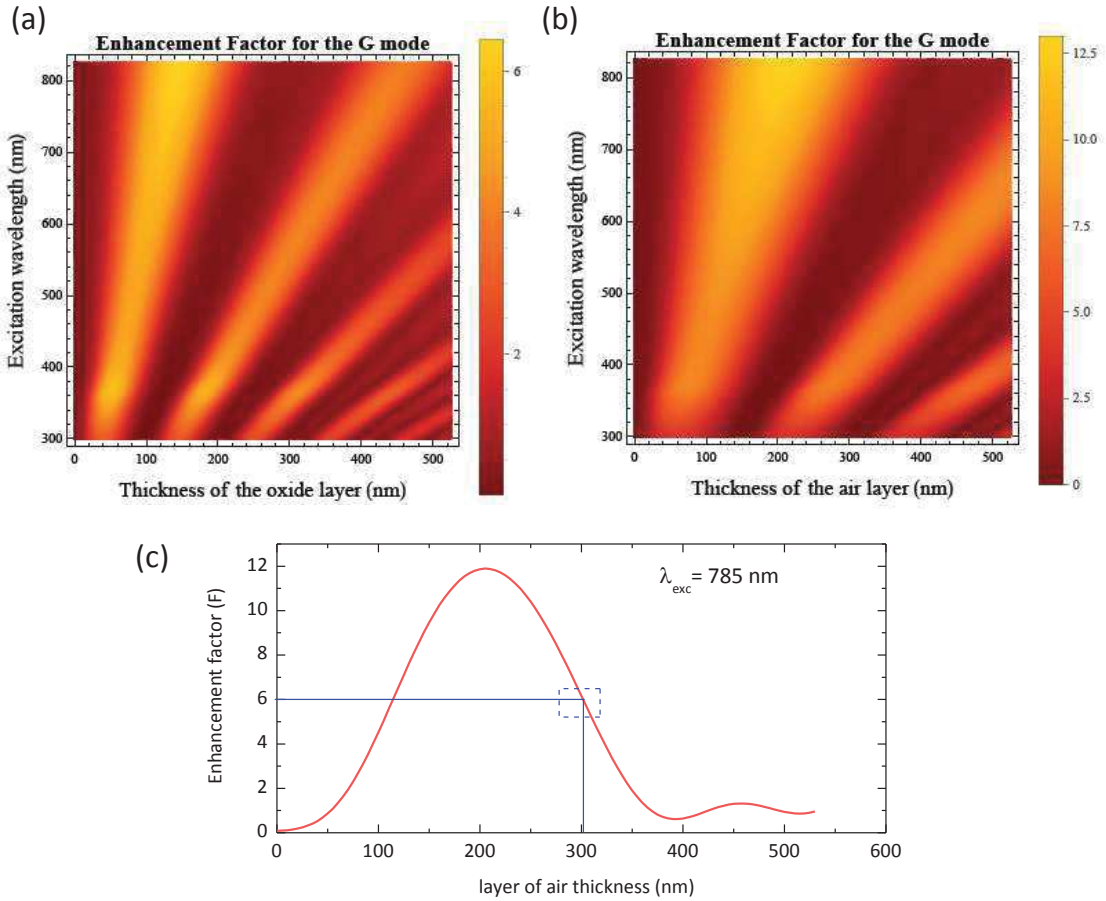

FIGURE 7.9: (a) False color map of the calculated Raman enhancement factor of the G band for graphene on SiO_2 as functions of the thickness of SiO_2 layer and the wavelength of the laser, and of the calculated Raman enhancement factor of the G band for suspended graphene over the Si substrate (b) as functions of the thickness of the hole depth filled with air and the wavelength of the laser. (c) The total enhancement factor for 785 nm excitation as a function of the depth of the hole in the oxide layer.

factor is ~ 6, which is in good agreement with the assumed mean value obtained from our Raman measurements.

Bibliography

[1] William M Haynes. *CRC handbook of chemistry and physics*. CRC press, 2014.

[2] MO Goerbig. Electronic properties of graphene in a strong magnetic field. *Rev. Mod. Phys.*, 83(4):1193, 2011.

[3] Linus Pauling. The nature of the chemical bond. application of results obtained from the quantum mechanics and from a theory of paramagnetic susceptibility to the structure of molecules. *Journal of the American Chemical Society*, 53(4): 1367–1400, 1931.

[4] Edward McCann. *Graphene Nanoelectronics: Metrology, Synthesis, Properties and Applications*, chapter Electronic Properties of Monolayer and Bilayer Graphene, pages 237–275. Springer Berlin Heidelberg, Berlin, Heidelberg, 2012. ISBN 978-3-642-22984-8. doi: 10.1007/978-3-642-22984-8_8. URL http://dx.doi.org/10.1007/978-3-642-22984-8_8.

[5] Charles Kittel. *Introduction to solid state physics*. Wiley, 2005.

[6] Kostya S Novoselov, Andre K Geim, SV Morozov, D Jiang, M Katsnelson, I Grigorieva, SV Dubonos, and AA Firsov. Two-dimensional gas of massless dirac fermions in graphene. *Nature*, 438(7065):197–200, 2005.

[7] Andre K Geim and Konstantin S Novoselov. The rise of graphene. *Nature materials*, 6(3):183–191, 2007.

[8] Konstantin S Novoselov, Z Jiang, Y Zhang, SV Morozov, HL Stormer, U Zeitler, JC Maan, GS Boebinger, P Kim, and AK Geim. Room-temperature quantum hall effect in graphene. *Science*, 315(5817):1379–1379, 2007.

[9] Yuanbo Zhang, Yan-Wen Tan, Horst L Stormer, and Philip Kim. Experimental observation of the quantum hall effect and berry's phase in graphene. *Nature*, 438 (7065):201–204, 2005.

[10] CWJ Beenakker. Colloquium: Andreev reflection and klein tunneling in graphene. *Reviews of Modern Physics*, 80(4):1337, 2008.

[11] N Stander, B Huard, and D Goldhaber-Gordon. Evidence for klein tunneling in graphene p- n junctions. *Physical Review Letters*, 102(2):026807, 2009.

[12] Rahul Raveendran Nair, Peter Blake, Alexander N Grigorenko, Konstantin S Novoselov, Tim J Booth, Tobias Stauber, Nuno MR Peres, and Andre K Geim. Fine structure constant defines visual transparency of graphene. *Science*, 320 (5881):1308–1308, 2008.

[13] Kin Fai Mak, Matthew Y Sfeir, Yang Wu, Chun Hung Lui, James A Misewich, and Tony F Heinz. Measurement of the optical conductivity of graphene. *Physical review letters*, 101(19):196405, 2008.

[14] Oskar Klein. Die reflexion von elektronen an einem potentialsprung nach der relativistischen dynamik von dirac. *Zeitschrift für Physik*, 53(3-4):157–165, 1929.

[15] Kostya S Novoselov, Andre K Geim, SV Morozov, D Jiang, Y Zhang, SV Dubonos, , IV Grigorieva, and AA Firsov. Electric field effect in atomically thin carbon films. *Science*, 306(5696):666–669, 2004.

[16] KS Novoselov, D Jiang, F Schedin, TJ Booth, VV Khotkevich, SV Morozov, and AK Geim. Two-dimensional atomic crystals. *Proceedings of the National Academy of Sciences of the United States of America*, 102(30):10451–10453, 2005.

[17] Philip Richard Wallace. The band theory of graphite. *Phys. Rev.*, 71(9):622, 1947.

[18] JC Slonczewski and PR Weiss. Band structure of graphite. *Phys. Rev.*, 109(2): 272, 1958.

[19] JW McClure. Band structure of graphite and de haas-van alphen effect. *Phys. Rev.*, 108(3):612, 1957.

[20] Claire Berger, Zhimin Song, Tianbo Li, Xuebin Li, Asmerom Y Ogbazghi, Rui Feng, Zhenting Dai, Alexei N Marchenkov, Edward H Conrad, Phillip N First, et al. Ultrathin epitaxial graphite: 2d electron gas properties and a route toward graphene-based nanoelectronics. *The Journal of Physical Chemistry B*, 108(52): 19912–19916, 2004.

[21] D. Gunlycke and C. T. White. Graphene valley filter using a line defect. *Phys. Rev. Lett.*, 106:136806, Mar 2011. doi: 10.1103/PhysRevLett.106.136806. URL http://link.aps.org/doi/10.1103/PhysRevLett.106.136806.

[22] Marcus Freitag. Graphene: Trilayers unravelled. *Nature Physics*, 7:596–597, 2011.

[23] JD Bernal. The structure of graphite. *Proceedings of the Royal Society of London*, 106(740):749–773, 1924.

[24] RR Haering. Band structure of rhombohedral graphite. *Canadian Journal of Physics*, 36(3):352–362, 1958.

[25] Kin Fai Mak, Jie Shan, and Tony F Heinz. Electronic structure of few-layer graphene: experimental demonstration of strong dependence on stacking sequence. *Phys. Rev. Lett.*, 104(17):176404, 2010.

[26] Kin Fai Mak, Matthew Y Sfeir, James A Misewich, and Tony F Heinz. The evolution of electronic structure in few-layer graphene revealed by optical spectroscopy. *Proceedings of the National Academy of Sciences*, 107(34):14999–15004, 2010.

[27] Chun Hung Lui, Zhiqiang Li, Zheyuan Chen, Paul V Klimov, Louis E Brus, and Tony F Heinz. Imaging stacking order in few-layer graphene. *Nano Lett.*, 11(1): 164–169, 2010.

[28] Kostya S Novoselov, Edward McCann, SV Morozov, Vladimir I Falko, M Katsnelson, U Zeitler, D Jiang, F Schedin, and AK Geim. Unconventional quantum hall effect and berry phase in bilayer graphene. *Nat. phys.*, 2(3):177–180, 2006.

[29] Yuanbo Zhang, Tsung-Ta Tang, Caglar Girit, Zhao Hao, Michael C Martin, Alex Zettl, Michael F Crommie, Y Ron Shen, and Feng Wang. Direct observation of a widely tunable bandgap in bilayer graphene. *Nature*, 459(7248):820–823, 2009.

[30] Mikito Koshino. Stacking-dependent optical absorption in multilayer graphene. *New J. Phys.*, 15(1):015010, 2013.

[31] Stéphane Berciaud, Marek Potemski, and Clément Faugeras. Probing electronic excitations in mono-to pentalayer graphene by micro magneto-raman spectroscopy. *Nano Lett.*, 14(8):4548–4553, 2014.

[32] Chun Hung Lui, Zhiqiang Li, Kin Fai Mak, Emmanuele Cappelluti, and Tony F Heinz. Observation of an electrically tunable band gap in trilayer graphene. *Nat. Phys.*, 7(12):944–947, 2011.

[33] Zhiqiang Li, Chun Hung Lui, Emmanuele Cappelluti, Lara Benfatto, Kin Fai Mak, G Larry Carr, Jie Shan, and Tony F Heinz. Structure-dependent fano resonances in the infrared spectra of phonons in few-layer graphene. *Phys. Rev. Lett.*, 108 (15):156801, 2012.

[34] A. Kumar, W. Escoffier, J. M. Poumirol, C. Faugeras, D. P. Arovas, M. M. Fogler, F. Guinea, S. Roche, M. Goiran, and B. Raquet. Integer quantum hall effect in trilayer graphene. *Phys. Rev. Lett.*, 107:126806, Sep 2011. doi: 10.1103/PhysRevLett.107.126806.

[35] Chun Hung Lui, Leandro M Malard, SukHyun Kim, Gabriel Lantz, François E Laverge, Riichiro Saito, and Tony F Heinz. Observation of layer-breathing mode vibrations in few-layer graphene through combination raman scattering. *Nano lett.*, 12(11):5539–5544, 2012.

[36] Song-Lin Li, Hisao Miyazaki, Haisheng Song, Hiromi Kuramochi, Shu Nakaharai, and Kazuhito Tsukagoshi. Quantitative raman spectrum and reliable thickness identification for atomic layers on insulating substrates. *ACS Nano*, 6(8):7381–7388, 2012.

[37] Liyuan Zhang, Yan Zhang, Jorge Camacho, Maxim Khodas, and Igor Zaliznyak. The experimental observation of quantum hall effect of l= 3 chiral quasiparticles in trilayer graphene. *Nat. Phys.*, 7(12):953–957, 2011.

[38] W. Bao, L. Jing, J. Velasco Jr, Y. Lee, G. Liu, D. Tran, B. Standley, M. Aykol, S. B. Cronin, D. Smirnov, M. Koshino, E. McCann, M. Bockrath, and C. N. Lau. Stacking-dependent band gap and quantum transport in trilayer graphene. *Nat. Phys.*, 7(12):948–952, 2011.

[39] Minoru Otani, Mikito Koshino, Yoshiteru Takagi, and Susumu Okada. Intrinsic magnetic moment on (0001) surfaces of rhombohedral graphite. *Phys. Rev. B*, 81: 161403, Apr 2010. doi: 10.1103/PhysRevB.81.161403. URL http://link.aps.org/doi/10.1103/PhysRevB.81.161403.

[40] NB Kopnin, M Ijäs, A Harju, and TT Heikkilä. High-temperature surface superconductivity in rhombohedral graphite. *Phys. Rev. B*, 87(14):140503, 2013.

[41] Richard Olsen, Ralph van Gelderen, and C Morais Smith. Ferromagnetism in abc-stacked trilayer graphene. *Phys. Rev. B*, 87(11):115414, 2013.

[42] Bart Partoens and FM Peeters. From graphene to graphite: Electronic structure around the k point. *Physical Review B*, 74(7):075404, 2006.

[43] Mikito Koshino. Interlayer screening effect in graphene multilayers with a b a and a b c stacking. *Phys. Rev. B*, 81(12):125304, 2010.

[44] Milan Orlita, Clément Faugeras, JM Schneider, Gérard Martinez, DK Maude, and Marek Potemski. Graphite from the viewpoint of landau level spectroscopy: An effective graphene bilayer and monolayer. *Phys. Rev. Lett.*, 102(16):166401, 2009.

[45] Mikito Koshino and Tsuneya Ando. Orbital diamagnetism in multilayer graphenes: Systematic study with the effective mass approximation. *Phys. Rev. B*, 76(8): 085425, 2007.

[46] M Orlita and M Potemski. Dirac electronic states in graphene systems: optical spectroscopy studies. *Semiconductor Science and Technology*, 25(6):063001, 2010.

[47] GI Finch and H Wilman. The diffraction of electrons by graphite. *Proceedings of the Royal Society of London. Series A, Mathematical and Physical Sciences*, 155 (885):345–365, 1936.

[48] A Taylor and D Laidler. Anomalous diffractions in the hull-debye-scherrer spectrum of graphite. *Nature*, 146(130), 1940.

[49] H Lipson and AR Stokes. The structure of graphite. In *Proceedings of the Royal Society of London A: Mathematical, Physical and Engineering Sciences*, volume 181, pages 101–105. The Royal Society, 1942.

[50] Hongki Min and AH MacDonald. Chiral decomposition in the electronic structure of graphene multilayers. *Phys. Rev. B*, 77(15):155416, 2008.

[51] Shengjun Yuan, Rafael Roldán, and Mikhail I Katsnelson. Landau level spectrum of aba-and abc-stacked trilayer graphene. *Phys. Rev. B*, 84(12):125455, 2011.

[52] Ching-Hong Ho, Cheng-Peng Chang, and Ming-Fa Lin. Evolution and dimensional crossover from the bulk subbands in abc-stacked graphene to a three-dimensional dirac cone structure in rhombohedral graphite. *Phys. Rev. B*, 93:075437, Feb 2016. doi: 10.1103/PhysRevB.93.075437.

[53] Debora Pierucci, Haikel Sediri, Mahdi Hajlaoui, Jean-Christophe Girard, Thomas Brumme, Matteo Calandra, Emilio Velez-Fort, Gilles Patriarche, Mathieu Silly, Gabriel Ferro, Veronique Souliere, Massimiliano Marangolo, Fausto Sirotti, Francesco Mauri, and Abdelkarim Ouerghi. Evidence for flat bands near the fermi level in epitaxial rhombohedral multilayer graphene. *ACS Nano*, 9(5):5432–5439, 2015.

[54] Y Lee, D Tran, K Myhro, J Velasco, N Gillgren, CN Lau, Y Barlas, JM Poumirol, D Smirnov, and F Guinea. Competition between spontaneous symmetry breaking and single-particle gaps in trilayer graphene. *Nat. Commun.*, 5:5656, December 2014.

[55] AA Burkov, MD Hook, and Leon Balents. Topological nodal semimetals. *Phys. Rev. B*, 84(23):235126, 2011.

[56] Tero T Heikkilä and Grigorii Efimovich Volovik. Dimensional crossover in topological matter: Evolution of the multiple dirac point in the layered system to the flat band on the surface. *JETP letters*, 93(2):59–65, 2011.

[57] F Guinea, AH Castro Neto, and NMR Peres. Electronic states and landau levels in graphene stacks. *Physical Review B*, 73(24):245426, 2006.

[58] Ruijuan Xiao, Ferenc Tasnadi, K Koepernik, JWF Venderbos, M Richter, and M Taut. Density functional investigation of rhombohedral stacks of graphene: Topological surface states, nonlinear dielectric response, and bulk limit. *Phys. Rev. B*, 84(16):165404, 2011.

[59] NB Kopnin, TT Heikkilä, and GE Volovik. High-temperature surface superconductivity in topological flat-band systems. *Physical Review B*, 83(22):220503, 2011.

[60] P Esquinazi, N García, J Barzola-Quiquia, P Rödiger, K Schindler, J-L Yao, and M Ziese. Indications for intrinsic superconductivity in highly oriented pyrolytic graphite. *Physical Review B*, 78(13):134516, 2008.

[61] Ana Ballestar, Jose Barzola-Quiquia, T Scheike, and P Esquinazi. Josephson-coupled superconducting regions embedded at the interfaces of highly oriented pyrolytic graphite. *New Journal of Physics*, 15(2):023024, 2013.

[62] R Ricardo Da Silva, JHS Torres, and Y Kopelevich. Indication of superconductivity at 35 k in graphite-sulfur composites. *Physical review letters*, 87(14):147001, 2001.

[63] T Scheike, W Böhlmann, P Esquinazi, J Barzola-Quiquia, A Ballestar, and A Setzer. Can doping graphite trigger room temperature superconductivity? evidence for granular high-temperature superconductivity in water-treated graphite powder. *Advanced Materials*, 24(43):5826–5831, 2012.

[64] FJ Ribeiro, A Latge, M Pacheco, and Z Barticevic. Quantum dots under electric and magnetic fields: Impurity-related electronic properties. *Journal of applied physics*, 82(1):270–274, 1997.

[65] Ch Sikorski and U Merkt. Spectroscopy of electronic states in insb quantum dots. *Physical review letters*, 62(18):2164, 1989.

[66] W Hansen, TP Smith III, KY Lee, JA Brum, CM Knoedler, JM Hong, and DP Kern. Zeeman bifurcation of quantum-dot spectra. *Physical review letters*, 62(18):2168, 1989.

[67] Jason R Petta, Alexander Comstock Johnson, Jacob M Taylor, Edward A Laird, Amir Yacoby, Mikhail D Lukin, Charles M Marcus, Micah P Hanson, and Arthur C Gossard. Coherent manipulation of coupled electron spins in semiconductor quantum dots. *Science*, 309(5744):2180–2184, 2005.

[68] Daniel C Tsui, Horst L Stormer, and Arthur C Gossard. Two-dimensional magnetotransport in the extreme quantum limit. *Physical Review Letters*, 48(22):1559, 1982.

[69] Michael Tinkham. *Introduction to superconductivity*. Courier Corporation, 1996.

[70] GM Luke, Y Fudamoto, KM Kojima, MI Larkin, J Merrin, B Nachumi, YJ Uemura, Y Maeno, ZQ Mao, Y Mori, et al. Time-reversal symmetry-breaking superconductivity in sr2ruo4. *Nature*, 394(6693):558–561, 1998.

[71] L. D. LANDAU and E. M. LIFSHITZ. *COURSE OF THEORETICAL PHYSICS*, volume 3. BUTTERWORTH-HEINEMANN, third edition, 1977.

[72] R Peierls. On the theory of diamagnetism of conduction electrons. *Z. Phys*, 80: 763–791, 1933.

[73] John David Jackson. *Classical electrodynamics*, volume 3. Wiley New York etc., 1962.

[74] Edward McCann and Vladimir I Falko. Landau-level degeneracy and quantum hall effect in a graphite bilayer. *Phys. Rev. Lett.*, 96(8):086805, 2006.

[75] Younes Henni, Hector Pablo Ojeda Collado, Karol Nogajewski, Maciej R Molas, Gonzalo Usaj, Carlos A Balseiro, Milan Orlita, Marek Potemski, and Clement Faugeras. Rhombohedral multilayer graphene: a magneto-raman scattering study. *Nano Letters*, 2016.

[76] Chandrasekhara Venkata Raman and Kariamanikkam Srinivasa Krishnan. A new type of secondary radiation. *Nature*, 121:501–502, 1928.

[77] Gr Landsberg and L Mandelstam. Über die lichtzerstreuung in kristallen. *Zeitschrift für Physik*, 50(11-12):769–780, 1928.

[78] Ado Jorio, Mildred S Dresselhaus, Riichiro Saito, and Gene Dresselhaus. *Raman spectroscopy in graphene related systems*. John Wiley & Sons, 2011.

[79] Peter Y Yu and Manuel Cardona. *Fundamentals of semiconductors*. Springer, 2005.

[80] YU Peter and Manuel Cardona. *Fundamentals of semiconductors: physics and materials properties*. Springer Science & Business Media, 2010.

[81] John R Ferraro. *Introductory raman spectroscopy*. Academic press, 2003.

[82] Mildred S Dresselhaus, Gene Dresselhaus, and Ado Jorio. *Group theory: application to the physics of condensed matter*. Springer Science & Business Media, 2007.

[83] LM Malard, MA Pimenta, G Dresselhaus, and MS Dresselhaus. Raman spectroscopy in graphene. *Physics Reports*, 473(5):51–87, 2009.

[84] Andrea C Ferrari and Denis M Basko. Raman spectroscopy as a versatile tool for studying the properties of graphene. *Nature nanotechnology*, 8(4):235–246, 2013.

[85] Alexander Grüneis, J Serrano, A Bosak, M Lazzeri, Sergeij L Molodtsov, Ludger Wirtz, Claudio Attaccalite, M Krisch, Angel Rubio, F Mauri, et al. Phonon surface mapping of graphite: Disentangling quasi-degenerate phonon dispersions. *Physical Review B*, 80(8):085423, 2009.

[86] J Maultzsch, S Reich, C Thomsen, H Requardt, and P Ordejón. Phonon dispersion in graphite. *Physical review letters*, 92(7):075501, 2004.

[87] Ado Jorio and Luiz Gustavo Cançado. Perspectives on raman spectroscopy of graphene-based systems: from the perfect two-dimensional surface to charcoal. *Physical Chemistry Chemical Physics*, 14(44):15246–15256, 2012.

[88] M Ramsteiner and J Wagner. Resonant raman scattering of hydrogenated amorphous carbon: Evidence for π-bonded carbon clusters. *Applied physics letters*, 51 (17):1355–1357, 1987.

[89] Istvan Pócsik, Martin Hundhausen, Margit Koós, and Lothar Ley. Origin of the d peak in the raman spectrum of microcrystalline graphite. *Journal of Non-Crystalline Solids*, 227:1083–1086, 1998.

[90] MJ Matthews, MA Pimenta, G Dresselhaus, MS Dresselhaus, and M Endo. Origin of dispersive effects of the raman d band in carbon materials. *Physical Review B*, 59(10):R6585, 1999.

[91] AC Ferrari, JC Meyer, V Scardaci, C Casiraghi, Michele Lazzeri, Francesco Mauri, S Piscanec, Da Jiang, KS Novoselov, S Roth, et al. Raman spectrum of graphene and graphene layers. *Physical review letters*, 97(18):187401, 2006.

[92] C Thomsen and S Reich. Double resonant raman scattering in graphite. *Phys. Rev. Lett.*, 85(24):5214, 2000.

[93] Stephanie Reich and Christian Thomsen. Raman spectroscopy of graphite. *Philosophical Transactions of the Royal Society of London A: Mathematical, Physical and Engineering Sciences*, 362(1824):2271–2288, 2004.

[94] DL Mafra, G Samsonidze, LM Malard, DC Elias, JC Brant, F Plentz, ES Alves, and MA Pimenta. Determination of la and to phonon dispersion relations of graphene near the dirac point by double resonance raman scattering. *Physical Review B*, 76(23):233407, 2007.

[95] Zhiqiang Luo, Chunxiao Cong, Jun Zhang, Qihua Xiong, and Ting Yu. Direct observation of inner and outer g band double-resonance raman scattering in free standing graphene. *Applied Physics Letters*, 100(24):243107, 2012.

[96] Stéphane Berciaud, Xianglong Li, Han Htoon, Louis E Brus, Stephen K Doorn, and Tony F Heinz. Intrinsic line shape of the raman 2d-mode in freestanding graphene monolayers. *Nano letters*, 13(8):3517–3523, 2013.

[97] PH Tan, WP Han, WJ Zhao, ZH Wu, K Chang, H Wang, YF Wang, N Bonini, N Marzari, N Pugno, G Savini, A Lombardo, and A C Ferrari. The shear mode of multilayer graphene. *Nature materials*, 11(4):294–300, 2012.

[98] Chun Hung Lui and Tony F Heinz. Measurement of layer breathing mode vibrations in few-layer graphene. *Physical Review B*, 87(12):121404, 2013.

[99] LG Cançado, A Reina, J Kong, and MS Dresselhaus. Geometrical approach for the study of g band in the raman spectrum of monolayer graphene, bilayer graphene, and bulk graphite. *Physical Review B*, 77(24):245408, 2008.

[100] Rohit Narula and Stephanie Reich. Double resonant raman spectra in graphene and graphite: A two-dimensional explanation of the raman amplitude. *Physical Review B*, 78(16):165422, 2008.

[101] Denis M Basko. Theory of resonant multiphonon raman scattering in graphene. *Physical Review B*, 78(12):125418, 2008.

[102] Duhee Yoon, Hyerim Moon, Young-Woo Son, G Samsonidze, Bae Ho Park, Jin Bae Kim, YoungPak Lee, and Hyeonsik Cheong. Strong polarization dependence of double-resonant raman intensities in graphene. *Nano letters*, 8(12):4270–4274, 2008.

[103] Satyaprakash Sahoo, R Palai, and RS Katiyar. Polarized raman scattering in monolayer, bilayer, and suspended bilayer graphene. *Journal of Applied Physics*, 110(4):044320, 2011.

[104] Chunxiao Cong, Ting Yu, Kentaro Sato, Jingzhi Shang, Riichiro Saito, Gene F Dresselhaus, and Mildred S Dresselhaus. Raman characterization of aba-and abc-stacked trilayer graphene. *ACS nano*, 5(11):8760–8768, 2011.

[105] Zhao Y. Rong and Pieter Kuiper. Electronic effects in scanning tunneling microscopy: Moiré pattern on a graphite surface. *Phys. Rev. B*, 48:17427–17431, Dec 1993. doi: 10.1103/PhysRevB.48.17427. URL http://link.aps.org/doi/10.1103/PhysRevB.48.17427.

[106] Konstantin V Emtsev, Aaron Bostwick, Karsten Horn, Johannes Jobst, Gary L Kellogg, Lothar Ley, Jessica L McChesney, Taisuke Ohta, Sergey A Reshanov, Jonas Röhrl, et al. Towards wafer-size graphene layers by atmospheric pressure graphitization of silicon carbide. *Nature materials*, 8(3):203–207, 2009.

[107] Wei Yang, Guorui Chen, Zhiwen Shi, Cheng-Cheng Liu, Lianchang Zhang, Guibai Xie, Meng Cheng, Duoming Wang, Rong Yang, Dongxia Shi, et al. Epitaxial growth of single-domain graphene on hexagonal boron nitride. *Nature materials*, 12(9):792–797, 2013.

[108] Ado Jorio and Luiz Gustavo Cançado. Raman spectroscopy of twisted bilayer graphene. *Solid State Communications*, 175:3–12, 2013.

[109] JMB Lopes Dos Santos, NMR Peres, and AH Castro Neto. Graphene bilayer with a twist: Electronic structure. *Physical review letters*, 99(25):256802, 2007.

[110] Sylvain Latil, Vincent Meunier, and Luc Henrard. Massless fermions in multilayer graphitic systems with misoriented layers: Ab initio calculations and experimental fingerprints. *Physical Review B*, 76(20):201402, 2007.

[111] G Trambly de Laissardière, Didier Mayou, and Laurence Magaud. Localization of dirac electrons in rotated graphene bilayers. *Nano letters*, 10(3):804–808, 2010.

[112] ML Sadowski, G Martinez, M Potemski, C Berger, and WA De Heer. Landau level spectroscopy of ultrathin graphite layers. *Phys. Rev. Lett.*, 97(26):266405, 2006.

[113] ML Sadowski, G Martinez, M Potemski, C Berger, and Walt A de Heer. Magnetospectroscopy of epitaxial few-layer graphene. *Solid state communications*, 143 (1):123–125, 2007.

[114] Milan Orlita, Clément Faugeras, Gérard Martinez, DK Maude, ML Sadowski, and Marek Potemski. Dirac fermions at the h point of graphite: magnetotransmission studies. *Physical review letters*, 100(13):136403, 2008.

[115] Milan Orlita, Clement Faugeras, J Borysiuk, JM Baranowski, W Strupiński, Mike Sprinkle, Claire Berger, Walt A De Heer, DM Basko, G Martinez, et al. Magneto-optics of bilayer inclusions in multilayered epitaxial graphene on the carbon face of sic. *Physical Review B*, 83(12):125302, 2011.

[116] Clément Faugeras, Anouck Nerrière, Marek Potemski, Ather Mahmood, Erik Dujardin, Claire Berger, and WA De Heer. Few-layer graphene on sic, pyrolitic graphite, and graphene: A raman scattering study. *App. Phys. Lett.*, 92(1):011914, 2008.

[117] A Luican, Guohong Li, A Reina, J Kong, RR Nair, Konstantin S Novoselov, Andre K Geim, and EY Andrei. Single-layer behavior and its breakdown in twisted graphene layers. *Physical review letters*, 106(12):126802, 2011.

[118] Kwanpyo Kim, Sinisa Coh, Liang Z Tan, William Regan, Jong Min Yuk, Eric Chatterjee, MF Crommie, Marvin L Cohen, Steven G Louie, and A Zettl. Raman spectroscopy study of rotated double-layer graphene: misorientation-angle dependence of electronic structure. *Physical review letters*, 108(24):246103, 2012.

[119] Rui He, Ting-Fung Chung, Conor Delaney, Courtney Keiser, Luis A Jauregui, Paul M Shand, CC Chancey, Yanan Wang, Jiming Bao, and Yong P Chen. Observation of low energy raman modes in twisted bilayer graphene. *Nano letters*, 13(8):3594–3601, 2013.

[120] Allan H MacDonald and Rafi Bistritzer. Materials science: graphene moiré mystery solved? *Nature*, 474(7352):453–454, 2011.

[121] vCH Johansson and JO Linde. Gitterstruktur und elektrisches leitvermögen der mischkristallreihen au-cu, pd-cu und pt-cu. *Annalen der Physik*, 387(4):449–478, 1927.

[122] Victor Carozo, Clara M Almeida, Erlon HM Ferreira, Luiz Gustavo Cancado, Carlos Alberto Achete, and Ado Jorio. Raman signature of graphene superlattices. *Nano letters*, 11(11):4527–4534, 2011.

[123] Cheol-Hwan Park, Li Yang, Young-Woo Son, Marvin L Cohen, and Steven G Louie. Anisotropic behaviours of massless dirac fermions in graphene under periodic potentials. *Nature Physics*, 4(3):213–217, 2008.

[124] Cheol-Hwan Park, Li Yang, Young-Woo Son, Marvin L Cohen, and Steven G Louie. New generation of massless dirac fermions in graphene under external periodic potentials. *Physical review letters*, 101(12):126804, 2008.

[125] Matthew Yankowitz, Jiamin Xue, Daniel Cormode, Javier D Sanchez-Yamagishi, K Watanabe, T Taniguchi, Pablo Jarillo-Herrero, Philippe Jacquod, and Brian J LeRoy. Emergence of superlattice dirac points in graphene on hexagonal boron nitride. *Nature Physics*, 8(5):382–386, 2012.

[126] Zhi-Guo Chen, Zhiwen Shi, Wei Yang, Xiaobo Lu, You Lai, Hugen Yan, Feng Wang, Guangyu Zhang, and Zhiqiang Li. Observation of an intrinsic bandgap and landau level renormalization in graphene/boron-nitride heterostructures. *Nature communications*, 5, 2014.

[127] CR Dean, L Wang, P Maher, C Forsythe, F Ghahari, Y Gao, J Katoch, M Ishigami, P Moon, M Koshino, T Taniguchi, K Watanabe, K L Shepard, J Hone, and P Kim. Hofstadter/'s butterfly and the fractal quantum hall effect in moire superlattices. *Nature*, 497(7451):598–602, 2013.

[128] G. L. Yu D. C. Elias R. Jalil A. A. Patel A. Mishchenko A. S. Mayorov C. R.Woods J. R.Wallbank M. Mucha-Kruczynski B. A. Piot M. Potemski I. V. Grigorieva K. S. Novoselov F. Guinea5 V. I. Falko A. K. Geim L. A. Ponomarenko, R. V. Gorbachev. Cloning of dirac fermions in graphene superlattices. *Nature*, 497(7451): 594–597, 2013.

[129] Hennrik Schmidt, Johannes C Rode, Dmitri Smirnov, and Rolf J Haug. Superlattice structures in twisted bilayers of folded graphene. *Nature communications*, 5, 2014.

[130] Guorui Chen Shuang Wu Guibai Xie Meng Cheng Duoming Wang Rong Yang Dongxia Shi Kenji Watanabe Takashi Taniguchi Christophe Voisin Bernard Placais Yuanbo Zhang Wei Yang, Xiaobo Lu and Guangyu Zhang. Hofstadter butterfly and many-body effects in epitaxial graphene superlattice. *Nano letters*, 16(4): 2387–2392, 2016.

[131] E Tosatti and L Pietrelli. *Fractals in physics*. Elsevier, 2012.

[132] J. S. Tu A. V. Kretinin Y. Cao R. Jalil F.Withers L. A. Ponomarenko B. A. Piot M. Potemski D. C. Elias-X. Chen K.Watanabe T. Taniguchi I. V. Grigorieva K. S. Novoselov V. I. Falko A. K. Geim A. Mishchenko G. L. Yu, R. V. Gorbachev. Hierarchy of hofstadter states and replica quantum hall ferromagnetism in graphene superlattices. *Nature physics*, 10(7):525–529, 2014.

[133] J. S.Wu Z. Fei M. D. Goldflam F. Keilmann B. Özyilmaz A. H. Castro Neto X. M. Xie M. M. Fogler D. N. Basov G. X. Ni, H.Wang. Plasmons in graphene moire superlattices. *Nature materials*, 2015.

[134] Axel Eckmann, Jaesung Park, Huafeng Yang, Daniel Elias, Alexander S Mayorov, Geliang Yu, Rashid Jalil, Kostya S Novoselov, Roman V Gorbachev, Michele Lazzeri, et al. Raman fingerprint of aligned graphene/h-bn superlattices. *Nano letters*, 13(11):5242–5246, 2013.

[135] Awnish K Gupta, Youjian Tang, Vincent H Crespi, and Peter C Eklund. Nondispersive raman d band activated by well-ordered interlayer interactions in rotationally stacked bilayer graphene. *Physical Review B*, 82(24):241406, 2010.

[136] B. Fragneaud P. M. Bedê M. V. O. Moutinho J. Ribeiro-Soares N. F. Andrade A. G. Souza Filho M. J. S. Matos-4 B. Wang M. Terrones Rodrigo B. Capaz A. Jorio

C. A. Achete L. G. Cançado V. Carozo, C. M. Almeida. Resonance effects on the raman spectra of graphene superlattices. *Physical Review B*, 88(8):085401, 2013.

[137] Vitor M Pereira, AH Castro Neto, and NMR Peres. Tight-binding approach to uniaxial strain in graphene. *Physical Review B*, 80(4):045401, 2009.

[138] II Naumov and AM Bratkovsky. Gap opening in graphene by simple periodic inhomogeneous strain. *Physical Review B*, 84(24):245444, 2011.

[139] F Guinea, Baruch Horovitz, and P Le Doussal. Gauge field induced by ripples in graphene. *Physical Review B*, 77(20):205421, 2008.

[140] F Guinea, MI Katsnelson, and AK Geim. Energy gaps and a zero-field quantum hall effect in graphene by strain engineering. *Nature Physics*, 6(1):30–33, 2010.

[141] F Guinea, AK Geim, MI Katsnelson, and KS Novoselov. Generating quantizing pseudomagnetic fields by bending graphene ribbons. *Physical Review B*, 81(3): 035408, 2010.

[142] N Levy, SA Burke, KL Meaker, M Panlasigui, A Zettl, F Guinea, AH Castro Neto, and MF Crommie. Strain-induced pseudo–magnetic fields greater than 300 tesla in graphene nanobubbles. *Science*, 329(5991):544–547, 2010.

[143] Tony Low and F Guinea. Strain-induced pseudomagnetic field for novel graphene electronics. *Nano letters*, 10(9):3551–3554, 2010.

[144] Mikael C Rechtsman, Julia M Zeuner, Andreas Tünnermann, Stefan Nolte, Mordechai Segev, and Alexander Szameit. Strain-induced pseudomagnetic field and photonic landau levels in dielectric structures. *Nature Photonics*, 7(2):153–158, 2013.

[145] Shuze Zhu, Yinjun Huang, Nikolai N Klimov, David B Newell, Nikolai B Zhitenev, Joseph A Stroscio, Santiago D Solares, and Teng Li. Pseudomagnetic fields in a locally strained graphene drumhead. *Physical Review B*, 90(7):075426, 2014.

[146] TMG Mohiuddin, A Lombardo, RR Nair, A Bonetti, G Savini, R Jalil, N Bonini, DM Basko, C Galiotis, N Marzari, et al. Uniaxial strain in graphene by raman spectroscopy: G peak splitting, grüneisen parameters, and sample orientation. *Physical Review B*, 79(20):205433, 2009.

[147] Mingyuan Huang, Hugen Yan, Tony F Heinz, and James Hone. Probing strain-induced electronic structure change in graphene by raman spectroscopy. *Nano letters*, 10(10):4074–4079, 2010.

[148] Duhee Yoon, Young-Woo Son, and Hyeonsik Cheong. Strain-dependent splitting of the double-resonance raman scattering band in graphene. *Physical review letters*, 106(15):155502, 2011.

[149] Jakob Zabel, Rahul R Nair, Anna Ott, Thanasis Georgiou, Andre K Geim, Kostya S Novoselov, and Cinzia Casiraghi. Raman spectroscopy of graphene and bilayer under biaxial strain: bubbles and balloons. *Nano letters*, 12(2):617–621, 2012.

[150] Otakar Frank, Marcel Mohr, Janina Maultzsch, Christian Thomsen, Ibtsam Riaz, Rashid Jalil, Kostya S Novoselov, Georgia Tsoukleri, John Parthenios, Konstantinos Papagelis, et al. Raman 2d-band splitting in graphene: theory and experiment. *Acs Nano*, 5(3):2231–2239, 2011.

[151] Stefano Piscanec, Michele Lazzeri, John Robertson, Andrea C Ferrari, and Francesco Mauri. Optical phonons in carbon nanotubes: Kohn anomalies, peierls distortions, and dynamic effects. *Physical Review B*, 75(3):035427, 2007.

[152] Anindya Das, S Pisana, B Chakraborty, S Piscanec, SK Saha, UV Waghmare, KS Novoselov, HR Krishnamurthy, AK Geim, AC Ferrari, et al. Monitoring dopants by raman scattering in an electrochemically top-gated graphene transistor. *Nature nanotechnology*, 3(4):210–215, 2008.

[153] Jun Yan, Erik A Henriksen, Philip Kim, and Aron Pinczuk. Observation of anomalous phonon softening in bilayer graphene. *Physical review letters*, 101(13):136804, 2008.

[154] C Casiraghi, S Pisana, KS Novoselov, AK Geim, and AC Ferrari. Raman fingerprint of charged impurities in graphene. *Applied Physics Letters*, 91(23):233108, 2007.

[155] Simone Pisana, Michele Lazzeri, Cinzia Casiraghi, Kostya S Novoselov, Andre K Geim, Andrea C Ferrari, and Francesco Mauri. Breakdown of the adiabatic born–oppenheimer approximation in graphene. *Nature materials*, 6(3):198–201, 2007.

[156] Jun Yan, Yuanbo Zhang, Philip Kim, and Aron Pinczuk. Electric field effect tuning of electron-phonon coupling in graphene. *Physical review letters*, 98(16): 166802, 2007.

[157] Martin Kalbac, Alfonso Reina-Cecco, Hootan Farhat, Jing Kong, Ladislav Kavan, and Mildred S Dresselhaus. The influence of strong electron and hole doping on the raman intensity of chemical vapor-deposition graphene. *Acs Nano*, 4(10): 6055–6063, 2010.

[158] Oleksiy Kashuba and Vladimir I Falko. Signature of electronic excitations in the raman spectrum of graphene. *Phys. Rev. B*, 80(24):241404, 2009.

[159] Oleksiy Kashuba and Vladimir I. Falko. Role of electronic excitations in magneto-raman spectra of graphene. *New J. Phys.*, 14:105016, Oct 2012.

[160] P Kossacki, C Faugeras, M Kühne, M Orlita, AAL Nicolet, JM Schneider, DM Basko, Yu I Latyshev, and M Potemski. Electronic excitations and electron-phonon coupling in bulk graphite through raman scattering in high magnetic fields. *Phys. Rev. B*, 84(23):235138, 2011.

[161] H. Farhat, S. Berciaud, M. Kalbac, R. Saito, T. F. Heinz, M. S. Dresselhaus, and J. Kong. Observation of electronic raman scattering in metallic carbon nanotubes. *Phys. Rev. Lett.*, 107:157401, Oct 2011. doi: 10.1103/PhysRevLett.107.157401.

[162] Yu S Ponosov, AV Ushakov, and SV Streltsov. Electronic raman scattering in graphite and single-layer and few-layer graphene. *Phys. Rev. B*, 91(19):195435, 2015.

[163] E Riccardi, M-A Méasson, M Cazayous, A Sacuto, and Y Gallais. Gate-dependent electronic raman scattering in graphene. *Physical review letters*, 116(6):066805, 2016.

[164] M Kuehne, C Faugeras, P Kossacki, AAL Nicolet, M Orlita, Yu I Latyshev, and M Potemski. Polarization-resolved magneto-raman scattering of graphenelike domains on natural graphite. *Phys. Rev. B*, 85(19):195406, 2012.

[165] C Faugeras, J Binder, AAL Nicolet, P Leszczynski, P Kossacki, A Wysmolek, M Orlita, and M Potemski. A micro-magneto-raman scattering study of graphene on a bulk graphite substrate. *EPL (Europhysics Letters)*, 108(2):27011, 2014.

[166] C Faugeras, S Berciaud, P Leszczynski, Y Henni, K Nogajewski, M Orlita, T Taniguchi, K Watanabe, C Forsythe, P Kim, et al. Landau level spectroscopy of electron-electron interactions in graphene. *Physical review letters*, 114(12):126804, 2015.

[167] Jens Martin, N Akerman, G Ulbricht, T Lohmann, JH v Smet, K Von Klitzing, and Amir Yacoby. Observation of electron–hole puddles in graphene using a scanning single-electron transistor. *Nature Physics*, 4(2):144–148, 2008.

[168] Yuanbo Zhang, Victor W Brar, Caglar Girit, Alex Zettl, and Michael F Crommie. Origin of spatial charge inhomogeneity in graphene. *Nature Physics*, 5(10):722–726, 2009.

[169] Clément Faugeras, Mario Amado, Piotr Kossacki, Milan Orlita, Matthias Kühne, AAL Nicolet, Yu I Latyshev, and Marek Potemski. Magneto-raman scattering of graphene on graphite: Electronic and phonon excitations. *Phys. Rev. Lett.*, 107 (3):036807, 2011.

[170] DM Basko, P Leszczynski, C Faugeras, J Binder, AAL Nicolet, P Kossacki, M Orlita, and M Potemski. Multiple magneto-phonon resonances in graphene. *2D Materials*, 3(1):015004, 2016.

[171] Marcin Mucha-Kruczynski, Oleksiy Kashuba, and Vladimir I Falko. Spectral features due to inter-landau-level transitions in the raman spectrum of bilayer graphene. *Physical Review B*, 82(4):045405, 2010.

[172] W. W. Toy, M. S. Dresselhaus, and G. Dresselhaus. Minority carriers in graphite and the *h*-point magnetoreflection spectra. *Phys. Rev. B*, 15:4077–4090, Apr 1977. doi: 10.1103/PhysRevB.15.4077. URL http://link.aps.org/doi/10.1103/PhysRevB.15.4077.

[173] SY Zhou, G-H Gweon, J Graf, AV Fedorov, CD Spataru, RD Diehl, Y Kopelevich, D-H Lee, Steven G Louie, and A Lanzara. First direct observation of dirac fermions in graphite. *Nature physics*, 2(9):595–599, 2006.

[174] Kenji Nakao. Landau level structure and magnetic breakthrough in graphite. *T. J. Phys. Soc. Jpn.*, 40(3):761–768, 1976.

[175] AF Garcia-Flores, H Terashita, E Granado, and Y Kopelevich. Landau levels in bulk graphite by raman spectroscopy. *Physical Review B*, 79(11):113105, 2009.

[176] John Bardeen, Leon N Cooper, and John Robert Schrieffer. Theory of superconductivity. *Physical Review*, 108(5):1175, 1957.

[177] S Piscanec, M Lazzeri, Francesco Mauri, AC Ferrari, and J Robertson. Kohn anomalies and electron-phonon interactions in graphite. *Physical review letters*, 93(18):185503, 2004.

[178] Michele Lazzeri, Stefano Piscanec, Francesco Mauri, AC Ferrari, and J Robertson. Phonon linewidths and electron-phonon coupling in graphite and nanotubes. *Physical review B*, 73(15):155426, 2006.

[179] Zhen Yao, Charles L Kane, and Cees Dekker. High-field electrical transport in single-wall carbon nanotubes. *Physical Review Letters*, 84(13):2941, 2000.

[180] Ji-Yong Park, Sami Rosenblatt, Yuval Yaish, Vera Sazonova, Hande Üstünel, Stephan Braig, TA Arias, Piet W Brouwer, and Paul L McEuen. Electron-phonon

scattering in metallic single-walled carbon nanotubes. *Nano Letters*, 4(3):517–520, 2004.

[181] Ali Javey, Jing Guo, Magnus Paulsson, Qian Wang, David Mann, Mark Lundstrom, and Hongjie Dai. High-field quasiballistic transport in short carbon nanotubes. *Physical Review Letters*, 92(10):106804, 2004.

[182] Vasili Perebeinos, J Tersoff, and Phaedon Avouris. Electron-phonon interaction and transport in semiconducting carbon nanotubes. *Physical review letters*, 94(8): 086802, 2005.

[183] Michele Lazzeri, S Piscanec, Francesco Mauri, AC Ferrari, and J Robertson. Electron transport and hot phonons in carbon nanotubes. *Physical review letters*, 95 (23):236802, 2005.

[184] S Hameau, Y Guldner, O Verzelen, R Ferreira, G Bastard, J Zeman, A Lemaitre, and JM Gérard. Strong electron-phonon coupling regime in quantum dots: evidence for everlasting resonant polarons. *Physical review letters*, 83(20):4152, 1999.

[185] Zhibin Lin, Leonid V Zhigilei, and Vittorio Celli. Electron-phonon coupling and electron heat capacity of metals under conditions of strong electron-phonon nonequilibrium. *Physical Review B*, 77(7):075133, 2008.

[186] W Kohn. Image of the fermi surface in the vibration spectrum of a metal. *Physical Review Letters*, 2(9):393, 1959.

[187] Neil W Ashcroft and N David Mermin. Solid state physics. 1976.

[188] A. C. Ferrari F. Mauri J. Robertson S. Piscanec, M. Lazzeri. Kohn anomalies in graphite and nanotubes. *Mater. Res. Soc. Symp. Proc.*, Vol. 858E, 2005.

[189] I Milošević, N Kepčija, E Dobardžić, M Damnjanović, M Mohr, J Maultzsch, and C Thomsen. Kohn anomaly in graphene. *Materials Science and Engineering: B*, 176(6):510–511, 2011.

[190] Tsuneya Ando. Anomaly of optical phonon in monolayer graphene. *Journal of the physical society of Japan*, 75(12):124701, 2006.

[191] AH Castro Neto and Francisco Guinea. Electron-phonon coupling and raman spectroscopy in graphene. *Physical Review B*, 75(4):045404, 2007.

[192] Tsuneya Ando. Anomaly of optical phonons in bilayer graphene. *Journal of the Physical Society of Japan*, 76(10):104711, 2007.

[193] Clément Faugeras, Mario Amado, Piotr Kossacki, Milan Orlita, Mike Sprinkle, Claire Berger, WA De Heer, and Marek Potemski. Tuning the electron-phonon coupling in multilayer graphene with magnetic fields. *Phys. Rev. Lett.*, 103(18): 186803, 2009.

[194] Tsuneya Ando. Magnetic oscillation of optical phonon in graphene. *T. J. Phys. Soc. Jpn.*, 76(2):024712, 2007.

[195] Przemyslaw Leszczynski, Zheng Han, Aurelien AL Nicolet, Benjamin A Piot, Piotr Kossacki, Milan Orlita, Vincent Bouchiat, Denis M Basko, Marek Potemski, and Clement Faugeras. Electrical switch to the resonant magneto-phonon effect in graphene. *Nano letters*, 14(3):1460–1466, 2014.

[196] MO Goerbig, J-N Fuchs, K Kechedzhi, and Vladimir I Falko. Filling-factor-dependent magnetophonon resonance in graphene. *Phys. Rev. Lett.*, 99(8):087402, 2007.

[197] Christoph Neumann, Sven Reichardt, Marc Dro geler, Bernat Terrés, Kenji Watanabe, Takashi Taniguchi, Bernd Beschoten, Slava V Rotkin, and Christoph Stampfer. Low b field magneto-phonon resonances in single-layer and bilayer graphene. *Nano letters*, 15(3):1547–1552, 2015.

[198] Walter Kohn. Cyclotron resonance and de haas-van alphen oscillations of an interacting electron gas. *Physical Review*, 123(4):1242, 1961.

[199] Andrew Iyengar, Jianhui Wang, HA Fertig, and Luis Brey. Excitations from filled landau levels in graphene. *Physical Review B*, 75(12):125430, 2007.

[200] K Shizuya. Many-body corrections to cyclotron resonance in monolayer and bilayer graphene. *Physical Review B*, 81(7):075407, 2010.

[201] Johannes Hofmann, Edwin Barnes, and S Das Sarma. Why does graphene behave as a weakly interacting system? *Physical review letters*, 113(10):105502, 2014.

[202] J González, F Guinea, and MAH Vozmediano. Marginal-fermi-liquid behavior from two-dimensional coulomb interaction. *Physical Review B*, 59(4):R2474, 1999.

[203] J. González, F. Guinea, and M.A.H. Vozmediano. Non-fermi liquid behavior of electrons in the half-filled honeycomb lattice (a renormalization group approach). *Nuclear Physics B*, 424(3):595 – 618, 1994. ISSN 0550-3213. doi: http://dx.doi.org/10.1016/0550-3213(94)90410-3. URL http://www.sciencedirect.com/science/article/pii/0550321394904103.

[204] Robert B Laughlin. Anomalous quantum hall effect: an incompressible quantum fluid with fractionally charged excitations. *Physical Review Letters*, 50(18):1395, 1983.

[205] Jainendra K Jain. *Composite fermions*. Cambridge University Press, 2007.

[206] Kirill I Bolotin, Fereshte Ghahari, Michael D Shulman, Horst L Stormer, and Philip Kim. Observation of the fractional quantum hall effect in graphene. *Nature*, 462(7270):196–199, 2009.

[207] Xu Du, Ivan Skachko, Fabian Duerr, Adina Luican, and Eva Y Andrei. Fractional quantum hall effect and insulating phase of dirac electrons in graphene. *Nature*, 462(7270):192–195, 2009.

[208] Patrick Maher, Lei Wang, Yuanda Gao, Carlos Forsythe, Takashi Taniguchi, Kenji Watanabe, Dmitry Abanin, Zlatko Papić, Paul Cadden-Zimansky, James Hone, et al. Tunable fractional quantum hall phases in bilayer graphene. *Science*, 345 (6192):61–64, 2014.

[209] Dong-Keun Ki, Vladimir I Falko, Dmitry A Abanin, and Alberto F Morpurgo. Observation of even denominator fractional quantum hall effect in suspended bilayer graphene. *Nano letters*, 14(4):2135–2139, 2014.

[210] Benjamin E Feldman, Jens Martin, and Amir Yacoby. Broken-symmetry states and divergent resistance in suspended bilayer graphene. *Nature Physics*, 5(12): 889–893, 2009.

[211] Thiti Taychatanapat, Kenji Watanabe, Takashi Taniguchi, and Pablo Jarillo-Herrero. Quantum hall effect and landau-level crossing of dirac fermions in trilayer graphene. *Nature Physics*, 7(8):621–625, 2011.

[212] Anya L Grushina, Dong-Keun Ki, Mikito Koshino, Aurelien AL Nicolet, Clément Faugeras, Edward McCann, Marek Potemski, and Alberto F Morpurgo. Insulating state in tetralayers reveals an even–odd interaction effect in multilayer graphene. *Nature communications*, 6, 2015.

[213] J González, F Guinea, and MAH Vozmediano. Electrostatic screening in fullerene molecules. *Modern Physics Letters B*, 7(24n25):1593–1599, 1993.

[214] Valeri N Kotov, Bruno Uchoa, Vitor M Pereira, F Guinea, and AH Castro Neto. Electron-electron interactions in graphene: Current status and perspectives. *Reviews of Modern Physics*, 84(3):1067, 2012.

[215] DC Elias, RV Gorbachev, AS Mayorov, SV Morozov, AA Zhukov, P Blake, LA Ponomarenko, IV Grigorieva, KS Novoselov, F Guinea, et al. Dirac cones reshaped by interaction effects in suspended graphene. *Nature Physics*, 7(9):701–704, 2011.

[216] DN Basov, MM Fogler, A Lanzara, Feng Wang, Yuanbo Zhang, et al. Colloquium: graphene spectroscopy. *Reviews of Modern Physics*, 86(3):959, 2014.

[217] Z Jiang, EA Henriksen, LC Tung, Y-J Wang, ME Schwartz, MY Han, P Kim, and HL Stormer. Infrared spectroscopy of landau levels of graphene. *Physical review letters*, 98(19):197403, 2007.

[218] Cory R Dean, Andrea F Young, Inanc Meric, Chris Lee, Lei Wang, S Sorgenfrei, K Watanabe, T Taniguchi, P Kim, KL Shepard, et al. Boron nitride substrates for high-quality graphene electronics. *Nature nanotechnology*, 5(10):722–726, 2010.

[219] CR Dean, AF Young, Pet Cadden-Zimansky, L Wang, H Ren, K Watanabe, T Taniguchi, P Kim, J Hone, and KL Shepard. Multicomponent fractional quantum hall effect in graphene. *Nature Physics*, 7(9):693–696, 2011.

[220] Aaron Bostwick, Florian Speck, Thomas Seyller, Karsten Horn, Marco Polini, Reza Asgari, Allan H MacDonald, and Eli Rotenberg. Observation of plasmarons in quasi-freestanding doped graphene. *Science*, 328(5981):999–1002, 2010.

[221] Choongyu Hwang, David A Siegel, Sung-Kwan Mo, William Regan, Ariel Ismach, Yuegang Zhang, Alex Zettl, and Alessandra Lanzara. Fermi velocity engineering in graphene by substrate modification. *Scientific reports*, 2, 2012.

[222] David A Siegel, Cheol-Hwan Park, Choongyu Hwang, Jack Deslippe, Alexei V Fedorov, Steven G Louie, and Alessandra Lanzara. Many-body interactions in quasi-freestanding graphene. *Proceedings of the National Academy of Sciences*, 108(28):11365–11369, 2011.

[223] S Reich, AC Ferrari, R Arenal, A Loiseau, I Bello, and J Robertson. Resonant raman scattering in cubic and hexagonal boron nitride. *Physical Review B*, 71(20): 205201, 2005.

[224] C Faugeras, P Kossacki, A A L Nicolet, M Orlita, M Potemski, A Mahmood, and D M Basko. Probing the band structure of quadri-layer graphene with magneto-phonon resonance. *New Journal of Physics*, 14(9):095007, 2012. URL http://stacks.iop.org/1367-2630/14/i=9/a=095007.

[225] Jun Yan, Sarah Goler, Trevor D. Rhone, Melinda Han, Rui He, Philip Kim, Vittorio Pellegrini, and Aron Pinczuk. Observation of magnetophonon resonance

of dirac fermions in graphite. *Phys. Rev. Lett.*, 105:227401, Nov 2010. doi: 10.1103/PhysRevLett.105.227401. URL http://link.aps.org/doi/10.1103/PhysRevLett.105.227401.

[226] Caiyu Qiu, Xiaonan Shen, Bingchen Cao, Chunxiao Cong, Riichiro Saito, Jingjiang Yu, Mildred S Dresselhaus, and Ting Yu. Strong magnetophonon resonance induced triple g-mode splitting in graphene on graphite probed by micromagneto raman spectroscopy. *Physical Review B*, 88(16):165407, 2013.

[227] R Roldán, J-N Fuchs, and MO Goerbig. Spin-flip excitations, spin waves, and magnetoexcitons in graphene landau levels at integer filling factors. *Physical Review B*, 82(20):205418, 2010.

[228] Roland Gillen and John Robertson. Density functional theory screened-exchange approach for investigating electronical properties of graphene-related materials. *Physical Review B*, 82(12):125406, 2010.

[229] JW McClure. Electron energy band structure and electronic properties of rhombohedral graphite. *Carbon*, 7(4):425–432, 1969.

[230] Jia-An Yan, WY Ruan, and MY Chou. Phonon dispersions and vibrational properties of monolayer, bilayer, and trilayer graphene: Density-functional perturbation theory. *Physical review B*, 77(12):125401, 2008.

[231] S Butscher, F Milde, M Hirtschulz, E Malić, and A Knorr. Hot electron relaxation and phonon dynamics in graphene. *Applied Physics Letters*, 91(20):203103, 2007.

[232] Tobias Kampfrath, Luca Perfetti, Florian Schapper, Christian Frischkorn, and Martin Wolf. Strongly coupled optical phonons in the ultrafast dynamics of the electronic energy and current relaxation in graphite. *Physical review letters*, 95 (18):187403, 2005.

[233] Martin Hulman, Miroslav Haluska, Giusy Scalia, Dirk Obergfell, and Siegmar Roth. Effects of charge impurities and laser energy on raman spectra of graphene. *Nano letters*, 8(11):3594–3597, 2008.

[234] Duhee Yoon, Hyerim Moon, Young-Woo Son, Jin Sik Choi, Bae Ho Park, Young Hun Cha, Young Dong Kim, and Hyeonsik Cheong. Interference effect on raman spectrum of graphene on sio 2/si. *Phys. Rev. B*, 80(12):125422, 2009.

[235] Bruno R Carvalho, Leandro M Malard, Juliana M Alves, Cristiano Fantini, and Marcos A Pimenta. Symmetry-dependent exciton-phonon coupling in 2d and bulk mos 2 observed by resonance raman scattering. *Phys. Rev. Lett.*, 114(13):136403, 2015.

[236] Marcin Mucha-Kruczyński, Oleksiy Kashuba, and Vladimir I. Fal'ko. Spectral features due to inter-landau-level transitions in the raman spectrum of bilayer graphene. *Phys. Rev. B*, 82:045405, Jul 2010. doi: 10.1103/PhysRevB.82.045405. URL http://link.aps.org/doi/10.1103/PhysRevB.82.045405.

[237] Kirill I Bolotin, KJ Sikes, Zd Jiang, M Klima, G Fudenberg, J Hone, Ph Kim, and HL Stormer. Ultrahigh electron mobility in suspended graphene. *Solid State Communications*, 146(9):351–355, 2008.

[238] Alexander S Mayorov, Roman V Gorbachev, Sergey V Morozov, Liam Britnell, Rashid Jalil, Leonid A Ponomarenko, Peter Blake, Kostya S Novoselov, Kenji Watanabe, Takashi Taniguchi, et al. Micrometer-scale ballistic transport in encapsulated graphene at room temperature. *Nano letters*, 11(6):2396–2399, 2011.

[239] Masa Ishigami, JH Chen, WG Cullen, MS Fuhrer, and ED Williams. Atomic structure of graphene on sio2. *Nano letters*, 7(6):1643–1648, 2007.

[240] Chun Hung Lui, Li Liu, Kin Fai Mak, George W Flynn, and Tony F Heinz. Ultraflat graphene. *Nature*, 462(7271):339–341, 2009.

[241] AF Young, CR Dean, I Meric, S Sorgenfrei, H Ren, K Watanabe, T Taniguchi, J Hone, KL Shepard, and P Kim. Electronic compressibility of layer-polarized bilayer graphene. *Physical Review B*, 85(23):235458, 2012.

[242] EH Hwang, S Adam, and S Das Sarma. Carrier transport in two-dimensional graphene layers. *Physical review letters*, 98(18):186806, 2007.

[243] Jian-Hao Chen, Chaun Jang, Shudong Xiao, Masa Ishigami, and Michael S Fuhrer. Intrinsic and extrinsic performance limits of graphene devices on sio2. *Nature nanotechnology*, 3(4):206–209, 2008.

[244] LA Ponomarenko, R Yang, TM Mohiuddin, MI Katsnelson, KS Novoselov, SV Morozov, AA Zhukov, F Schedin, EW Hill, and AK Geim. Effect of a high-κ environment on charge carrier mobility in graphene. *Physical Review Letters*, 102(20): 206603, 2009.

[245] Myrsini Lafkioti, Benjamin Krauss, Timm Lohmann, Ute Zschieschang, Hagen Klauk, Klaus v Klitzing, and Jurgen H Smet. Graphene on a hydrophobic substrate: doping reduction and hysteresis suppression under ambient conditions. *Nano letters*, 10(4):1149–1153, 2010.

[246] Lei Liao, Jingwei Bai, Yongquan Qu, Yu Huang, and Xiangfeng Duan. Single-layer graphene on al2o3/si substrate: better contrast and higher performance of graphene transistors. *Nanotechnology*, 21(1):015705, 2009.

[247] Hugo Anders. Thin films in optics. *London: Focal Press, 1967*, 1, 1967.

[248] P Blake, EW Hill, AH Castro Neto, KS Novoselov, D Jiang, R Yang, TJ Booth, and AK Geim. Making graphene visible. *Applied Physics Letters*, 91(6):063124, 2007.

[249] C Casiraghi, Achim Hartschuh, E Lidorikis, Huihong Qian, Hayk Harutyunyan, Tobias Gokus, KS Novoselov, and AC Ferrari. Rayleigh imaging of graphene and graphene layers. *Nano letters*, 7(9):2711–2717, 2007.

[250] Inhwa Jung, Matthew Pelton, Richard Piner, Dmitriy A Dikin, Sasha Stankovich, Supinda Watcharotone, Martina Hausner, and Rodney S Ruoff. Simple approach for high-contrast optical imaging and characterization of graphene-based sheets. *Nano Letters*, 7(12):3569–3575, 2007.

[251] S Roddaro, P Pingue, V Piazza, V Pellegrini, and F Beltram. The optical visibility of graphene: interference colors of ultrathin graphite on sio2. *Nano letters*, 7(9): 2707–2710, 2007.

[252] DSL Abergel, Alan Russell, and Vladimir I Fal'ko. Visibility of graphene flakes on a dielectric substrate. *arXiv preprint arXiv:0705.0091*, 2007.

[253] J-C Charlier, PC Eklund, J Zhu, and AC Ferrari. Electron and phonon properties of graphene: their relationship with carbon nanotubes. In *Carbon nanotubes*, pages 673–709. Springer, 2007.